

Sheffield Hallam University

Conformational studies of lithium phenyl stearate.

BARRON, Christopher.

Available from the Sheffield Hallam University Research Archive (SHURA) at:

<http://shura.shu.ac.uk/19323/>

A Sheffield Hallam University thesis

This thesis is protected by copyright which belongs to the author.

The content must not be changed in any way or sold commercially in any format or medium without the formal permission of the author.

When referring to this work, full bibliographic details including the author, title, awarding institution and date of the thesis must be given.

Please visit <http://shura.shu.ac.uk/19323/> and <http://shura.shu.ac.uk/information.html> for further details about copyright and re-use permissions.

100322959 X

TELEPEN



Fines are charged at 50p per hour

10 OCT 2003

ProQuest Number: 10694204

All rights reserved

INFORMATION TO ALL USERS

The quality of this reproduction is dependent upon the quality of the copy submitted.

In the unlikely event that the author did not send a complete manuscript and there are missing pages, these will be noted. Also, if material had to be removed, a note will indicate the deletion.



ProQuest 10694204

Published by ProQuest LLC (2017). Copyright of the Dissertation is held by the Author.

All rights reserved.

This work is protected against unauthorized copying under Title 17, United States Code
Microform Edition © ProQuest LLC.

ProQuest LLC.
789 East Eisenhower Parkway
P.O. Box 1346
Ann Arbor, MI 48106 – 1346

Conformational Studies of Lithium Phenyl Stearate

by

Christopher Barron

A thesis submitted to the Council for National Academic Awards in partial fulfilment of the requirements for the degree of doctor of philosophy.

Sponsoring Establishment: Dept. of Applied Physics
Sheffield City Polytechnic.

Collaborating Establishment: Unilever Research
Port Sunlight.

Sheffield City Polytechnic Library

August 1991

REFERENCE ONLY



Conformational Studies of Lithium Phenyl Stearate
by Christopher Barron

Abstract

The structure and conformation of lithium phenyl stearate (and to a lesser extent, for comparative purposes, cadmium stearate) was investigated using Fourier transform infrared spectroscopy, and various modelling techniques. The infrared results for LiPS show that the aliphatic portion of the soap molecule is much more ordered at room temperature than had been expected, having only 0.62 and 0.60 gtg and gg defects per molecule respectively, where an isotropic chain would have 1.35 and 1.21 gtg and gg defects per chain respectively. As the temperature is increased the number of conformational defects increases continuously, until at $\approx 130^{\circ}\text{C}$ the chain reaches an isotropic degree of disorder. At this point the phase transition begins, so the chain reaches liquid like disorder before the phase transition begins.

Modelling of the phenyl stearic acid showed that the phenyl group was restricted to certain angle of rotation values, and that the bonds close to the phenyl group were prevented from attaining true rotational isomeric state conformations. gtg defects near the phenyl group were distorted only slightly from their usual angular position, and an additional band in the infrared spectrum of LiPS at 1363 cm^{-1} has been assigned to this distorted gtg/gtg' defect. The gg defects near the phenyl group have a much greater distortion (and energy) resulting in a much reduced probability of occurrence. The number of gg defects present at the phase transition ($\approx 130^{\circ}\text{C}$) was only 75% of that expected for an isotropic n-alkane of equivalent chain length, indicating that the four bonds nearest to the phenyl group have a reduced probability of forming a gg defect.

The modelling of the ionic core of LiPS gives a reasonable estimate of between 5.6 to 7.1Å for the core radius. When this is used to calculate the hexagonal cylinder diameter, at room temperature, along with the average chain extension, it gives a value for the cylinder diameter of between 33.9 to 36.8Å. The hexagonal lattice parameter determined by X-ray diffraction has a value 35.9Å. Also after the LiPS sample has gone through the phase transition beginning at $\approx 130^{\circ}\text{C}$, the hexagonal lattice parameter is 31.4Å while the cylinder diameter lies between 30.2 and 33.2Å.

Crystalline cadmium stearate was found to contain two crystal forms, orthorhombic which has lattice dimensions of $a_0=5.05\text{Å}$, $b_0=7.35\text{Å}$ and $c_0=48.6\text{Å}$ and the other either monoclinic or triclinic. In the reverse hexagonal phase, the cadmium stearate molecule behaves like an isotropic n-alkane of equivalent chain length. The model used to predict the core radius of divalent metal soaps gives rise to some inconsistencies: the cylinder diameter thus determined gives a result between 28.8Å to 31.7Å, while the lattice parameter determined by X-ray diffraction gives a value of 36.9Å. The assumption that the n-carboxylate ions in a divalent metal soap behave like two independent monovalent metal ion soaps appears to be incorrect.

Acknowledgements

The author would like to thank Dr S.J. Spells and Prof. J.S. Brooks for their organisation of the project and for their patience and guidance through out the investigation. The author would also like to thank the following people:

Dr M.P. McDonald for his discussions on the physical behaviour of soaps systems and additional suggestions for the project, and also Dr W.J. Harrison for providing materials and discussion in the initial stages of the project.

The staff at Unilever Research Port Sunlight for the use of equipment, but especially to Dr J. Tipping and Dr S. Johnson for their liaison and Dr A. Allen and the infrared spectroscopy department who provided access to their FTIR facilities.

Dr B. Taylor of the Dept. of Chemistry, Sheffield University for producing high resolution NMR spectra of various samples.

Dr C. Booth, Dept. of Chemistry, Manchester University, for the use of the Raman spectrometer.

The author would also like to give grateful thanks to the staff of the School of Science, Sheffield City Polytechnic who gave assistance during this project, but who are too numerous to mention.

Chapter 1

1 Amphiphilic mesophases	2
1.1 Thermotropic behaviour of alkali metal soaps .	2
1.1.1 Lithium soaps	3
1.1.2 Sodium Soaps	5
1.1.3 Other alkali metal soaps	8
1.2 Soaps of divalent metals	9
1.3 Phenyl stearic acid	13
1.3.1 Lithium phenyl stearate	14
1.4 Aims	15
1.5 References	16

1 Amphiphilic mesophases

Liquid crystalline phases, or mesophases, are thermodynamically distinct states of matter, that have differing degrees of order, lying between the long range order of crystalline solids and the long range statistical disorder of liquids and gases (1).

Amphiphilic mesophases are based not on the structural arrangements of individual molecules, as is the case with most liquid crystals (1), but on the arrangement of multi-molecular units (aggregation of molecules) termed "micelles". The formation of these amphiphilic mesophases depends broadly on two types of interaction (2,3,4), short range intramolecular interactions which determine the shape (disc, cylinder, sphere or sheet) and size, and the long range interactions determining the mutual orientation of the micelles (hexagonal, cubic or lamellar lattice).

Some of the simplest molecules to form amphiphilic mesophases are the salts of long chain carboxylic acids, the fatty acid soaps. These are capable of forming mesophases on heating (2,5) and the alkali metal soaps also form mesophases on the addition of a solvent, most commonly water (2-5). These phases and are known as thermotropic and lyotropic mesophases respectively.

1.1 Thermotropic behaviour of alkali metal soaps

The soaps of fatty acids can undergo a series of complex stepwise melting transitions involving one or more intermediate phase between the crystalline solid and isotropic liquid (2,5), depending on the carboxylic acid and the cation present.

1.1.1 Lithium soaps

Using X-ray diffraction, Gallot et al (6) investigated the thermotropic behaviour of the lithium soaps LiC_{10} ¹ to LiC_{18} , and found that each formed 2 crystalline lamellar (C.L.) structures. For N_c , the number of carbon atoms in the chain, being greater than or equal to 12, a 2 dimensional ribbon type structure (B.R.) was also observed. These structures were confirmed by Skoda (7), for LiC_{14} to LiC_{18} , using dilatometric investigation. Table 1.1 shows the phases and transition temperatures observed by Gallot and Skoulios (6), for long chain lithium soaps.

Ferloni et al (8,9,10), investigated all the lithium n-alkanoates from LiC_1 to LiC_{12} using DSC, confirming the transition temperatures of Gallot (6), but also found a remarkable odd/even effect for the transition temperature between the two lamellar crystalline phases. Although the temperature and enthalpy increases with increasing N_c , the number of carbon atoms, the transition temperatures and enthalpy were higher for odd chains lengths (LiC_9 and LiC_{11}) than for even chains lengths (LiC_8 , LiC_{10} and LiC_{12}) (8). The isotropic melting point shows no such behaviour, with the transition temperature decreasing with increasing chain length, and the enthalpy increasing up to LiC_{11} and then decreasing rapidly for LiC_{12} . Ferloni et al (9,10) also showed that for the lithium n-alkanoates, from LiC_1 to LiC_7 , only LiC_5 and LiC_7 showed the two crystalline lamellar forms. So we can conclude that for lithium alkanoates, only soaps with

¹ C_n refers to the n-carboxylic acid with n carbon atoms.

$N_c \geq 12$ show any thermotropic liquid crystalline phases.

Table 1.1 Thermotropic phases occurring on heating of lithium soaps from room temperature to isotropic melt.

LiC_{10}	LiC_{12}	LiC_{14}	LiC_{16}	LiC_{18}
C.L. ₁				
—39 ⁰ C—				
	—67 ⁰ C—			
		—87 ⁰ C—		
			—102 ⁰ C—	
				—122 ⁰ C—
C.L. ₂				
			—190 ⁰ C—	—190 ⁰ C—
			B.R.	B.R.
		—210 ⁰ C—	—211 ⁰ C	—215 ⁰ C
		B.R.		—219 ⁰ C—
	—229 ⁰ C—	—231 ⁰ C	—223 ⁰ C—	
	B.R.			
—238 ⁰ C—	—239 ⁰ C—	—239 ⁰ C—		
I	I	I	I	I

(N.B. not to scale)

C.L. is Crystalline Lamellar

B.R. is a 2 dimensional Ribbon lattice

I is the Isotropic Melt

1.1.2 Sodium Soaps

The phase behaviour of sodium soaps is much more complicated than the case of lithium soaps, and has been subjected to extensive studies. M.J. Vold (11) et al observed the phase behaviour of the even homologues from NaC_6 to NaC_{22} using polarising microscopy and dilatometric observations. The phases observed were named from their different textures and are labelled "Crystalline", "Curd", "Sub-waxy", "Waxy", "Super-waxy", "Sub-neat", "Neat" and Isotropic melt.

Skoulios and Luzzati (12) used X-ray diffraction to observe the even homologues from NaC_{12} to NaC_{18} . The different phases were found to result from the lattice changing from 3 to 2-dimensional order, from 2 to 1-dimensional order and becoming isotropic on melting. In the transition from crystalline to curd the lattice remains 3-dimensional with the short spacings changing slightly. The sharp crystalline spacings change to a single diffuse band at about 4.6\AA on transition from the curd to sub-waxy (in some cases waxy) phase. This is associated with the melting of the hydrocarbon portion of the soap, and also there is a change from 3 to 2-dimensional lattice. Skoulios (12) also showed that the phase transitions sub-waxy to waxy, waxy to super-waxy and super-waxy to sub-neat correspond to abrupt changes in the length and width of the 2-dimensional lattice (see figure 1.1). The transition sub-neat to neat corresponds to a transition from a 2 dimensional lattice to a 1-dimensional lamellar phase. Table 1.2 shows the transition temperatures for various sodium soaps (NaC_{12} to NaC_{18}) (5).

Table 1.2 Phase transition temperatures of the various phases present in the sodium soaps NaC_{12} to NaC_{18} .

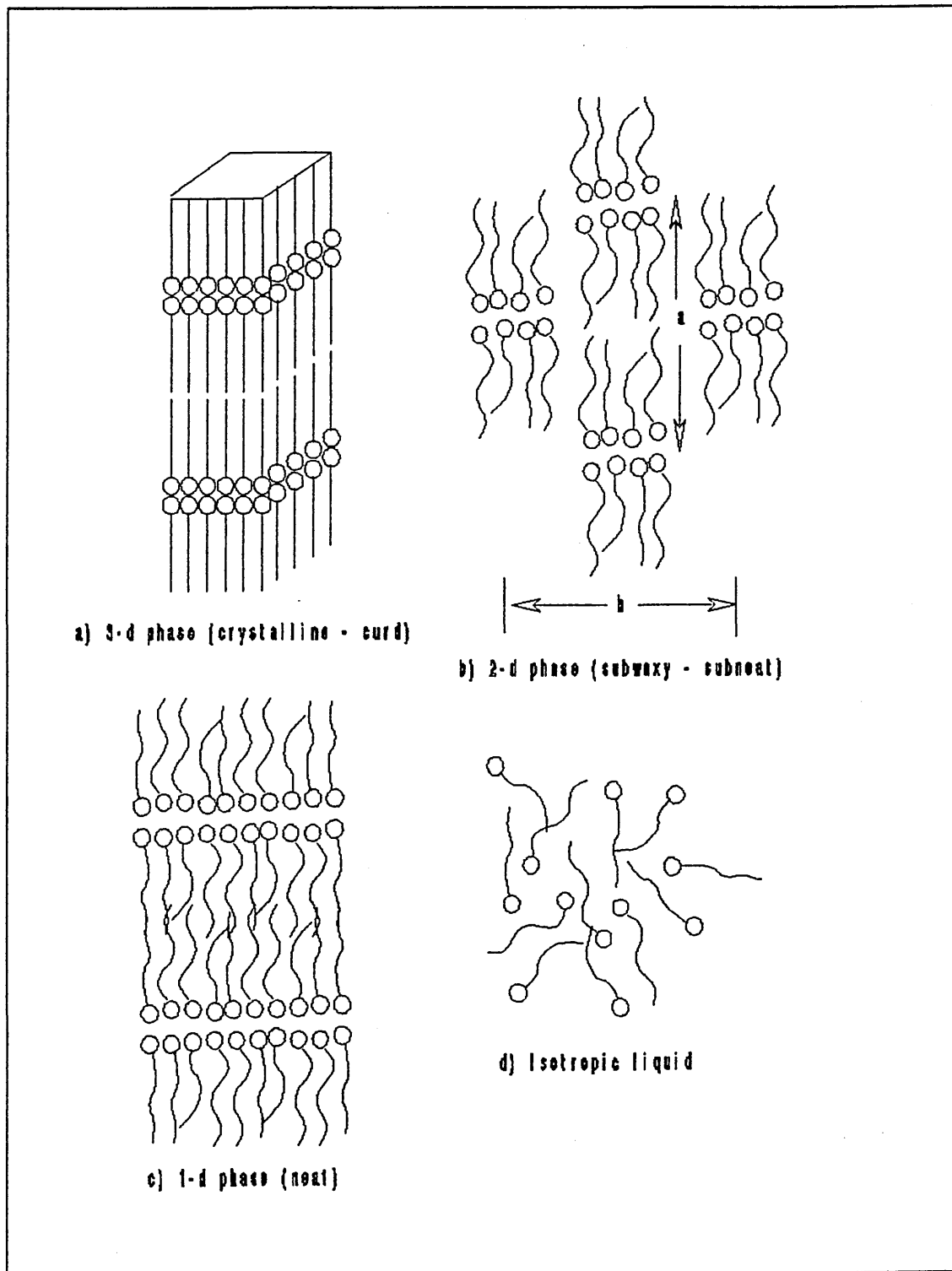
Phase	NaC_{12}	NaC_{14}	NaC_{16}	NaC_{18}
Crystalline	—	80	82	85
Curd	104	108	113	114
Sub-waxy	147-149	141	142-144	131
Waxy	191	182	172-175	151-159
Super-waxy	200	202-204	200	178-181
Sub-neat	250	240	250	255
Neat	330	315	290	280
Melt				

(N.B. all temperatures are in $^{\circ}\text{C}$)

Ferloni et al (8) found that as with lithium soaps there is an odd/even effect, which produces a higher transition temperature and enthalpy for odd chain soap molecules (NaC_9 and NaC_{11}) than for even chain soaps (NaC_8 , NaC_{10} and NaC_{12}) for the curd to sub-waxy phase transition. The isotropic melt shows no such behaviour with both the neat to isotropic transition temperature and enthalpy decreasing with increasing chain length.

Ferloni et al (9,10) also showed when investigating sodium soaps NaC_1 to NaC_7 , with DSC, that the smallest sodium soap to show any polymorphism was sodium n-butanoate ($N_c=4$). For chain lengths of N_c greater than 3, the soap passes through 3 transitions with temperature, denoted by Ferloni as T_A , T_F and T_{Cl} . The T_A transition is the curd to sub-waxy transition discussed earlier. T_F is a type of "melting"

Figure 1.1 Phases present in sodium stearate, a) Crystalline and Curd, b) Sub-way to Sub-neat, c) Neat and d) Isotropic melt.



transition, which results in the formation of a turbid, anisotropic liquid crystalline phase which only melts to an isotropic liquid at a remarkably high temperature, T_{C1} (13). For the soap NaC_8 the value of T_{C1} was estimated by Ferloni (8) to be $\approx 365^\circ\text{C}$.

1.1.3 Other alkali metal soaps

Non-sodium alkali metal soaps, such as potassium soaps also go through a series of thermotropic phases (14,15). Gallot and Skoulios (16,17,18) studied the phase behaviour of potassium, rubidium and caesium soaps, and found that potassium soaps formed similar phases to the sodium soaps, with a 3-dimensional crystal form, a 2-dimensional ribbon form and the 1-dimensional lamellar form.

The rubidium soaps do not show the ribbon structure, but undergo chain melting to a lamellar phase, which then breaks up into a structure of discs oriented into planes, and then reforms the lamellar phase again with different dimensions (18). The caesium soaps melt to an island phase, consisting of regularly fractured lamellae, similar to the disc like phases formed by rubidium soaps, and characterised by islands of polar groups packed in a quasi-crystalline lattice. This then melts to a lamellar phase and finally to the isotropic liquid (17).

The cation has an effect on the isotropic melting temperature of the alkali metal soaps. Lithium stearate melts at $\approx 230^\circ\text{C}$ (6), sodium stearate melts at $\approx 290^\circ\text{C}$ (6) and caesium stearate melts at $\approx 370^\circ\text{C}$ (17). This shows that by increasing the cationic radius, the melting temperature of the corresponding soap is increased.

As with sodium soaps there is a minimum chain length below which the K, Rb and Cs soaps show only conventional melting from crystalline solid to isotropic liquid. For potassium soaps N_c must be greater than 3, for rubidium soaps N_c must be greater than 4 and for caesium N_c must be greater than 5 (10,13).

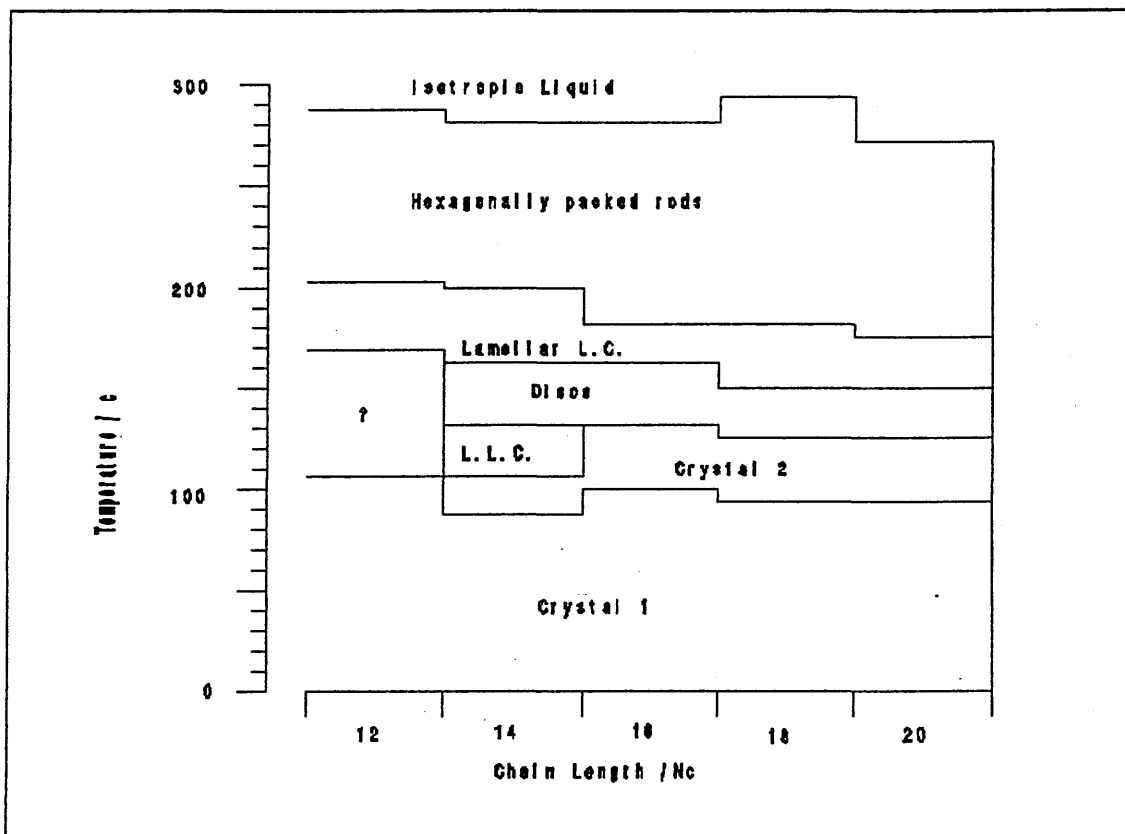
1.2 Soaps of divalent metals

Divalent metals have the capacity to link two fatty acid chains together, giving many of these soaps a very regular crystalline lattice. On heating, the crystalline lattice often undergoes chain melting before ionic lattice disruption, giving rise to thermotropic mesophases. Hattiangdi et al (19) studied the heats of transition and transition temperatures of the soaps of stearic and palmitic acids with a divalent cation. Most of the soaps exhibited a complex series of transitions, with the formation of a mesomorphic phase prior to the actual melting. It was also found (19) that stearates and palmitates of the same metal show similar transitions, but soaps of even chemically similar metals show individual behaviour. This was confirmed with X-ray analysis by M.J. Vold et al (20) for various alkaline earth metal soaps.

R.D. Vold et al (21,22), investigating the crystal structure and polymorphic behaviour of anhydrous calcium stearate and calcium stearate monohydrate, found that the anhydrous calcium stearate goes through a phase transition at about $\approx 150^{\circ}\text{C}$. The phase above 150°C is translucent and is an anisotropic liquid (liquid crystal), showing birefringence between crossed polaroids.

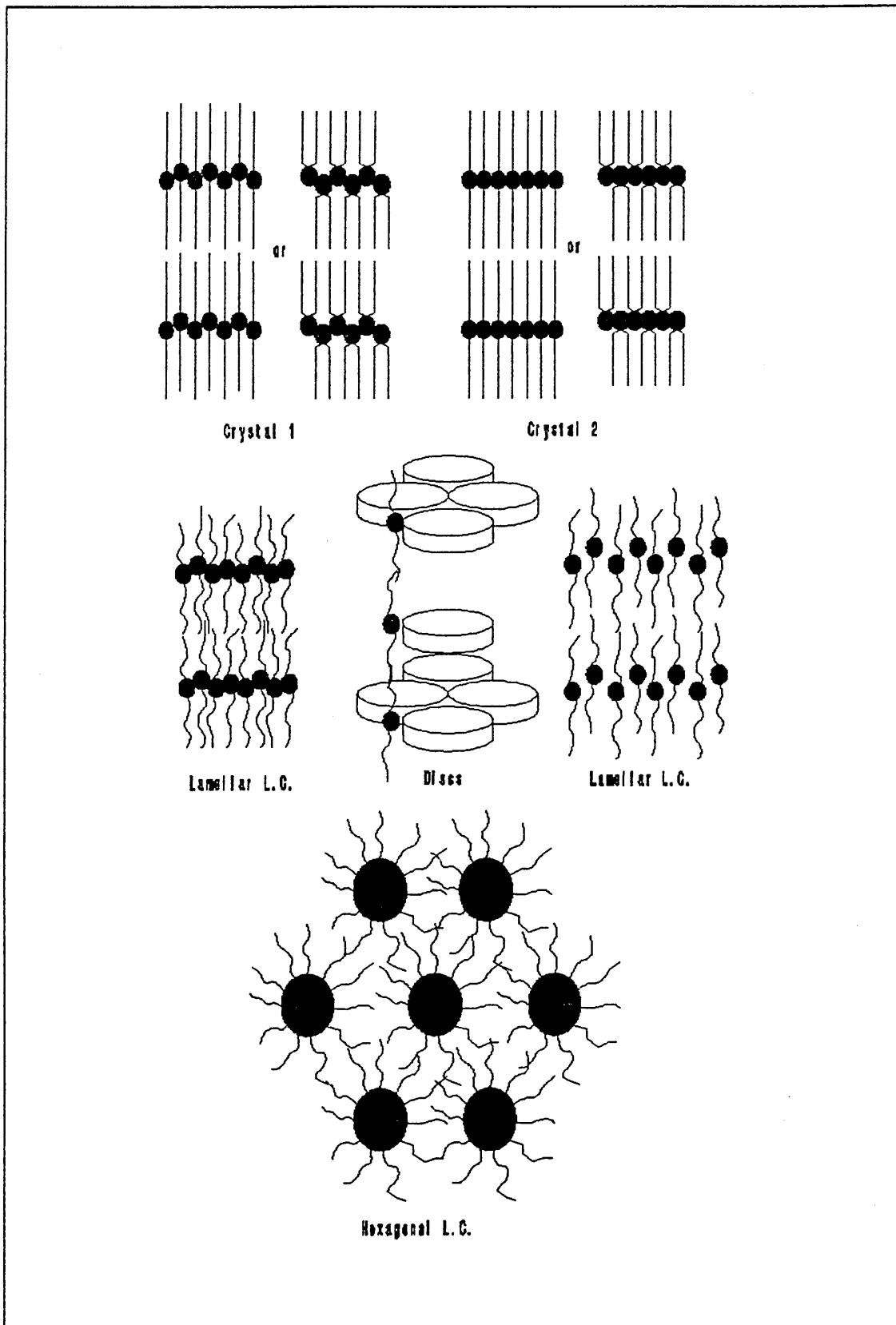
Spegt et al (23), investigated the phase behaviour of calcium dicarboxylate soaps CaC_{12} to CaC_{20} using X-ray diffraction, and found that each soap with the exception of CaC_{12} showed at least five separate phases before melting. Among these are two crystal phases with 3-dimensional lattices, a discotic phase with the polar groups packed on to an orthorhombic lattice, a lamellar phase having the same distance between the layers as in the discotic phase, and finally a reversed hexagonal phase. Figure 1.2 shows the phases and transition temperatures for the soaps CaC_{12} to CaC_{20} and figure 1.3 shows a representation of these phases.

Figure 1.2 The phases and phase transition temperatures of the calcium soaps CaC_{12} to CaC_{20} .



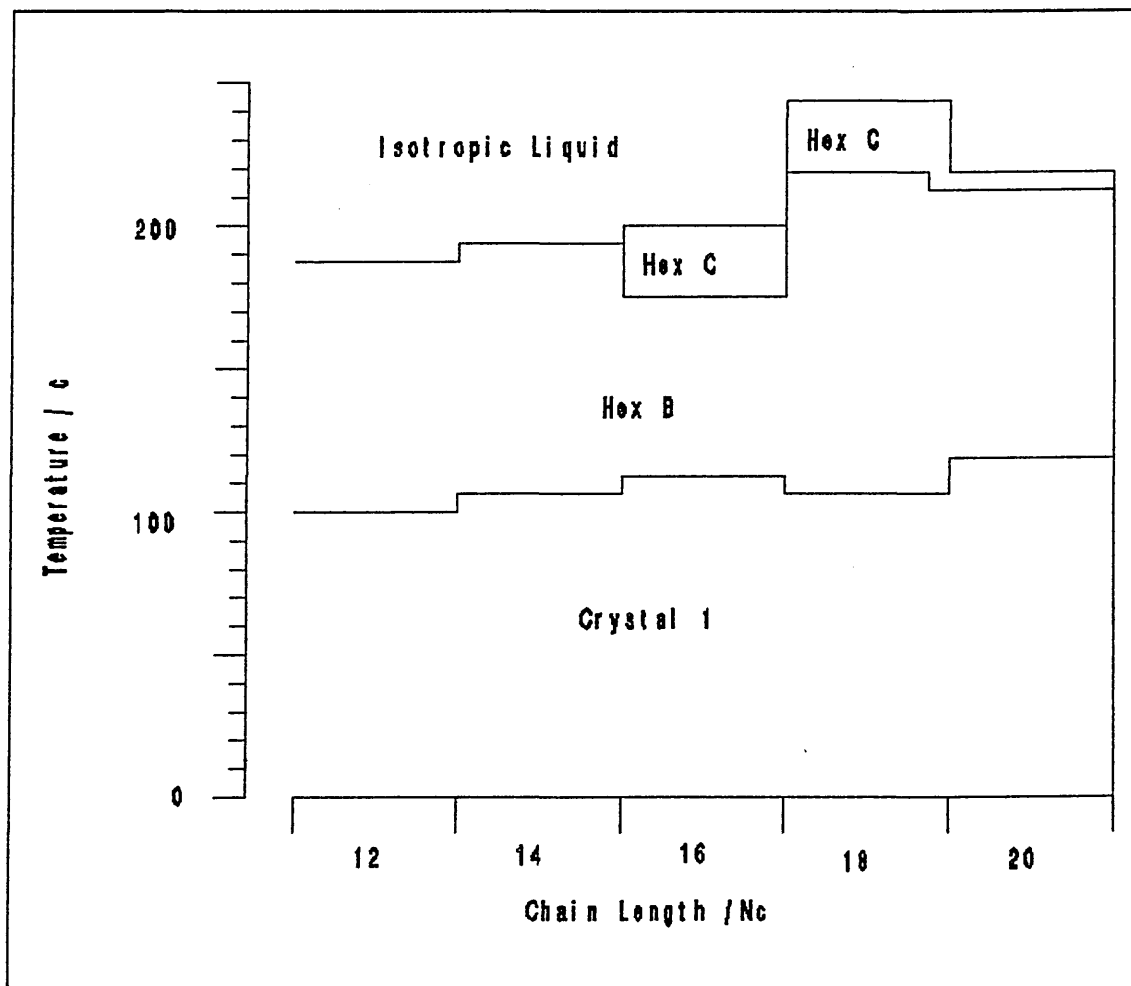
L.L.C. is a lamellar liquid crystal phase

Figure 1.3 A schematic representation of the phases present in calcium soaps.



Spegt at al (24,25) also investigated the phase behaviour of magnesium and cadmium soaps, with chain lengths from C_{12} to C_{20} . These were found to have much simpler phase behaviour than the calcium soaps. These soaps only showed around 2 or 3 phases before the isotropic melt: a crystalline phase, a reverse hexagonal phase (Hexagonal B) and, for chain lengths greater than 14, a Hexagonal C phase (see figure 1.4). The Hexagonal C phase has a slightly different lattice parameter as compared with Hexagonal B phase.

Figure 1.4 Phases and transition temperatures of the cadmium soaps CdC_{12} to CdC_{20} .



The hexagonal phase gives a 2-dimensional lattice which is characterised by a series of X-ray line spacings with the ratios $1 : 1/\sqrt{3} : 1/\sqrt{4} : 1/\sqrt{7} : 1/\sqrt{9}$. The wide angle region of the X-ray diffraction pattern for cadmium soaps in the reverse hexagonal phase shows a single broad peak at 4.6\AA (25). This is consistent with the aliphatic portion of the chain behaving like a liquid.

1.3 Phenyl stearic acid

Phenyl stearic acid (PSA) obtained by a Friedel-Crafts reaction of oleic acid with benzene, was originally thought to consist of either 1 isomer (26) (10-phenyl stearic acid) or of approximately equal portions of the 9- and 10-phenyl stearic acid isomers (27). Smith et al (28) have shown, using gas chromatography of the alkyl aryl ketones obtained from chromic acid oxidation, that phenyl stearic acid is in fact a mixture of 12 positional isomers with the phenyl group occurring preferentially at the 9 and 10 positions (the position of the double bond in oleic acid) (see table 1.3). Substitution at positions lower than carbon number 6 (carbon number 1 is part of the carboxyl group) does not occur, and is thought to be prevented by the repulsive action of the carboxylate group.

Phenyl stearic acid is a liquid at room temperature as a result of the 12 positional isomers. The isomeric mixture also gives the soaps of phenyl stearic acid different structures from those expected for an unsubstituted aliphatic chain.

Table 1.3 Percentage of each isomer present in phenyl stearic acid.

Isomer (phenyl group position)	Percentage of isomer (28)
17	6.1
16	3.6
15	4.7
14	7.5
13	8.9
12	10.7
11	12.8
10	16.5
9	14.7
8	8.5
7	3.9
6	2.0

1.3.1 Lithium phenyl stearate

Lithium phenyl stearate (LiPS) is a near white waxy solid when in the anhydrous state. Kagarise (29) investigating various anhydrous soaps of phenyl stearic acid, found that after exposure to moist air, the lithium soap at no time showed any detectable amount of water present. This is not the case with sodium, potassium and calcium soaps.

An investigation of LiPS by Harrison et al (30) , using DSC, showed that LiPS goes through 3 first order transitions, and these transitions were labelled H_2 , H_3 and H_4 . The types of phases formed were confirmed by polarising microscopy, X-ray diffraction and ^7Li NMR linewidth studies. The X-ray diffraction showed that at room temperature LiPS is in a reverse hexagonal phase, and on going through the transition H_2 at 154°C it remains in a reverse hexagonal phase, but the lattice parameter changes from 36\AA to 31.5\AA . The ^7Li NMR linewidth narrows on going through the H_2 transition, which could indicate the onset of limited rotational and

translational motion within the polar region of the hexagonally packed cylinders. They also made the assumption that the aliphatic chains are liquid like at room temperature, and therefore play no part in the transition H_2 .

Above the transition H_3 at 227°C a birefringent focal conic texture of a fused hexagonal mesophase was observed using polarising microscopy. The X-ray diffraction results confirmed that LiPS still packs with some sort of hexagonal ordering at temperatures above the H_3 transition. Transition H_4 lead to the isotropic melt, and at 370°C is at a much higher temperature than is observed for lithium stearate (6), which has a isotropic melting transition of 219°C .

1.4 Aims

The aims of the current investigation were to try and determine the effect of the hydrocarbon portion of the lithium phenyl stearate molecule on the phase, and also to determine the effect of the phenyl group on the conformations allowed in the aliphatic backbone. Infrared spectroscopy was used to determine the numbers of gtg/gtg' and gg defects present in the aliphatic backbone at various temperatures. Cadmium stearate was also investigated, as this also forms a reverse hexagonal phase on heating, but does not have the problem of the phenyl group. Thus using cadmium stearate as a model compound we were able to determine the effect of the phenyl group on the backbone of lithium phenyl stearate.

1.5 References

- 1) S. Chandrasekhar, "Liquid Crystals", Cambridge University press, 1977
- 2) "Liquid crystals and plastic crystals", Vol. 1, Ed. G.W. Gray and P.A. Winsor, Ellis Horwood, Chichester, U.K., 1974
- 3) P.A. Winsor, Chem. Rev. 68(1), 1, 1968
- 4) G.J.T. Tiddy, Physics Reports 57(1), 1, 1980
- 5) D.M. Small, "Handbook of lipid research", Vol. 4, Plenum Press, New York, 1986
- 6) B. Gallot and A. Skoulios, Kolloid Z. and Z. Polymere 209, 164, 1966
- 7) W. Skoda, Z. Kolloid and Z. Polymere 234, 1128, 1968
- 8) P. Ferloni, M. Zangen and P. Frenzonsin, Z. Naturforsch 32a, 627, 1977
- 9) M. Sanesi, P. Ferloni and P. Frenzonsin, Z. Naturforsch 32a, 1173, 1977
- 10) P. Ferloni, M. Sanesi and P. Frenzonsin, Z. Naturforsch 30a, 1454, 1975
- 11) M.J. Vold, M. Macomber and R.D. Vold, J. Am. Chem. Soc. 63, 168, 1941
- 12) A. Skoulios and V. Luzzati, Acta Cryst. 14, 278, 1961
- 13) H.J. Michels and R. Ubbelohde, J. Chem. Soc. Perkin Trans. II 1879, 1972
- 14) D.P. Benton, P.G. Howe and I.E. Puddington, Can. J. Chem. 33, 1384, 1955
- 15) D.P. Benton, P.G. Howe and I.E. Puddington, Can. J. Chem. 33, 1798, 1955
- 16) B. Gallot and A. Skoulios, Acta Cryst. 15, 826, 1962

- 17) B. Gallot and A. Skoulios, Z. Kolloid and Z. Polymere 213, 143, 1968
- 18) B. Gallot and A. Skoulios, Z. Kolloid and Z. Polymere 222, 51, 1968
- 19) G.S. Hattiangdi, M.J. Vold and R.D. Vold, Ind. Eng. Chem. 41, 2320, 1949
- 20) M.J. Vold and R.D. Vold, J. Am. Oil Chem. Soc. 26, 529, 1949
- 21) R.D. Vold, J.D. Grandine^{2nd} and M.J. Vold, J. Colloid Sci. 3, 339, 1948
- 22) R.D. Vold, J.D. Grandine^{2nd} and M.J. Vold, J. Colloid Sci. 4, 93, 1949
- 23) P.A. Spegt and A.E. Skoulios, Acta Cryst. 17, 198, 1964
- 24) P.A. Spegt and A.E. Skoulios, Compt. Rend. Acad. Sci. 254, 4316, 1962
- 25) P.A. Spegt and A.E. Skoulios, Acta Cryst. 16, 301, 1963
- 26) B.H. Nicolet and C.M. DeMilt, J. Am. Chem Soc. 49, 1103, 1927
- 27) J. Harmon and C.S. Maruel, J. Am. Chem. Soc. 54, 2515, 1932
- 28) F.D. Smith, A.J. Stirton and C.J. Dooley, J. Am. Oil Chem. Soc. 48(4), 160, 1971
- 29) R.E. Kagarise, J. Phys. Chem. 59, 271, 1955
- 30) W.J. Harrison, M.P. McDonald and G.J.T. Tiddy, Liquid Crystals 7(4), 509, 1990

Chapter 2

2 Molecular vibrational spectroscopy	19
2.1 Infrared spectroscopy	19
2.1.1 Characteristic frequencies	21
2.2 Fourier transform infrared spectroscopy	21
2.2.1 Monochromatic light source	23
2.2.2 Data collection	23
2.2.3 Cubic corner interferometers	24
2.2.4 Resolution	26
2.2.5 Under sampling	27
2.2.6 Zero filling	28
2.2.7 Apodization	28
2.2.8 Interferometer advantages	29
2.3 Interpretation	31
2.3.1 Subtraction of spectra	31
2.3.2 Spectral derivatives	32
2.3.3 Fourier self deconvolution	33
2.4 References	42

2 Molecular vibrational spectroscopy

Molecular vibrational spectroscopy is an important tool that is used for the identification of molecules and analysis of molecular structure. These molecular vibrations occur in the infrared region of the electromagnetic radiation spectrum, from $\approx 1 \times 10^{12}$ Hz to $\approx 300 \times 10^{12}$ Hz ($\approx 3 \text{ cm}^{-1}$ to $10,000 \text{ cm}^{-1}$). There are two spectroscopic methods used to "view" the molecular vibrational spectrum of a molecule: these are infrared, which will be discussed further, and Raman spectroscopy (1). These techniques have different selection rules for which vibrations appear in the spectrum, and as such are not mutually exclusive but complimentary techniques.

2.1 Infrared spectroscopy

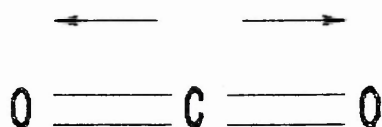
Infrared spectroscopy is a technique used to examine the vibrational modes of polyatomic molecules (1,2,3), the incident infrared energy being absorbed at the frequency of the vibration. The number of vibrational modes produced by a molecule is $3N-6$ or $3N-5$ for linear molecules, where N is the number of atoms in the molecule, and so for example CO_2 has four vibration modes. For a vibrational mode to be infrared active (visible to infrared spectroscopy, if not too weak), there has to be a change in the dipole moment of the molecule during the vibration, i.e.:-

$$\Delta\mu = qr \neq 0 \quad (2.1)$$

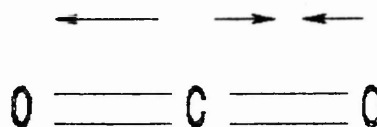
where $\Delta\mu$ is the change in dipole moment
 r is the distance the centre of charge moves
 q is the charge

This can be affected by the symmetry of the molecule; the higher the symmetry the molecule possesses, the less

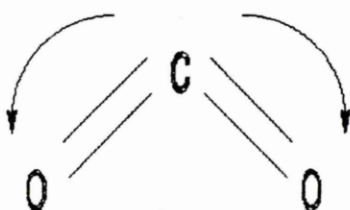
Figure 2.1 The vibration modes of carbon dioxide a) symmetrical stretching, b) ^{anti}symmetrical stretching, c) in plane bending and d) out of plane bending.



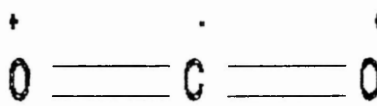
a) Symmetrical Stretching



b) ^{anti}symmetrical Stretching



c) In Plane Bending



d) Out of Plane Bending

probable it becomes that there will be of a change in dipole moment. Also because of symmetry elements present in a molecule, many vibrations could be degenerate. Figure 2.1 shows the vibrational modes present in carbon dioxide, namely 2 stretching and 2 bending vibrations. Of the stretching vibrations only the asymmetrical vibration gives rise to a change in dipole moment $\Delta\mu$ and so only this vibration is visible in the infrared spectrum. The bending vibrations both give rise to a change in dipole moment, and therefore are both infrared active, but the symmetry of the CO_2 molecule makes these vibrations identical, and therefore degenerate, so only one bending vibration is seen in the infrared spectrum. So from the four vibrations only two are seen in

the infrared spectrum. Along with the low intensity of some vibration modes, this reduces the number of vibration that are observed in the infrared spectrum of any polyatomic molecule.

2.1.1 Characteristic frequencies

It was noted early in the history of infrared spectroscopy that many of the functional groups present in a molecule, such as C=O, vibrate at approximately the same frequency irrespective of the molecule to which the group is attached (1). For example the vibrational spectra of n-heptane, n-octane and n-nonane will have a number of bands in common. The characteristic frequencies of these vibrations are usually only perturbed slightly by the presence of other functional groups, making the identification of the functional groups present in a molecule easy. There are however exceptions to this rule: hydrogen bonding for example can for example cause a shift in the frequency of the O-H and N-H stretching vibrations.

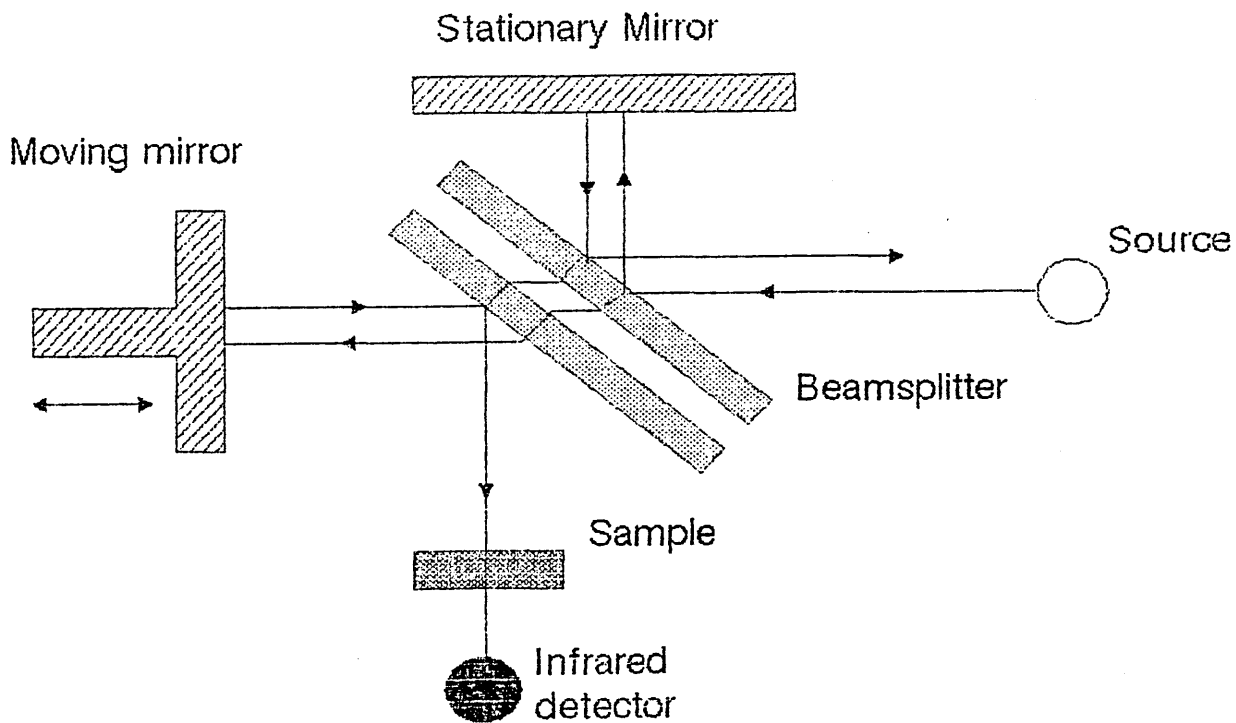
The characteristic, or group frequencies can be used in qualitative analysis, such as identification of the homologous series to which a molecule belongs. For example the C-H Stretching vibration of hydrocarbons appear at $\approx 2995 \text{ cm}^{-1}$ for a methylene group, $\approx 3025 \text{ cm}^{-1}$ for an ethene group, $\approx 3055 \text{ cm}^{-1}$ for a phenyl group and $\approx 3334 \text{ cm}^{-1}$ for an ethylene group.

2.2 Fourier transform infrared spectroscopy

Fourier transform infrared spectrometers are a relatively new instrument in most laboratories, increasing in number over the last 20 years. This increase in number was

caused by the development of a fast Fourier transform algorithm by Cooley and Tukey (4), and also the introduction of cheaper and more powerful microcomputers. At the heart of a Fourier transform infrared spectroscopy (FTIR) is a Michelson interferometer (see figure 2.2), with one mirror allowed to move back and forth. A half silvered mirror, reflects a portion of the incident radiation onto a stationary mirror, and transmits the remainder through to a moving mirror. These are then reflected back to the beam splitter, and recombined, with a portion of the recombined radiation going back to the source, and the remainder going to the detector. When the two beams recombine at the beam splitter, an interference pattern (interferogram) is generated and the pattern varies with displacement of the moving mirror along its axis.

Figure 2.2 Schematic diagram of a Michelson interferometer.



2.2.1 Monochromatic light source

As well as the infrared source (which emits radiation over a broad range of frequencies) a monochromatic Helium-Neon laser is used as a master clock signal to time data collection. If the stationary mirror and moving mirror are equidistant from the beam splitter then the two split laser beams travel equal distances and return to the beam splitter in phase and interfere constructively, and the beam splitter (ideally) reflects the recombined laser beams back to the source.

If the moving mirror is moved by a quarter of the wavelength of the laser source, then the portion of the beam travelling to the moving mirror has to travel an extra half wavelength before returning to the beam splitter, making it 180° out of phase with the beam travelling to the stationary mirror. The recombining beams interfere destructively, and the beam splitter (ideally) reflects all the light to the detector and none to the source. Thus the movement of the mirror generates alternate light and dark bands at the detector, which is in fact a sine wave with a wavelength of half that of the laser source. By counting the fringes of the detected laser signal, the scanning mirror displacement can be determined accurately.

2.2.2 Data collection

Before an infrared spectrum can be produced an interferogram has to be collected. As mentioned before a helium-neon laser source, which generates a sinusoidal interferogram, is used to determine the mirror position by counting the interference fringes. If a data point is sampled

at every zero crossing, when intensity of the He-Ne¹ laser interference fringes are at minimum, the mathematics of the Fourier transformation provides a spectrum from 0 to 15798 cm⁻¹ with 31596 data points².

Mattson instruments (5) use a more sophisticated method for sensing the position and velocity of mirror. The He-Ne laser is still used as above but a quarter-wave delay plate and polariser are placed in the returning beam of the interferometers fixed arm (see figure 2.3). Together, the delay plate and polarisers generate a beam composed of 2 sine waves at right angles and 90⁰ out of phase with each other. The two components (detected at photo diodes A1 and A2 (see figure 2.3)) not only indicate the position of the mirror but also the direction in which it is travelling. This allows collection of data in both directions of mirror travel, reducing time the required to collect large numbers of scans.

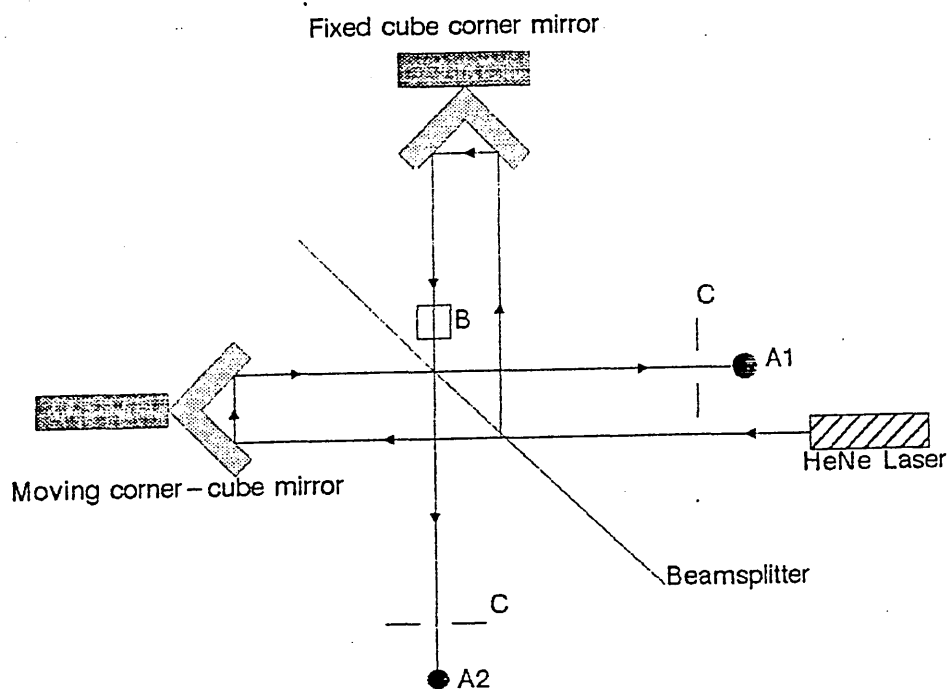
2.2.3 Cubic corner interferometers

In many interferometer designs flat mirrors are used to reflect the incident radiation. Flat mirrors work satisfactorily, as long as they remain exactly perpendicular to the incident beam. When the mirror tilts the beam diverges and loses coherence (the ability to produce a proper interference signal) at the beam splitter.

¹ The He-Ne laser has a wavelength of $\approx 633 \times 10^{-9}$ m and a frequency of 15798 cm⁻¹.

² See Transform techniques in chemistry (6) for details of discrete Fourier transforms.

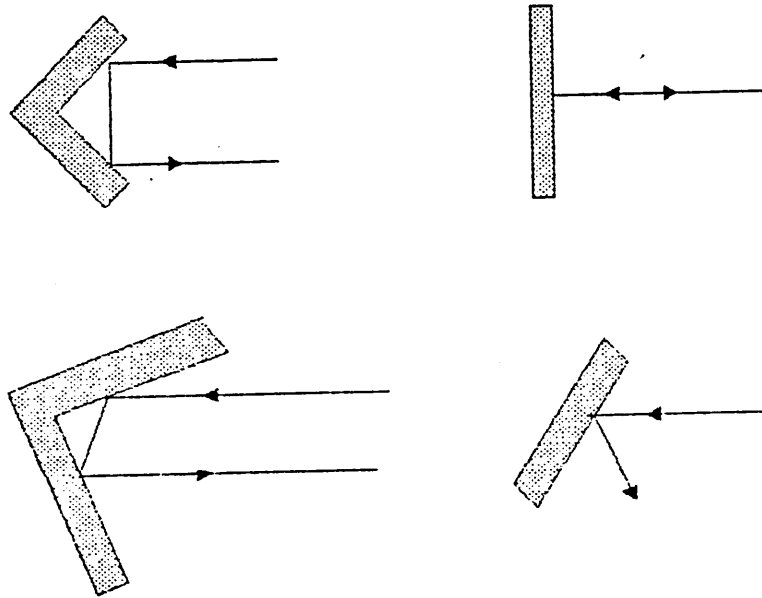
Figure 2.3 Interferometer used to determine position and direction of moving mirror. A1 and A2 are photo diodes, B is the quarter-wave delay plate and C are polarisers.



One solution to this problem is to use air bearings, where the mirror travels on a cushion of pressurised gas and is virtually friction free. This has its draw backs in that the system is expensive and requires a supply of compressed gas.

Another solution is to use corner cube mirrors. These consist of 3 mirrors placed perpendicular to each other. This has the advantage that the outgoing beam is always reflected parallel to the incoming beam (see figure 2.4). So corner cube mirrors can be built with the more rugged and reliable mechanical bearing, and still produce the high resolution and the stability required for FTIR.

Figure 2.4 Comparison of corner cube and flat mirrors.



2.2.4 Resolution

In dispersive infrared spectrometers, the resolution is dependent on the slit width and on the reciprocal of the linear displacement of the diffraction grating (see figure 2.5). As the slit width is narrowed the range of frequencies passed to the detector decreases, resulting in higher resolution. In FTIR the resolution is increased by increasing the maximum displacement of the mirror from the equilibrium position, and the resolution is given by:-

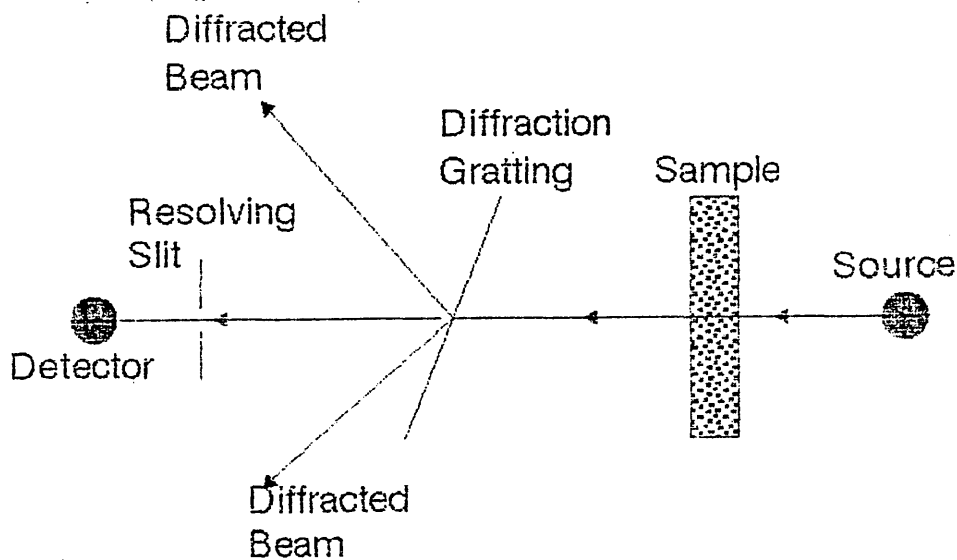
$$R = \frac{1}{d} \quad (2.2)$$

where d is the displacement of the mirror

Nyquist sampling theory dictates that at least 2 data points are required in the frequency range ν to $\nu + R$, where ν is the frequency and R is the resolution, to prevent

aliasing³. So if the resolution is 1 cm^{-1} and the frequency range is 0 to 15798 cm^{-1} , then 31596 data points are required to represent the spectrum, with data points every 0.5 cm^{-1} . If the resolution was changed to 2 cm^{-1} , then only 15798 data points would be required, with a data point every 1 cm^{-1} .

Figure 2.5 Schematic diagram of a dispersive infrared spectrometer.



2.2.5 Under sampling

As mentioned before, if a data point is sampled at each zero crossing point of the He-Ne laser interferogram, then we have a spectrum of bandwidth 0 to 15798 cm^{-1} . If this is sampled at one wavenumber resolution then 31596 data points are required per spectrum. This is a large amount of data to process and store, but it is possible to sample the interferogram less often. For example if the data is sampled

³ Nyquist sampling theorem states that the highest frequency sine wave in a spectrum must be sampled at rate of at least two points per cycle in order to be represented accurately. If less than 2 points are used then the sine wave will appear to have a lower frequency than it actually has, which is called aliasing.

at every other zero crossing of the He-Ne laser interferogram, then the number of data points will be halved. This has no effect on resolution, as this is dependent solely on the optical retardation of the mirror (distance mirror moves), but the bandwidth is halved so the frequency range is 0 to 7899 cm^{-1} . As the mid infrared region is ≈ 400 to 4000 cm^{-1} no penalty is incurred, but the data set is half the size and the processing time is reduced.

2.2.6 Zero filling

Zero filling is a technique used to increase the number of data points in a spectrum (the digital resolution), thus improving the spectral representation, without increasing the spectral resolution, which increases scan time. If N is the number of data points in the interferogram, then to double the digital resolution $N/2$ zero data points are added to each side of the interferogram before it is Fourier transformed (6). The zero data is automatically interpolated into the spectrum by the Fourier transform, giving a spectrum containing $2N$ points. This technique is particularly useful when investigating bands with small band widths such as gas rotation bands. It also improves the reliability of removing water and carbon dioxide bands at high resolution ($R \leq 1\text{ cm}^{-1}$) and when the ratio of a single beam sample spectra with single beam background spectra is taken.

2.2.7 Apodization

To be of any practical use the data collected as an interferogram has to be processed by a Fourier transform algorithm to produce a spectrum. A problem arises when calculating the Fourier transform: to calculate the Fourier

transform we need to integrate from negative to positive infinity. However, the data collected only goes between $\pm d/2$, where d is the optical retardation for the mirror. This produces in effect the infinite data set multiplied by a boxcar function (boxcar has values of 1 between $\pm d/2$ and 0 elsewhere). The truncation of the interferogram abruptly can cause problems of "ringing"⁴ and increase background noise. This can be improved if the interferogram is multiplied by a function which reduces gradually to zero at the truncation point. Typical apodization functions include triangular, Bessels and sinc functions, and all have varying advantages, which tend ^{to} mean that the more the ringing and noise is improved the lower the resolution of the resulting spectrum. So the choice is between a noisier spectrum or reducing the resolution.

2.2.8 Interferometer advantages

A Fourier transform infrared spectrometer has several advantages over dispersive instruments which are as follows:-

- i) Multiplexing advantage (Fellgett's advantage): An interferometer does not separate the incident radiation into individual frequencies before measurement. So each point on the interferogram contains information from each wavelength present in the input signal. This means that if 8000 points are collected along the interferogram, each wavelength is sampled 8000 times. By contrast when a dispersive instrument is used,

⁴ Ringing is the name given to oscillations that can occur around the base of bands in the infrared spectrum.

measurement of 8000 individual points across the spectrum samples each wavelength only once.

- ii) Throughput advantage (Jacquinot's advantage): The simple optical path of the interferometer (no slits and fewer optical elements than a dispersive instrument) permits much more energy to reach the detector than is possible with a dispersive instrument (much of the energy being lost at the slit). This increases the potential signal to noise ratio of the spectrum. Thus, with Fellgett's advantage, an FTIR spectrometer can produce high quality infrared spectra in a fraction of the time required to obtain the same spectrum on a dispersive instrument.

Also, as the resolution is increased on a dispersive instrument, the slit must be narrowed, thus reducing the energy to the detector. In a FTIR spectrometer only the mirror's optical retardation increases with increased resolution, with no resulting decrease in energy throughput.

- iii) Frequency precision (Conne's advantage): With dispersive instruments, the frequency precision and accuracy depends on calibration with external standards, and on the ability to move the gratings and slits uniformly throughout the scan. By contrast an FTIR spectrometer has its own frequency standard present, usually a He-Ne laser. The mirror movement and beam sampling are clocked by the fringes from the monochromatic interferogram. All frequencies of the output spectrum are calculated from the frequency of the laser source which does not vary. So FTIR spectrometers can achieve a frequency precision

of better than $\pm 0.01 \text{ cm}^{-1}$.

- iv) Constant spectral resolution: In a FTIR spectrometer the resolution of the measured spectrum is frequency independent. This is not the case with a fixed slit dispersive instrument which has a frequency dependent resolution. To keep the resolution frequency independent for a dispersive instrument requires a complex drive system for the slit, varying the slit width as the frequency changes.

2.3 Interpretation

Among the problems with infrared spectroscopy is the interpretation of data gathered, and the prediction of the frequency and intensity. Maroncelli (7) and Jona (8), among others, have had considerable success predicting frequencies of vibrations produced by *n*-alkanes (even for non-linear conformations) using normal co-ordinate analysis. Jona (9,10) has also had limited success predicating the intensity of infrared vibrations for *n*-alkanes and polyethylene. Problems still remain where band contours overlap, or baseline and band profiles change when the phase of a sample changes. There are several techniques available to the spectroscopist to aid in the interpretation of these changes.

2.3.1 Subtraction of spectra

Subtraction of spectra is a technique which can be used to find changes in the area, the frequency and the profile of infrared bands. It can also be used to find any bands that have appeared or disappeared on going through a phase transition, or to remove the solvent contribution from a solvent/sample spectrum.

To achieve a reasonable subtraction of spectra, a band is required that is present in both spectra and is unaffected by temperature or phase. This band is then used to calculate a weighting factor for the two spectra before subtraction, and this is then used to normalise the spectra. The resulting subtraction spectrum should have zero intensity at this band position, while the rest of the spectrum shows up any differences.

2.3.2 Spectral derivatives

Spectral derivatives can be applied to the problem of estimating the peak position of bands within a multiplet. The technique is applicable to many different spectroscopic techniques, and produces a band sharpening effect, but requires only limited computer power. The second and fourth derivatives are the ones usually applied to spectra, as these produce maxima at the position of the peaks within the spectra (second derivatives have to be inverted to produce the maxima at the peak position).

Figure 2.6 shows a synthesised overlapping band contour and its inverted second derivative: the positions of the bands within the band contour can be seen clearly. The problem with derivative spectra is that although large peaks can be clearly resolved, a deterioration in the signal to noise ratio occurs with the derivative operation, so small peaks may be hidden in the noise.

The intensities of the derivative components have no direct relationship to the intensities of the original bands, so only the positions and not the intensities can be determined from the derivative spectrum. Another problem with

this technique is the derivative process itself, for a single peak spectrum an n^{th} order derivative will generate n zero crossing points and $n+1$ turning points. So for the second order derivative there are three turning points (2 maxima and 1 minimum) present in the spectrum (the minimum being at the actual peak position). So if the number of bands in the original spectrum is increased then the complexity of the derivative spectrum increases, and the interpretation can become more difficult.

2.3.3 Fourier self deconvolution

Bands present in the infrared spectrum may have many different contributions to the band profile, including the intrinsic linewidth of the vibration and instrumental broadening. By removing some of the contributions to the linewidth and lineshape of a band, the bandwidth can be narrowed, giving an apparent improvement in resolution. Fourier self deconvolution is one of the techniques which have been developed for removing a contributing lineshape from a band profile, and thus increasing the apparent resolution of overlapping band contours.

The original spectrum (undeconvoluted) can be seen as the convolution of the lineshape we wish to remove, with the deconvoluted spectrum. Mathematically this can be written as:-

$$E(\nu) = E'(\nu) * E_0(\nu) \quad (2.3)$$

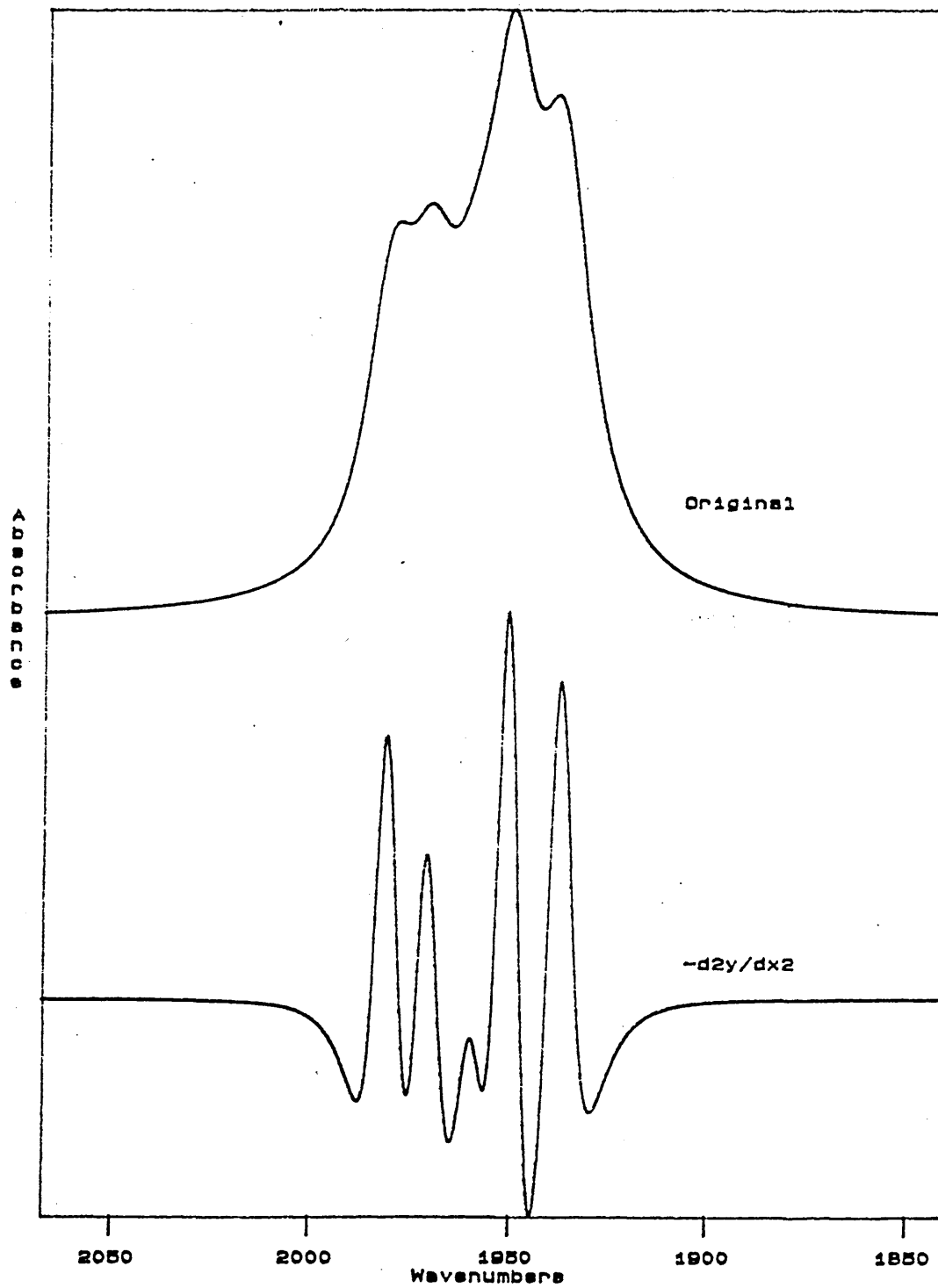
where

$E(\nu)$ is the observed band profile.

$E_0(\nu)$ is the lineshape to be removed.

$E'(\nu)$ is the deconvoluted spectrum.

Figure 2.6 A synthesised band contour with the inverted second derivative.



$E_o(\nu)$, the lineshape to be removed, is assumed to be a Lorentzian line.

Fourier self deconvolution was developed for infrared spectroscopy by Kauppinen et al (11,12,13) who demonstrated the mathematics and possible applications and limitations of the technique.

The Fourier self deconvolution technique operates on the inverse Fourier transform of the frequency spectrum $E(\nu)$, $I(x)$.

The Lorentzian lineshape has the form:-

$$E_o(\nu) = \frac{\sigma/\pi}{\sigma^2 + \nu^2} \quad (2.4)$$

where σ is the half width at half height of the Lorentzian band.

ν is the frequency.

The inverse Fourier transform⁵ of eqn. 2.4 is:-

$$I_o(x) = e^{-2\pi\sigma|x|} \quad (2.5)$$

where $I_o(x)$ is the inverse Fourier transform of $E_o(\nu)$

By taking the inverse Fourier transform of eqn. 2.3 we get:-

⁵ The Fourier transform of the function $f(x)$ is defined as:-

$$g(\nu) = \int_{-\infty}^{\infty} f(x) e^{-i2\pi\nu x} dx$$

The inverse Fourier transform of the function $g(\nu)$ is defined as:-

$$f(x) = \int_{-\infty}^{\infty} g(\nu) e^{i2\pi\nu x} d\nu$$

$$I'(x) = \frac{I(x)}{I_o(x)} \quad (2.6)$$

The deconvoluted spectrum $E'(v)$ is found by taking the Fourier transform of $I'(x)$

There is a problem with using equation 2.6, in that the noise in the spectrum is amplified excessively. The noise can be reduced by the introduction of an apodization function, which truncates the interferogram at a point L . So that when multiplied by the interferogram $I'(x)$, this gives a resulting interferogram which is equal to $I'(x) \times D_g(x)$ up to the point L and zero for the rest ($D_g(x)$ is the apodization function)

The resulting interferogram is given by:-

$$I'(x) = \frac{I(x) \times D_g(x)}{I_o(x)} \quad (2.7)$$

and the deconvoluted spectrum is given by:-

$$E'(v) = \mathcal{F}\{I'(x)\} \quad (2.8)$$

where $\mathcal{F}\{I'(x)\}$ is the Fourier transform operation.

The apodization function can be one of many functions. One example is the triangular squared function. This has the form:-

$$\begin{aligned} D_g(x) &= \left(1 - \frac{x}{L}\right)^2 & |x| \leq L \\ D_g(x) &= 0 & |x| > L \end{aligned} \quad (2.9)$$

where L is the truncation point of the interferogram.

The apparent resolution enhancement is given by (14):-

$$K = \frac{\delta_{1/2}}{\delta'_{1/2}} \quad (2.10)$$

where $\delta_{1/2}$ is the full width at half height of the original spectrum.

$\delta'_{1/2}$ is the full width at half height of the deconvoluted spectrum.

K can also be defined as (13):-

$$K = 4\sigma \frac{L}{a} \quad (2.11)$$

where σ is the half width at half height of the deconvolution intrinsic lineshape function.

L is the truncation point of the interferogram.

a is a constant dependent upon the apodization function used.

James et al (14) investigated the effect of apodization function on a single synthetic peak of FWHH = 50.14 cm^{-1} and an intensity of 0.2 absorbance units. Figure 2.7 shows the effect of apodization function on the Gibbs oscillations (ringing) (K is taken to be 3, σ is taken to be 49 cm^{-1}). Some functions reduce the ringing more effectively than others, but at a cost of reducing the resolution enhancement.

Figure 2.8 shows the same synthetic spectrum as used in Figure 2.6, and its deconvoluted equivalent. As can be seen the Fourier self deconvolution produces an enhancement in the spectral resolution, so peak positions can be found with greater accuracy. Also, in theory, if the correct line shape has been removed from the spectrum, the integrated intensity of a band in the deconvoluted spectrum should be the same as the integrated intensity of the same band in the original spectrum.

Figure 2.7 The effect of apodization function on Gibbs oscillations in the deconvolution of a single peak, with $K = 3$ and $\sigma = 49 \text{ cm}^{-1}$.

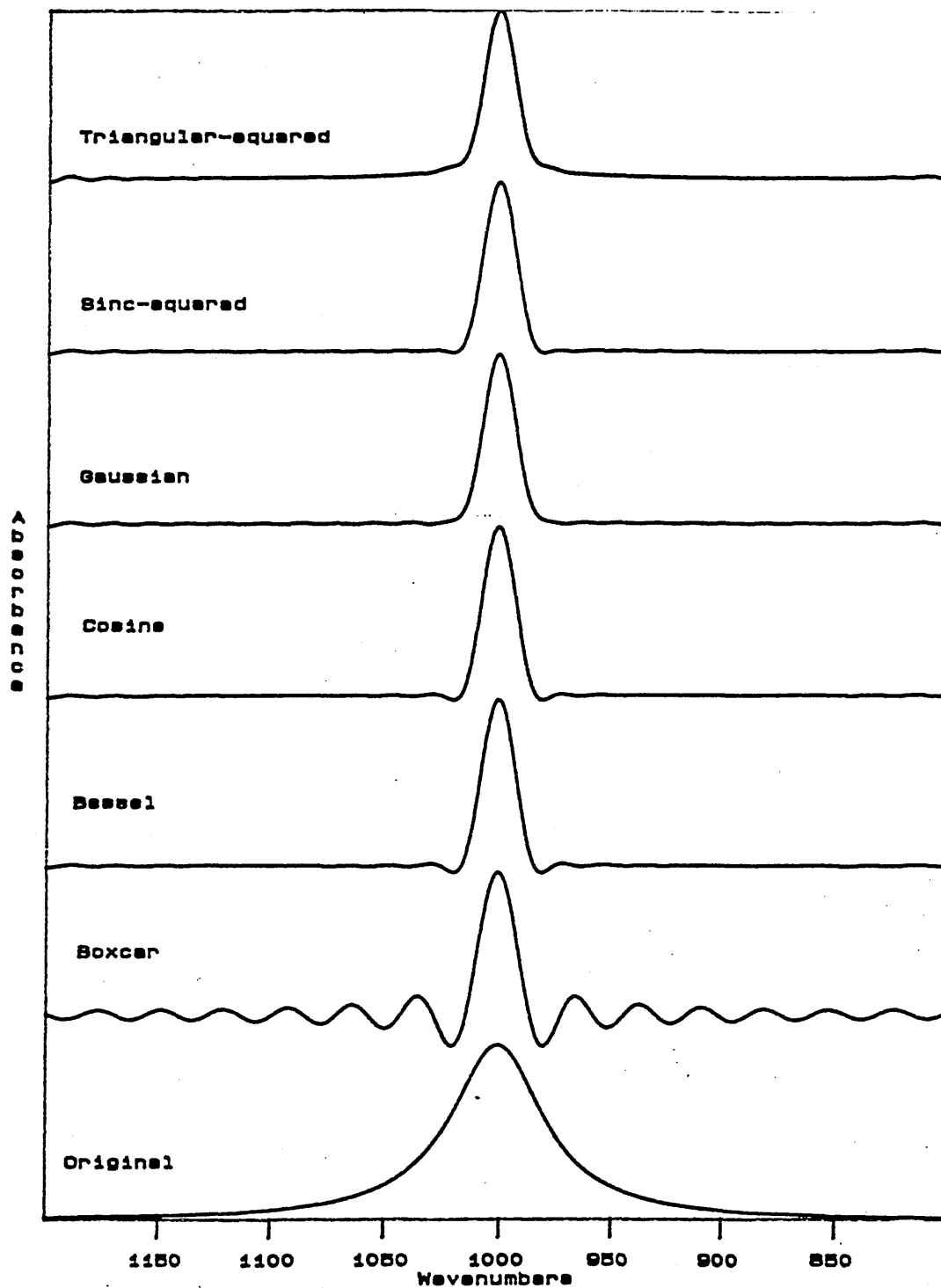
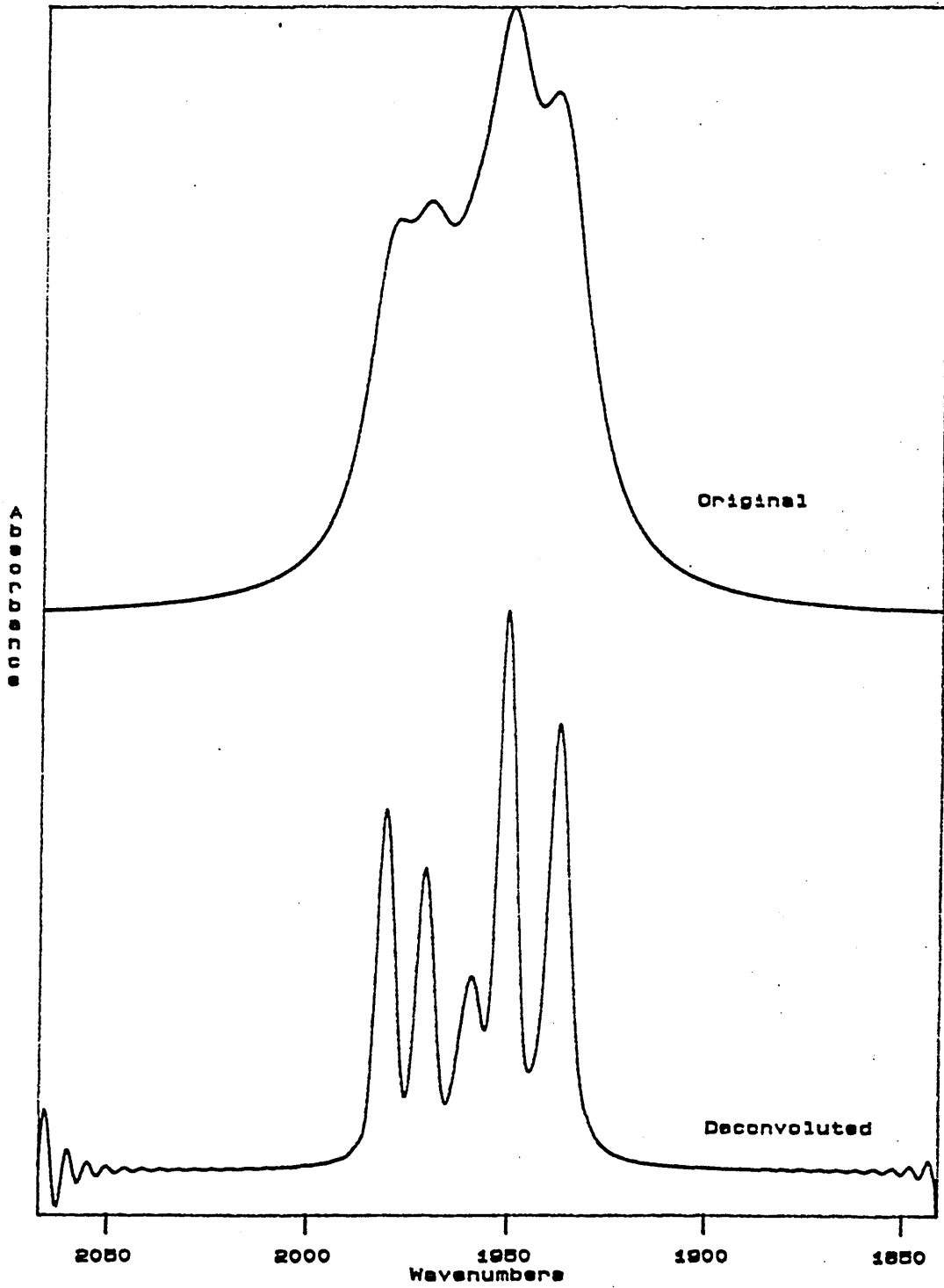
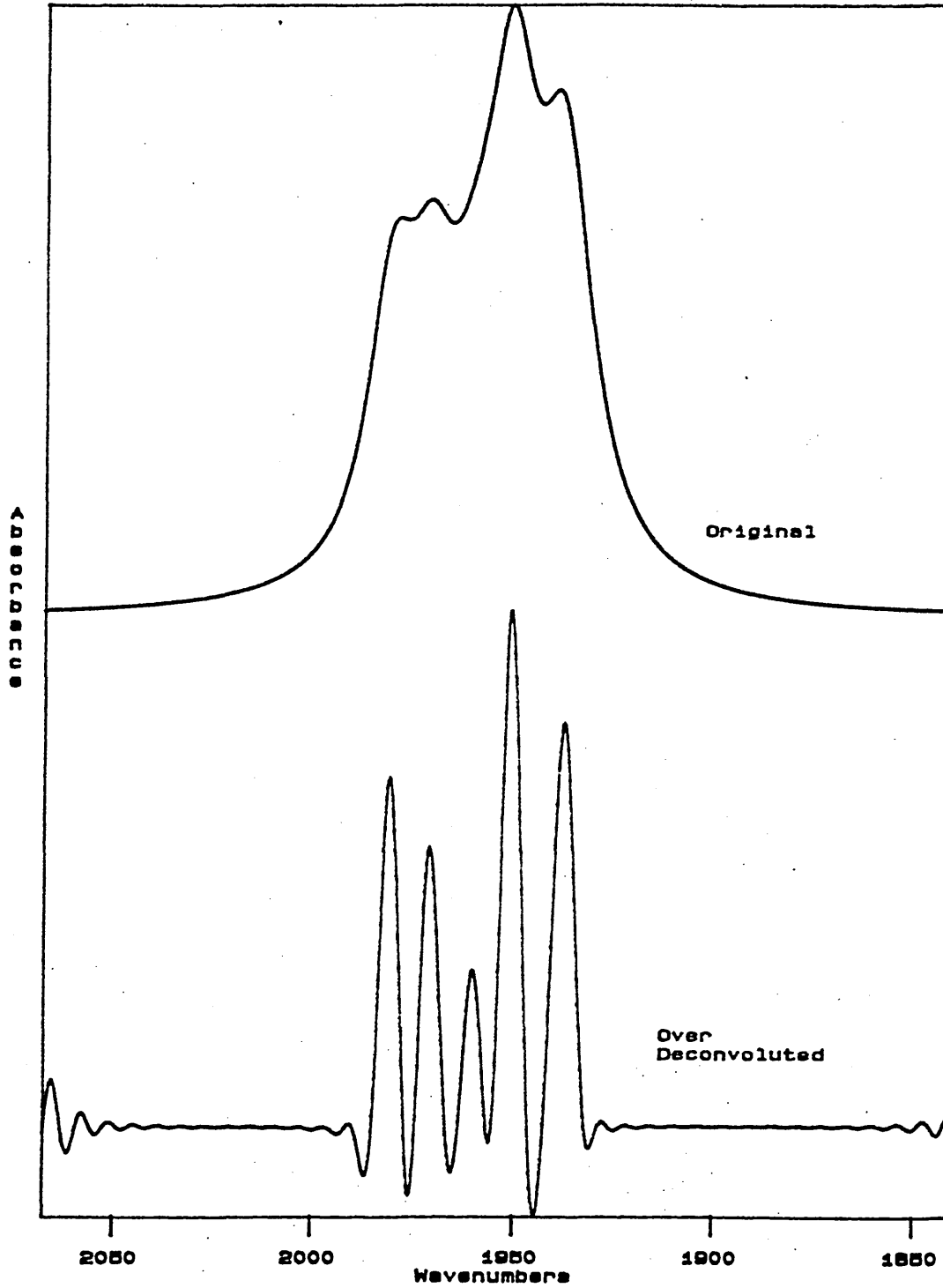


Figure 2.8 A synthesised band contour with its Fourier self deconvoluted spectrum.



Fourier self deconvolution does have its limitations, in the fact that the bandwidth of the removed Lorentzian line is limited to the minimum bandwidth within the original spectrum. If the bandwidth of the removed Lorentzian line is larger than the minimum bandwidth in the original spectrum, then side lobes begin to appear in the deconvolution, as in figure 2.9 which is an over deconvoluted version of the spectrum of figure 2.8.

Figure 2.9 A synthesised band contour with its Fourier self deconvoluted spectrum, which has been over deconvoluted.



2.4 References

- 1) N.B. Colthup, L.H. Daly and S.E. Wiberley, "Introduction to infrared and Raman spectroscopy", Academic Press, 1975
- 2) A. Lee Smith, "Applied spectroscopy", Ed. P.J. Elving and J.D. Winefordner, John Wiley and Son inc., 1979
- 3) "Infrared spectroscopy and molecular structure", Ed. Mansel Davis, Elsevier, 1963
- 4) J.W. Cooley and J. Tukey, Math. Comp. 19, 297, 1965
- 5) Galaxy FTIR Spectrometer User Manual, Mattson, 1989
- 6) R. Griffiths, "Transform techniques in chemistry", Plenum Press, 1978
- 7) M. Maroncelli, S.P. Qi, H.L. Strauss and R.G. Snyder, J. Am. Chem. Soc. 104, 6237, 1987
- 8) P. Jona, M. Gussoni and G. Zerbi, J. Mole. Struc. (Thermo. Chem.) 119, 329, 1985
- 9) P. Jona, M. Gussoni and G. Zerbi, J. Mole. Struc. (Thermo. Chem.) 119, 347, 1985
- 10) P. Jona, M. Gussoni and G. Zerbi, J. Mole. Struc. (Thermo. Chem.) 142, 221, 1986
- 11) J.K. Kauppinen, D.J. Moffat, H.H. Mantsch and D.G. Cameron, App. Spect. 35, 271, 1981
- 12) J.K. Kauppinen, D.J. Moffat, H.H. Mantsch and D.G. Cameron, App. Optics, 20, 1866, 1981
- 13) J.K. Kauppinen, D.J. Moffat, H.H. Mantsch and D.G. Cameron, Anal. Chem. 53, 1454, 1981
- 14) D.I. James, W.F. Maddams and P.E. Tooke, App. Spect. 41, 1362, 1987

Chapter 3

3 Non planar conformations in n-alkanes	44
3.1 n-Alkanes	44
3.1.1 Rotator phase	44
3.1.2 Kink block model	45
3.2 Rotational isomeric state model	46
3.2.1 Statistical weight	48
3.3 Infrared and Raman studies of n-alkanes . .	52
3.3.1 Low frequency Raman spectroscopy . .	52
3.3.2 Conformationally sensitive infrared bands	55
3.4 References	63

3 Non planar conformations in n-alkanes and their derivatives

Many organic compounds undergo a series of solid-solid phase transition prior to melting (1-3). The simplest class of organic molecules to exhibit this type of behaviour are the n-alkanes. The n-alkanes are one of the most studied groups of compound (especially if the limiting case of high molecular weight polyethylene is included) (4-8), and an understanding of the polymorphism of n-alkanes is useful in the understanding of more complex molecules which have an aliphatic portion, such as fatty acids, soaps and phospholipids (9,10).

3.1 n-Alkanes

In the crystalline phase n-alkanes show a variety of crystalline structures that depend upon the number of carbon atoms present and if this number is odd or even (4,5,6,9). Short chain n-alkanes with even numbers of carbon atoms have been shown to pack on to triclinic unit cells, at least up to n-octadecane (6,9), but for longer chain lengths they can pack with orthorhombic or monoclinic crystal structures (5,6,9). In the crystalline phase odd n-alkanes with nine or more carbon atoms show nearly identical orthorhombic packing (5,6,9,12), while shorter chains show triclinic packing (6,9). This would tend to indicate that for longer chain n-alkanes the odd/even effect on crystal structure is reduced.

3.1.1 Rotator phase

The phase behaviour of n-alkanes is quite complex (11), but all the odd n-alkanes $n\text{-C}_9\text{H}_{20}$ and $n\text{-C}_{45}\text{H}_{92}$ undergo at least one pre-melting phase transition (7). Muller (4), in an early study of solid-solid phase transitions of n-alkanes showed,

using X-ray diffraction techniques, that over one of the solid-solid phase transitions the unit cell changes so as to approach hexagonal symmetry (only molecules longer than $n\text{-C}_{21}\text{H}_{44}$ give true hexagonal symmetry (13)). The study showed that the phase transitions were accompanied by orientational disordering: the molecules were envisaged as executing a more or less complete rotational jump about the long axis while maintaining a fully extended conformation. Models based on the assumption that the n-alkane molecules rotate in the high temperature solid phase, have been moderately successful in predicting thermodynamic data (14). In fact the rotator model found acceptance to such an extent that the high temperature phases of n-alkanes and similar compounds are often called rotator phases.

3.1.2 Kink block model

Absent from the rotator phase model in its original form is the consideration of conformational disorder. Blasenbry and Pechhold (15) proposed a model based on conformational defects termed "kinks". This required that the concentration of gauche bonds in the n-alkane $\text{C}_{19}\text{H}_{40}$, for example, would be between 4 and 8 per molecule, if the rotator phase was entirely due to kink defects.

Barnes and Fanconi (16) studied $\text{C}_{19}\text{H}_{40}$ in the high temperature rotator phase using Raman spectroscopy. They found that the concentration of gauche defects required by the kink block model was not present in the high temperature "rotator" phase, and concluded that "kinks" were not important in the rotator transition. Maroncelli et al (11) showed that although the concentration of gauche defects in

$n\text{-C}_{21}\text{H}_{44}$ is less than 4 per molecule, it is not negligible.

Strobl and his co-workers (17,18,19) found that the highest temperature rotator phase of $n\text{-C}_{33}\text{H}_{68}$ is reached through a series of at least 3 distinct phase transitions, rather than a single transition as had previously been believed. Strobl estimated that between 40 and 70% of the molecules in $n\text{-C}_{33}\text{H}_{68}$ are non-planar in the highest temperature rotator phase. These estimates were based on small angle X-ray studies and assumed the existence of kink defects proposed by Blasenbry and Pechhold (15). Zerbi (20) has also provided evidence for the presence of gauche bonds near the end of the $n\text{-C}_{19}\text{H}_{40}$ molecule in its high temperature solid phase, using infrared spectroscopy.

To summarise, this all seems to indicate that non-planar conformations have a significant role to play in the mechanisms involved in the phase transitions of n -alkanes, and molecules containing a aliphatic portion.

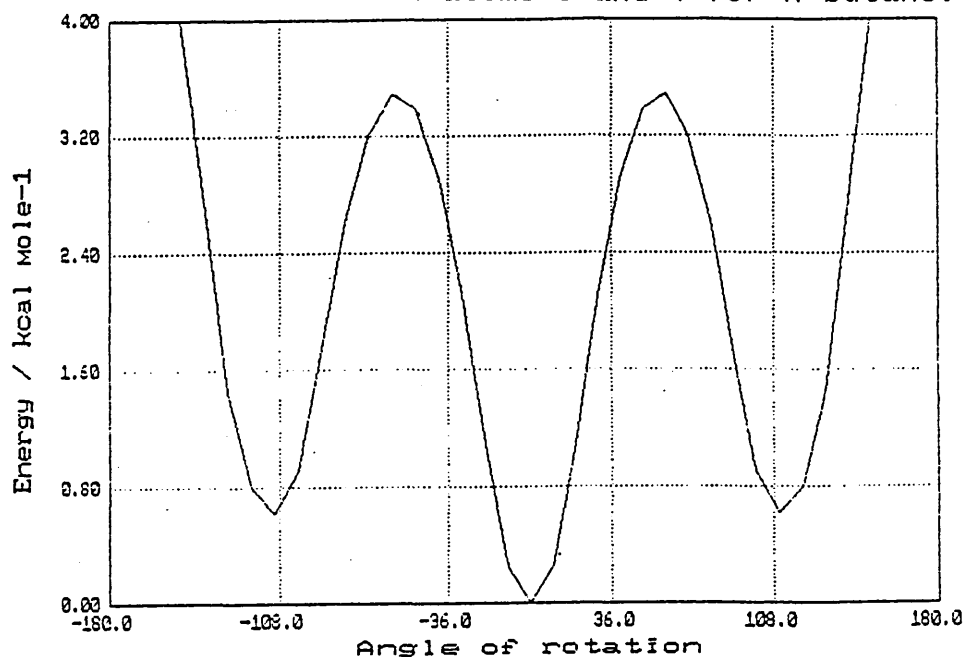
3.2 Rotational isomeric state model

There are many models used to describe the conformational behaviour of isotropic chain molecules. These include freely jointed chains, rotating chains, Porod-Kratky worm like chains and the rotational isomeric state model. The mathematical complexity of these models increases from freely jointed chains to the rotational isomeric state model. Of these, the latter provides the most realistic representation of the conformational characteristics of a real chain (21).

The rotational isomeric state model developed by Flory (22), assumes that the bonds of a polyethylene chain are

restricted to 3 positions, trans where the angle of rotation¹ $\phi=0$, gauche where $\phi=120^\circ$ and gauche' where $\phi=-120^\circ$. Figure 3.1 shows the potential energy $E(\phi)$ for rotating the bond between carbon atoms 2 and 3 in n-butane between $\phi = -180^\circ$ and 180° (this was calculated using the computer package Moly '86: see section 4.3). This shows that the minima are at 0° and $\pm 115^\circ$ ², with the potential walls in $E(\phi)$ sufficiently steep to confine the majority of the bonds in n-butane at ordinary temperatures (0-300°C) to states of torsional oscillation near one of the minima in $E(\phi)$. So the assumption that there are only 3 possible rotational positions for a bond in a polymethylene chain is reasonable.

Figure 3.1 The potential energy from rotating the bond between carbon atoms 3 and 4 for n-butane.



¹ The angle of rotation, ϕ , is the angle rotated by the bond between the carbon atoms C_i and C_{i+1} .

² The value of $\pm 120^\circ$ for the gauche bonds is taken from ethane, but for longer molecules there is a slight variation from this value. This is not a problem as when calculating the number of gauche defects present the RISM only uses the energy differences between gauche and trans not the angle.

3.2.1 Statistical weight

The rotational isomeric state model only takes into account the nearest neighbour interactions when calculating the probability of a gauche defect at bond position i . This is a reasonable approximation as, over a short range, modelling shows that only the nearest neighbour hydrogen atoms interact significantly (22). Interactions with hydrogen atoms at a longer range are dependent on the probability of the isotropic chain trajectory folding back on itself, which is low for any particular pair of hydrogen atoms (22). The energies for the various bond pairs ($i-1$ and i) in n -alkanes and polyethylene molecules are as follows³ (23):-

$$E_{\mu t} = 0 \text{ for } \mu=t, g \text{ and } g'$$

$$E_{t\mu} = 500 \text{ cal mole}^{-1}$$

$$E_{gg} = E_{g'g'} = E_{t\mu}$$

$$E_{gg'} = E_{g'g} = 3000 \text{ cal mole}^{-1}$$

The statistical weight corresponding to these energies is given by:-

$$u_{\mu\eta:i} = \frac{-E_{\mu\eta}}{RT} \quad (3.1)$$

where R is the gas constant (8.31 J K^{-1}).

T is the temperature in degrees kelvin.

η is t, g or g' and i bond position.

So by setting:-

$$\sigma = e^{-\frac{500}{RT}} \quad (3.2)$$

³ 1 cal = 4.18 joules.

and

$$\omega = e^{-\frac{3000}{RT}} \quad (3.3)$$

We obtain a statistical weight matrix of:-

$$U_i = \begin{matrix} & \begin{matrix} t & g & g' \end{matrix} \\ \begin{matrix} t \\ g \\ g' \end{matrix} & \begin{bmatrix} 1 & \sigma & \sigma \\ 1 & \sigma & \omega \\ 1 & \omega & \sigma \end{bmatrix} \end{matrix} \quad (3.4)$$

A partition function can then be calculated from the statistical weight matrix and is given by:-

$$z = j^* \left(\prod_{i=2}^{n-1} U_i \right) j \quad (3.5)$$

where

$$j^* = [1 \ 0 \ 0] \quad \text{and} \quad j = \begin{bmatrix} 1 \\ 1 \\ 1 \end{bmatrix}$$

n is the number of skeletal bonds in the chain backbone.

The a priori probability for the bond pair i-1 and i occurring in the state $\mu\eta$ is given by:-

$$P_{\mu\eta:i} = z^{-1} j^* \left(\prod_{j=2}^{i-1} U_j \right) U'_{\mu\eta:i} \left(\prod_{k=i+1}^{n-1} U_k \right) j \quad (3.6)$$

where $U'_{\mu\eta:i}$ is the statistical weight matrix U_i with all the elements set to zero except $U_{\mu\eta:i}$, and $2 < i < n-1$.

The special cases of $i=2$ and $i=n-1$ are given by:-

$$P_{\mu\eta:2} = z^{-1} j^* U'_{\mu\eta:2} \left(\prod_{k=3}^{n-1} U_k \right) j \quad (3.7)$$

$$P_{\mu\eta:i-1} - P_{\mu\eta:i} \quad (3.8)$$

Figure 3.2 shows the probability of trans-trans conformations at bond positions $i-1$ and i . As can be seen from the figure, the probability of a tt sequence approaches a constant value with increasing chain length and bond position i . The tt defect is of lower probability near the end of a polymethylene chain than in the middle of the chain. This is not the case with the tg defect: figure 3.3 shows the probability of a trans-gauche defect at bond position $i-1$ and i and, as can be seen, the probability decreases with increasing chain length and position of defect i , reaching a constant value at bond positions greater than 5.

Figures 3.2 and 3.3 show that for shorter chains the end effect on defect probabilities can be quite significant. As the molecules become longer the end effect becomes less and less. We can deduce from this that for polyethylene the probability of a specific defect can be assumed to be the same at all positions along the chain. The probability will be equal to the value from figures 3.2 and 3.3 for values of i greater than 5 and n greater than 3.

Figure 3.2 The probability of a tt defect in a polymethylene chain of length n at bond position i .

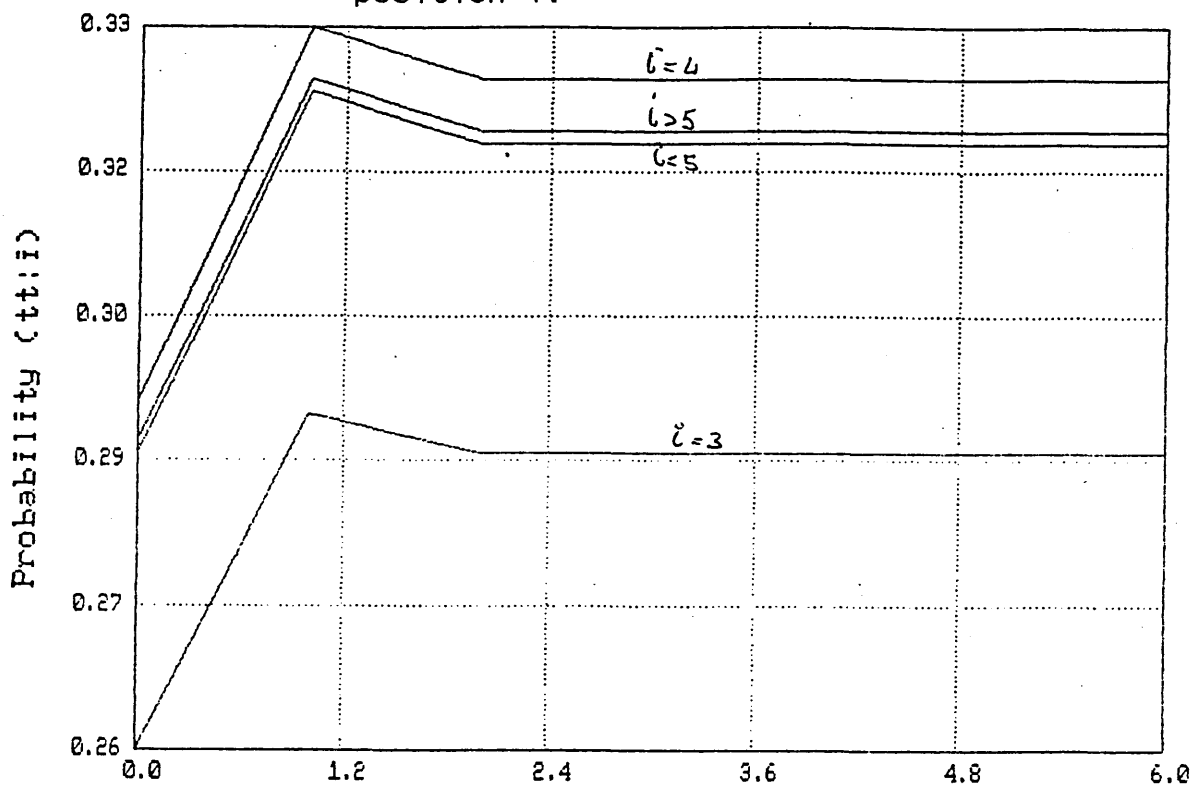
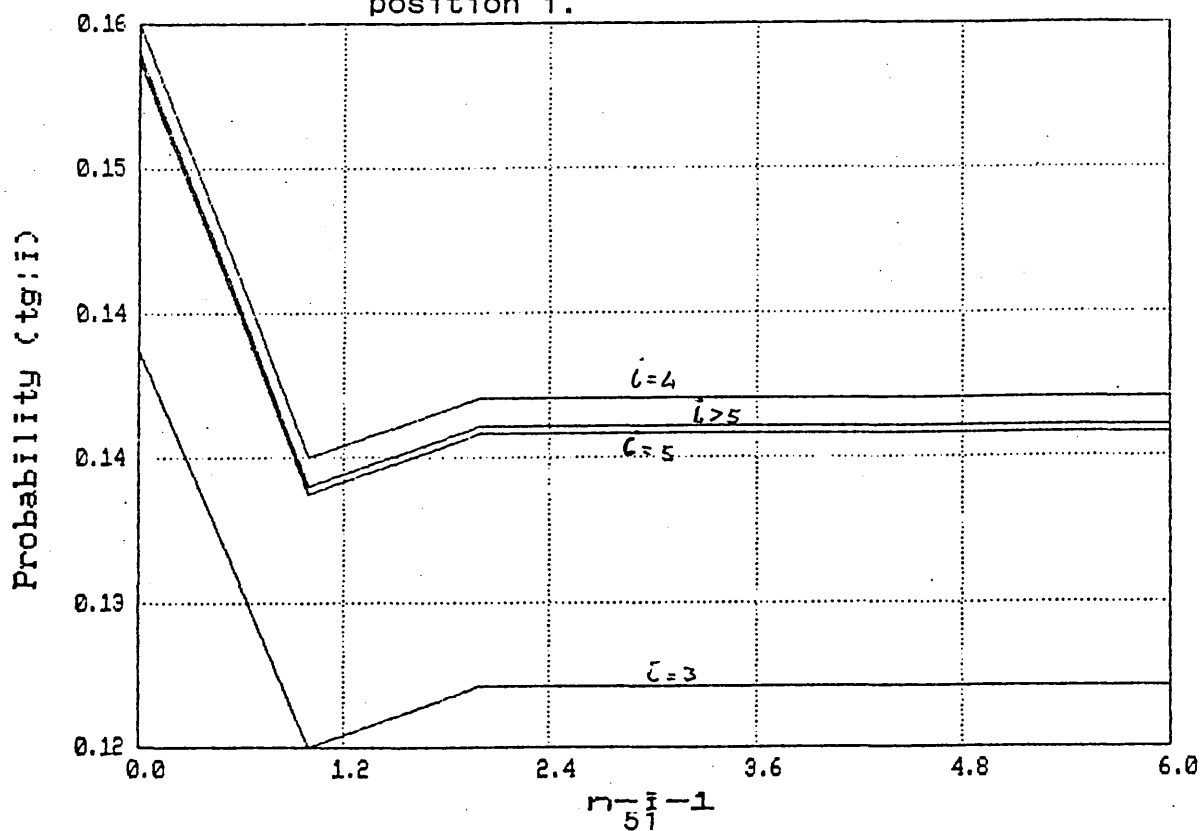


Figure 3.3 The probability of a tg defect in a polymethylene chain of length n at bond position i .



3.3 Infrared and Raman studies of n-alkanes

The infrared and Raman spectra of solid state n-alkanes have been well studied, with most of the peaks having been assigned to particular vibrations. Snyder (24,25,26) in the 1960's classified many of the peaks in the infrared spectra of n-alkanes $n\text{-C}_3\text{H}_8$ to $n\text{-C}_{30}\text{H}_{62}$, and also some of the conformations present in liquid n-alkanes and molten polyethylene (27).

Many of the peaks present in the infrared and Raman spectrum are characteristic of the phase of the sample. In the crystalline phase, peaks tend to be sharper than the corresponding liquid phase peaks. Several peaks split into doublets in the orthorhombic crystalline phase of n-alkanes. Among these are the 720 cm^{-1} rocking and 1465 cm^{-1} bending vibrations (20,28), which have additional peaks at 730 cm^{-1} and 1475 cm^{-1} respectively. These latter peaks approach zero intensity on melting or on changing from an orthorhombic lattice.

Several bands have a negative temperature co-efficient (29,30), (i.e. as the temperature increases the band intensity decreases), to be taken into account when looking for changes in the spectrum with changing temperature. These bands can still however be used to observe the changes in order/disorder as the temperature coefficient can change over phase transition (29).

3.3.1 Low frequency Raman spectroscopy

Raman spectroscopy is a technique used to investigate the vibrational modes of polyatomic molecules. The technique involves the scattering of the monochromatic source by the

molecules present in the sample. A photon from the source interacts with a sample molecule by inducing a dipole moment, the photon can then be scattered to a lower frequency, with the frequency shift corresponding to one of the vibrational modes of the molecule, this is known as a Stokes shift. The interaction of the photon with the molecule is a statistical event and as such the majority of the source passes through the sample without being affected.

One of the most important bands for measuring order in the Raman spectra of n-alkanes (and related molecules) is the low frequency longitudinal acoustical mode (LAM). This vibration involves the motion of the whole molecule, in a manner similar to an accordion. The frequency of the vibration is dependent on the chain length within the crystal (i.e. the crystal traverse) (31). By treating the alkane chain as a homogeneous elastic rod, Schaufele et al (31) derived an expression for the LAM frequency, expressed as a function of the chain length L :-

$$v = \frac{1}{2L} \sqrt{\frac{E_c}{\rho}} \quad (3.9)$$

where E_c is the Young's modulus
 ρ is the density of the n-alkane
 v is the frequency in Hertz.

L , the chain length, is the length of an all trans section of an n-alkane or polyethylene molecule. If a gauche defect appears in that section, then the section would effectively become two shorter sections, thus vibrating at 2 new frequencies and affecting the intensity of the original LAM vibration. This makes the vibration sensitive to any

conformational change. Khoury et al (32) observed slightly different frequencies for the orthorhombic forms of $n\text{-C}_{36}\text{H}_{74}$ and $n\text{-C}_{94}\text{H}_{190}$ and the monoclinic forms. For $n\text{-C}_{36}\text{H}_{74}$ the frequency of the LAM1 band for the orthorhombic form is 66.1 cm^{-1} and for the monoclinic form is 68.8 cm^{-1} . The difference in density and end-to-end carbon distance of the two forms, gives rise to the frequency difference, so the LAM mode can be used to identify different crystal forms of the same molecule.

Fraser et al (33) have used the technique of observing the LAM vibration, to analyse the effect of a swelling agent on mats of polyethylene crystallised from solution. A small decrease in the frequency of the LAM vibration is observed on swelling the crystal, indicating a small increase in the all-trans length in L . The swelling effect seems to involve a layer of a few loose chains rather than the majority of the folds at the lamellar surface.

Present in the liquid and non-crystalline phases of n -alkanes and polyethylene is the D-LAM vibration, and it is attributed to a LAM-like "in phase", or "breathing" vibration of the contributing modes. This accounts for the LAM part of the name, and the "D" denotes a disordered phase. The frequency of the D-LAM depends on the trans/gauche ratio and the number of carbon atoms N_c , in the chain (34). The bandwidth of the D-LAM is determined by the variance in the distribution of the trans/gauche ratio. This means that the narrower the distribution of the trans/gauche ratio, then the narrower the bandwidth of the D-LAM. The frequency of the D-LAM is given by (34):-

$$\nu = \nu_0 + \frac{B}{N_c^2} \quad (3.10)$$

where ν_0 and B are constants and N_c is the number of carbon atoms in the molecule chain.

Snyder et al (35), have used the D-LAM to observe the non-crystalline component of the bulk crystallised polyethylene, and found that the non-crystalline component was conformationally liquid like, even when the crystallinity of the sample was greater than 90%. The frequency of the D-LAM determined by Snyder (35) of semi-crystalline and liquid samples of polyethylene was 206 and 202 cm^{-1} with bandwidths of 56 and 60 cm^{-1} respectively. Equation 3.10 would seem to indicate that for shorter chain n-alkanes the D-LAM would have a higher frequency than polyethylene.

3.3.2 Conformationally sensitive infrared bands

There are many bands in the infrared (and Raman) spectrum which are sensitive to non-planar conformations (11,20,27,36), but the frequencies of some of these peaks are dependent on the length of the hydrocarbon chain. These include peaks in the CH_2 rocking region of the spectrum (1000-700 cm^{-1}) (11). Snyder (27) observed several bands in the CH_2 wagging region of the spectra of n-alkanes (1400-1200 cm^{-1}), which he assigned to various conformational defects, and confirmed these using normal co-ordinate analysis. These bands are as follows:-

gtg/gtg'	1368 and 1308 cm^{-1}
gg/g'g'	1352 cm^{-1}
tg	1344 cm^{-1} end gauche

gttg 1338 cm⁻¹

These were later revised (7) giving new frequencies of:-

$t_m(\text{gtg}'/\text{gtg})t_{m*}$	Kink	1366 cm ⁻¹	$m, m* \geq 0$
$t_m(\text{gg})t_{m*}$		1353 cm ⁻¹	$m, m* \geq 0$
(gt_m)	end gauche	1341 cm ⁻¹	$m \geq 1$
$t_m(\text{gtg}')t_{m*}$	Kink	1306 cm ⁻¹	$m, m* \geq 0$

m represents the minimum number of trans bonds required so that, if the $(m+1)^{\text{th}}$ bond is gauche the frequency of the vibrational mode will be within 5 cm⁻¹ of the limiting frequency for large m .

Maroncelli et al (11) found that for the homologous series of n -alkanes the vibration very quickly approached an asymptotic frequency, with increasing chain length. Also the CH₂ wagging defect frequency was found to vary slightly, depending on the position of the defect in the chain. This only affects defects near the end of the molecule.

By using the rotational isomeric state model (22), Maroncelli (11) was able to calculate the theoretical concentration of gtg and gg defects in the isotropic liquid phase of $n\text{-C}_{27}\text{H}_{56}$ at 70^oc. By measuring the intensity of the gtg and gg non-planar conformational bands of $n\text{-C}_{27}\text{H}_{56}$ at 70^oc, Maroncelli was able to find a calibration constant relating to the number of defects in any n -alkane at any temperature. It was assumed that the peak intensities were directly proportional to the number of non-planar conformations such that:-

$$n_{gtg} = \frac{I_{gtg} \times N_{C27gtg70}}{I_{C27gtg70}} \quad (3.11)$$

where n_{gtg} is the unknown number of gtg defects
 I_{gtg} is the intensity of the gtg band for the
 "unknown" sample
 $n_{C_{27}H_{56}70}$ is the number of defects calculated for n-
 $C_{27}H_{56}$ at 70⁰c
 $I_{C_{27}H_{56}70}$ is the intensity of the gtg defect band of
 n- $C_{27}H_{56}$ at 70⁰c.

This gave results for n- $C_{27}H_{56}$ in the rotator phase (solid
 II) of:-

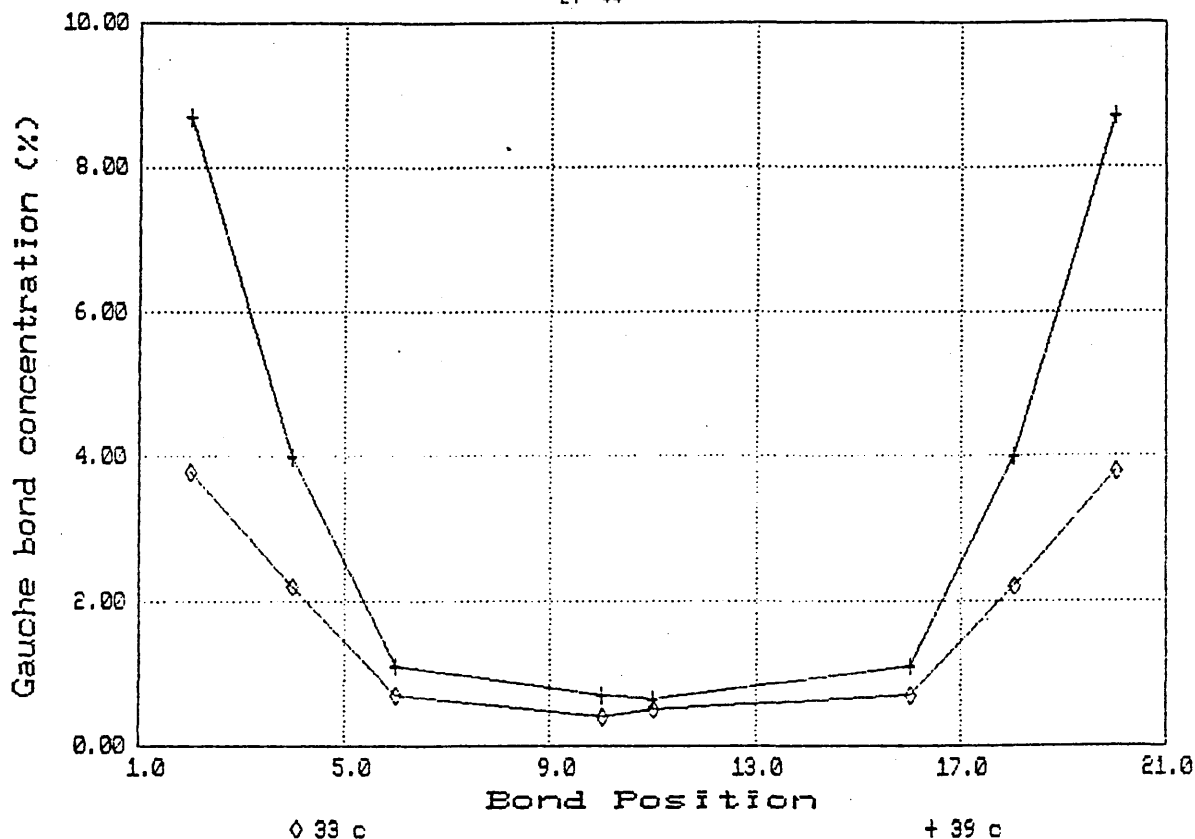
$$n_{gtg} = 0.38-0.64 \text{ per molecule}$$

$$n_{gg} \leq 0.002 \text{ per molecule.}$$

In the liquid phase at 70⁰C $n_{gtg} = 2.55$ and $n_{gg} = 2.34$,
 leading to the conclusion that the rotator phase contains
 about 20% of the gtg defects present in the liquid state,
 which is not an insignificant amount as suggested by Barnes
 et al (16). The value of n_{gg} in the rotator phase is very
 small, because the gg defect is much more difficult to
 accommodate in an ordered solid than a gtg' kink.

Snyder et al (37,38) investigated the distribution of
 gauche conformations in the rotator phase of the n-alkane n-
 $C_{21}H_{44}$, with two of the hydrogen atoms of n- $C_{21}H_{44}$ substituted
 with deuterium, using infrared spectroscopy. The defects
 found were almost entirely gtg' kinks, as these are the
 easiest to accommodate in a solid. Figure 3.4 (taken from
 reference 37) shows the concentration of gauche bonds at
 various sites along the chain. The highest concentration is
 near the end of the chain, and the concentration decreases
 rapidly towards the middle (38).

Figure 3.4 Variation of gauche concentration along the chain of $n\text{-C}_{21}\text{H}_{44}$, at 30 and 39°C.



This result is at odds with the assumption of a uniform distribution used in the interpretation of the X-ray diffraction measurements of the rotator phase by Strobl (17). However approximately 1% of the molecules have bonds near the centre of the chain with a gauche defect, contrary to the results of Zerbi (20) who observed gauche defects only near the end of the chain.

Kim et al (39) observed, using infrared spectroscopy, the increase in the concentration of gauche bonds with temperature for n -alkanes $n\text{-C}_n\text{H}_{2n+2}$, where $n=17, 25, 26, 36, 50$ and 60. Each n -alkane showed an increase in the gauche concentration as the melting point approached. For C_{17} , C_{25} , C_{26} and C_{36} this increase begins abruptly and occurs in association with a solid-solid phase transition. For the C_{50}

and C_{60} n-alkanes the onset of disorder is not associated with a solid-solid phase transition, and occurs gradually. Despite this difference, Kim et al found many similarities, including the temperature range from the onset of disorder to melting, total concentrations of defects and their distribution. They also found that for melt crystallised n-alkanes there was an inherent disorder, the extent being independent of temperature up to the pre-melting point, and on the basis of the number of gauche bonds per number of bonds available in the chain, the value was the same for all n-alkanes studied. Hagemann et al (40) used the technique of infrared CH_2 wagging defect modes to observe the effect of temperature on glassy films of $n-C_{21}H_{44}$ and low molecular weight polyethylene deposited on CsI windows held at 7 K. The samples were warmed upto 300 K and the spectrum was observed. Hagemann found that for both $n-C_{21}H_{44}$ and polyethylene, the chains went through a series of ordering transitions, as follows:-

	Chain	Monoclinic	Orthorhombic	Orthorhombic
Glass	-> Fully	-> Subcell	-> Subcell	-> Crystal
	Extended			Lattice

Spells et al (8) investigated polyethylene single crystals grown from various solvents in an attempt to observe bands in the defect region ($1400-1200\text{ cm}^{-1}$) of the infrared spectrum which could be assigned to regular folding at the surface of the crystal. A peak was observed at 1346 cm^{-1} and the behaviour of this band on annealing and quenching from the melt was consistent with a regular chain fold. This could not be assigned to a specific type of fold ($\{110\}$ or $\{200\}$).

Ungar et al (41) observed the infrared spectra of once folded $n-C_{198}H_{398}$ (F) and fully extended $n-C_{198}H_{398}$ (E). The layer

periodicities (taken from small angle X-ray patterns) for E and F were 253Å and 125Å respectively, and similar values were obtained by Ungar using Raman LAM frequencies. This shows that in the F form, all but a few methylene groups are contained in equally long extended chain portions on each side of the fold, the fold being adjacent and reasonably tight (and in a {110} plane).

By subtracting the E spectrum from the F spectrum, Ungar was able to observe any bands that might be assigned to a {110} fold. Bands at 1369, 1352, 1346, 1342, 1306 and 1295 cm^{-1} were found. The bands at 1369 and 1306 cm^{-1} had previously been assigned to *gtg* and *gtg'* defect bands (7), the 1352 cm^{-1} band to *gg* defects (7), and the 1342 cm^{-1} band to the end-gauche defect (*gt*) (7). The 1295 cm^{-1} band was thought to be a slightly off-centre CH_2 wagging mode (B_{2g}) which is strongly Raman active. The 1346 cm^{-1} was assigned to an adjacent tight {110} fold.

Wolf et al (42) confirmed these assignments using Green's functions to calculate the defect density of states for a tight {110} fold in the frequency range 500-1400 cm^{-1} . Resonance modes for the {110} fold were calculated to be at 1348, 1343 and 1288 cm^{-1} , and were assigned by Wolf to the infrared bands at 1346, 1342 and 1295 cm^{-1} . Wolf showed that the {110} fold is approximately a *g'g'ggtg* defect, so that the contribution to the 1369 cm^{-1} kink and the 1352 cm^{-1} double gauche bands found by Ungar (41) becomes apparent.

The technique of investigating the number of defects present in an alkane chain has been applied to other systems containing a polymethylene portion. Zerbi et al (28,43) used

several bands in the infrared and Raman spectra of fatty acids (28), to analyse the melt and pre-melt phase behaviour. In the case of both the fatty acids and $[\text{CH}_3(\text{CH}_2)_{13}\text{NH}_3]_2\text{MnCl}_4$, the CH_2 rocking and bending vibrations at $720\text{--}730\text{ cm}^{-1}$ and $1475\text{--}1485\text{ cm}^{-1}$ respectively remain as doublets throughout the pre-melt phase, reverting to singlets only when the molecules actually melt. Of the defect modes, only the kink defect (1369 and 1306 cm^{-1}) bands appear on the transition from crystalline to pre-melt phase. This is consistent with the model proposed by Zerbi (28) that only the gtg' (kink) defect occurs in the pre-melt phase. The gtg' defects are easier to accommodate in the crystal lattice than gg or gtg defects, because the direction in which the chain travels remains the same, but for gg and gtg defects the direction changes dramatically.

As the molecules melt the intensities of the gtg/gtg' bands at 1369 and 1306 cm^{-1} go through a step, and the number of gtg defects becomes the same as that for an isotropic n -alkane of equivalent chain length and at the same temperature. Also the band at 1352 cm^{-1} (gg) appears after melting and gives the same intensity as an isotropic n -alkane of equivalent length and at the same temperature.

This method has also been used in the conformational analysis of surfactant molecules in water solutions. Holler (44) investigated sodium dodecyl sulphate (SDS) using the technique of defect mode analysis. SDS forms micelles at a minimum concentration of 0.2% w/w with water. The proportion of surfactant used was 10% w/w, and it was estimated to contain about 98% of the SDS molecules in micelles. The

results showed that the concentrations of gtg and gg defects were the same as for an alkane of equivalent length. Hence in micelles the aliphatic portions of SDS behave like a liquid.

Senak et al (45) used the 1369 cm^{-1} and 1352 cm^{-1} defect modes to quantify the disorder present in two phospholipids, 1,2-dipalmitoylphosphatidylethanolamine (DPPE) and 1,2-dipalmitoylphosphatidylcholine (DPPC). On calibrating the intensity of these bands using n-alkanes and the rotational isomeric state model (using a peak fitting program to determine intensities), Senak found that the intensity of the 1352 cm^{-1} gg defect increased with temperature as expected, but the 1369 cm^{-1} defect mode intensity decreased with increasing temperature. This latter result is contrary to the result predicted by the RISM, and may be as a result of the peak fitting algorithm. Also the value of n_{gtg} determined by Senak from the RISM for n-C₂₇H₅₆ at 70°C differs from that determined by Maroncelli et al (11) having values of 2.29 and 2.55 gtg defects per molecule respectively. The values of n_{gg} determined by Senak and Maroncelli are 2.35 and 2.34 respectively. The expected result for n_{gtg} should be higher than n_{gg} , as the probability of a gtg defect is greater.

The number of defects determined by Senak for DPPC was found to be $n_{gtg}=1.0$ and $n_{gg}=0.4$ in a CHCl₃ solution just above the gel/liquid crystal phase transition, while DPPE in a CHCl₃ solution in the L_α phase is more ordered with $n_{gtg}=1.0$ and $n_{gg}=0.2$, but both are lower than values determined for an isotropic n-alkane of equivalent chain length, showing that the aliphatic chains in DPPC and DPPE are much more ordered.

3.4 References

- 1) J. Tsu and D.F.R. Gilson, J. Phys. Chem. 72(12), 4082, 1968
- 2) M.R. Barr, B.A. Dunell and R.F. Grant, Can. J. Chem. 41, 118, 1963
- 3) D.C. Basset and B. Turner, Nature Phys. Sci. 240, 6237, 1972
- 4) A. Muller, Proc. Royal Soc. London Ser. A, 138, 514, 1932
- 5) H.M.M. Shearer and V. Vand, Acta Cryst. 9, 379, 1956
- 6) M.G. Broadhurst, J. Research of National Bureau of Standards - A Phys. and Chem. 66, 241, 1962
- 7) R.G. Snyder, M. Maroncelli, S.P. Qi and H.L. Strauss, Science 214(9), 188, 1981
- 8) S.J. Spels, S.J. Organ, A. Keller and G. Zerbi, Polymer 28, 697, 1987
- 9) D.M. Small, "Handbook of lipid research 4, The physical chemistry of lipids", Plenum Press, New York, 1986
- 10) "Liquid crystals and plastic crystals Volume 1, Physical and chemical properties and methods of investigation", Ed. G.W. Gray and P.A. Winsor, Ellis Horwood Ltd, Chichester 1974
- 11) M. Maroncelli, S.P. Qi, H.L. Strauss and R.G. Snyder, J. Am. Chem. Soc. 104, 6237, 1982
- 12) A.E. Smith, J. Chem. Phys. 21, 2229, 1953
- 13) J. Doucet, I Denicolo, A. Craievich and A. Collet, J. Chem. Phys. 75, 5125, 1981
- 14) D.W. McClure, J. Chem. Phys. 49, 1830, 1968
- 15) S. Blasenbry and W. Pechhold, Rheol. Acta 6, 174, 1967

- 16) J. Barnes and B.M. Fanconi, J. Chem. Phys. 56, 5190, 1972
- 17) G.R. Strobl, B. Ewen, E.W. Fischer and W. Piesczek, J. Chem. Phys. 61, 5257, 1974
- 18) B. Ewen, E.W. Fischer, W. Piesczek and G.R. Strobl, J. Chem. Phys. 61, 5257, 1974
- 19) B. Ewen, G.R. Strobl and D. Richter, Faraday Discuss. Chem. Soc. 69, 19, 1980
- 20) G. Zerbi, R. Magni, M. Gussoni, K.H. Moritz, A. Bigotto and S. Dirlikov, J. Chem. Phys. 75, 3175, 1981
- 21) R.L. Jernigan and P.J. Flory, J. Chem. Phys. 50, 4178, 1969
- 22) P.J. Flory, "Statistical mechanics of chain molecules", Interscience, New York, 1969
- 23) R.L. Jernigan and P.J. Flory, J. Chem. Phys. 50, 4165, 1969
- 24) R.G. Snyder, J. Mol. Spec. 4, 411, 1960
- 25) R.G. Snyder, J. Mol. Spec. 5, 116, 1961
- 26) R.G. Snyder and J.H. Schachtschneider, Spect. Acta 19, 85, 1963
- 27) R.G. Snyder, J. Chem. Phys. 47, 1316, 1967
- 28) G. Zerbi, G. Conti and G. Minoni, J. Phys. Chem. 91, 2386, 1987
- 29) R.G. Snyder, M. Maroncelli, R.L. Strauss and V.M. Hallmark, J. Phys. Chem. 90, 5623, 1987
- 30) H. Hagemann, R.G. Snyder, A.J. Peacock and L. Mandelkern. Macromolecules 22, 3600, 1989
- 31) R.F. Schaufele and T. Shimanouchi, J. Chem. Phys. 47, 3605, 1967

- 32) F. Khoury, B. Fanconi, J.D. Barnes and L.H. Bolz, J. Chem. Phys. 59, 5849, 1973
- 33) G.V. Fraser, A. Keller, E.J. George and D. Dreyfuss, J. Macromol. Sci. Phys. B16, 295, 1979
- 34) R.G. Snyder J. Chem. Phys. 76, 3921, 1982
- 35) R.G. Snyder, N.E. Schlotter, R. Alamo and L. Mandelkern, Macromolecules 19, 621, 1986
- 36) P. Jona, M. Gussoni and G. Zerbi, J. Mol. Struc. 142, 211, 1986
- 37) R.G. Snyder, M. Maroncelli and H.L. Stauss, J. .Am. Chem. Soc. 105, 133, 1983
- 38) M. Maroncelli, H.L. Strauss and R.G. Snyder, J. Chem Phys. 82, 2813, 1985
- 39) Y. Kim, H.L. Stauss and R.G. Snyder, J. Phys. Chem. 93, 7520, 1989
- 40) H. Hagemann, H.L. Strauss and R.G. Snyder, Macromolecules 20, 2810, 1987
- 41) G. Ungar, S.J. Organ, A. Keller and G. Zerbi, Polymer 28, 697, 1987
- 42) S. Wolf, C. Schmid and P.C. Hagele, Polymer 31, 1222, 1990
- 43) C. Almirante, G. Minoni and G. Zerbi, J. Phys. Chem. 91, 2386, 1990
- 44) F. Holler and J.B. Callis, J. Phys. Chem. 93, 2053, 1989
- 45) L Senak, M. A. Davis and E. Mendelsohn, J. Phys. Chem. 95, 2565, 1991

Chapter 4

4 Molecular modelling	67
4.1 Maximum Chain Extension	67
4.1.1 Rotational isomeric state model	68
4.1.2 Constant temperature calculations	69
4.1.3 Constant chain length calculations	71
4.1.4 Chain dimensions	76
4.2 Ionic core radius	85
4.2.1 New model	89
4.3 Graphics modelling package	95
4.3.1 Moly '86	95
4.3.2 Analysis	96
4.3.3 Lithium phenyl stearate	98
4.3.4 Maximum phenyl group rotation	111
4.4 References	117

4 Molecular modelling

In addition to various experimental techniques used to determine the structure of lithium phenyl stearate (LiPS) (see chapters 5,6,7), various modelling techniques have been employed to assist in the interpretation of the spectroscopic data. The structural information required was the maximum chain extension of the aliphatic portion of the hexagonal cylinders in LiPS, the ionic core radius of the hexagonal cylinders, and the effect of the phenyl group on the chain conformation of the aliphatic portion of the soap.

4.1 Maximum Chain Extension

The chain extension of any chain molecule depends upon the bond conformations present in the chain, so by determining the number of defects present in a chain, it should be possible to determine the chain extension. The maximum chain extension of the aliphatic portion of LiPS can be determined from the intensity of the infrared bands at 1369 cm^{-1} and 1352 cm^{-1} , representing gtg'/gtg and $gg/g'g'$ defects respectively. The intensity of these bands is directly proportional to the numbers of defects e.g.

$$n_{gtg} = K_{gtg} I_{gtg} \quad (4.1)$$

where K_{gtg} is a calibration constant and is unknown.

n_{gtg} is the number of gtg' and gtg defects

I_{gtg} is the intensity of the gtg and gtg' defects

The constant K_{gtg} can be determined from the defect modes for n-alkanes in the isotropic state and the number of defects (n_{gtg} and n_{gg}) calculated from the rotational isomeric state model for the same n-alkane at the same temperature (1).

This gives:-

$$K_{gtg} = \frac{n_{gtg_{RISM}}}{I_{gtg_{Infrared}}} \quad (4.2)$$

4.1.1 Rotational isomeric state model

Within the rotational isomeric state model (RISM) developed by P.J. Flory (2), the number of gauche defects ($n_g + n_g'$ referred to simply as n_g) present in various n-alkanes was estimated over a range of temperatures. A fuller mathematical description of the model is given in section 3.2.

The required inputs for the model are the chain length (number of carbon atoms in chain backbone, N_c), temperature and the energy required for various conformations at bond pair $i-1$ and i . The energies are as follows(3):-

$$E_{\mu t} = 0 \quad \text{for the } (i-1)^{\text{th}} \text{ bond } \mu = t, g \text{ and } g'$$

$$E_{t\mu} = 500 \text{ cal mole}^{-1} \text{ for the } i^{\text{th}} \text{ bond } \mu = g \text{ and } g',^1$$

$$E_{gg} = E_{g'g'} = E_{t\mu}$$

$$E_{gg'} = E_{g'g} = 3000 \text{ cal mole}^{-1}$$

It is assumed that the energy of the various conformations is independent of the bond position along the chain. In the simulation, each n-alkane molecule was simulated 10,000 times, so if the average number of defects present in a molecule is 1 then the precision of the estimate would be ± 0.01 . Also the two end bonds (1 and N_c) were not considered, as rotation of these bonds would have no effect on the conformation.

¹ mole value used here is Avogadro's number (6.02×10^{23}).
1 cal = 4.14 joules

The number of defects calculated and presented are as follows:-

$$n_{gtg}^2 = n_{gtg}^3 + n_{gtg'} + n_{g'tg} + n_{g'tg'} \quad (4.3)$$

$$n_{gg}^2 = n_{gg}^3 + n_{g'g'} \quad (4.4)$$

$$n_g^2 = n_g^3 + n_{g'} \quad (4.5)$$

4.1.2 Constant temperature calculations

The number of g, gtg and gg (n_g , n_{gtg} and n_{gg}) bond conformations was determined for n-alkanes 6 to 30 (n-C₆H₁₄ to n-C₃₀H₆₂) at constant temperature (20°C). n-Alkanes having more than 16 carbon atoms are solid at room temperature (4), and so the model is not valid for these molecules, but the results have been included to show the general trend. Figure 4.1 shows the variation in the numbers of g, gtg and gg non-planar conformations with the number of carbon atoms in the n-alkane. Numbers of g,gtg and gg defects all increase linearly with chain length. The form of this variation was found from data in figure 4.1 to be described by:-

$$n_g = 0.359N_c - 0.882 \quad (4.6)$$

$$n_{gg} = 0.093N_c - 0.362 \quad (4.7)$$

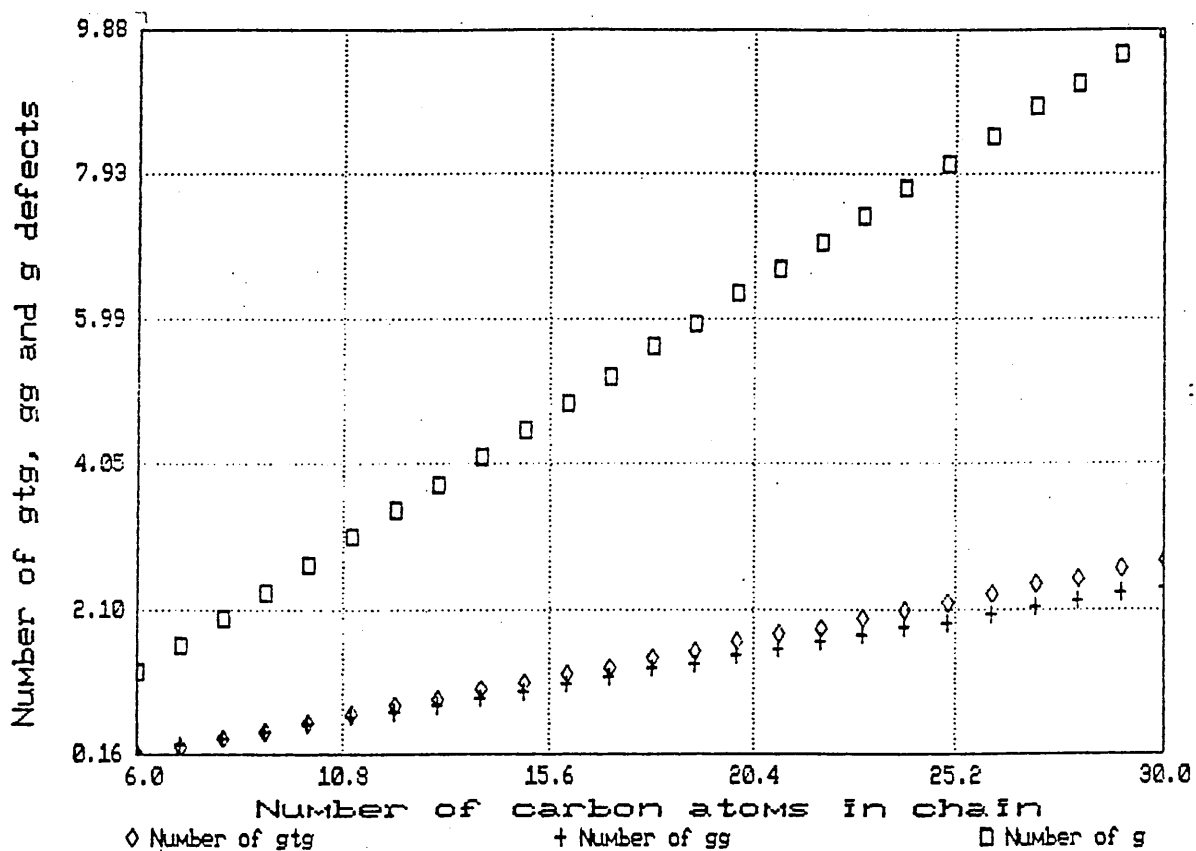
$$n_{gtg} = 0.109N_c - 0.497 \quad (4.8)$$

where N_c is the number of carbon atoms present in the n-alkane.

² These values represent the sum of all similar defects i.e. $n_g = n_g + n_{g'}$, and is the value referred to henceforth in this thesis.

³ These values represent the numbers of these particular defects (g is sometimes referred to in the other literature as g[†]) such that n_{gtg} is $n_g + n_{tg}$.

Figure 4.1 Variation in the numbers of g, gg and gtg defects with number of carbon atoms in the alkane chain.



Plots of n_{defect} versus N_c intercept the N_c axis at $N_c = 2.45, 3.91$ and 4.58 carbon atoms for n_g, n_{gg} and n_{gtg} respectively. As the number of carbon atoms is physically restricted to an integer, then the smallest n-alkane required to obtain each defect is n-butane for a g defect, n-pentane for a gg defect and n-hexane for gtg defect. If the rotational isomeric state model is a reasonable approximation to actual conformations present in n-alkanes, one would expect the intensity of the infrared gtg and gg defect bands to increase linearly with increasing chain length. This provides a test for the validity of the RISM (see section 6.2).

4.1.3 Constant chain length calculations

The numbers of g, gg and gtg conformations were calculated within the temperature range -270 to 500⁰C for n-heptadecane. n-Heptadecane was chosen because it has the same number of -CH₂- groups as LiPS, and so could provide a direct comparison. Figure 4.2 and figure 4.3 show the variation of the numbers of g, gg and gtg defects with temperature. The figures show that for all the defects, the concentration increases non-linearly with temperature. The number of gg defects becomes greater than the number of gtg defects in the region 140 to 210⁰C. This is expected as the number of available trans sites becomes less and less as the temperature increases. Eventually, the number of gtg conformations is expected to pass through a maximum and ultimately to decrease as the number of trans units becomes increasingly scarce. This behaviour is not predicted for the temperature range -270 to 500⁰C (figure 4.3), although the gradient progressively decreases. The temperature at which the number of gtg is a maximum is very high and has not been achieved experimentally.

One significant feature in figure 4.3 is that although the predicted number of gtg and gg defects increases with temperature, the change for an isotropic n-alkane is quite small, eg. the number of gg defects only doubles over the temperature range 0 to 500⁰C. This fact is important because the error in measuring the intensity of infrared bands can be as much as 20%. Taking the temperature range from 300 to 500⁰C, the number of gg defects only increases by 15%, so that any changes in the absorbance would be difficult to

detect. Over the range (0 to 200°C) in which the spectroscopic studies were carried out, the number of g defects is expected to increase by 50% if the aliphatic portion of the molecule is behaving like an isotropic chain, so that the changes in the infrared absorbances should be measurable.

Figure 4.2 Variation in the number of g defects with increasing temperature.

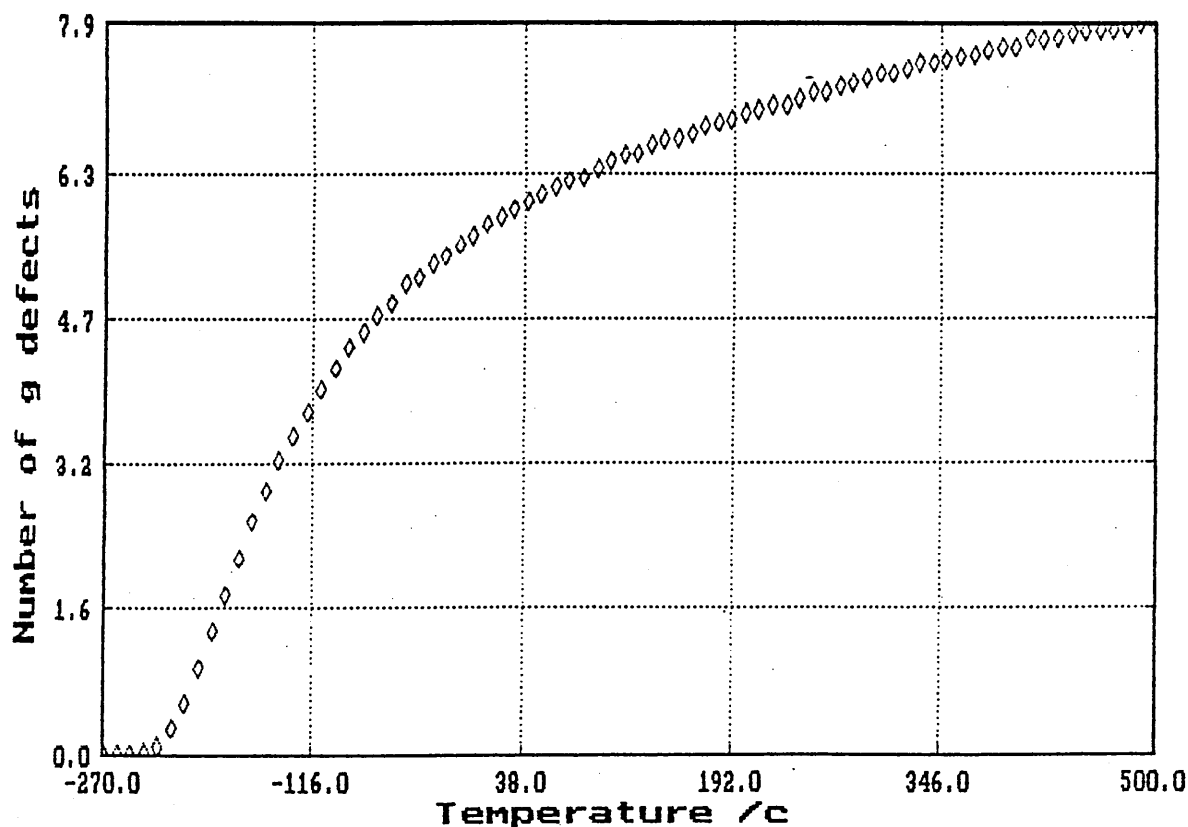


Figure 4.3 Variation in the number of gtg and gg defects with increasing temperature.

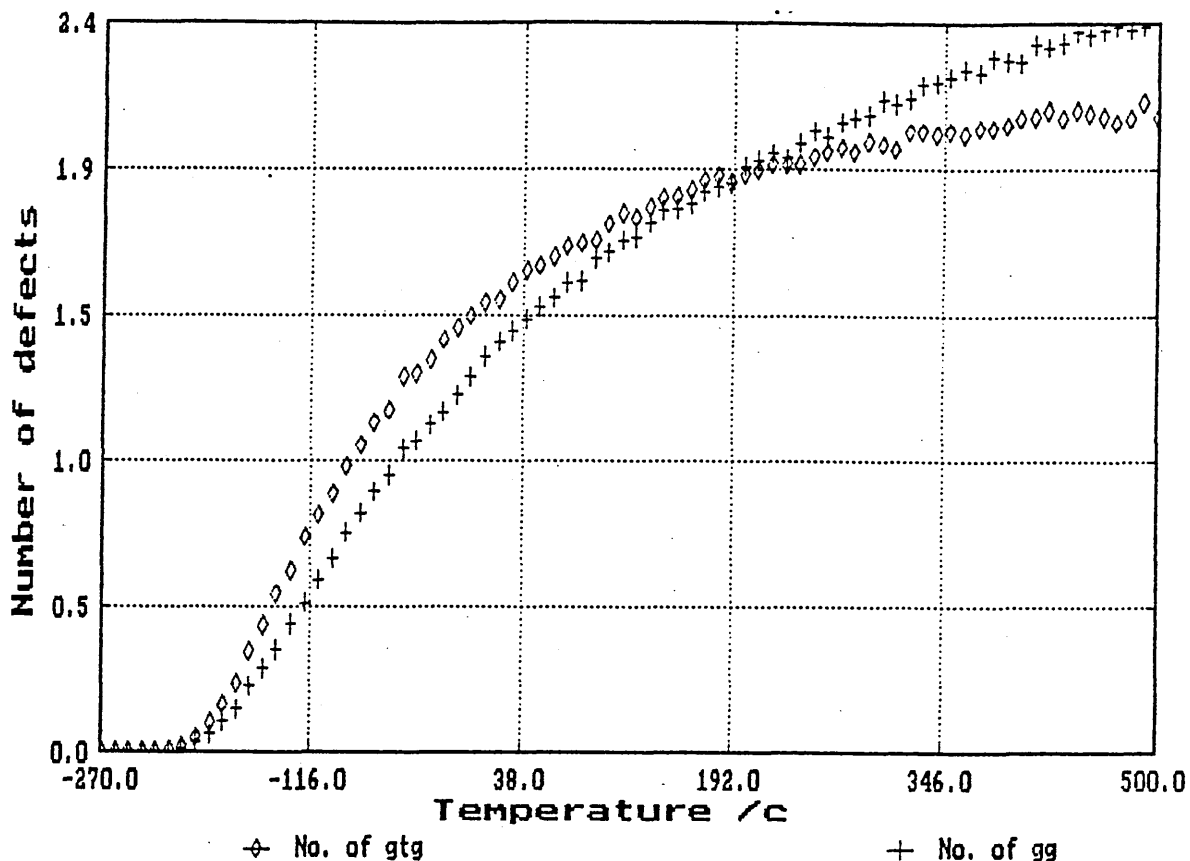


Figure 4.4 shows the variation of the numbers of gtg and gg defects with the number of g defects. This is required because calculating maximum chain extension requires the number of g defects (n_g), but infrared spectroscopy can only indicate the proportions of gg and gtg/gtg' defects and not directly the number of g bonds present. The variation of the number of gtg and gg defects with number of g defects is non-linear, both increasing slowly at first with increasing number of g defects ($0 < n_g < 2.3$). This is expected for low n_g , as the probability of 2 g defects coming together to form either gtg or gg defects is low. As the number of gauche increases, both the numbers of gtg and gg defects increase steadily, but at $n_g \approx 5.6$ the gradient of the gtg curve begins

to decrease, and the number of gtg defects becomes equal to the number of gg defects for $n_g \approx 6.9$. This is expected: as the number of g units increase, the number of available t sites decreases. It is expected that the number of gtg defects will decrease as the population of g and t inverts ($n_g > n_t$).

The number of gg defects, on the other hand continues to increase. Again this be expected: as n_g increases the probability of it forming a pair with another gauche increases, so that n_{gg} increases. The only thing limiting the number of gg defects (and of course n_g) in theory is the chain length of the molecule, limiting n_g to the number of bonds in the chain.

Figure 4.4 Variation in the number of gtg and gg defects with increasing number of g defects.

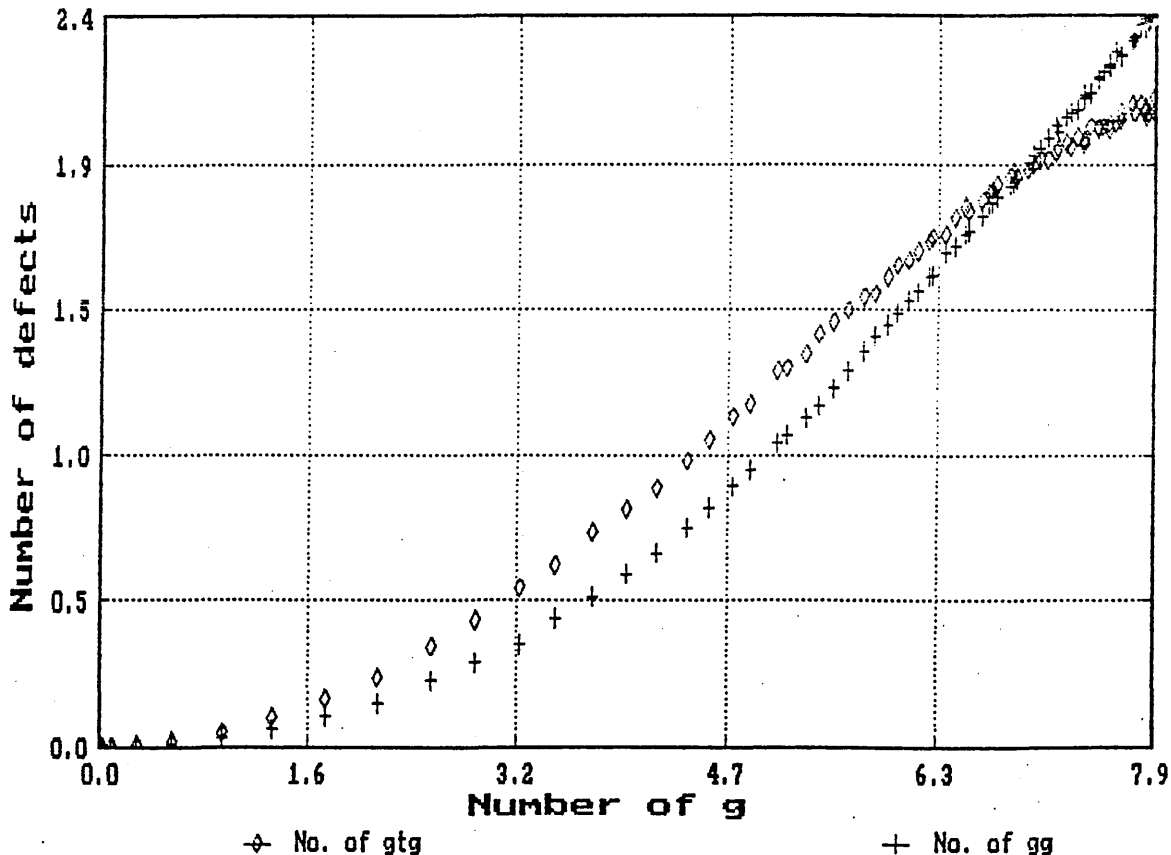
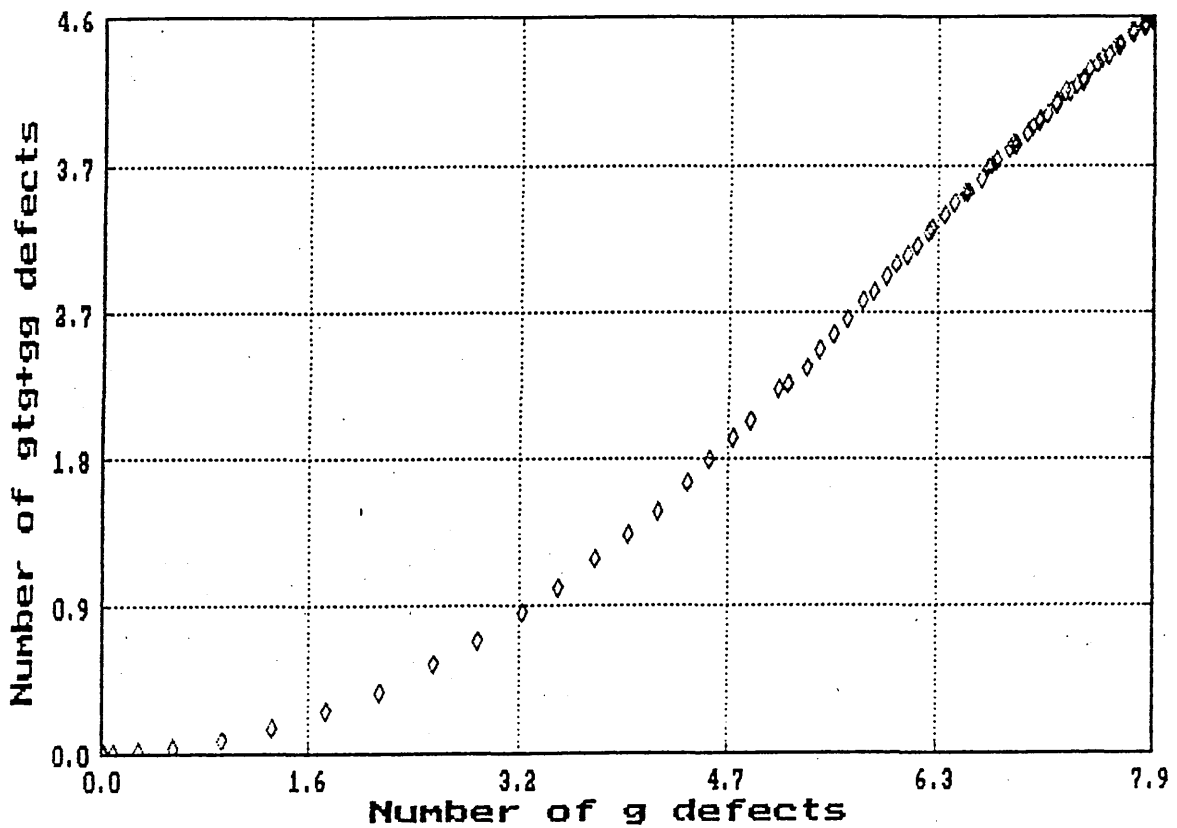


Figure 4.5 shows the variation in the total number of both gtg and gg defects with number of g defects. The curve is non-linear, but the addition improves the statistics, giving a much smoother curve and making prediction of the number of g defects from the number of gtg and gg defects more precise.

Figure 4.5 Variation of the total number of gtg and gg defects with increasing number of g defects.



4.1.4 Chain dimensions

Having determined the number of gauche conformations (n_g) present in LiPS, from the infrared data and the rotational isomeric state model, it becomes possible to calculate the dimensions of the molecule (eg end-to-end length) allowing the estimation of molecular volume etc (5). Figure 4.6 shows the standard chain conformation (i.e. all trans) for a linear n-alkane containing N_c carbon atoms. All the carbon atoms lie in the x-y plane (hydrogen atoms are ignored in the diagram), with each successive atom having a greater positive x-value, while y alternates between zero and a positive value and $z=0$. This gives a "standard" (all trans) vector position of the j^{th} skeletal atom of \underline{v}_j^0 . If all the bonds are allowed to rotate then the j^{th} skeletal co-ordinate vector is given by (5):-

$$\underline{v}_j = \underline{v}_0^0 + \sum_{m=1}^j \left[\prod_{l=1}^m T_{\phi_l} (\underline{v}_m^0 - \underline{v}_{m-1}^0) \right] \quad (4.9)$$

where ϕ_l is the angle rotated by the l^{th} bond and T_{ϕ_l} is defined as:-

$$T_{\phi_l} = T_{\alpha_l} T_{\phi_l} T_{\alpha_l} \quad (4.10)$$

where:-

$$T_{\alpha_l} = \begin{bmatrix} \cos \alpha_l & \sin \alpha_l & 0 \\ -\sin \alpha_l & \cos \alpha_l & 0 \\ 0 & 0 & 1 \end{bmatrix} \quad (4.11)$$

and

$$\alpha_1 = \tan^{-1} \left(\frac{y_1^o - y_{1-1}^o}{x_1^o - x_{1-1}^o} \right) \quad (4.12)$$

where α_1 is the angle between the $1-1^{\text{th}}$ and 1^{th} bonds on the x-axis and is alternatively positive and negative.

$$T_{\phi_1} = \begin{bmatrix} 1 & 0 & 0 \\ 0 & \cos\phi_1 & \sin\phi_1 \\ 0 & -\sin\phi_1 & \cos\phi_1 \end{bmatrix} \quad (4.13)$$

where ϕ_1 is the angle of rotation of 1^{th} bond.

These factors can be combined into a single matrix:-

$$T_{\phi_1} = \begin{bmatrix} \cos^2\alpha_1 + \cos\phi_1 \sin^2\alpha_1 & \cos\alpha_1 \sin\alpha_1 (1 - \cos\phi_1) & -\sin\alpha_1 \cos\phi_1 \\ \cos\alpha_1 \sin\alpha_1 (1 - \cos\phi_1) & \sin^2\alpha_1 + \cos^2\alpha_1 \cos\phi_1 & \cos\alpha_1 \sin\phi_1 \\ \sin\phi_1 \sin\alpha_1 & -\sin\phi_1 \cos\alpha_1 & -\cos\phi_1 \end{bmatrix} \quad (4.14)$$

The above model can then be used to determine the maximum chain extension (i.e. the furthest distance from the origin reached by any atom of the chain), for a chain containing N_c carbon atoms and having n_g gauche defects. The maximum chain extension, R , can be represented thus:-

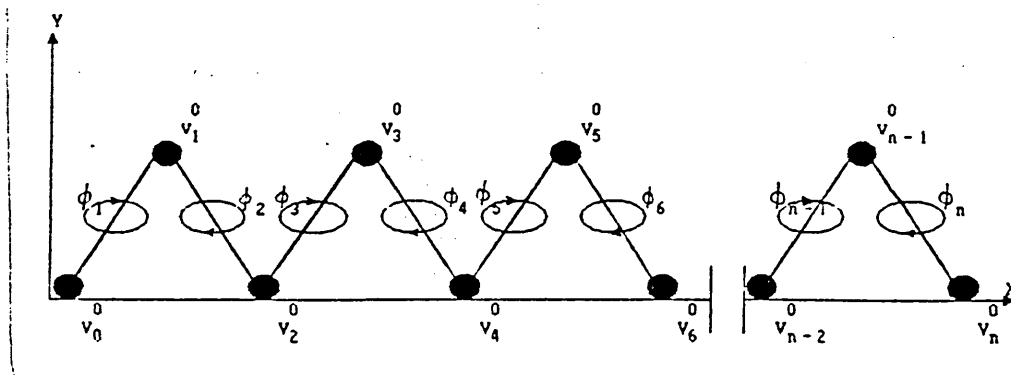
$$R = \sqrt{(x_1 - x_0)^2 + (y_1 - y_0)^2 + (z_1 - z_0)^2} \quad (4.15)$$

where x_i , y_i and z_i are such that R is maximized.

The co-ordinates of \underline{y}_0 are such that $x_0=0$, $y_0=0$ and $z_0=0$, thus simplifying eqn 4.15 to:-

$$R = \sqrt{x_1^2 + y_1^2 + z_1^2} \quad (4.16)$$

Figure 4.6 The co-ordinate system for the all-trans conformation of an n-alkane with N_c carbon atoms in the backbone (hydrogen atoms are not shown).



This particular quantity was chosen because it best represents the extent to which a molecule may extend beyond the ionic core of a reverse hexagonal phase. The chain end-to-end distance was not used, for example, because this would give a very small value in the case of the chain folding back on itself.

When the calculation is applied to the reversed hexagonal phase of lithium phenyl stearate, it was assumed that the first carbon atom lies on the surface of the ionic core, with the co-ordinate system defined by the first two

bonds so that the carbon atom at \underline{v}_2 lies on the x-axis. The y-axis is then a tangent to the ionic core surface at \underline{v}_0 . Having determined the quantity R in this way, the value was taken to be the maximum possible extension of the chain perpendicular to the ionic core surface.

A computer simulation to calculate the maximum chain length of n-heptadecane was performed, with the n-heptadecane containing between 1 and 15 gauche defects, and a simulation of 10,000 molecules. It was assumed that the molecule was idealized, i.e. that the C-C bond is 1.54Å (6), and the C-C-C bond angle is tetrahedral ($109^{\circ}28'$), giving a value for α_1 of $\pm 35^{\circ}16'$, and the bond rotation was the idealized gauche angle of $\pm 120^{\circ}$ ($\phi_1=120^{\circ}$). Figure 4.7 shows the variation of the average value of R , R_{2V} , with number of gauche defects. As can be seen, the chain extension decreases with increasing proportions of gauche defects, as the chain trajectory becomes more compact. This leads to the result that for an isotropic n-heptadecane with 5.6 gauche defects per chain (see Figure 4.5) at room temperature, the chain extension, R_{2V} , is found to be 9.8Å while at 500°C (7.9 gauche defects per chain) a chain extension of 8.7Å is obtained. This shows that once the molecule is in an isotropic phase, the chain extension, R_{2V} , is relatively constant, and is therefore insensitive to temperature because of the relatively large numbers of gauche bonds.

Figures 4.8 to 4.15 show the distribution of chain lengths for various numbers of gauche defects. This shows that when the number of gauche defects is 1 the distribution is very narrow. As the number of gauche bonds increases

(figures 4.9 and 4.10) the distribution becomes very broad as the number of permutations of the positions of the gauche bonds has a significant effect on the chain extension from the ionic core. Then as n_g is increased even more (figures 4.11 to 4.15) the distributions begin to narrow with R_{av} approaching a minimum value of 7.3Å for 15 gauche defects. This narrowing of the distributions is caused by the reduction in the number of permutations of the position of the gauche bonds.

Figure 4.7 The variation of the average chain extension, R_{av} , for n-heptadecane with increasing number of gauche defects.

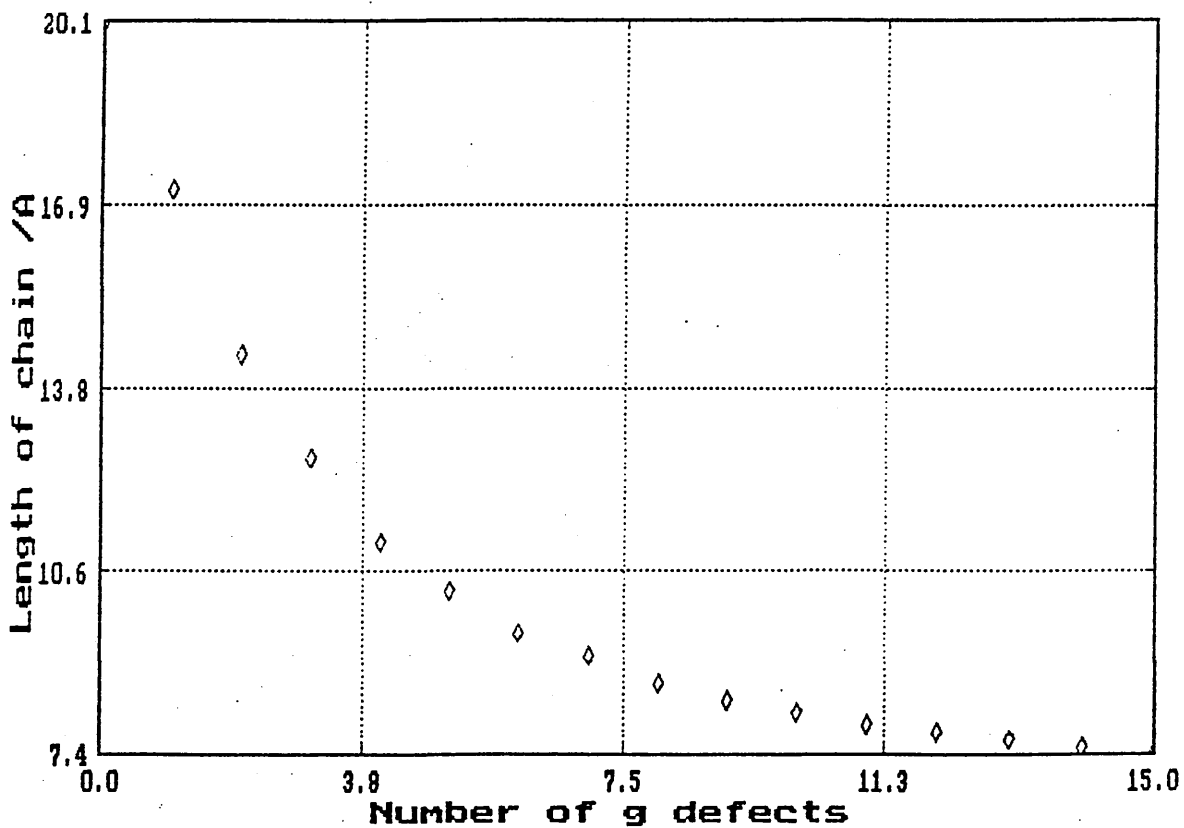


Figure 4.8 Distribution of chain extension, R , for $n_g=1$

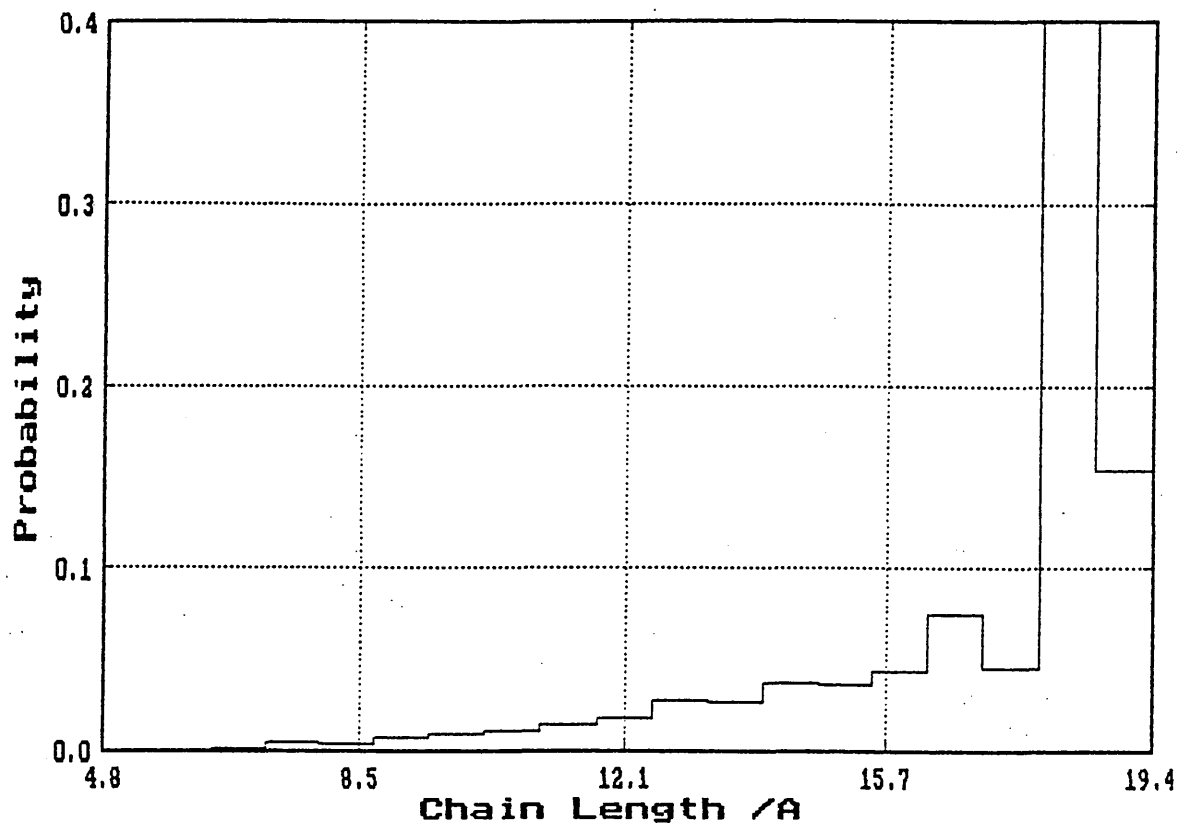


Figure 4.9 Distribution of chain extension, R , for $n_g=3$

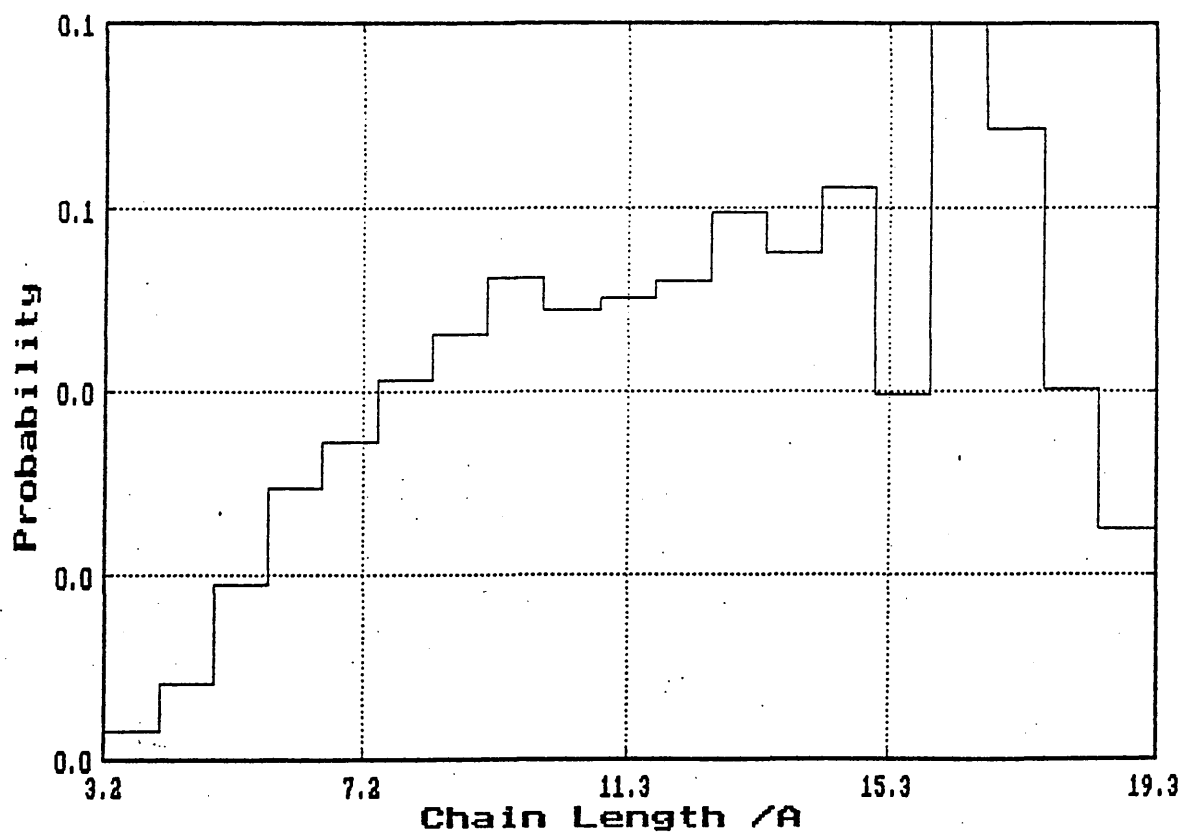


Figure 4.10 Distribution of chain extension, R , for $n_g=5$

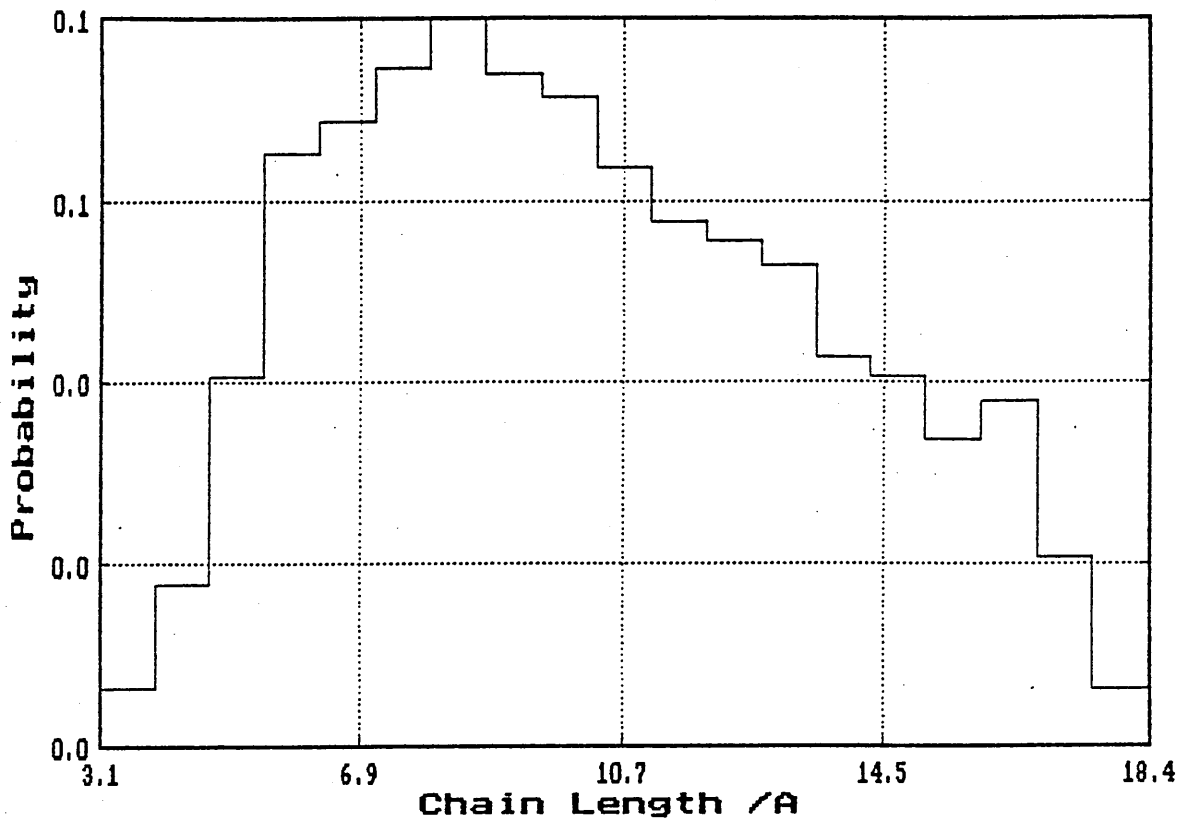


Figure 4.11 Distribution of chain extension, R , for $n_g=7$

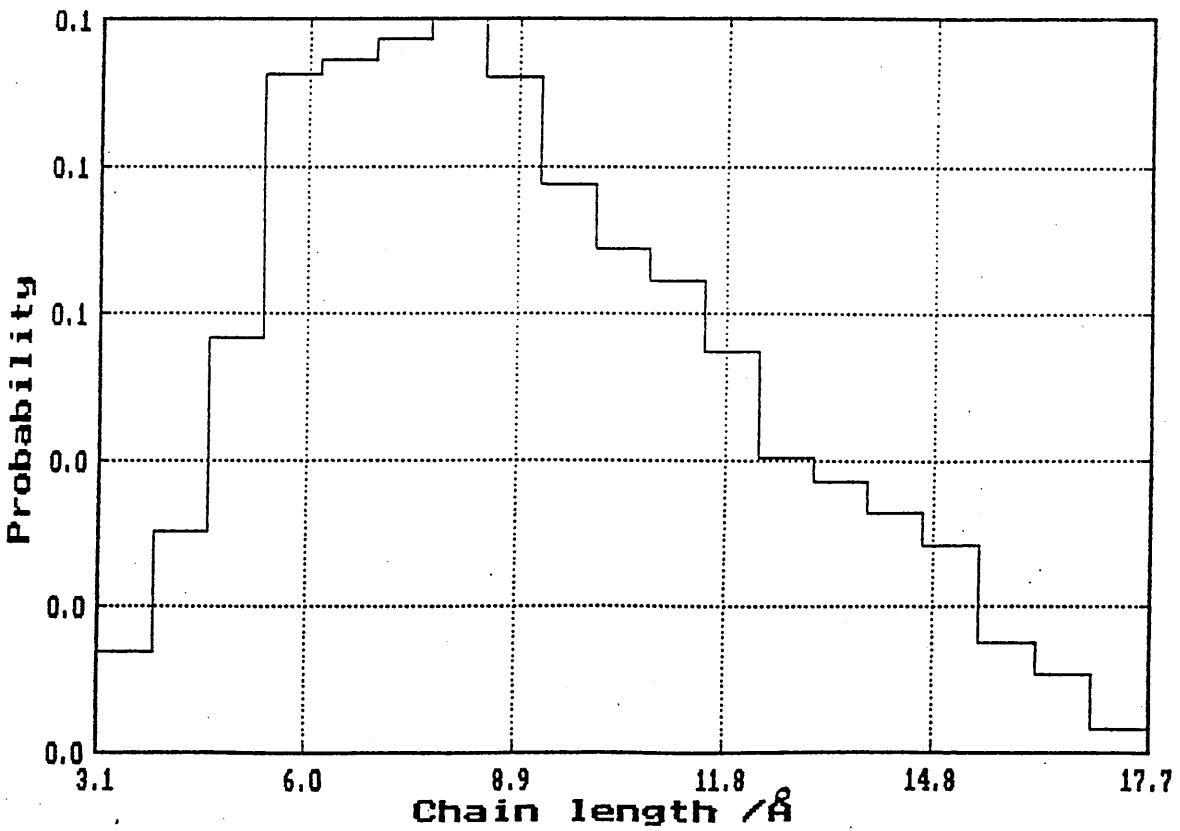


Figure 4.12 Distribution of chain extension, R , for $n_g=9$

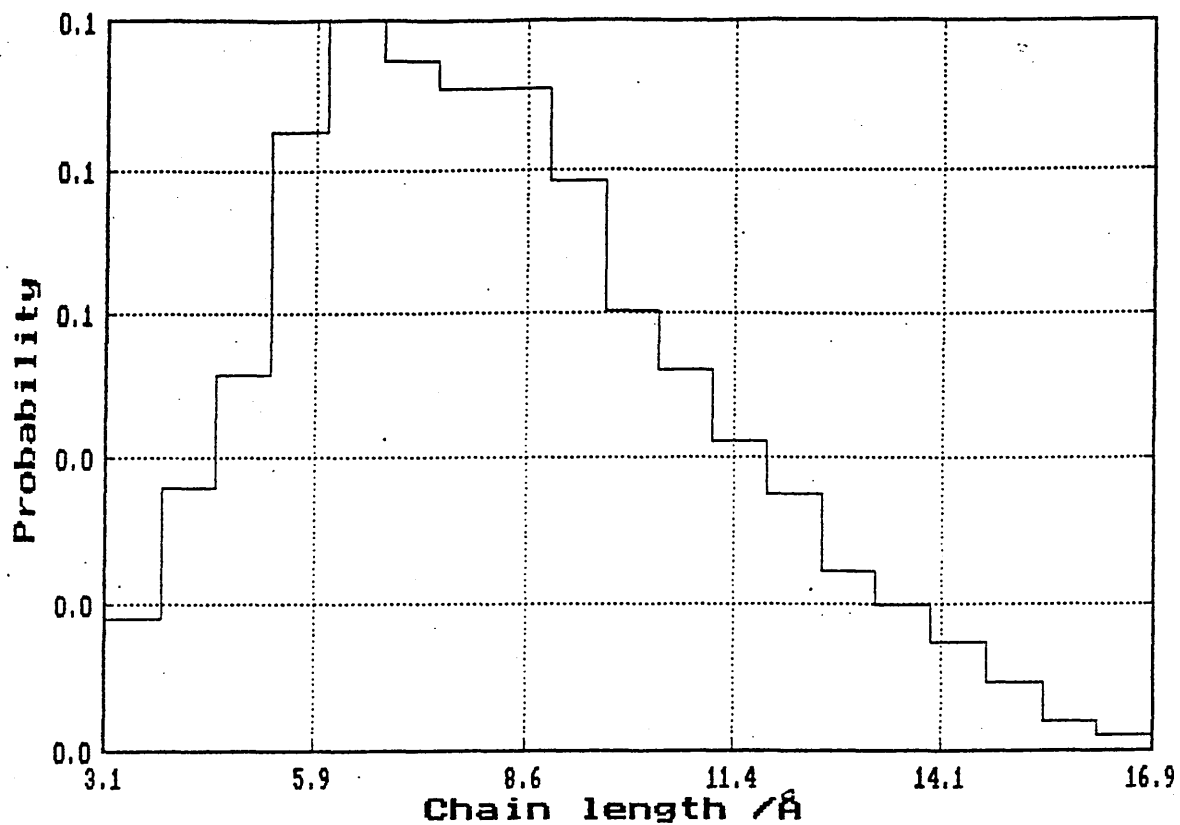


Figure 4.13 Distribution of chain extension, R , for $n_g=11$

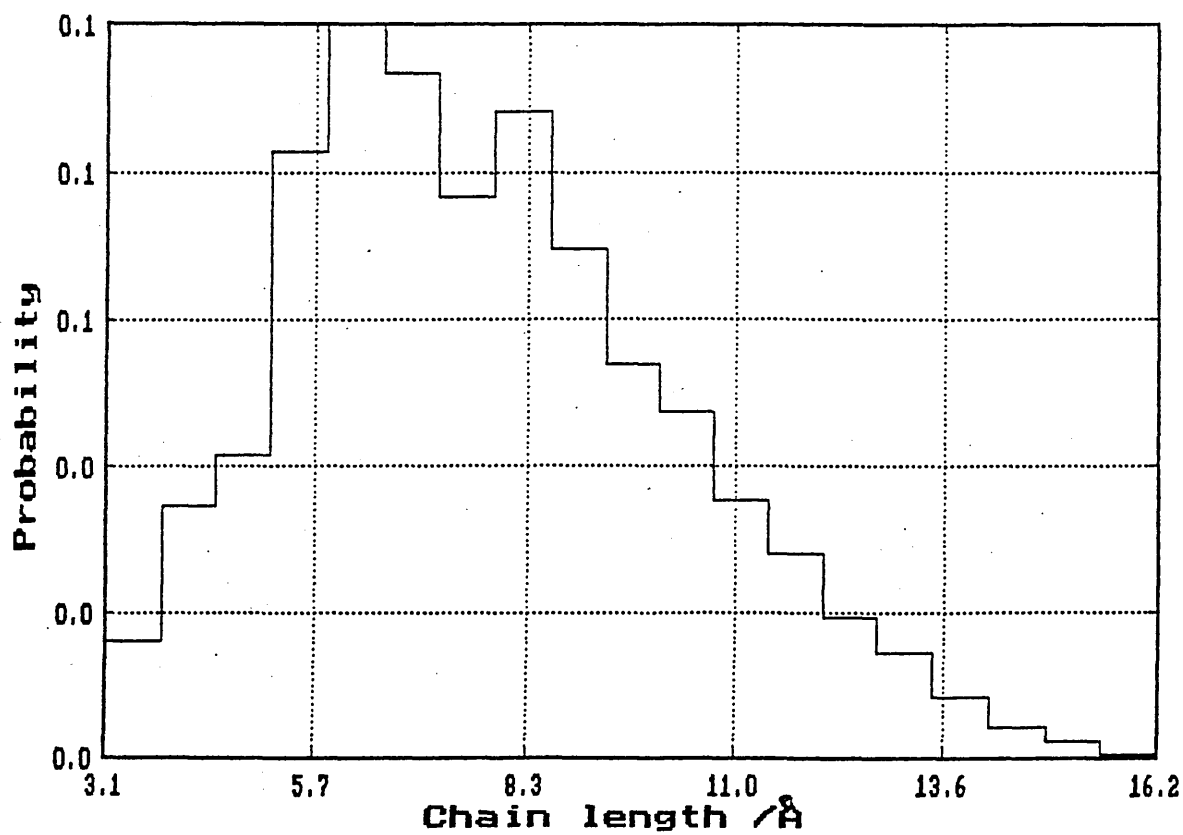


Figure 4.14 Distribution of chain extension, R , for $n_g=13$

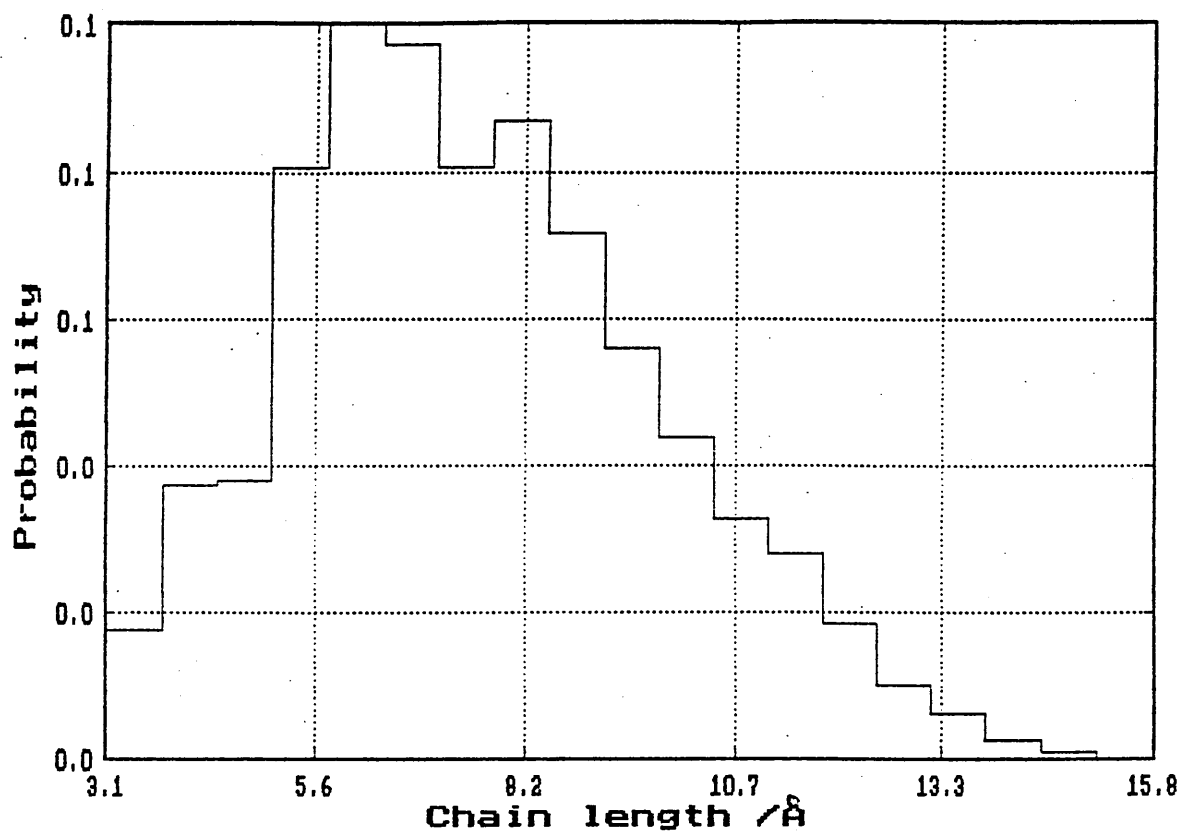
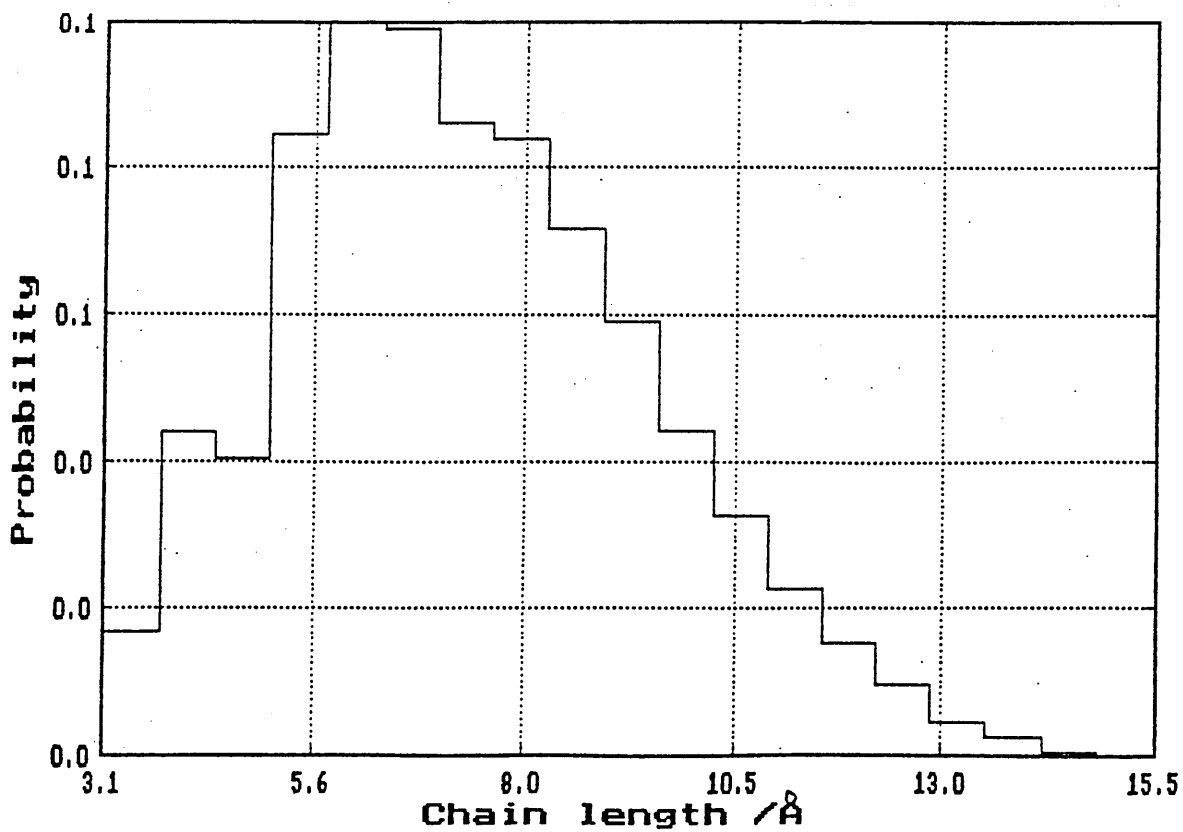


Figure 4.15 Distribution of chain extension, R , for $n_g=15$



4.2 Ionic core radius

One problem associated with measuring the dimensions of a reversed hexagonal phase is the need to find the ionic core radius. This cannot be measured directly using spectroscopic techniques, but has to be estimated from other structural data of the soap. Spegt (7) used a method for estimating this value, which employed both crystalline and hexagonal phase data and is outlined below.

The Bragg spacing, d , for a hexagonal phase, as determined by X-ray scattering, can be used to calculate the distance between the centres of cylinders, a , as follows:-

$$a = \frac{2d}{\sqrt{3}} \quad (4.17)$$

The number of polar groups per unit length of cylinder can be determined from:-

$$n = \frac{\sqrt{3}Na^2\delta}{2m} \quad (4.18)$$

where $\sqrt{3}a^2/2$ is the cross sectional area of the hexagonal phase unit cell

N is Avogadro's Number (6.02×10^{26} kmole⁻¹)

δ is the density in kg m⁻³

m is the mass of the soap in kg kmole⁻¹

The total volume of the crystalline soap can be written as:-

$$V_{\text{soap}} = V_{\text{pol}} + V_{\text{par}} \quad (4.19)$$

where V_{soap} is the volume of the soap calculated from the density, δ , and the mass, m .

V_{pol} is the polar head group volume

V_{par} is the volume of the aliphatic portion of the

soap

V_{par} can be expressed as:-

$$V_{par} = (N_c - 2)V_{CH_2} + V_{CH_3} \quad (4.20)$$

where N_c is the number of carbon atoms in the backbone. From eqn 4.19 it is possible to obtain the polar volume V_{pol} of the reversed hexagonal phase cylinders, and from this calculate the radius of the ionic core. nV_{pol} (where n is taken from eqn 4.18) gives the molar volume per unit length of the ionic cores, so that the radius of one ionic core is given by:-

$$R_c = \sqrt{\frac{nV_{pol}}{N\pi}} \quad (4.21)$$

Harrison (8) determined the ionic core radius for LiPS to be 4.8Å, using a value for n , determined from eqn. 4.18, of 1.8Å⁻¹. The value for V_{soap} used by Harrison, was determined from the density of lithium stearate at 25°C and was 1.04x10³kgm⁻³ (9).

The value of V_{CH_2} used by Harrison (14x10⁻³ m³kmole⁻¹) was obtained by von Sydow (10) for the crystalline β-form of stearic acid with orthorhombic packing of chains. The value of V_{CH_3} used (31.6x10⁻³ m³kmole⁻¹) was determined from the difference in volumes of two crystalline n-alkanes, eicosane (C₂₀H₄₂) and triacontane (C₃₀H₆₂) at 20°C (11).

In earlier work Spegt (7) determined the ionic core radius of the reversed hexagonal phase of cadmium stearate to be 4.1Å. The value of V_{par} (643.6x10⁻³m³kmole⁻¹) used was that determined by Doolittle (12) from the density of n-heptadecane at ≈150°C. Using a value of V_{par} at this elevated

temperature (comparable with that at which CdSt_2 forms a reverse hexagonal phase) gives a more acceptable result than using crystalline n-alkane data. Both methods assume that the core has crystalline packing, and as such V_{pol} is the minimum possible volume, ^{and} R_c is therefore also a minimum (see eqn. 4.21).

Small (13), using Spegt's data (7), extrapolated back from the graph of the distance between the centres of the polar cylinders, a , for soaps cadmium laurate to cadmium arachidate, versus number of carbon atoms in the soap chain, to obtain a value of a for the number of carbon atoms equal to 1 (the value at $N_c=1$ was assumed to be the core radius). A value for R_c , for the cadmium soaps, of 8.5\AA was obtained (note that Spegt's own calculation using eqn 4.21 gives 4.1\AA). This does not take into account any possibility of the soap molecules from neighbouring cylinders interleaving (see Figure 4.16).

The differences in the value of R_c calculated by Spegt and Small (Small's value is double the value calculated by Spegt) can be explained by the fact that Spegt used crystalline data, thus giving a minimum value for R_c . Small on the other hand used data from the reversed hexagonal phase, which would be expected to give a higher value for R_c , and assumed a linear increase in a , the distance between cylinder centres, with increasing chain length N_c , which may not in fact be the case.

Figure 4.16 The possible packing of rods in the reverse hexagonal phase: a) separate hexagonal rods b) hexagonal rods interleaved comb like.

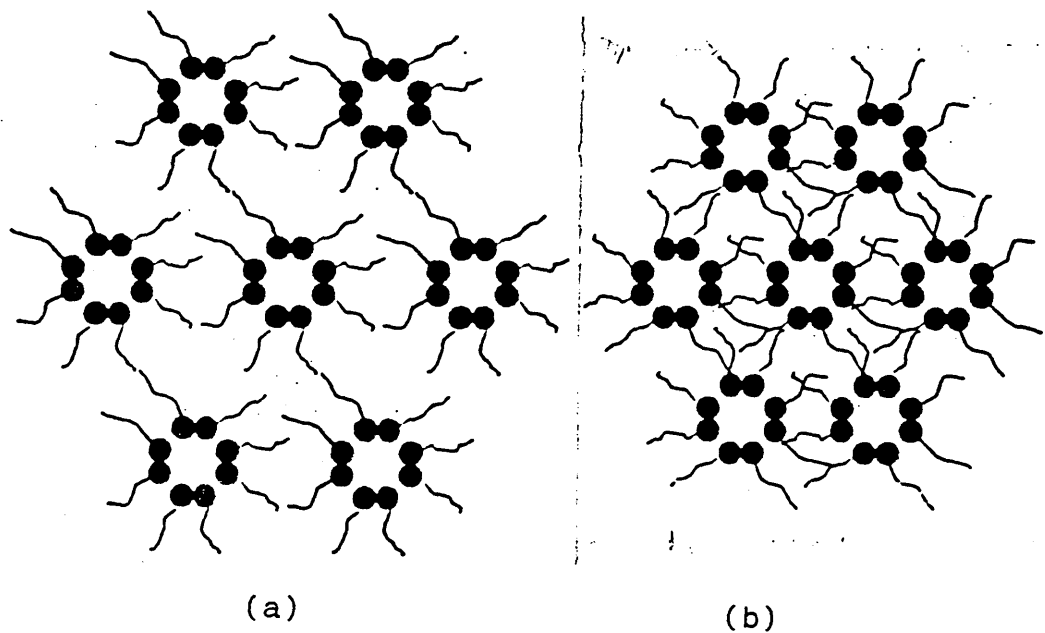
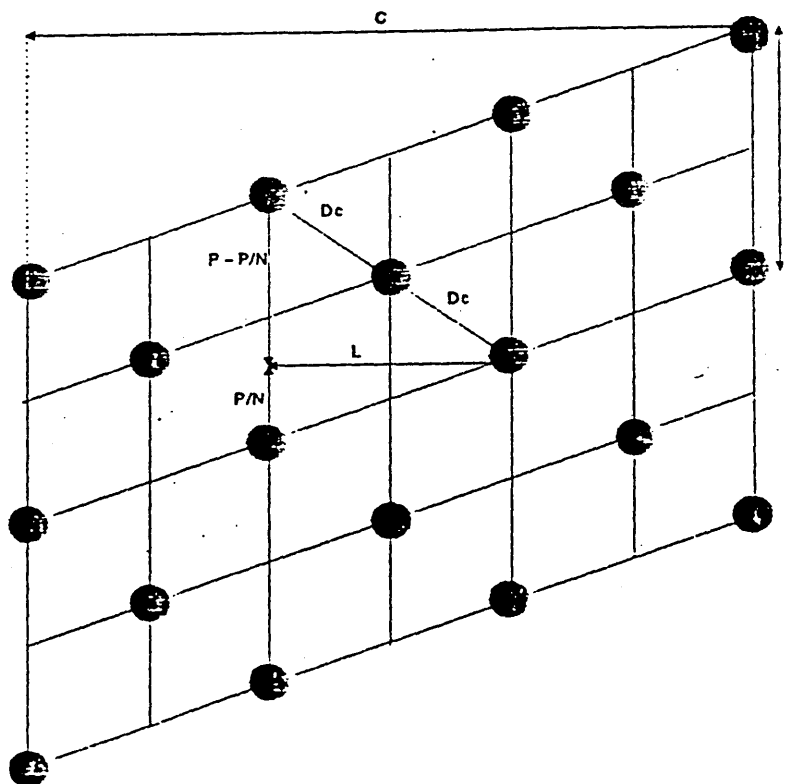


Figure 4.17 2-dimensional representation of the double helical packing of LiPS molecules on the ionic core.



4.2.1 New model

With the problem of using crystalline data applied to the (non-crystalline) reversed hexagonal phase, and the possibility of chain interleaving, it was decided to try to develop a model that required only two parameters, the number of ions per unit length of chain, n , and D_c , the smallest distance allowed between two molecules. Both these quantities can be estimated to a reasonable degree of accuracy. As a first approximation it was assumed that the soap molecules pack onto the ionic core with some sort of regular ordering, and if the core surface is "unrolled", it can be treated as a 2-dimensional array of points. There are 3 possible 2-dimensional crystal lattices: rectangular, obtuse and hexagonal. There is also the possibility of (less regular) packing of the molecules helically onto the core surface.

If a crystal lattice is chosen, for example a square lattice, there is a problem of rationalising the dimensions of the square to the number of ions per unit length. i.e. if the dimensions of the square are D_c (the smallest distance allowed between two molecules), then it is possible to find a radius of the ionic core that will accommodate the lattice, but cannot be made compatible with the number of ions per unit length. Conversely, if a value of R_c is chosen to accommodate n , the number of ions per unit length, then it is impossible to pack the lattice completely onto the ionic core.

So, having rejected crystalline packing for the model, helical packing remains a possibility, with either a single or double helix. Both can accommodate R_c , D_c and n because the

pitch of the helix is infinitely variable, but it was decided to use the double helix model as this packs the molecules much more efficiently onto the core. Figure 4.17 shows the 2-dimensional representation of a double helix packed onto a ionic core of circumference C .

A diffuse X-ray peak is observed for LiPS at a Bragg spacing of 4.6\AA (8). This may be considered as a typical distance between neighbouring chains. Since there will be few chains with smaller separation, this figure will be used to provide the minimum separation between the chains, D_c . So by fixing D_c and varying the pitch, P , of the double helix it is possible to calculate how R_c varies with P .

Let the number of molecules in pitch, P , be $2N$, and for the first and the $2N^{\text{th}}$ molecule to be vertically aligned, we require that:-

$$P = \frac{2N}{n} \quad (4.22)$$

where n is the number of cations in the cylinder per unit length calculated from eqn. 4.18.

From the planar projection of the helical surface (figure 4.17) we obtain:-

$$L = \frac{2\pi R_c}{N} \quad (4.23)$$

where R_c is the radius of the ionic core.

Referring to figure 4.17 it becomes apparent that:-

$$\left(P - \frac{P}{N}\right)^2 + L^2 = (2D_c)^2 \quad (4.24)$$

Combining this with eqn. 4.23 leads to :-

$$P^2(N^2-2N+1)+4\pi^2R_c^2 = 4N^2D_c^2 \quad (4.25)$$

By rearranging and substituting for N from eqn. 4.22 we obtain:-

$$R_c = \frac{P}{2\pi} \sqrt{n^2D_c^2 - \frac{P^2n^2}{4} + Pn - 1} \quad (4.26)$$

Figure 4.18 shows the variation of R_c with pitch, P , for LiPS, assuming $D_c=4.6\text{\AA}$ and $n=1.8\text{\AA}^{-1}$ (8). The condition that $D_c=4.6\text{\AA}$ means that the pitch, P , cannot be less than 4.6\AA , thus setting a minimum value on P . Also because D_c is fixed, the geometry of the model restricts the pitch to be less than $2D_c$, so we have the condition:-

$$D_c \leq P \leq 2D_c \quad (4.27)$$

This sets a minimum value for R_c , for a constant value of n , and as can be seen from figure 4.18 the curve also has a maximum value. Hence it is possible to predict the range of values within which R_c falls, for a specific value of n .

By using different values of n , it is possible to generate a series of curves like figure 4.18, and from these curves it is possible to find the maximum and minimum values of R_c for each value on n . Figure 4.19 shows the maximum and minimum values of R_c varying with n the number of ions per unit length, and gives the result that:-

$$R_{c_{\min}} = 2.94n + 0.32 \quad (4.28)$$

$$R_{c_{\max}} = 3.35n + 1.09 \quad (4.29)$$

For divalent metal soaps we assume that each n -carboxylate group behaves as a monovalent soap, so n , the number of metal ions per unit length (as calculated from eqn 4.18) needs to be doubled, to give $2n$ soap molecules per unit length.

Table 4.1 shows a comparison of the various methods used to calculate R_c . The results from the above model are of the same order of magnitude as the calculations by Spegt (7,14) and Small (13). R_c falls within the range of the other two methods for calculating R_c , so the model provides a more restricted range of values for R_c . This model gives a more realistic result for R_c for LiPS than the method described by Spegt (7) and used by Harrison (8), because it assumes the aliphatic portion of LiPS is liquid-like (the value for D_c used, is the same as the Bragg spacing observed for Liquid n -alkanes(13)). A direct comparison with Small's method (13) cannot be made because it would require the lithium soaps of the phenyl n -carboxylic acids from $N_c=12$ to $N_c=20$ to calculate the hexagonal lattice parameter a , and thus estimate R_c .

Table 4.1 Comparison of the various techniques used to estimate the value of R_c , the ionic core radius

Soap	n number of ions/Å	Spegt $R_c/\text{Å}$	D.M Small $R_c/\text{Å}$	Calculated $R_c/\text{Å}$	
				Min	Max
CdSt ₂	0.78 ⁴	4.1 ⁴	8.5 ⁴	4.9	6.3
CaSt ₂	0.535 ⁵	3.6 ⁵	7.0 ⁵	3.5	4.6
LiPS	1.80 ⁶	4.6 ⁶	----	5.6	7.1

⁴ Data taken from ref 7, D.M. Small used data from this reference to calculate his own value of R_c .

⁵ Data taken from ref 14, D.M. Small used the data from this reference to calculate his own value of R_c .

⁶ Data take from reference 8.

Figure 4.18 The variation of the radius of the ionic core, R_c , with increasing pitch of helix, P .

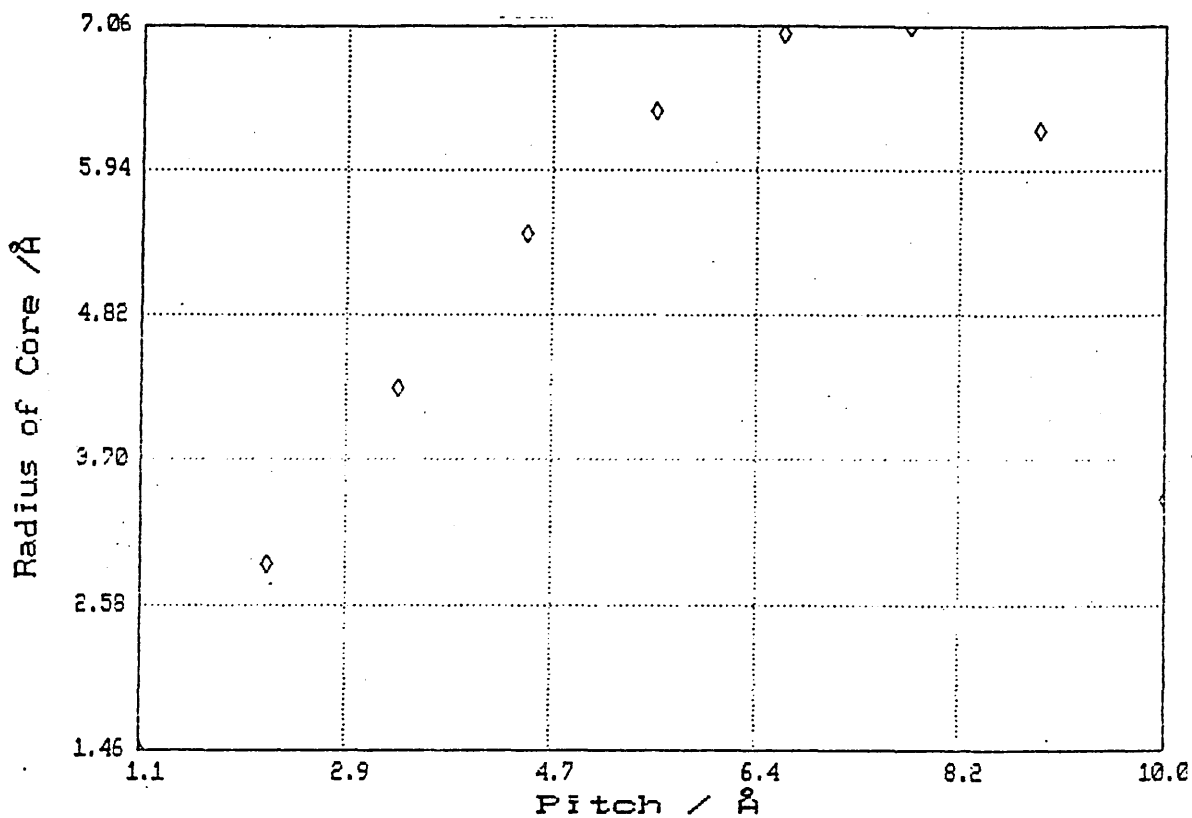
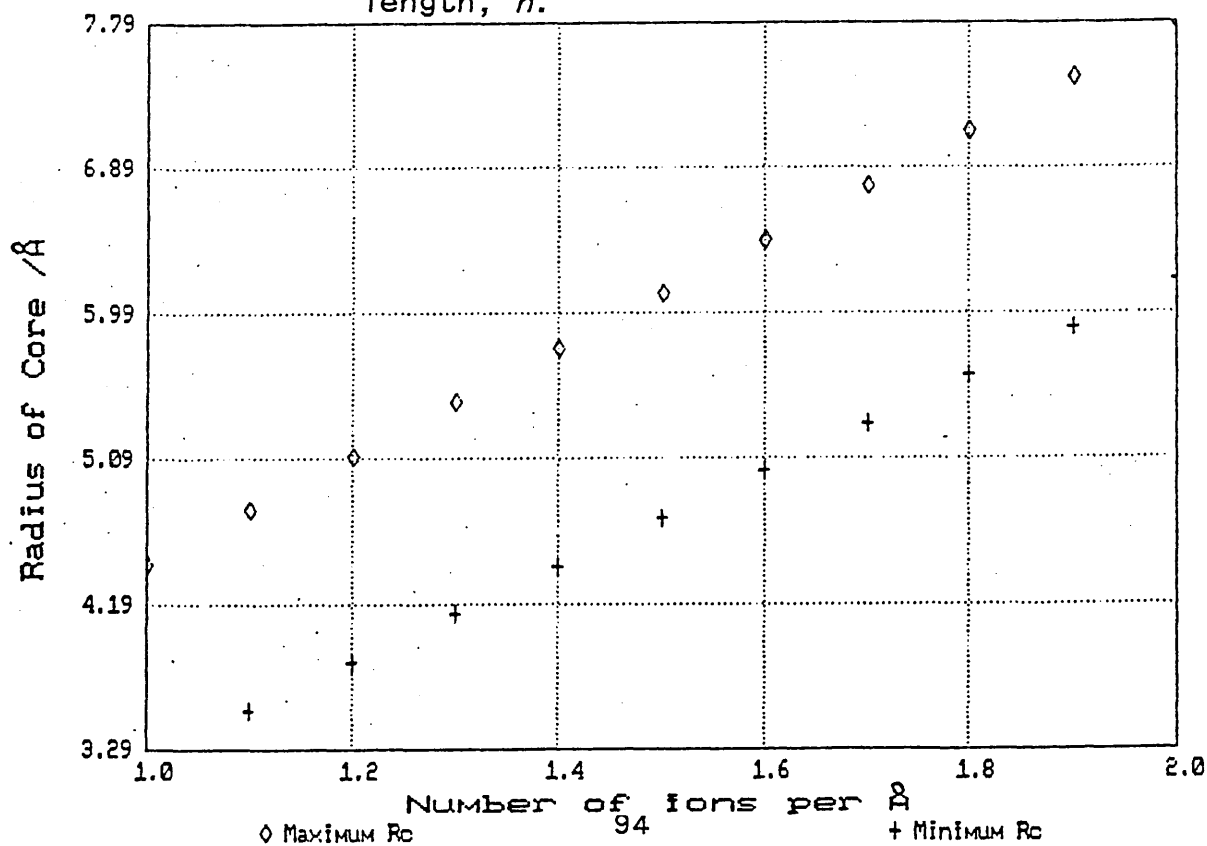


Figure 4.19 The maximum and minimum value of R_c as a function of the number of ions per unit length, n .



4.3 Graphics modelling package

The modelling techniques described above to calculate structural parameters of LiPS have taken, as a model for LiPS, a simple aliphatic soap with no phenyl group attached to the backbone. To examine the effects of the phenyl group on the backbone conformations, and also the influence of the backbone on rotational freedom of the phenyl ring, a more detailed model is required.

4.3.1 Moly '86

Moly '86 is a molecular graphics package developed by Rohm and Haas, which was run on an Apollo 4000 series work station. The molecular co-ordinates can be entered graphically, and the bond angles and bond lengths are assumed to have their idealized values, although these can be changed later if required. Conformational analysis can then be performed on the molecule. The conformational energy is given by (15):-

$$E_{conf} = E_{vdw} + E_{coul} + E_{hbond} + E_{conj} \quad (4.30)$$

where E_{vdw} is the Van der Waals term accounting for steric hinderance and takes the form of a Lennard-Jones 12-6 potential:-

$$E_{vdw} = \frac{A_{ij}}{d^{12}} - \frac{B_{ij}}{d^6} + \frac{C_{ij}}{d} \quad (4.31)$$

where A_{ij} is a repulsive constant dependent on atoms i, j
 B_{ij} is a attractive constant dependent on atoms i, j
 C_{ij} is a repulsive correction constant which terminates the attraction at 6\AA
 d is the distance between atoms i and j

E_{coul} is the columbic interaction term to account for partial charge interaction.

$$E_{coul} = \frac{332.0}{\epsilon} \cdot \frac{q_i q_j}{d} \quad (4.32)$$

where ϵ is the dielectric constant
 q_i is partial charge on atom i

E_{hbond} is the hydrogen bonding term :-

$$E_{hbond} = E \left(\frac{r_o}{r_{HX}} \right)^{12} - 20E \left(\frac{r_o}{r_{HX}} \right)^{10} \quad (4.33)$$

where E is an energy constant dependent on the atoms participating in the hydrogen bonding.

r_o is the inter-nuclear distance parameter, dependent on the type of atoms.

r_{HX} is the Euclidean distance between donor and acceptor atoms.

E_{conj} takes into account the effect of any conjugation of bonds near the bond of interest:-

$$E_{conj} = B \sin^2(N\theta) \quad (4.34)$$

where B is half the energy of the barrier to complete rotation.

N is a symmetry factor (2 for conjugated bonds and 3 for non-conjugated bonds).

θ is the angle of rotation.

E_{coul} , E_{hbond} and E_{conj} were not used to determine the conformational energy, as reasonable agreement with literature results was obtained using only the Van de Waals interaction.

4.3.2 Analysis

The Moly '86 model was used to determine the effect of the phenyl group on the aliphatic backbone of LiPS, and vice-versa. The effect of the phenyl group on the backbone was checked by systematically rotating individual bonds in the backbone while also rotating the phenyl group, to find the effect on the energy minima etc. The effect of backbone conformation on the phenyl rotation was investigated by placing the bonds in specific conformations and rotating the phenyl group to find the minimum energy and the maximum possible angle of rotation. First Moly '86 was used to determine the values of energy minima when rotating bonds in a n-alkane, and comparing these with known literature values.

Flory (2) showed that the gauche defects in n-alkanes do not occur at the idealized values of $\phi_g = \pm 120^\circ$, but at angles of ϕ dependent on the conformational defects. Modelling n-pentane, with bonds 1 and 4 in the trans position ($\phi_1 = \phi_4 = 0^\circ$) and rotating bonds 2 and 3, (ϕ_2, ϕ_3 varying between 0 and 360°), Flory showed that tg and gt defects are equivalent, and with energy minima of $500 \text{ cal mole}^{-1}$ at $\phi_2=0^\circ$; $\phi_3=\pm 112.5^\circ$ and $\phi_2=\pm 112.5^\circ$; $\phi_3=0^\circ$. The energy minima of gg and g'g' defects were also found to be equivalent and occurred at $\phi_2=\phi_3=\pm 110^\circ$ with a conformational energy of $1180 \text{ cal mole}^{-1}$. This value is approximately twice the value for 1 gauche bond alone, so the energy for neighbouring gauche bonds can be treated as approximately additive.

Instead of a single minimum for the defects g'g and gg', Flory found the 2 minima occurred either side of the expected value for gg' bond angles of $\phi_2=120^\circ$ and $\phi_3=-120^\circ$. These minima

occur at $\phi_2=115^\circ$, $\phi_3=-77^\circ$ and $\phi_2=77^\circ$, $\phi_3=115^\circ$ for gg', and $\phi_2=-115^\circ$, $\phi_3=77^\circ$ and $\phi_2=-77^\circ$, $\phi_3=115^\circ$ for g'g, and the energy of these minima is 3200 cal mole⁻¹.

The program Moly '86 was used to check these values, and figure 4.20 shows the energy contour map for the rotation of bonds 2 and 3 of n-pentane (while bonds 1 and 4 are kept constant at 0°). The contour values are as follows:-

Line No.	Energy/kcal mole ⁻¹
1	0.5
2	1.0
3	1.5
4	2.0
5	2.5
6	3.0
7	3.5
8	4.0
9	5.0
10	6.0

ϕ_2 and ϕ_3 were increased in steps of 5°, and this increment was chosen because it was the minimum practical increase within the constraints of computer time and memory. Steps of 5° generate 5184 conformations, whereas 2° steps would generate 32400 conformations. As can be seen from figure 4.20 the tg and gt conformations occur at $\phi_2 \approx \pm 115^\circ$, $\phi_3 \approx \pm 5^\circ$ and $\phi_2 \approx \pm 5^\circ$, $\phi_3 \approx \pm 115^\circ$ respectively and have energies of less than 500 cal mole⁻¹. This shows that the gauche units cause a small deviation in the trans rotational angle. The gg and g'g' defects occur at $\phi_2 \approx 110^\circ$, $\phi_3 \approx 110^\circ$ and $\phi_2 \approx -110^\circ$, $\phi_3 \approx -110^\circ$ respectively and have energies of 1500 < E < 2000 cal mole⁻¹. The gg' and g'g defects occur at $\phi_2 \approx 115^\circ$, $\phi_3 \approx -80^\circ$ and $\phi_2 \approx 80^\circ$, $\phi_3 \approx -115^\circ$ for gg', and $\phi_2 \approx -115^\circ$, $\phi_3 \approx 80^\circ$ and $\phi_2 \approx -80^\circ$, $\phi_3 \approx 115^\circ$ for g'g and have energies of 2500 < E < 3000 cal mole⁻¹. These values are close enough to those of Flory's (when considering the resolution used for angular rotation) to give confidence

in the later calculations.

4.3.3 Lithium phenyl stearate

All previous models used here ignored the phenyl group attached to the backbone of LiPS, but this could be very important in determining the chain conformation. LiPS is made up of a mixture of 12 isomers (see section 1.3). Provided that the phenyl group is not attached near to either end of the molecule, the conformations of the bonds close to the phenyl group are unlikely to be influenced to any great extent by the position of the phenyl group along the chain. Modelling was therefore carried out, using Moly '86, for the most common isomer present in LiPS, which has the phenyl group attached to the soap backbone at carbon atom number 10 (see figure 4.21). The calculations of the effect of the phenyl rotation on various bonds are shown in figures 4.22 to 4.27, and the contours are as follows:-

Line No.	Energy/kcal mole ⁻¹
1	1
2	2
3	3
4	4
5	6
6	10
7	14
8	20

The step size used for the bond rotation was again 5°.

Rotation of the bond between atoms 10 and 19 corresponds to the rotation of the phenyl group (ϕ_{phenyl}), and rotation of the bond between atoms 6 and 7 corresponds to rotating bond 6 (ϕ_6) etc.

Figure 4.22 shows the effect of rotating the phenyl group and bond 6 (minima occur at $\phi_6=0, 115$ or 245° when $\phi_{phenyl}=60$ or 240°). The phenyl ring has therefore no effect on

the CH₂ backbone at bond 6, since the energy minima are identical to those for n-alkanes. Figure 4.23 shows a similar result obtained by rotating ϕ_{phenyl} and ϕ_7 with the energy minima again at $\phi_7=0, 115$ or 245° when $\phi_{\text{phenyl}}=60$ or 240° , so we again conclude that the phenyl ring has no effect on the CH₂ backbone at bond 7.

Figure 4.24 shows the energy contour map for rotation of the phenyl ring and bond 8 (ϕ_{phenyl} and ϕ_8). This shows a distortion to the conformations allowed for the backbone. The energy minima are at $\phi_8=0, 90$ or 245° when $\phi_{\text{phenyl}}=60$ or 240° . The energy minimum at $\phi_8=90^\circ$ is of a higher energy (between 1 and 2 kcal mole⁻¹) than would be expected for a standard gauche bond. Within the range $100^\circ < \phi_8 < 240^\circ$, no conformations are energetically feasible, assuming that any conformation with an energy greater than 5 kcal mole⁻¹ above the minimum energy conformation, is of such low probability that it can be ignored. Hence the phenyl ring rotation has a clear effect on the backbone at bond 8 and possibly restricts the molecule to t and g' defects, with the g defect ($\phi_8=90^\circ$) reduced in probability because of the increase in energy.

Figure 4.25 shows the energy contour map for the rotation of the phenyl group and bond 9. This shows a distortion in the conformation near the site of the g' defect ($\phi_9=-115^\circ, \phi_{\text{phenyl}}=80$ or 260°) for bond 9, and has an energy of ≈ 4 kcal mole⁻¹ above the minimum energy value, making the g' defect very improbable, and effectively restricting bond 9 to t and g defects.

Results for the rotation of the bonds on the other side of the phenyl ring are shown in figures 4.26 and 4.27. These

plots are similar to those of figure 4.25 and 4.24 respectively, except the effects are mirrored and inverted. The general conclusion is that the phenyl ring does have an effect on the backbone conformations, but only over a limited number of bonds. If the phenyl group is attached at carbon atom 10 (see figure 4.21) then it will distort the possible bond conformations of bonds 8,9,10 and 11, but will have no effect on the other bonds. The bonds listed are restricted to t or g', t or g, t or g' and t or g for bonds 8,9,10 and 11 respectively. There is the possibility of bonds 8 and 11 adopting distorted gauche conformations at 90 and -90° respectively, but this has approximately twice the energy of normal gauche conformations, and so the probability of it occurring is reduced. For bonds 9 and 10 there is the possibility of adopting distorted gauche conformations at -115 and 115° respectively. These have an energy of ≈ 4 kcal mole⁻¹ above minimum energy, and as such it is very improbable that these conformations will be adopted.

It may be possible to see the effect of these distortions in the infrared spectrum of LiPS: the gtg' band at 1369 cm⁻¹ may show a shoulder resulting from a small shift in frequency, as is the case with polyethylene crystals with {110} chain folds (16). The gg band at 1352 cm⁻¹, should remain unaffected as bonds 8,9,10 and 11 can only form t or g', t or g, t or g' and t or g respectively (bonds 8 and 11 have a reduced probability of forming g and g' defects respectively). If the conclusion that bond pairs 8 & 9, 9 & 10 and 10 & 11 cannot form gg or g'g' defect pairs is correct, then this should reduce the number of bonds

available to form gg pairs by at least 2 (bonds 9 and 10 cannot form gg or g'g' pairs, but bond 8 could with bond 7, and bond 11 could with bond 12). This should be observable in infrared spectrum, if the aliphatic portion of LiPS behaves like an isotropic material, as a reduction in the number of gg defects estimated from the infrared data compared with the number of gg estimated from the rotational isomeric state model for an n-alkane of the same chain length (see section 5.3.2).

Figure 4.20 Energy contour map of the rotation of bonds 2 and 3 of n-pentane.

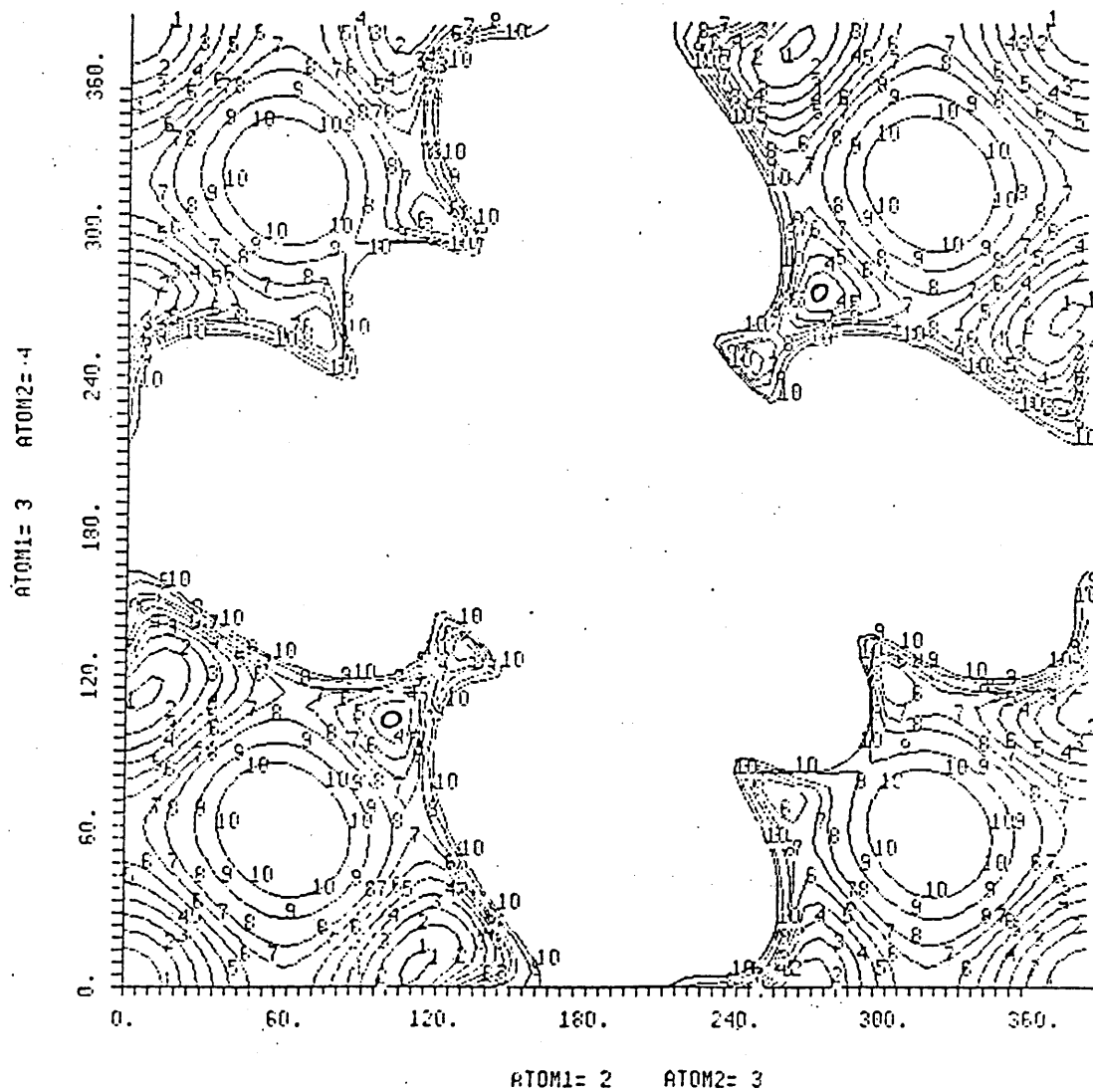


Figure 4.21 Representation of the isomer of Lithium Phenyl Stearate, where the phenyl group is attached at to carbon number 10.

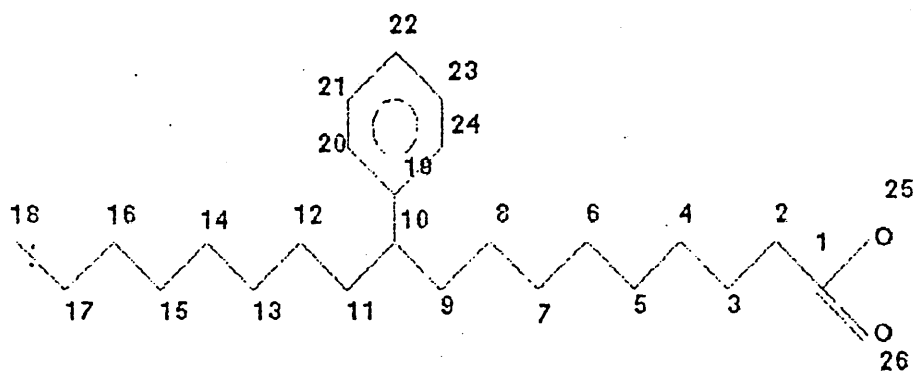


Figure 4.22 Energy contour map of the rotation of bond 6 and the phenyl group.

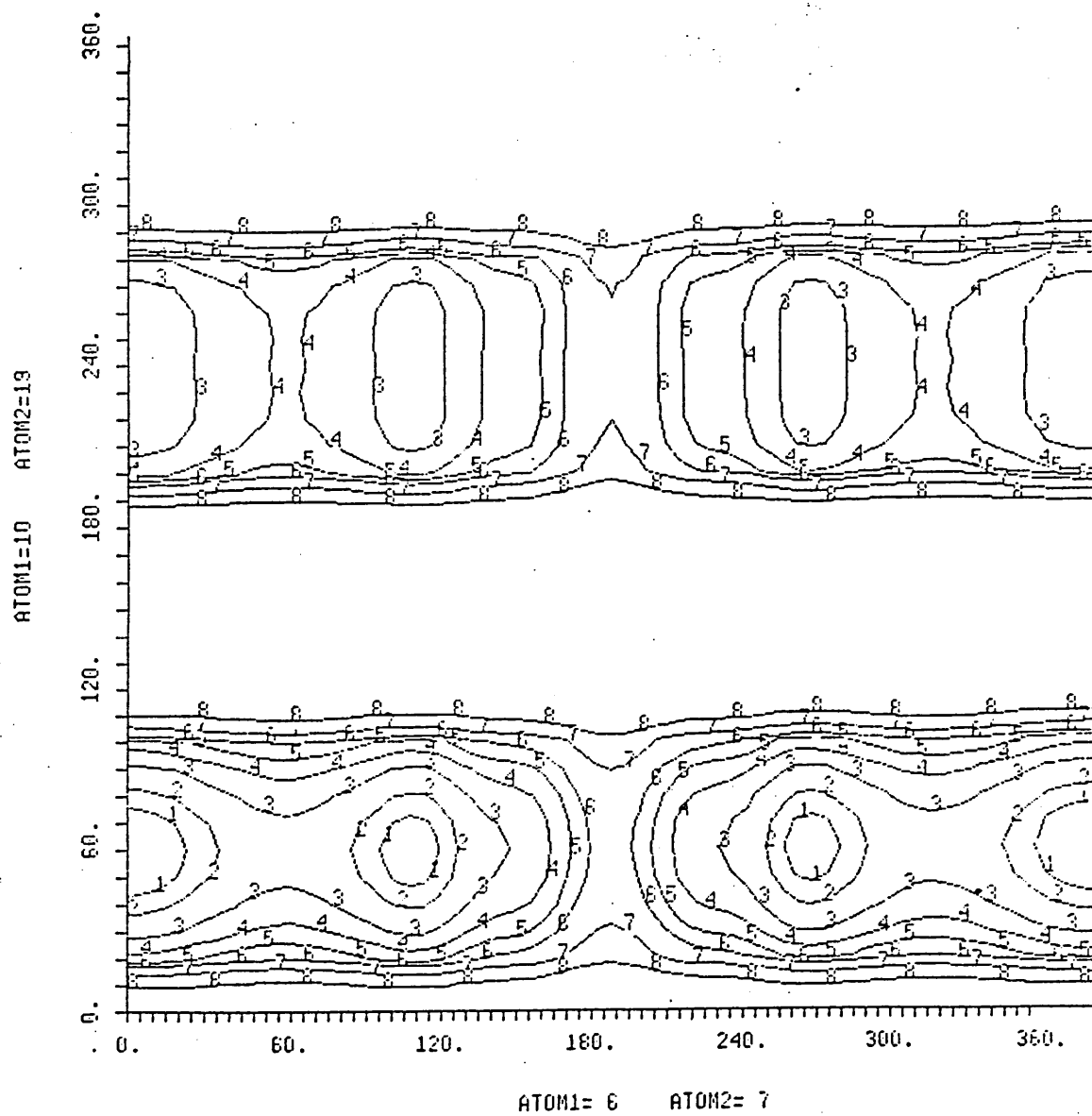


Figure 4.23 Energy contour map of the rotation of bond 7 and the phenyl group.

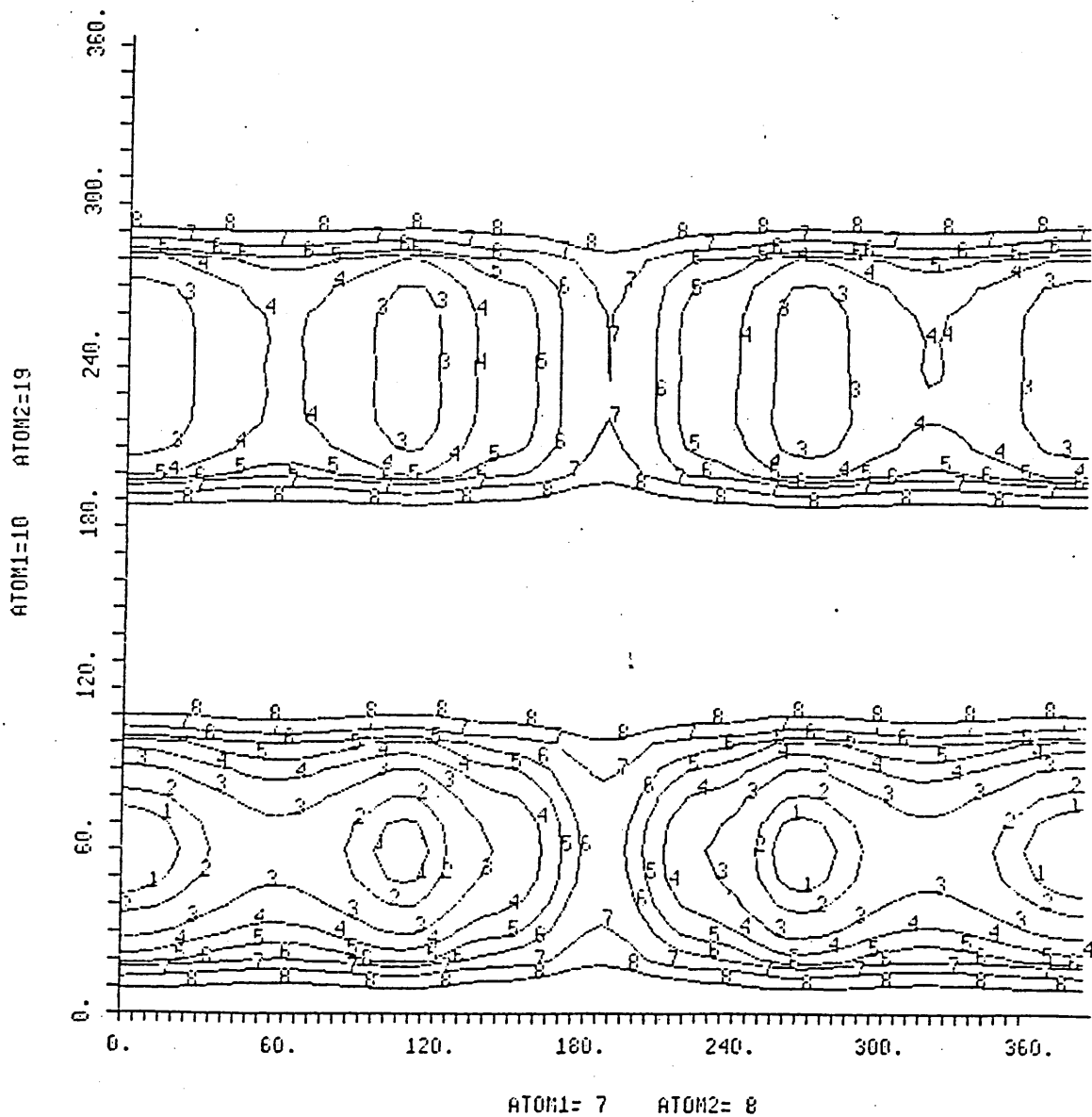


Figure 4.24 Energy contour map of the rotation of bond 8 and the phenyl group.

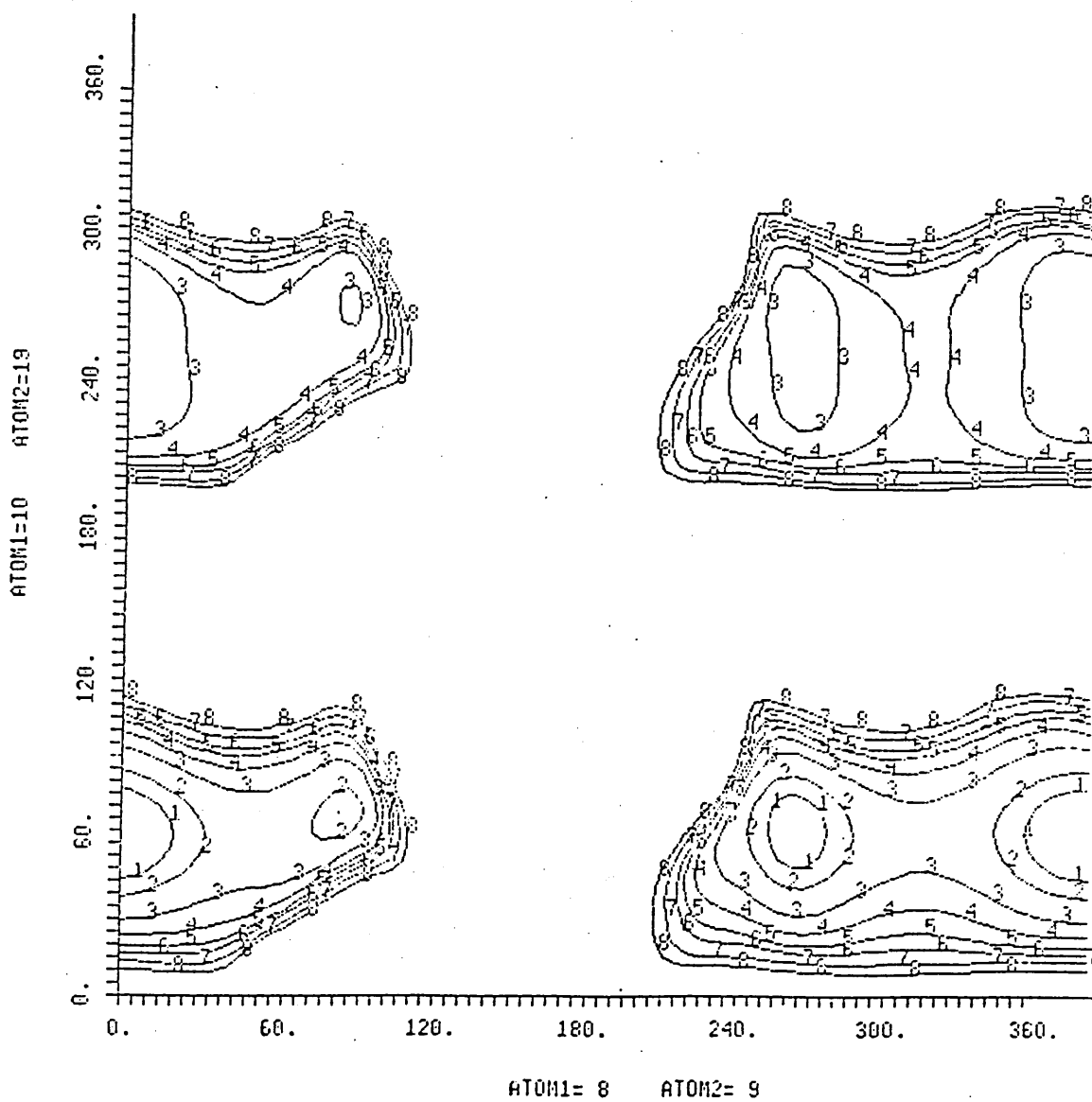


Figure 4.25 Energy contour map of the rotation of bond 9 and the phenyl group.

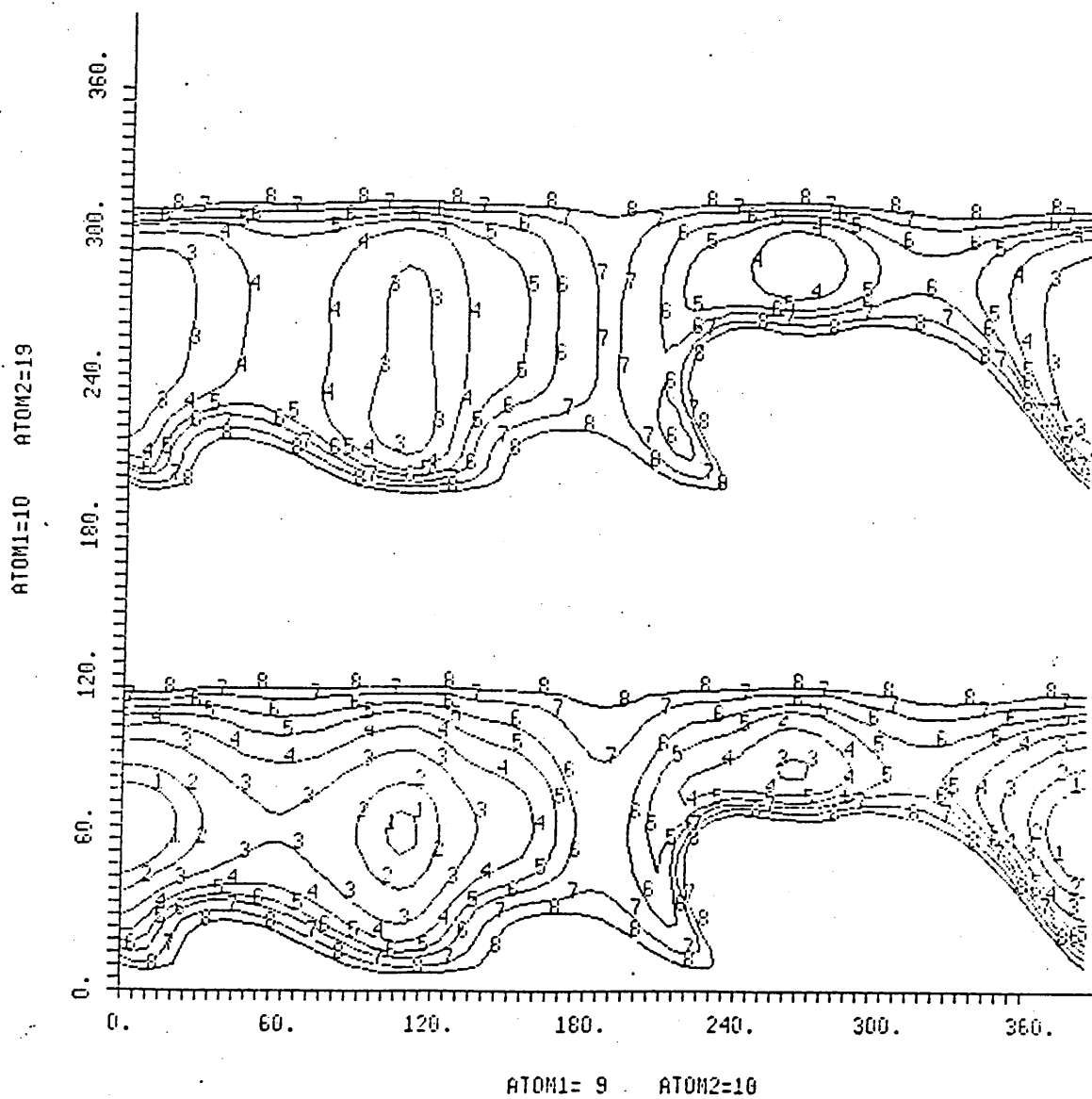


Figure 4.26 Energy contour map of the rotation of bond 10 and the phenyl group.

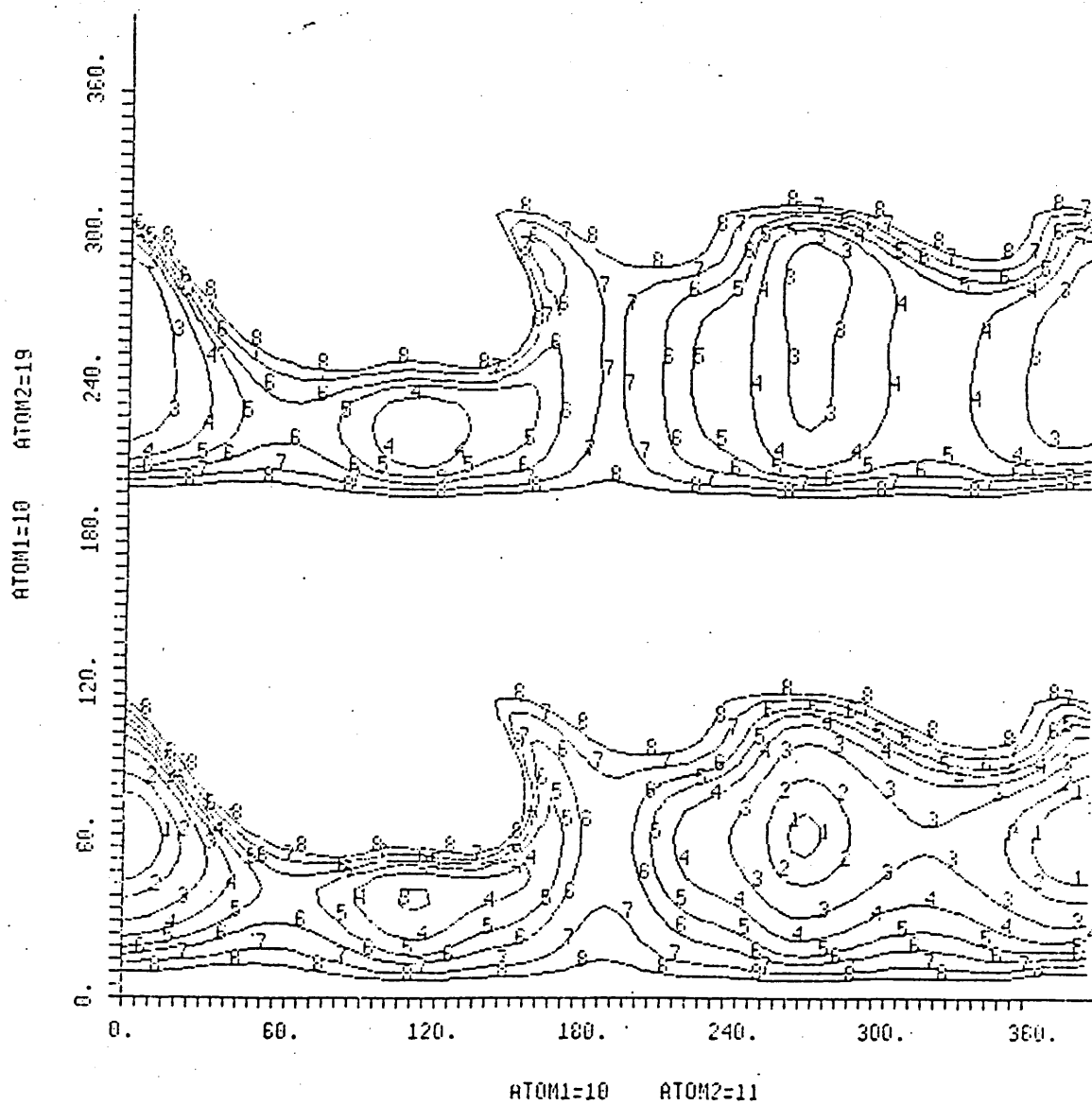
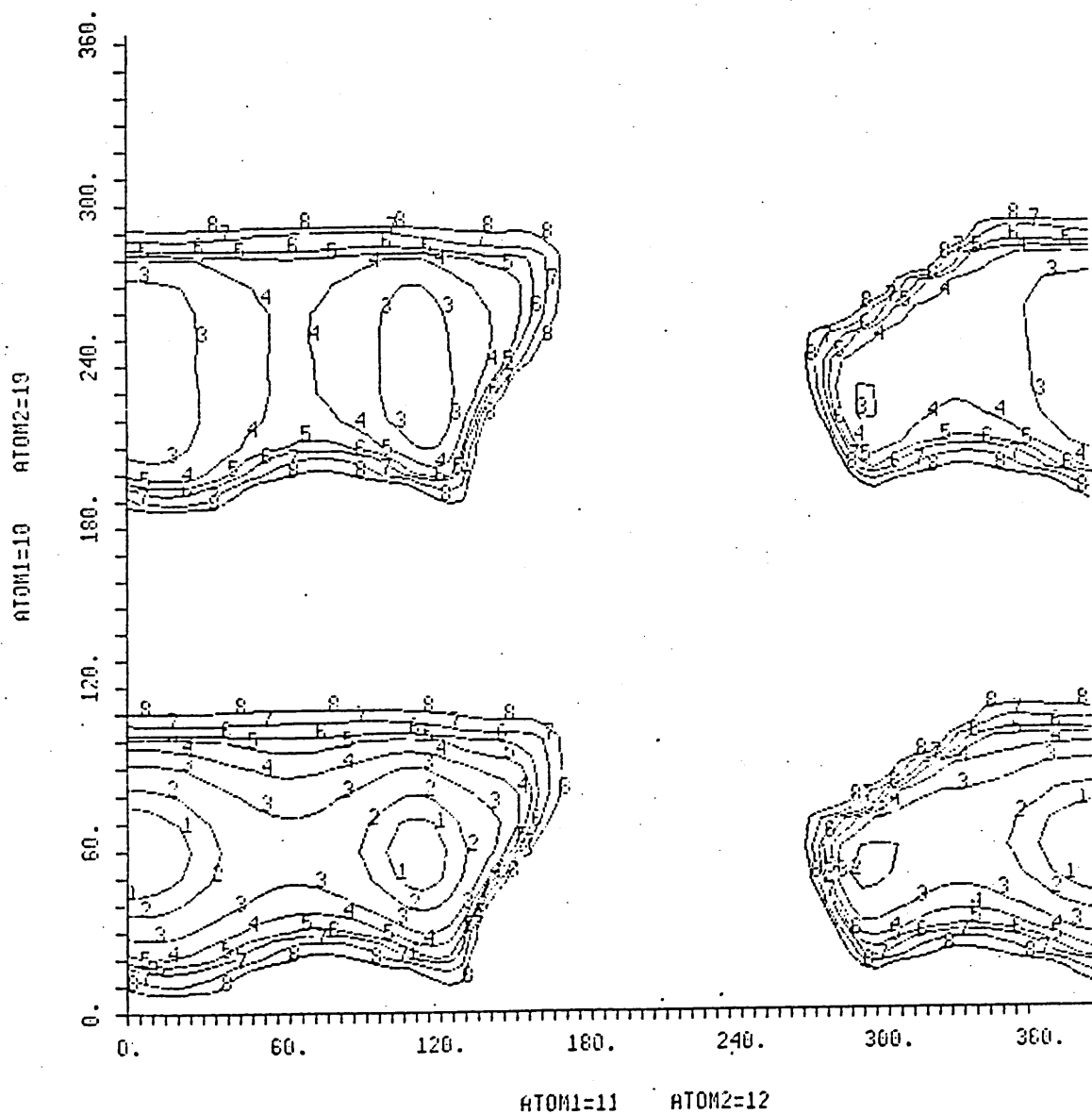


Figure 4.27 Energy contour map of the rotation of bond 11 and the phenyl group.



4.3.4 Maximum phenyl group rotation

Having examined the effect of the phenyl group on individual bonds, we need to examine the effect of various defects on conformational energy and the feasibility of phenyl rotation. From this it should be possible to find the most probable defects, and determine if the conclusions from section 4.3.3 are in fact correct.

In determining the maximum oscillation angle of the phenyl group, an energy cut-off point is required. It was decided to use the 99% probability limit (the energy below which there is a 99% probability of finding the phenyl group). To determine this energy value we assumed that the phenyl group has a constant angular velocity, ω , giving an energy of :-

$$E = \frac{1}{2} I \omega^2 \quad (4.35)$$

where I is the moment of inertia

This gives a constant energy for constant angular velocity, and can then be applied directly to a Maxwell distribution (17):-

$$P(\sigma) = \frac{4\sigma^2}{\sqrt{\pi}} e^{-\sigma^2} \quad (4.36)$$

where

$$\sigma^2 = \frac{E}{RT} \quad (4.37)$$

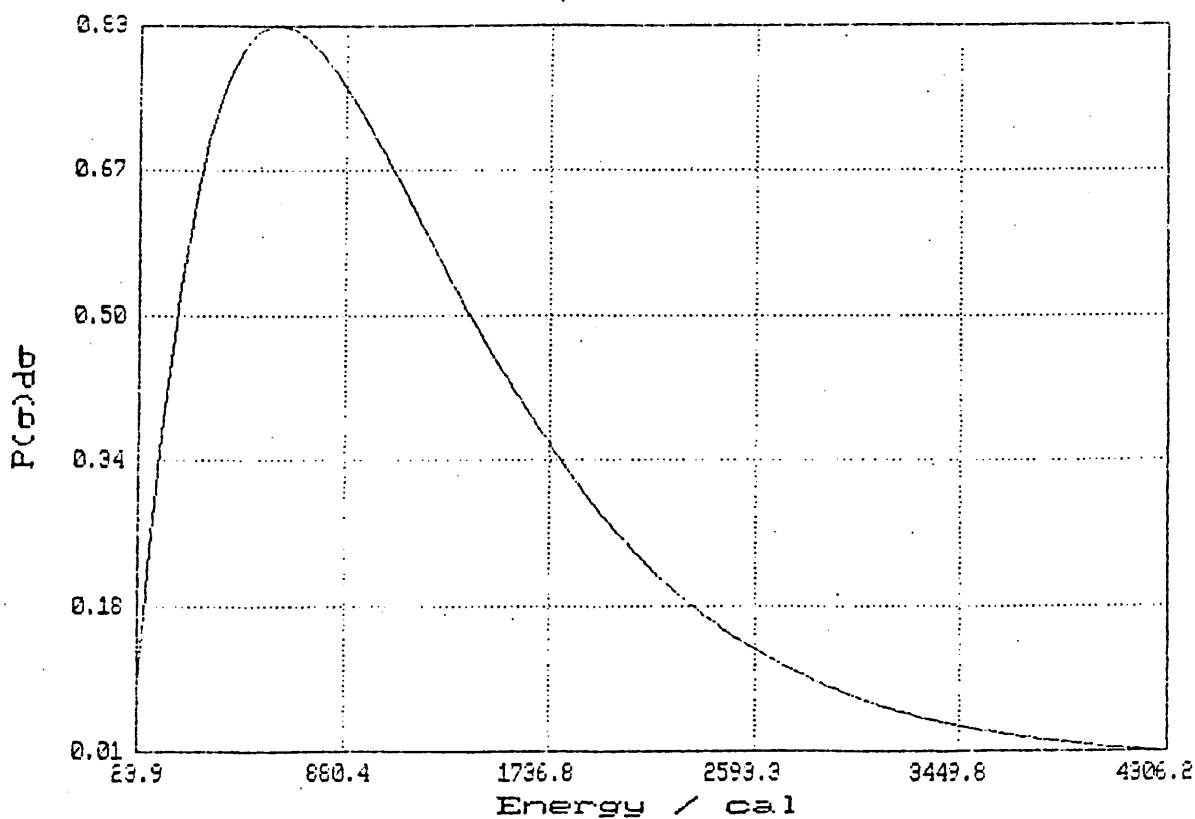
where E is the energy from eqn 4.35

R is the gas constant, $8.3143 \text{ J K}^{-1} \text{ mole}^{-1}$

T is the temperature / K and is take as room temperature, 293 K.

Figure 4.29 shows the energy distribution for the thermally activated rotation of the phenyl group, calculated from equation 4.37, at room temperature (293 K). This gives a most probable energy, RT , of $596.7 \text{ cal mole}^{-1}$, an average energy, E_{av} , of $759.2 \text{ cal mole}^{-1}$ and a root mean square energy, E_{rms} of $895 \text{ cal mole}^{-1}$. The value of E_{av} was taken as the reference energy point, which gives a value of E_{ggx} of $3859.2 \text{ cal mole}^{-1}$, meaning that E_{ggx} is $3100 \text{ cal mole}^{-1}$ above the reference energy value. This value coincides with a value of maximum rotational energy of a phenyl group in polystyrene used by Tonelli (18). So the maximum angle of oscillation of the phenyl group was taken to be the angular rotation from the position of $E_{min}+3100 \text{ cal mole}^{-1}$, through E_{min} and back up to $E_{min}+3100 \text{ cal mole}^{-1}$.

Figure 4.29 The energy distribution of the thermally activated phenyl group rotation at room temperature.



There are 81 possible rotational isomeric states, if bonds 8,9,10 and 11 are allowed to adopt any of the t, g or g' rotational positions. Table 4.2 shows the effect of all these defects on the minimum energy, E_{min} , and the maximum angle of rotation of the phenyl group (some of the defects are paired because of symmetry and are effectively the equivalent). The conformations used were the standard conformations given by Flory (2), such as tg (with the g defect at an angle of 112.5°) or gg (where the g defects are both at 110°). With the gg' defect there is a possibility of two minima, one at $\phi_g=115^{\circ}$, $\phi_{g'}=-75^{\circ}$, the other at $\phi_g=75^{\circ}$, $\phi_{g'}=-115^{\circ}$. Only one of these minima is given in the table, the one giving the lowest energy conformation.

It is important to note the relationship between conformation as written, and the bonds represented: reading the conformation from left to right represents bonds 11,10,9 and 8. For example t_gt_g' has bond angles as follows:- $\phi_{11}=0^{\circ}$, $\phi_{10}=112.5^{\circ}$, $\phi_9=0^{\circ}$ and $\phi_8=-112.5^{\circ}$.

From table 4.2 it can be seen that no conformation allows complete rotation of the phenyl group, and in fact the maximum angle is $65\pm 5^{\circ}$ (because of possible asymmetry in the potential energy, the angle quoted is the maximum arc describe by the rotation of the phenyl ring). Also conformations with minimum energies greater than 3100 cal mole⁻¹ above the all trans conformation are improbable, so this limits the angle of rotation for LiPS to between 50° and 60° . It is very improbable that one of the states with a smaller maximum angle of oscillation will be occupied.

From table 4.2 it is possible to identify several

conformations which are observable in the infrared spectrum, and have a significant probability of occurring (energy minimum is less than 3100 cal mole⁻¹). The gg'tg'/gtgg' defect contains a gtg defect, but its energy is much lower than would normally be expected for this defect, 628 cal mole⁻¹ instead of 3000 cal mole⁻¹ expected with a conformation with only a gg' unit present. The energy of a single gauche defect in an n-alkane is 500 cal mole⁻¹(2), so the phenyl ring reduces the conformational energy of this particular conformation, and thus increases the probability of a gg'tg'/gtgg' defect. The gtgt/tg'tg' defect is also present, and has an energy of 1194 cal mole⁻¹ which is close to the expected value of ≈ 1000 cal mole⁻¹; so the probability is similar to that for a gtg defect in an n-alkane.

gg and g'g' defects were predicted to be of low probability in section 4.3.3 from the data presented. What can be seen from table 4.2 is that no conformation containing gg or g'g' at bonds 9 and 10 has a minimum energy of less than 3100 cal mole⁻¹ above the all-trans energy. This confirms the hypothesis from section 4.3.3, that these bonds are the ones most affected and that they do not form gg or g'g' conformations at bonds 9 and 10. Defects g'g'tt/ttgg, g'g'gg and gtgg/g'g'tg' contain a gg or g'g' pair and have energies less than 3100 cal mole⁻¹ (2199, 2207 and 2251 cal mole⁻¹ respectively). A gg or g'g' defect in an n-alkane has an energy of 1180 cal mole⁻¹ (2), this makes the g'g'tt g'g'gg and gtgg defects much less probable than would be expected if the phenyl group was not present (with a weighting factor ($e^{-E/kT}$, as defined by Flory (2)) approximately 0.2 times the value

for n -alkane).

These results confirm the hypothesis from section 4.3.3 that the gg and $g'g'$ sequences have a reduced probability in the vicinity of the phenyl group, thus giving rise to behaviour similar to that of a shorter chain. However, the gtg defect is not affected to such an extent, and may even show a small increase in probability as compared with an n -alkane.

Table 4.2 Conformational energy of g, g' and t defects at bonds positions 8-9, 9-10, 10-11 and 11-12 and maximum phenyl rotation thus allowed.

Conformation	Energy Kcal/mole	E _{min} -E Kcal/mole	Phenyl angle of rotation /degrees
t t t t	-31.011	0.000	50
g t t t / t t t g'	-30.704	0.307	50
g t t g'	-30.472	0.539	50
g g't g' / g t g g'	-30.383	0.628	55
g g't t / t t g g'	-30.300	0.711	55
t g't t / t t g t	-30.063	0.948	55
t g'g t	-29.951	1.060	65
g t g t / t g't g'	-29.817	1.194	55
g'g't t / t t g g	-28.812	2.199	55
g'g'g g	-28.804	2.207	65
g t g g / g'g't g'	-28.760	2.251	55
g'g'g t / t g'g g	-27.875	3.136	65
t g t t / t t g't	-27.246	3.765	25
g g'g't / t g g g'	-27.111	3.900	20
g t g't / t g t g'	-26.649	4.362	25
t g g t / t g'g't	-26.579	4.432	50
g'g'g't / t g g g	-24.702	6.309	50
g t g'g / g'g t g'	-24.453	6.558	15
g'g g t / t g'g'g	-12.403	18.608	5
g'g g g / g'g'g'g	-11.263	19.748	5
g'g t t / t t g'g	-0.777	30.234	5
g' t t t / t t t g	1.820	32.831	10
g t t g / g't t g'	2.080	33.091	10
g g't g / g't g g'	2.618	33.629	10
g' t g t / t g' t g	2.822	33.833	10
g g'g'g / g'g g g'	2.830	33.841	15
g'g't g / g't g g	4.090	35.101	10
g' t g't / t g t g	9.571	40.582	5
t g g't	26.920	57.931	5
g g g t / t g'g'g'	36.371	67.382	5
g g g g' / g'g'g'g'	37.002	68.013	5
g g g g / g'g'g'g'	38.242	69.253	5
g't t g	40.293	71.304	5
g g t g' / g t g'g'	41.295	72.306	5
g g g t t / t t g'g'	41.511	72.522	5
g g t g / g't g'g'	247.989	279.000	5
g'g t g / g't g'g	321.453	352.464	5
g g'g'g'	1000000	-----	--
g g g'g'	1000000	-----	--
g g g't / t g g'g'	1000000	-----	--
g g'g t / t g'g g'	1000000	-----	--
g'g g'g'	1000000	-----	--
g g g'g / g'g g'g'	1000000	-----	--
g'g g't / t g g'g'	1000000	-----	--
g g'g g / g'g g'g'	1000000	-----	--

4.4 References

- (1) M. Maroncelli, S.P. Qi, H.L. Strauss and R.G. Snyder, J. Am. Chem. Soc. 104, 6237, 1982.
- (2) P.J. Flory, "Statistical mechanics of chain molecules", Interscience, New York, 1969.
- (3) R.L. Jernigan and P.J. Flory, J. Chem. Phys. 50(10), 4165, 1969.
- (4) M.G. Broadhurst, J. of Research of National Bureau of Standards - A, Phys. and Chem. 66, 241, 1962.
- (5) A.J. Hopfinger, "Conformational properties of macromolecules", Academic Press, New York, 1973.
- (6) Handbook of Chemistry and Physics, 49th Ed. 1968-1969, The Chemical Rubber Co.
- (7) P. Spegt and A. Skoulios, Acta Cryst. 16, 301, 1963.
- (8) W.J. Harrison, PhD Thesis, Sheffield City Polytechnic, 1987.
- (9) D.P. Benton, P.G. Howe, R. Farnand and I.E. Puddington, Can. J. Chem. 33, 1798, 1955.
- (10) E. von Sydow, Acta cryst. 8, 557, 1955.
- (11) F. Wolf, D. Kline and H.S. Story, J. Chem. Phys. 53, 3538, 1970.
- (12) K. Doolittle, J. App. Phys. 22, 1471, 1952.
- (13) D.M. Small, "Handbook of lipids research, 4. The physical chemistry of lipids", Plenum Press, New York, 1986.
- (14) P. Spegt and A. Skoulios, Acta Cryst. 17, 198, 1964.
- (15) Moly '86 Manual, Rohm and Haas, Edited by M.A. Bright, T.T. Fujimoto, T.H. Pierce and C.H. Reynolds.
- (16) S.J. Spells, S.J. Organ, A. Keller and G. Zerbi, Polymer 28, 697, 1987.

(17) B. Flowers and E. Mendoza, "Properties of matter",
Wiley, London, 1970

(18) A.E. Tonelli, *Macromolecules* 5, 683, 1973.

Chapter 5

5 Lithium phenyl stearate	120
5.1 Preparation	120
5.2 Infrared spectroscopy	121
5.2.1 Sample preparation	123
5.2.2 Peak assignments	123
5.3 Defect region	126
5.3.1 Variation of defect concentration	130
5.3.2 Numbers of defects	135
5.4 Hexagonal phase dimensions	140
5.5 Effect of sample preparation	144
5.5 References	146

5 Lithium phenyl stearate

This chapter deals with the examination of the structure of lithium phenyl stearate using the technique of infrared spectroscopy. These results will be combined with the modelling results from chapter 4 to determine the dimensions of the aliphatic portion of the reverse hexagonal phase rods, and any effect the phenyl group may have on the chain backbone.

5.1 Preparation

Phenyl stearic acid was prepared by the Friedel-Crafts reaction of oleic acid (cis-9-octadecenoic acid) with an excess of benzene using aluminium chloride as the catalyst under anhydrous conditions (1) (this was prepared by W.J. Harrison). An ethanolic solution of phenyl stearic acid was titrated with a 1 molar 50% water, 50% ethanol solution of lithium hydroxide to a phenolphthalein end point. This was then dried for about 24 hours over silica gel under vacuum. The soap was then washed with water and ethanol at 60⁰C, then filtered, to remove any impurities, and then finally washed with acetone. Finally to remove any excess water, the lithium phenyl stearate (LiPS) sample was dried in a vacuum over P₂O₅ at ≈100⁰C for 2 hours.

The purity of the lithium phenyl stearate sample was checked using elemental micro analysis (MEDEC LTD., Brunel University, Uxbridge), and gave carbon and hydrogen percentages of 78.02% and 10.59% respectively. The expected values for carbon and hydrogen are 78.64% and 10.72% respectively. The difference in these values is probably

caused by water attached to the polar head group, but it is impossible to be certain of this without the oxygen concentration.

If we assume that water is the only impurity it is possible to estimate the number of water molecules per LiPS molecule. Anhydrous LiPS has a molar mass of $366.5 \text{ g mole}^{-1}$, the atomic masses of individual elements being taken from Kaye and Laby (2). By using the percentage of carbon found from micro analysis, the molar mass of LiPS plus water was found to be $369.5 \text{ g mole}^{-1}$. This gives 3g of water per mole of LiPS, giving 1 molecule of water for every 6 molecules of LiPS.

This indicates that the LiPS sample used was almost anhydrous, and Kagarise (3) showed that lithium phenyl stearate is not hygroscopic, so exposure to air should not affect LiPS significantly. As a precaution the sample was kept in a sealed jar in a desiccator, and was dried under vacuum regularly.

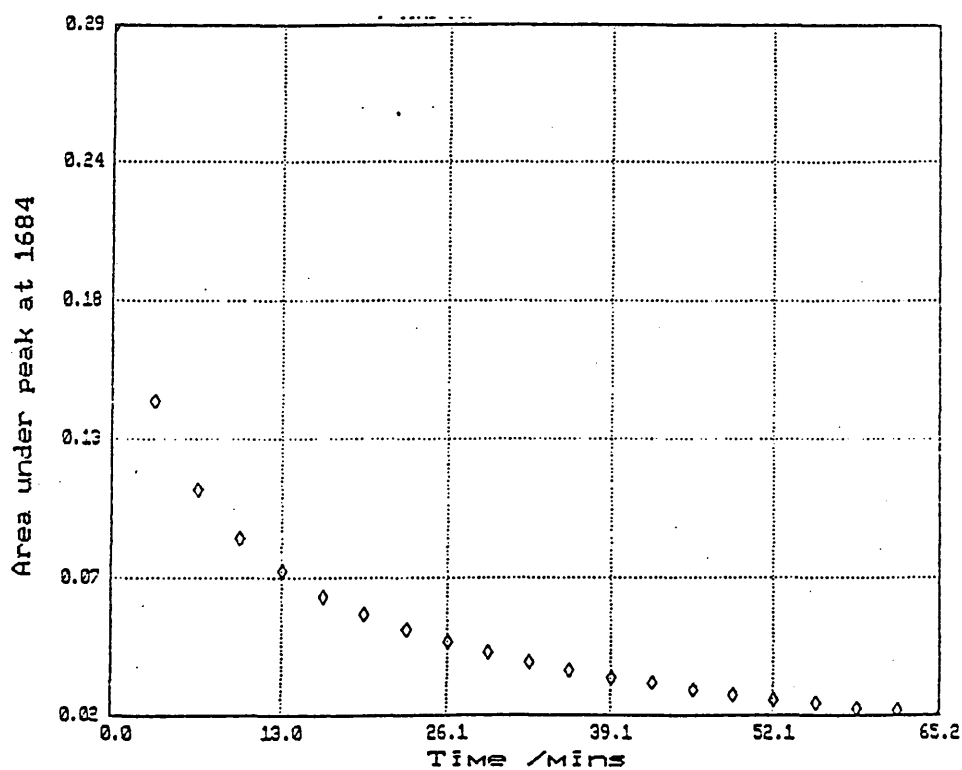
5.2 Infrared spectroscopy

All spectra reported here were recorded on a Mattson Galaxy 6020 single beam Fourier transform infrared spectrometer. The resolution used was 1 cm^{-1} , with triangular apodization and zero filling doubling the number of data points, giving enhanced digital resolution. Fourier self deconvolution was used to enhance the spectral resolution of several spectra, using the technique developed by Kauppinen et al (4,5).

The air in the spectrometer was purged using a Balston Filter Products clean air unit, which helped to keep the air

moisture and carbon dioxide concentrations low. Figure 5.1 shows the variation in intensity of the 1684 cm^{-1} water band in the background spectrum, relative to the intensity of this band with no purge, with time from the beginning of the purge. As can be seen, by about 30 minutes, the rate of change in the intensity of the 1684 cm^{-1} band has slowed sufficiently to allow experimental data to be taken without water vapour bands interfering significantly. As a routine precaution, the sample was placed in the spectrometer and allowed to reach equilibrium for 30 minutes.

Figure 5.1 Variation in the intensity of the 1684 cm^{-1} water vapour band with time from beginning of purge.



5.2.1 Sample preparation

A 0.5% w/w solution of LiPS in toluene was prepared, which was cast onto potassium bromide plates and dried to a constant weight. For a standard spectrum (one with all vibrational modes having a peak height of less than ≈ 1.5 absorbance units) only 5mg of sample was required, but for the defect bands (in the region $1400-1200\text{ cm}^{-1}$) which are very weak, about 15mg of sample was used.

LiPS degrades in air at temperatures above $\approx 150^{\circ}\text{C}$, so to prevent this occurring, and also to prevent the cell from leaking, the potassium bromide plates were first sealed with PTFE tape, and then this was sealed with silicone rubber, which is stable upto $\approx 250^{\circ}\text{C}$.

5.2.2 Peak assignments

Figure 5.2 shows the infrared spectrum of LiPS at room temperature in the region 4000 to 600 cm^{-1} . Several bands can be seen in the region 700 to 600 cm^{-1} , but these have been ignored, because in this region the MCT detector is approaching the limits of detection (Mattson quote a frequency range of 6000 to 660 cm^{-1} for this MCT detector). Table 5.1 shows the frequency assignments of most of the peaks present in the spectrum of LiPS, and a reference is given where possible.

Figure 5.2 Infrared spectrum of lithium phenyl stearate at room temperature.

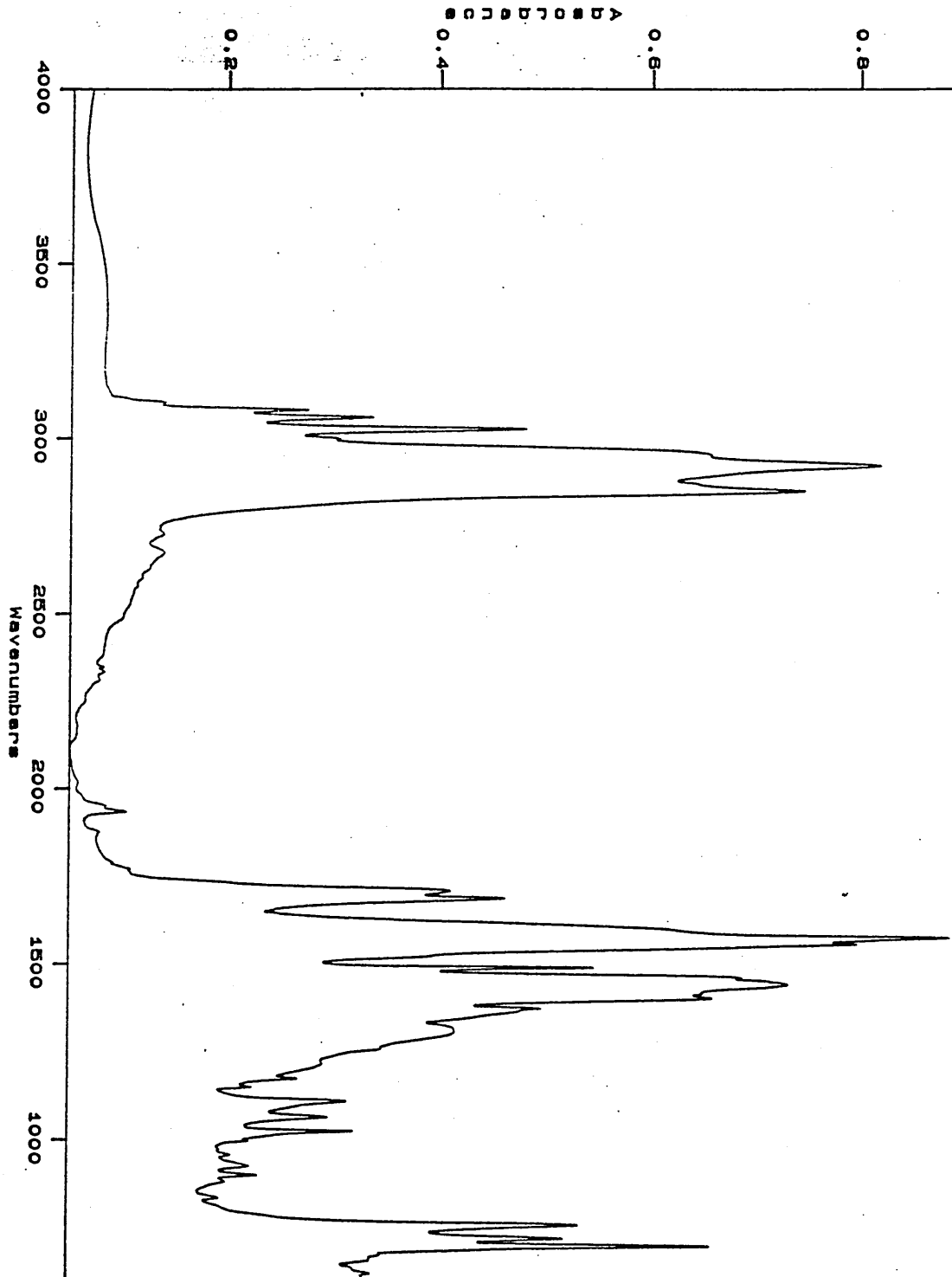


Table 5.1 Assignment of peaks in the infrared spectrum of lithium phenyl stearate.

Frequency cm ⁻¹	Vibrational type	Intensity	Source
3105	Arom C-H St _a	w sh	(6)
3083	Arom C-H St _a	m	(3,6)
3061	Arom C-H St _a	m	(3,6)
3026	Arom C-H St _s	m	(3,6)
3000	Arom C-H St _a	w sh	(3,6)
2954	Alip CH ₃ St _a	sh	(3)
2922	Alip CH ₂ St _a	s	(3)
2881	Alip CH ₃ St _s	sh	(3)
2851	Alip CH ₂ St _s	s	(3)
1951	Arom	w	(3)
1943	Arom]-combination	w	(3)
1885	Arom	w	(3)
1713	CO ₂ ⁻ St _a ?	m	
1691	CO ₂ ⁻ St _s ?	m	
1604	Arom C=C St _a	sh	(3,6)
1577	Arom C=C St _a	s	(3,6)
1559	CO ₂ ⁻ B _a	s	(3)
1493	Arom C-H B _a	s	(3,6)
1464	Alip CH ₂ B _a	s	(3)
1445	CO ₂ ⁻ B _s	s	(3)
1419	Alip CH ₂ B _s	s	(3)
1406	Alip CH ₃ B _s	s	(3)
1377	Alip CH ₃ U	w	(7)
1369	Alip CH ₂ gtg	w sh	(7)
1363	Alip CH ₂ gtg ?	w sh	
1352	Alip CH ₂ gg	w	(7)
1341	Alip CH ₂ end gt	w	(7)
1311	Alip CH ₂ gtg	w	(7)
1265	Alip CH ₂ Wa	w sh	(8)
1222	Alip CH ₂ Wa	w sh	(8)
1180	Arom C=C B	sh	(6)
1155	Arom C=C B	w sh	(3,6)
1114	Arom C=C B	m	(3,6)
1070	Arom + Alip C-C St	m	(3,6)
1029	Arom CH B \ \ plane	m	(3,6)
1003	Arom	w sh	(6)
979	Arom	w	(6)
963	Arom	w	(6)
905	Arom	w	(3,6)
889	Arom	w	(6)
841	Arom	w	(3,6)
760	Arom CH B ⊥ plane	s	(3,6)
721	Alip CH ₂ R	s	(3,6)
699	Arom CH B ⊥ Plane	s	(3,6)

s - Strong vibration St - Stretching
m - Medium vibration Wa - Wagging
w - Weak vibration B - Bending
sh - Shoulder R - Rocking
a - asymmetric s - Symmetric

Reference 3 refers to the assignments of bands in phenyl stearic acid, while reference 6 compares the observed and calculated frequencies of benzene derivatives, such as toluene and isotactic polystyrene.

The bands at 1713 and 1691 cm^{-1} have been assigned as CO_2^- stretching vibrations. These bands appear at frequencies normally associated with the carbonyl stretching vibration of carboxylic acids (9), but other evidence points away from phenyl stearic acid contamination as the source of this band. This evidence is:-

- (i) If a carboxylic acid was present then a broad intense OH stretching band at $\approx 3500 \text{ cm}^{-1}$ would also be present and this is not the case.
- (ii) The carbonyl vibration at 1710 cm^{-1} produced by a carboxylic acid is a singlet, whereas the vibration observed consists of at least 2 peaks.
- (iii) There is a possibility of some of the LiPS molecules oxidising, producing ketones or aldehydes. The carbonyl vibration of ketones and aldehydes is normally at a higher frequency ($\approx 1750 \text{ cm}^{-1}$ (8)).

A major factor against the assignment of these vibrations to CO_2^- stretching modes is the lack of supporting evidence in the literature. In a review (10), Chapman found that sodium salts of fatty acids do not show a vibration in the region 1730 to 1690 cm^{-1} , so the assignment here is only tentative.

5.3 Defect region

Figure 5.3 shows the defect CH_2 -wagging region of LiPS

at room temperature from 1391 to 1340 cm^{-1} . This shows an additional band in the spectrum at $\approx 1363 \text{ cm}^{-1}$ which was not predicted by Maroncelli et al (7). Figure 5.4 shows the same spectrum as figure 5.3, but where the background, approximated by a series of straight lines, has been removed showing the peaks used (and the additional band at 1363 cm^{-1}) much more clearly. We have assumed that this additional band is a variant of the $\text{gtg/gtg}'$ vibration. There are several possible explanations for this additional band, which are:-

- (i) The band is a result of the reverse hexagonal phase (see section 6.3)
- (ii) The additional band is due to a weak phenyl group vibration (see section 6.2)
- (iii) The band is due to the phenyl group decoupling the aliphatic backbone of LiPS, creating in effect 2 shorter chains. Maroncelli et al (7) observed that certain vibrations in this region, although localised, were affected by chain length. So by examining short chain fatty acids (see section 6.1) it is possible to check to see if this band is due to decoupling of the backbone.
- (iv) The band is due to a distortion in the backbone caused by the phenyl group preventing the chain adopting true rotational isomeric state conformations (see section 4.3). An additional band was observed by Spels et al in tight folded polyethylene: the 1342 cm^{-1} band was assigned to a distorted form of the defect ggtgg , the distortion shifting the gg defect mode from 1352 cm^{-1} .

Figure 5.3 The CH₂ defect wagging region of the spectrum of lithium phenyl stearate at room temperature.

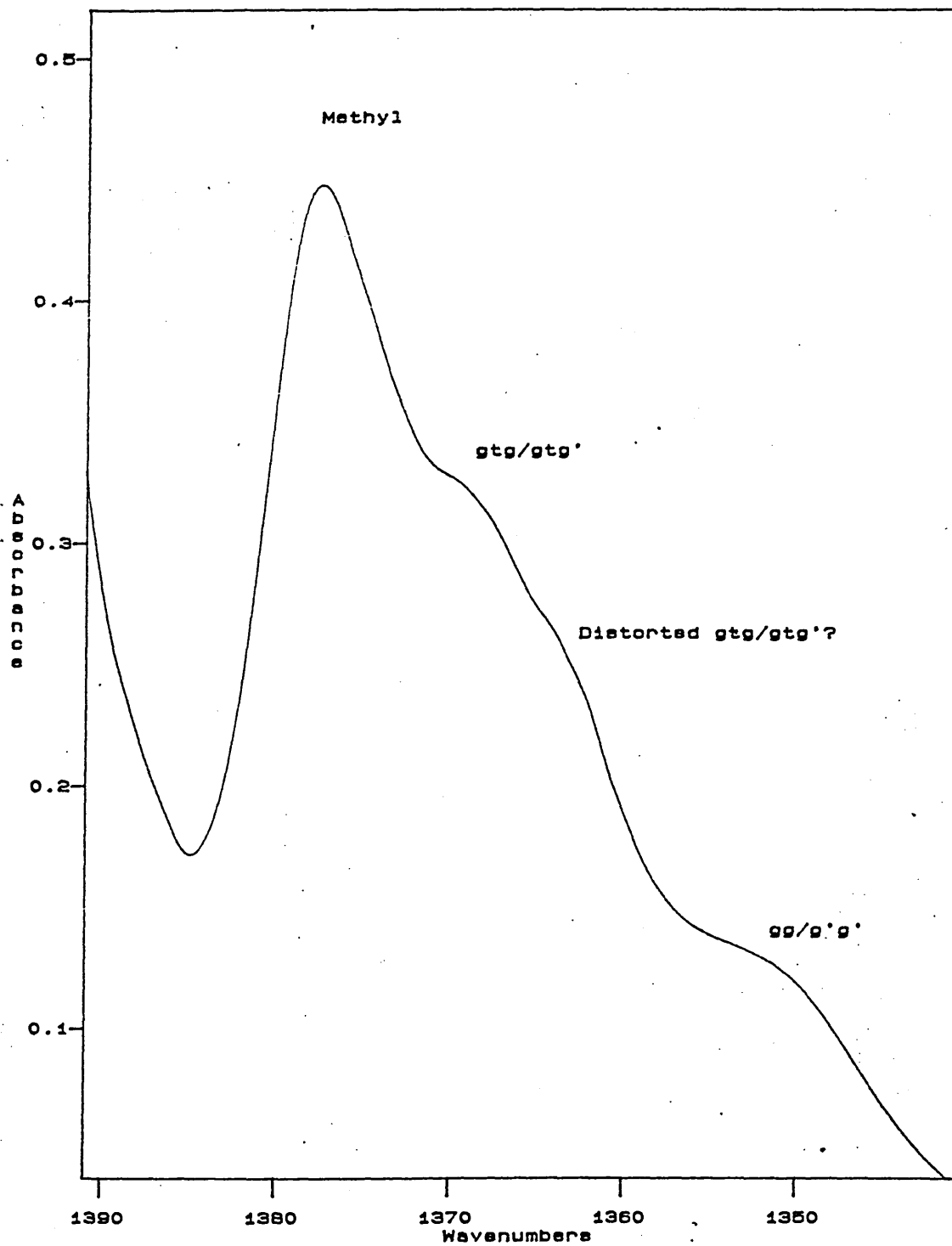
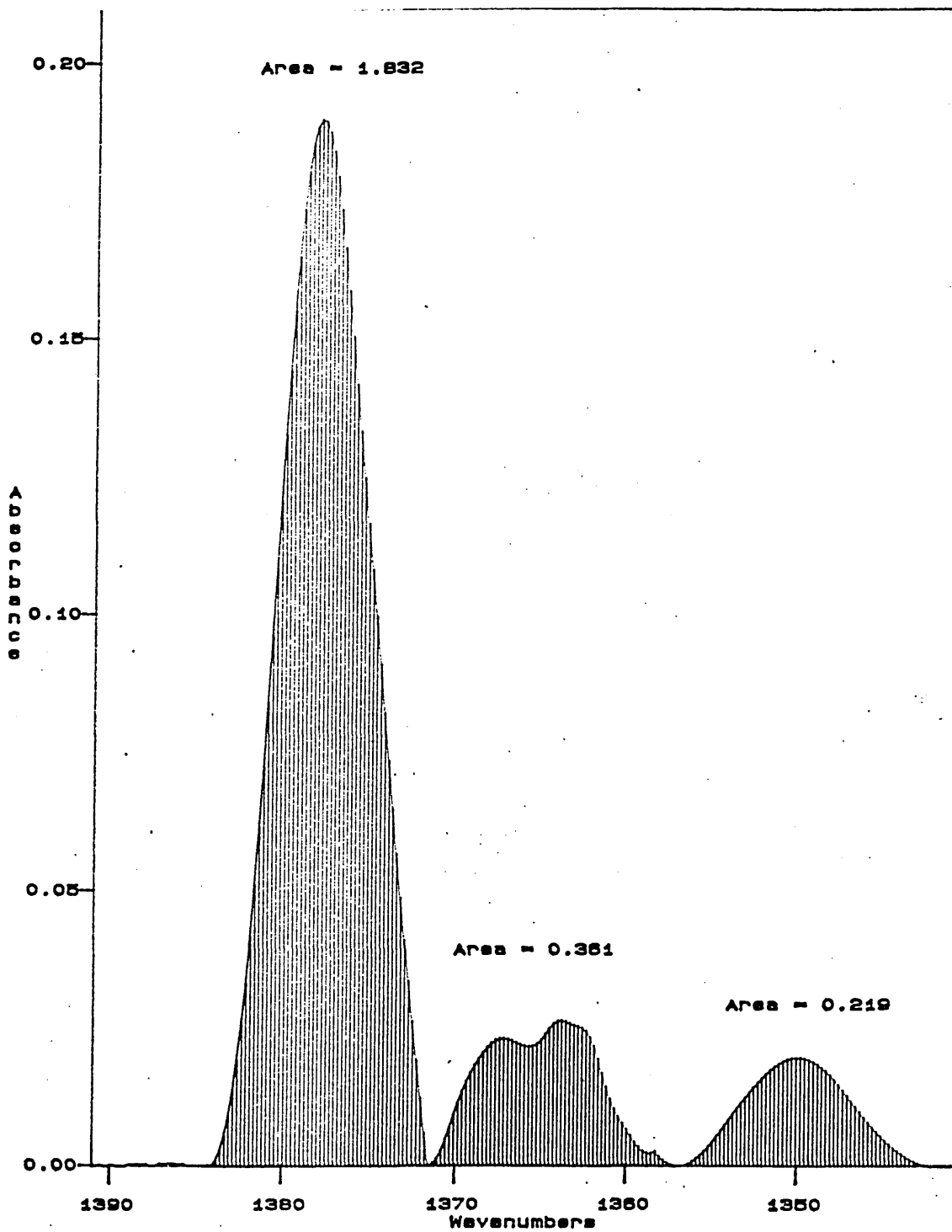


Figure 5.4 The CH₂ defect wagging region of the spectrum of lithium phenyl stearate at room temperature, with the background removed



A detailed discussion of the relevance of the results to the points made above will be appear in chapter 6.

5.3.1 Variation of defect concentration with temperature

Harrison et al (12) found that anhydrous LiPS goes through a series of high temperature phases before melting to the isotropic state at a remarkably high temperature of 370⁰C. These include a phase transition beginning at ≈130⁰C, with endothermal heat flow from the DSC peaking at ≈151⁰C and the transition complete by ≈170⁰C. The X-ray data of Harrison et al (12), shows that there is a change in the hexagonal lattice parameter, *a*, of LiPS across the phase transition beginning at ≈130⁰C, but it remains in a reverse hexagonal phase. Also the ⁷Li NMR data of Harrison et al (12) shows a line narrowing across the phase transition beginning at ≈130⁰C, showing the core is becoming more liquid like but is not fused.

Infrared spectroscopy was used to investigate the phase transition of LiPS beginning at ≈130⁰C, using the defect bands at 1369 and 1352 cm⁻¹ (gtg and gg respectively) to see if the backbone plays any part in the phase transition. Figure 5.5 shows the evolution of the wagging vibration from room temperature to 155⁰C. The intensity the defect bands may be affected by the phase transition, or by thermal expansion of the sample, giving an apparent decrease in intensity with increasing temperature. So to observe the "true" effect of temperature on the intensity of the gtg and gg defects bands, we need to normalise the intensity of each band against a standard which is not conformationally sensitive, or expected to be affected by the phase transition. Maroncelli et al (7)

chose the methyl umbrella mode CH_3U at 1377 cm^{-1} . Figure 5.6 shows the variation of bandwidth of the CH_3U vibration with temperature, which remains constant (within experimental error) for all temperatures. This gives us confidence that any changes observed in the normalised intensities of the defect bands will be due directly to a change in the defect population, and not to the methyl band.

The intensity of each the bands was determined by fitting a background and several peaks to the CH_3U 1377 cm^{-1} vibration (these synthetic peaks were used to determine the intensity of the methyl vibration), and then subtracting this from the original. This enabled the determination of the intensity of the gtg (1369 cm^{-1}) and gg (1352 cm^{-1}) bands directly from the spectrum after subtraction (for further details see section 8.1).

Figure 5.7 and Figure 5.8 show the variation in the normalised intensity (divided by the 1377 cm^{-1} band intensity) of the gtg (1369 cm^{-1}) and gg (1352 cm^{-1}) defects respectively, with the intensity of the gtg band including the shoulder at 1363 cm^{-1} . The relative error in estimating the intensity of each band increases with increasing temperature, and is about $\pm 5\%$ at 47°C and about $\pm 10\%$ at 171°C . This increase in error is caused by the decrease in intensity of both the methyl band and the defect band with increasing temperature.

Figure 5.7 and Figure 5.8 show that the normalised intensity of both the gtg and gg defect modes rises steadily with increasing temperature, and then begins to level off at $\approx 130^\circ\text{C}$, the beginning of the phase transition. When a phase transition is caused by the melting of the aliphatic chain,

then one should see a sudden change in the intensity of the conformational sensitive bands (7,9), but this is not the case with LiPS. This shows that, although the aliphatic chains play no major part in the phase transition beginning at 130°C, the chains reach approximately an isotropic degree of disorder before the phase transition occurs.

Figure 5.5 The CH₂ defect wagging region of the LiPS infrared spectrum, at temperatures from 25°C to 155°C.

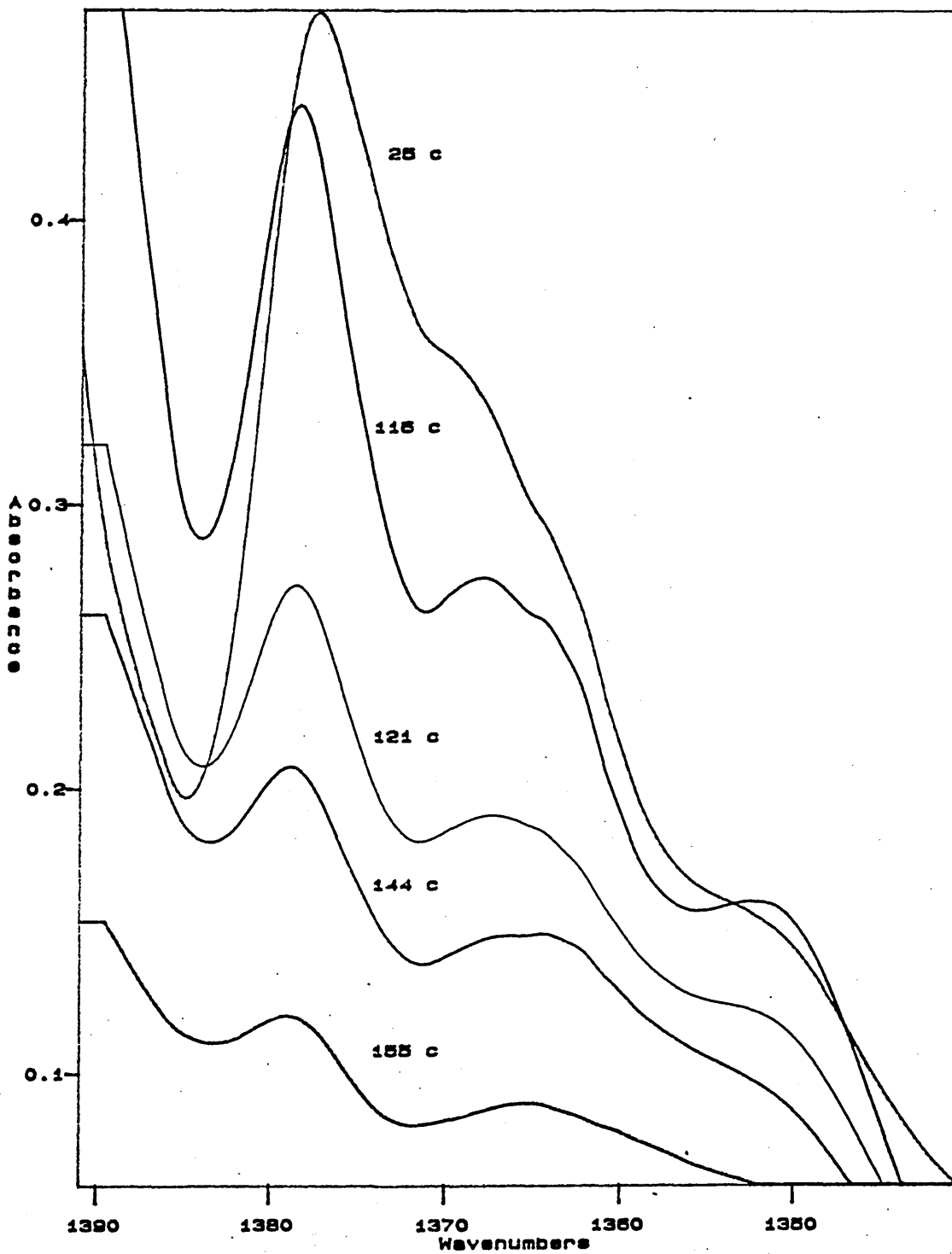


Figure 5.6 Variation of the full width at half height of the 1377 cm^{-1} CH_3U vibration, with temperature.

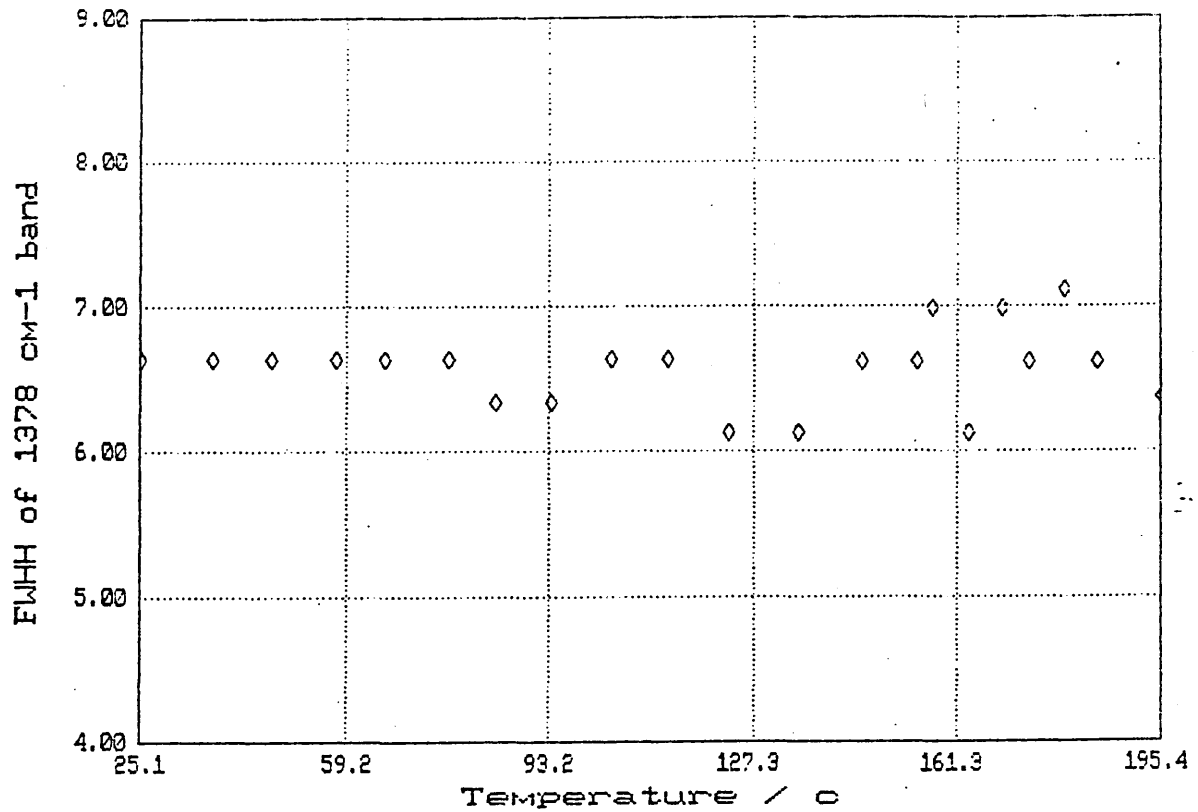


Figure 5.7 Variation of the normalised intensity of the 1369 cm^{-1} gtg band of LiPS, with temperature.

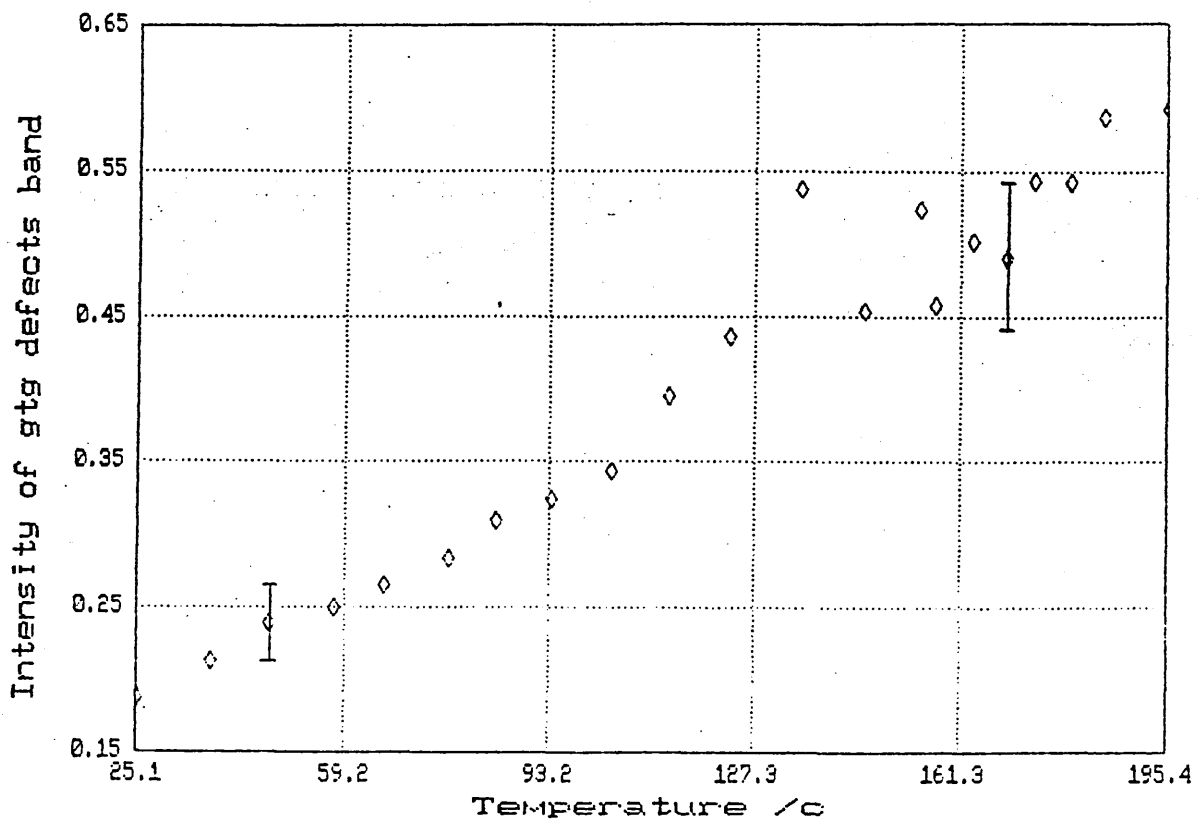
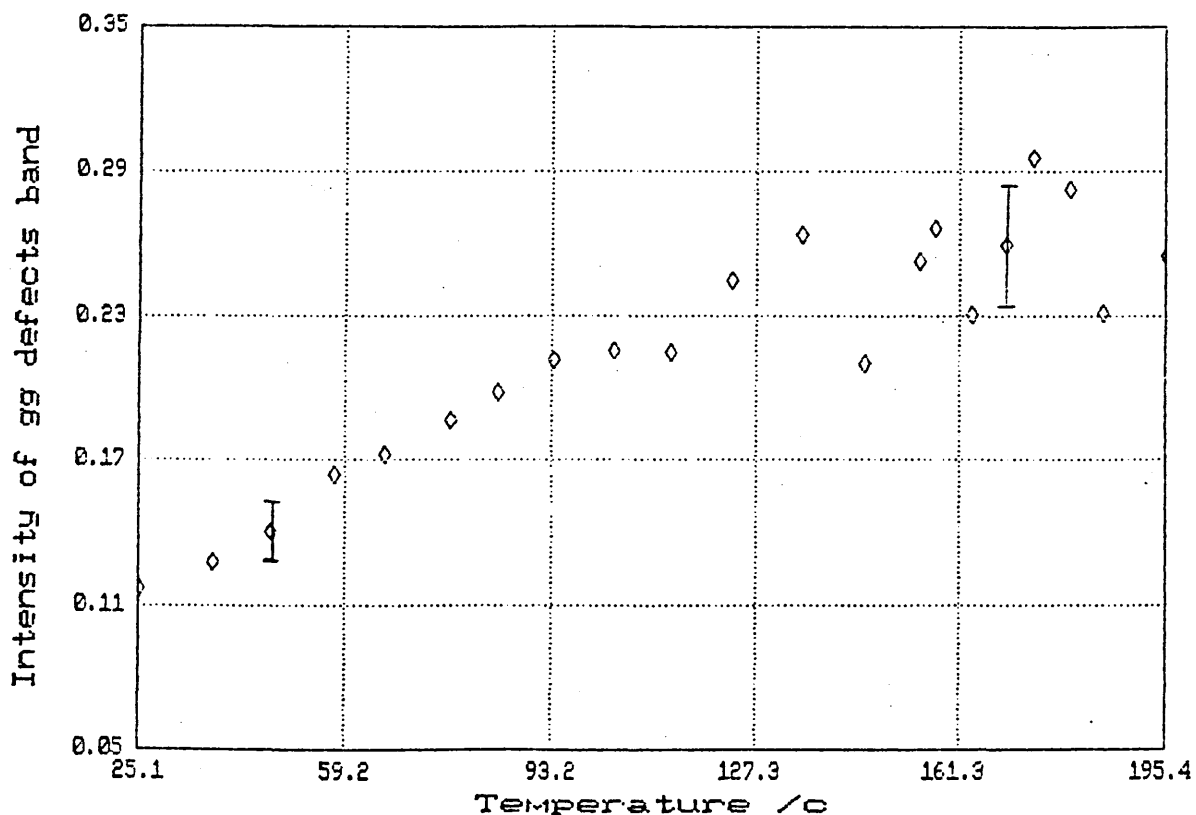


Figure 5.8 Variation of the normalised intensity of the 1352 cm⁻¹ gg band of LiPS, with temperature.



5.3.2 Numbers of defects

To estimate the number of gtg and gg defects present in LiPS, a calibration constant is required. It is assumed for a molten material that the intensity of the defect bands is directly proportional to the number of defects present as determined by the RIS model, such that:-

$$n_{\text{defect}} = K_{\text{defect}} \times I_{\text{defect}} \quad (5.1)$$

where n_{defect} is the number of defects estimated from the rotational isomeric state model.

I_{defect} is the intensity of a particular defect band normalised against the 1377 cm⁻¹ CH₃U band.

K_{defect} is the calibration constant.

The constant, K_{defect} , is assumed to be the same for any molecule with a polymethylene portion containing that

specific defect.

It is possible to estimate the number of defects per chain for any n-alkane using the rotational isomeric state model (see section 4.1), and I_{defect} can be measured for the same n-alkane, so an estimate of K_{defect} is possible. Figure 5.9 shows the defect region of the spectrum of the n-alkane n-hexadecane. The integrated intensity of the various bands for a known sample thickness are as follows:-

$$I_{me} = 2.203 \text{ units}^1$$

$$I_{gtg} = 0.457 \text{ units}$$

$$I_{gg} = 0.225 \text{ units}$$

The numbers of defects estimated from the rotational isomeric state model, for n-hexadecane at the same temperature as the infrared results are:-

$$n_{gtg} = 1.356 \text{ defects per molecule}$$

$$n_{gg} = 1.210 \text{ defects per molecule}$$

Having estimated these values it is possible to estimate K_{defect} for both the gtg and gg defects. Taking into account the difference in the number of methyl groups per molecule for LiPS and n-hexadecane, K_{defect} for LiPS becomes:-

$$K_{defect} = \frac{n_{defect} \times I_{me}}{2 \times I_{defect}} \quad (5.2)$$

So the value of K_{defect} for the gtg and gg defects is:-

$$K_{gtg} = 3.267 \text{ per molecule}$$

$$K_{gg} = 5.221 \text{ per molecule}$$

¹ 1 unit = 1 absorbance unit multiplied by 1 cm⁻¹.

Figure 5.9 The infrared spectrum of n-hexadecane in the CH_2 defect wagging region, at 25°C .

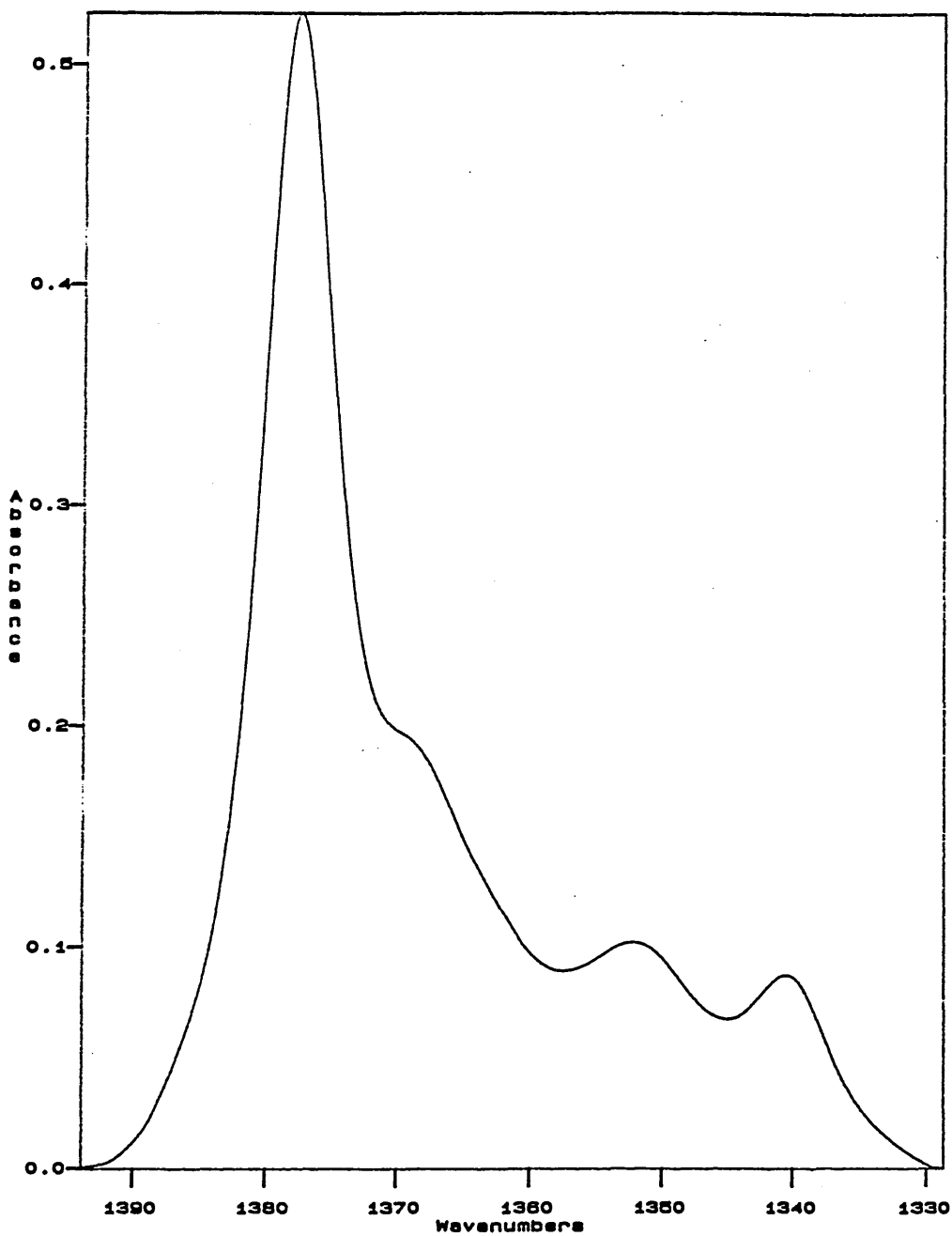


Figure 5.10 and Figure 5.11 show the variation of the numbers of gtg and gg defects respectively observed for LiPS, together with the numbers of gtg and gg defects estimated for n-heptadecane from the rotational isomeric state model. From figure 5.10 it becomes apparent that at room temperature the number of gtg defects per molecule ($n_{gtg}=0.625$) is about 45% of the value that would be expected for an isotropic phase, but by the time the molecule begins to go through the phase transition beginning at $\approx 130^{\circ}\text{C}$ the number of gtg defects per molecule has reached the same value as for the isotropic phase with chains of equal length. From figure 5.11, the variation in the number of gg defects per molecule with temperature shows a similar behaviour to the number of gtg defects (from figure 5.10), except that on reaching the phase transition temperature, the number of gg defects per molecule is only $\approx 75\%$ of the number expected for an isotropic chain of equal length.

The room temperature values of n_{gtg} and n_{gg} , seem to disprove the assumption made by Harrison (12) and Spegt and Skoulios (13,14), that the aliphatic portion of a soap in a reverse hexagonal phase is liquid like. This may be the case with some soaps, but is obviously not the case with LiPS. In fact both n_{gtg} and n_{gg} , for LiPS at room temperature, are less than half the values expected for isotropic (liquid) n-heptadecane, so the aliphatic portion of LiPS is more ordered than expected for an isotropic melt-like phase.

Another curious feature is that at the beginning of the phase transition (130°C) the number of gtg defects per molecule is approximately that expected for a liquid-like

chain of equal length, but the number of gg defects per molecule is only 75% of the value expected for a liquid-like chain of equal length. For cadmium stearate in the reverse hexagonal phase (temperature greater than 115°C), not only is the number of gtg defects per molecule present equivalent to the number for an isotropic n-alkane of the same length and at the same temperature, but also the number of gg defects present is equivalent to an isotropic n-alkane (see section 6.3). This shows that the number of gg units is not restricted by phase. One explanation for this is that the phenyl group prevents adjacent bonds from adopting gg or g'g' defects, or at least reduces the probability of gg or g'g' defects occurring (see section 4.3).

Figure 5.10 Variation in the number of gtg defects per molecule present in LiPS, with increasing temperature.

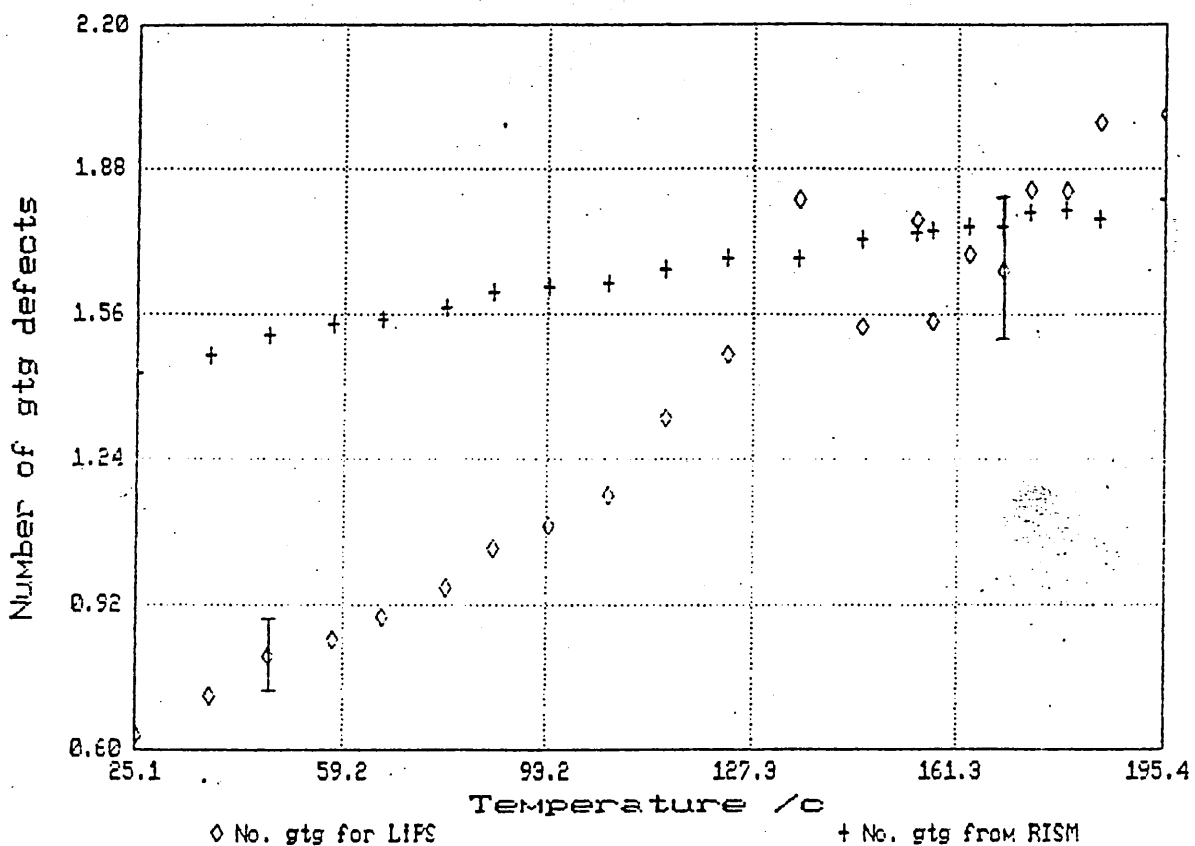
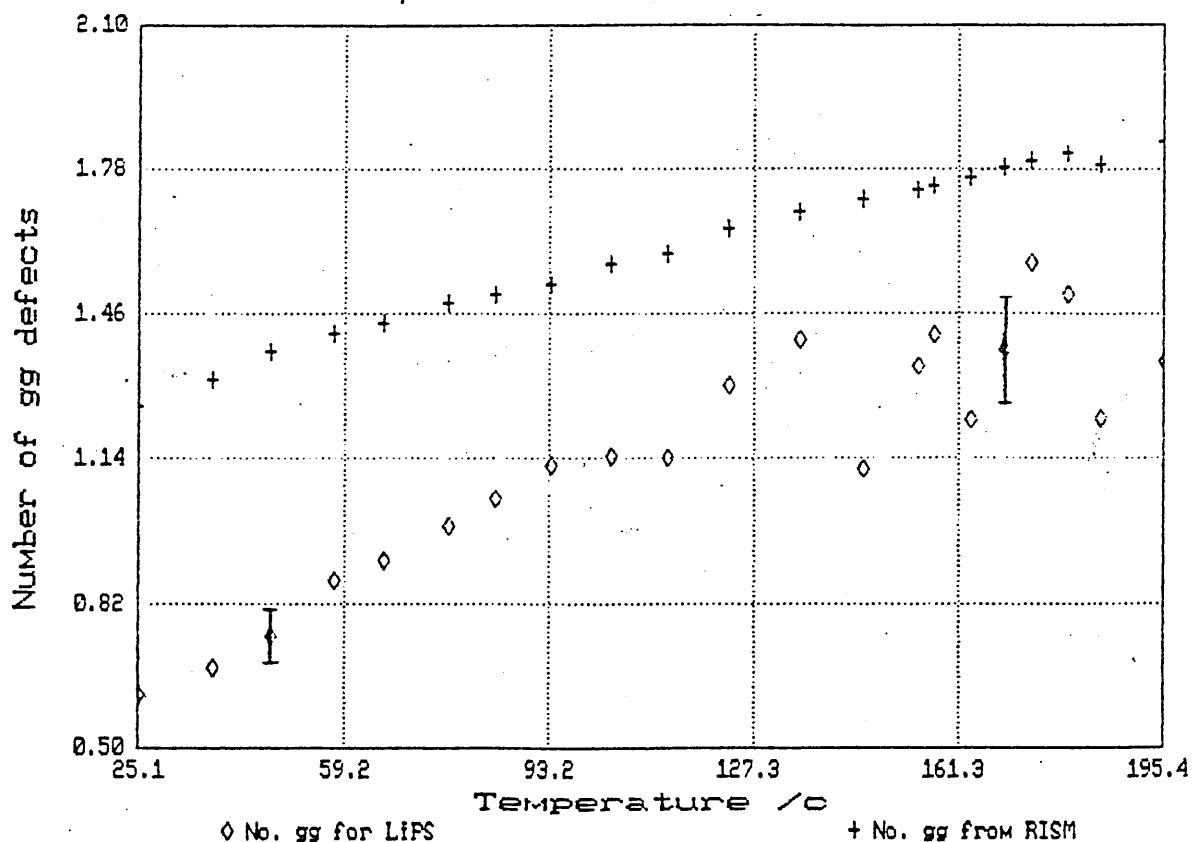


Figure 5.11 Variation in the number of gg defects per molecule present in LiPS, with increasing temperature.



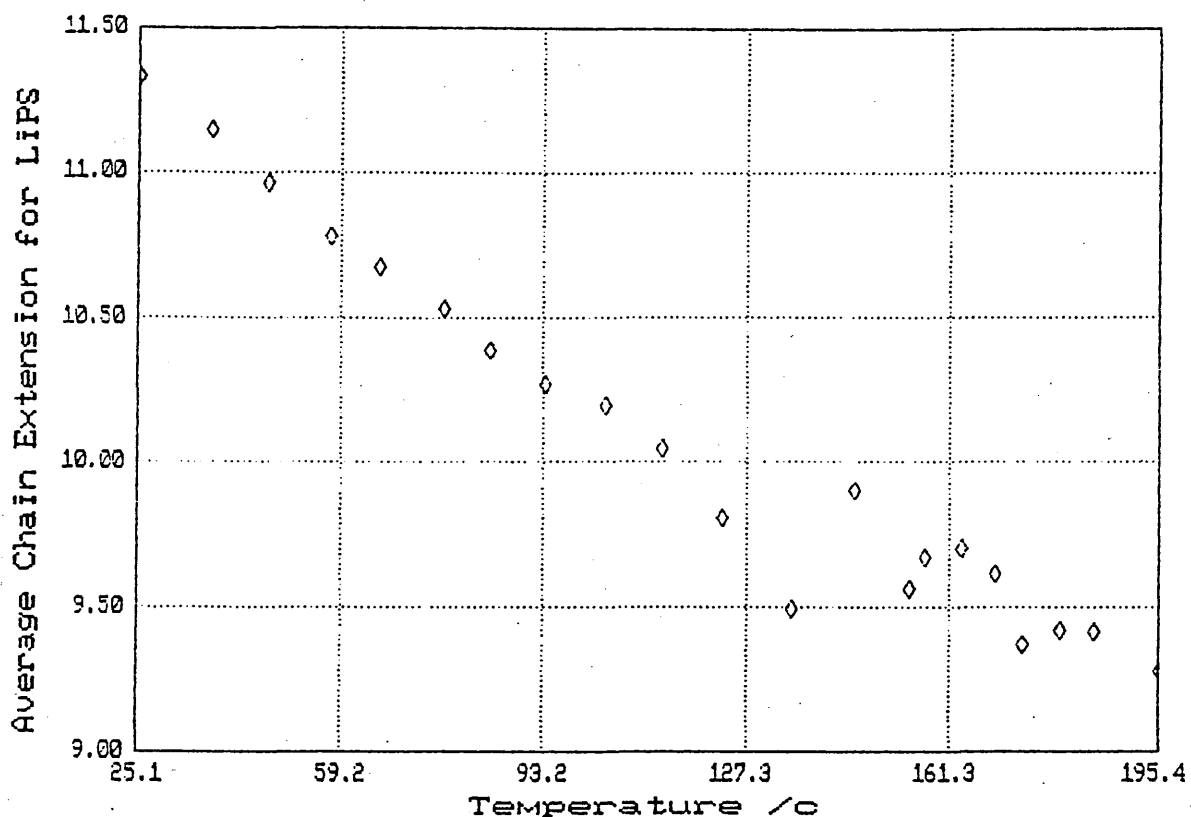
5.4 Hexagonal phase dimensions

Harrison et al (12), found that the hexagonal lattice parameter, a , for LiPS increases slightly from 35.9Å to 36.1Å on heating from 25°C to ≈130°C. At 140°C there is a change in lattice parameter to 31.4Å. So over the phase transition (beginning at 130°C) there is a change in the packing of chains.

Figure 5.12 shows the variation in the average chain extension, R_{av} (determined from the experimental defect concentration, using the method described in chapter 4.1), for LiPS with increasing temperature upto 195°C, which includes the phase transition. The chain length decreases in an approximately linear manner from 25°C to ≈123°C and then

the gradient decreases sharply once the transition begins, at 130°C. The scatter of the data in this region 130–195°C hides any underlying trend, i.e. R_{av} could be decreasing or could be constant to within experimental errors.

Figure 5.12 Variation in the average chain extension, R_{av} , for LiPS, with increasing temperature.



Having estimated the core radius in section 4.2, it is now possible to determine the dimensions of individual cylinders within the reverse hexagonal phase. The ionic core radius, R_c , has been calculated to lie between a minimum of 5.6Å and a maximum of 7.12Å. Table 5.2 shows a comparison between the hexagonal lattice parameter, a , determined by Harrison et al (12) from X-ray diffraction, and the dimensions estimated from infrared spectroscopy. The calculation of the dimensions of the cylinders assumes that

n , the number of ions per unit length of core does not change with temperature. This is probably not true, but the range of values quoted for R_c , the core radius, will probably cover any change. Figure 5.13 shows the dimensions that have been measured and are compared in table 5.2.

Table 5.2 Dimensions of the reverse hexagonal phase of LiPS, using X-ray diffraction and infrared spectroscopy.

Temperature /°C	X-ray (12) $a/\text{Å}$	Infrared D min /Å	Infrared D max /Å
25.1	35.9	33.8	36.8
123.0	36.1	30.8	33.8
135.2	31.4	30.2	33.2

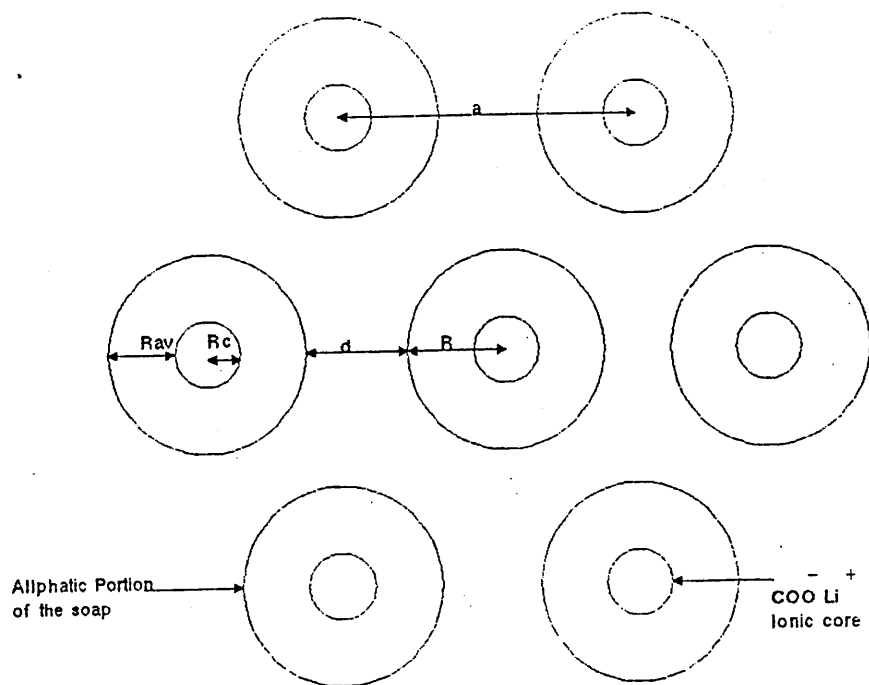
where D is the diameter of a cylinder.

One must remember that the average chain extension R_{av} , defines a cylindrical surface which is not a hard, impenetrable physical boundary, but an average position of a penetrable boundary. For example at 25°C, the average chain extension, R_{av} , has a value of 11.9Å and has a probability of 0.42 of extending beyond R_{av} . At 135°C, the average chain extension is 9.5Å and there is a probability of 0.40 of chain extending beyond this point.

The physical significance of these results seems to be that at room temperature the hexagonal lattice parameter and the cylinder dimensions are approximately the same (within experimental error). As the temperature of the LiPS sample is increased the average chain extension decreases continuously, and thus the cylinder dimensions, while the hexagonal lattice spacing remains almost constant. Then as the aliphatic chain

reaches "liquid like" disorder, the hexagonal lattice rearranges giving a lattice parameter, a , which is again approximately equal to the cylinder dimensions. Also ^7Li NMR (12) shows that the ionic core has become more disordered. The fact that the hexagonal lattice begins to rearrange and the core begins to melt at approximately the same temperature as the aliphatic chain reaches "liquid like" disorder may just be coincidental, but if there is some link between these events the mechanism at present is unknown.

Figure 5.13 Schematic representation of the reverse hexagonal phase of LIPS, showing the dimensions measured



5.5 Effect of sample preparation

One of the problems associated with infrared spectroscopy, is that in most cases the sample has to be pre-treated to get it into a state where it can be observed with infrared spectroscopy. However, all the measurements done by Harrison (12) were carried out on untreated samples. In our case a thin film was required which could either be pressed or cast from a solution. Pressing the sample could impose some additional order onto the sample, so this technique was ignored. Solvent casting could also affect the sample, by leaving the aliphatic chains in a more ordered state as the solvent evaporates. Thus the fact that LiPS does not have a "liquid-like" chain at room temperature could be due to the effect of solvent casting.

The effect of the solvent casting has been investigated with DSC, looking at the heat of transition for the phase transition beginning at $\approx 130^{\circ}\text{C}$ for both solvent cast and untreated LiPS samples (see section 7.1.1) (however, this will only show up differences in the structure, and not effects of orientation). The results show no conclusive evidence for an effect on the heat of transition.

Harrison (12) showed that the phase transition beginning at $\approx 130^{\circ}\text{C}$ is irreversible. So if the ordering present in LiPS at 25°C is due to the solvent casting, then it would be reasonable to expect the backbone chain to remain "liquid-like" on cooling from above the phase transition. Additional infrared readings were taken after the sample had been heated up through the phase transition and allowed to cool down. Table 5.3 shows the number of gtg and gg defects per molecule

for LiPS at various stages of in the heating and cooling cycle, determined from the infrared data, and also includes the number of gtg and gg defects per molecule for an isotropic liquid having the same chain length. The results show that although there is an increase in the number of defects per molecule after cooling from above the phase transition temperature, the structure is still much more ordered than for the case of the isotropic n-alkane. This would seem to show that the ordering of the chain in LiPS at room temperature is not predominantly caused by solvent casting.

Table 5.3 The effect of heating and cooling on the number of gtg and gg defects per molecule, present in LiPS.

Temperature /°C	Sample on Heating		Sample on Cooling		Calculations for Isotropic Liquid	
	n_{gtg}	n_{gg}	n_{gtg}	n_{gg}	n_{gtg}	n_{gg}
25	0.64	0.62	0.86	0.82	1.54	1.35
57	0.94	0.90	1.36	1.32	1.64	1.51

5.5 References

- (1) W.J. Harrison, PhD. Thesis, Sheffield City Polytechnic, 1988
- (2) G.W. Kaye and T.H. Laby, "Physical and Chemical constants", 15th Ed., Longman (London and New York), 1986
- (3) R.E. Kagarise, J. Phys. Chem. 59, 271, 1955
- (4) J.K. Kauppinen, D.J. Moffat, H.H. Mantsch and D.G. Cameron, Appl. Spec. 35, 271, 1981
- (5) J.K. Kauppinen, D.J. Moffat, H.H. Mantsch and D.G. Cameron, Anal. Chem 53, 1453, 1981
- (6) R.W. Snyder and P.C. Painter, Polymer 22, 1633, 1981
- (7) M. Maroncelli, S.P. Qi, H.L. Strauss and R.G. Snyder, J. Am. Chem. Soc. 104, 6237, 1982
- (8) "Introduction to infrared and Raman spectroscopy", 2nd ed., N.B. Colthup, L. Daly and S.E Wiberley, Academic Press, London, 1975.
- (9) G. Zerbi, G. Conti, G Minoni, S. Pison and A. Bigotto, J. Phys. Chem. 91, 2386, 1987
- (10) D. Chapman, "Structure of Lipids", Methuen and Co, London, 1965
- (11) S.J. Spells, S.J. Organ, A. Keller and G. Zerbi, Polymer 28, 697, 1987
- (12) W.J. Harrison, M.P. McDonald and G.J.T. Tiddy, Liquid Crystals 7(4), 509, 1990
- (13) P.A. Spegt and A.E. Skoulios, Acta Cryst. 16, 301, 1963
- (14) P.A. Spegt and A.E. Skoulios, Acta Cryst. 17, 198, 1964

Chapter 6

6 Fatty acids and cadmium stearate	148
6.1 Fatty acids	148
6.1.1 n-Carboxylic acids	148
6.1.2 Phenyl undecanoic acid	151
6.1.3 Phenyl stearic acid	153
6.2 Rotational isomeric state model	153
6.3 Cadmium stearate	155
6.3.1 Preparation	157
6.3.2 Crystalline phase	158
6.3.3 Reverse hexagonal phase	164
6.4 References	169

6 Fatty acids and cadmium stearate

The additional defect band, observed in the infrared spectrum of lithium phenyl stearate at 1363 cm^{-1} , could have several origins, as stated in section 5.3. Among these are:-

- i) The phenyl group decouples the aliphatic backbone, giving effectively two shorter chains which could affect the frequency of the gtg defect mode (1).
- ii) The band is a phenyl vibration.
- iii) The band is a result of the reverse hexagonal phase.

6.1 Fatty acids

By examining the frequency of the gtg/gtg' defect mode (which in longer chain acids occurs at 1369 cm^{-1}) of various n-carboxylic acids, it is possible to find the effect of chain length (number of carbon atoms in the backbone, N_c) on the frequency.

6.1.1 n-Carboxylic acids

The n-carboxylic acids used, n-pentanoic to n-nonanoic acid were purchased from the Aldrich Chemical Company, and were of the highest purity available (gold label), 99% minimum assay. All are liquids at room temperature, so samples were simply prepared by sandwiching a few drops between two sodium chloride plates with a $50 \times 10^{-6}\text{m}$ PTFE spacer. The spectrometer used was the Mattson Galaxy 6020 which set on 1 cm^{-1} resolution and averaged over 100 scans.

Figure 6.1 shows part of the defect region of the n-carboxylic acids n-pentane to n-nonanoic acid. For n-pentanoic acid no vibrational peak or shoulder is observed at 1369 cm^{-1} . This is expected as the minimum requirement for a gtg/gtg' defect to be obtainable is six carbon atoms in the

backbone (corresponding to n-hexanoic acid). The remaining acids shown in figure 6.1 show an increase in the intensity of the 1369 cm^{-1} defect vibration relative to the methyl vibration (1377 cm^{-1}) as the chain length is increased, but no change in frequency. There are two effects involved here: as the chain length increases, the percentage of CH_3 groups decreases, and so the absolute methyl vibration intensity decreases. Also as the chain length increases the number of gtg/gtg' defects increases for an isotropic liquid (2), and therefore the intensity of the gtg/gtg' vibration increases.

One effect that can be seen from figure 6.1 is that of the chain length on the frequency of the methyl group vibration. Figure 6.2 shows the change in peak frequency with number of carbon atoms, N_c , in the backbone. The methyl frequency from $N_c=18$ was provided by phenyl stearic acid, which is the fatty acid from which lithium phenyl stearate is produced. This result shows that the methyl group vibration in phenyl stearic acid is characteristic of the complete chain, and not of two shorter chains, as may have been the case if the phenyl group decoupled the backbone vibrational component.

This result, along with the absence of any significant change in the frequency of the gtg/gtg' defect mode at 1369 cm^{-1} for short chain fatty acids n-hexanoic acid to n-nonanoic acids, leads to the conclusion that the 1363 cm^{-1} peak has other origins.

Figure 6.1 The infrared spectrum of n-pentanoic acid to n-nonanoic acid, in the CH_2 wagging defect region at room temperature, with the same absorbance scale but maximum absorbance has been shifted.

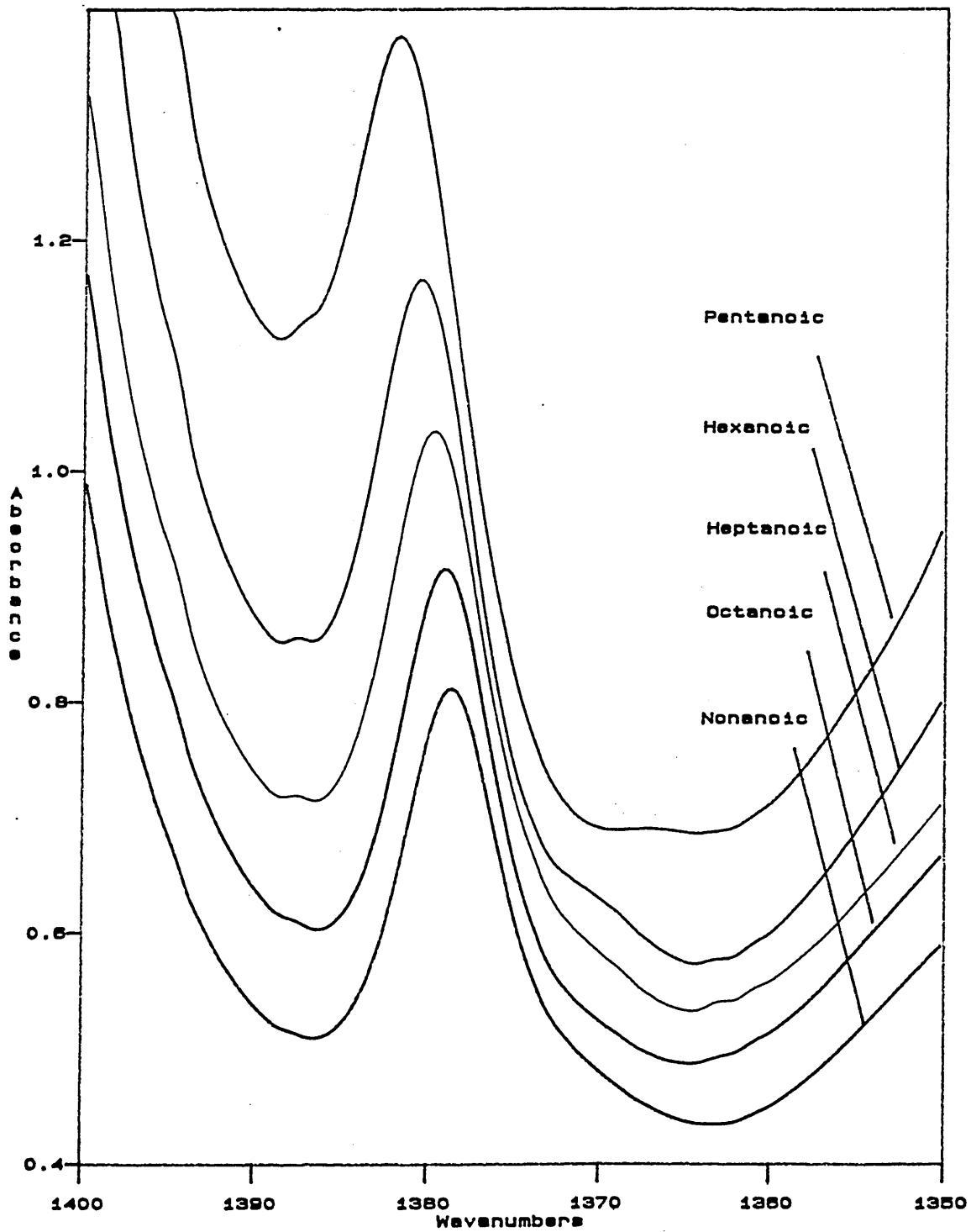
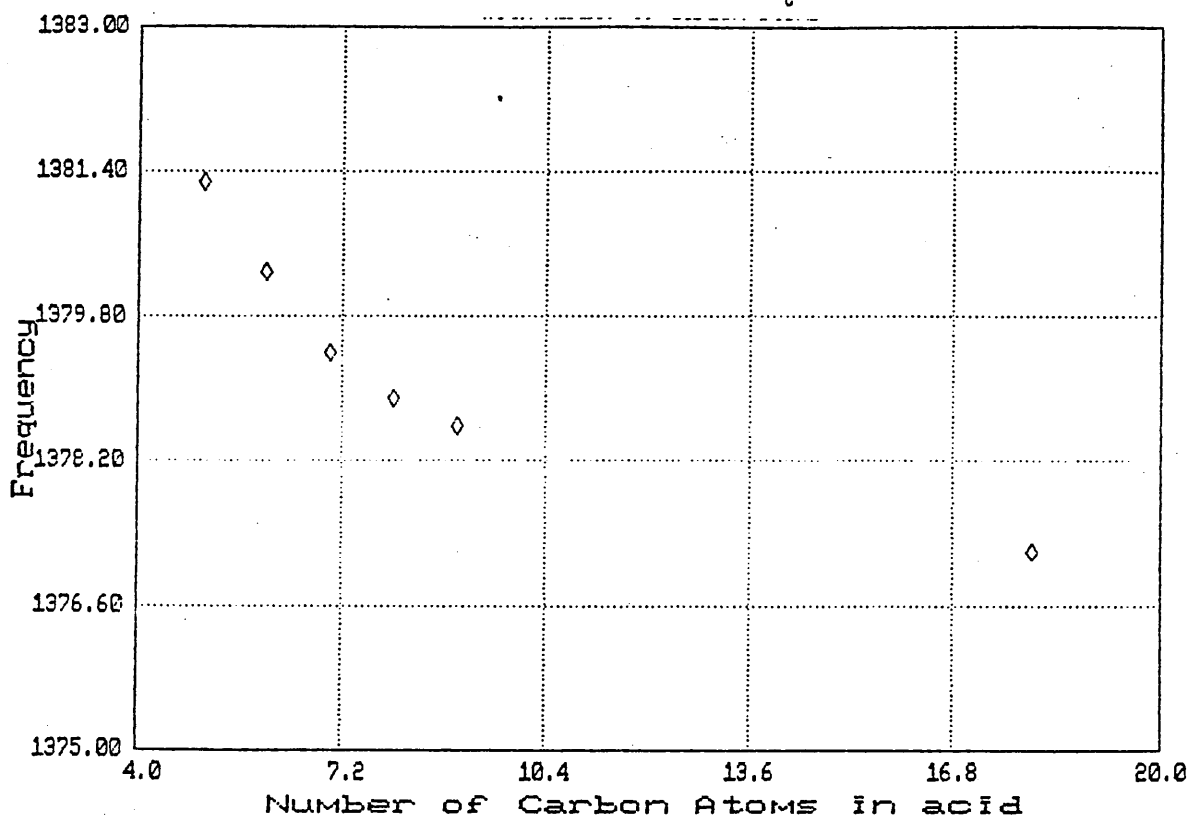


Figure 6.2 Variation of the peak frequency of the CH_3U vibration of the n-carboxylic acids with number of carbon atoms N_c .

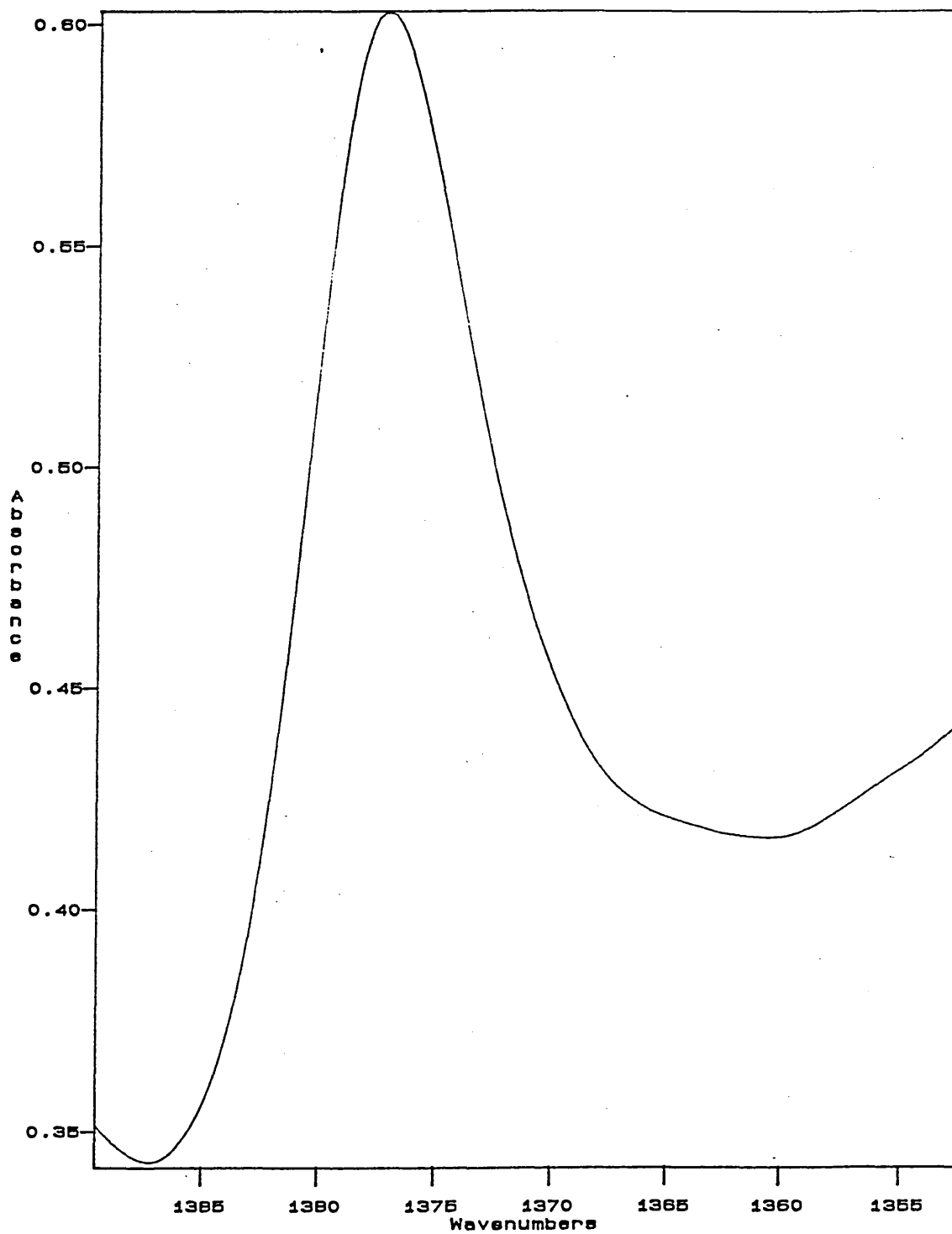


6.1.2 Phenyl undecanoic acid

The phenyl undecanoic acid sample was purchased from Pfaltz and Bauer inc. and has a minimum assay of 99%. It is a liquid at room temperature, so an infrared sample was prepared by sandwiching the liquid between 2 sodium chloride plates with a 50×10^{-6} m PTFE spacer.

Figure 6.3 shows part of the CH_2 defect wagging region for phenyl undecanoic acid. The methyl vibration is very broad, making it difficult to observe the 1369 cm^{-1} gtg/gtg' defect band. This broadening is presumably caused by the phenyl group being attached to the same carbon atom as the methyl group. No additional band is seen at 1363 cm^{-1} , showing that the band is not due to a weak phenyl vibration. Also,

Figure 6.3 Infrared spectrum of phenyl undecanoic acid at room temperature, in the CH₂ defect wagging region of the spectrum.



because the phenyl group is attached at the end of the aliphatic chain, it cannot have a significant effect on the backbone molecular conformations.

6.1.3 Phenyl stearic acid

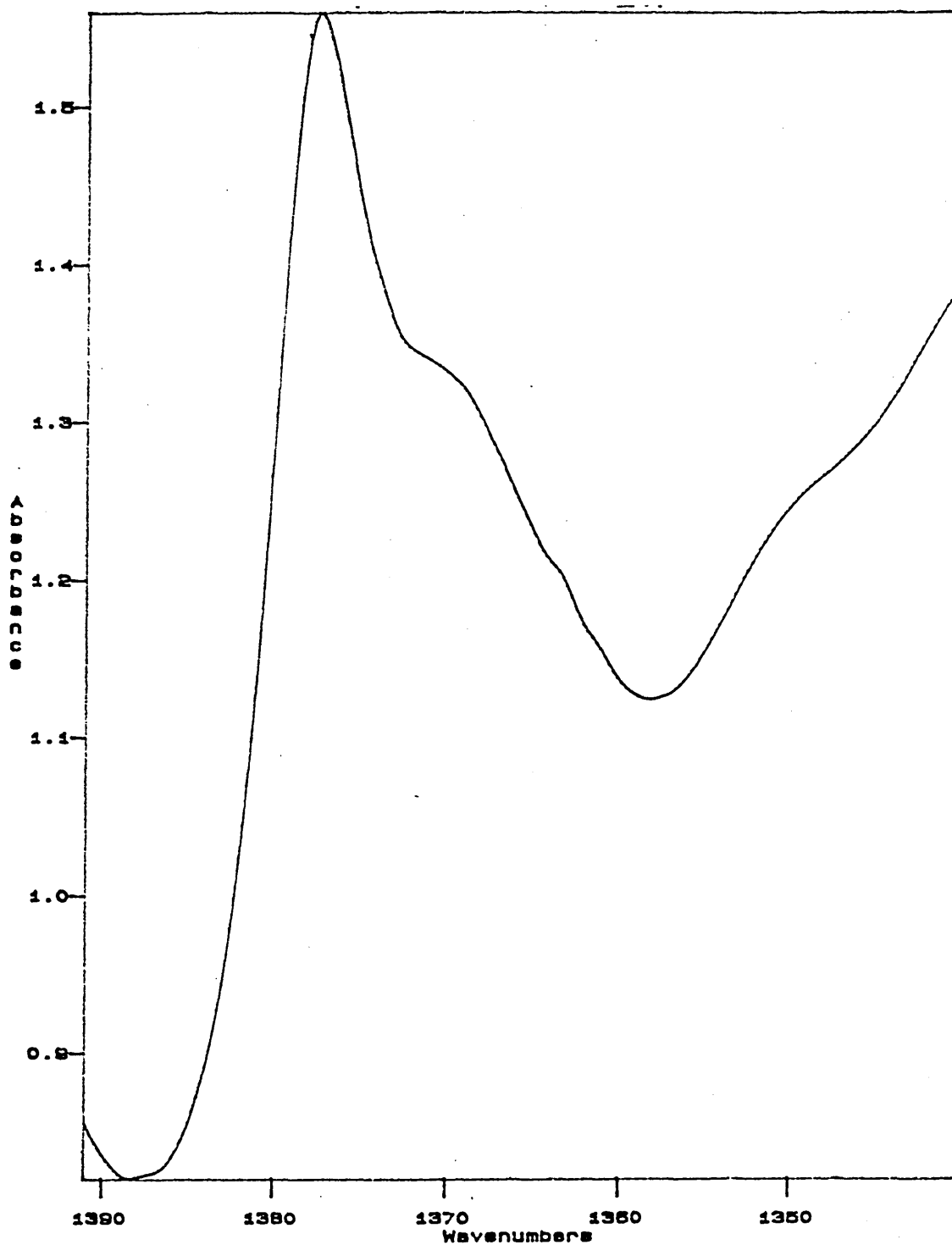
The phenyl stearic acid was produced by a Friedel-Crafts reaction of oleic acid (cis-9-octadecanoic acid) with an excess of benzene using aluminium chloride as a catalyst under anhydrous conditions (this was prepared by W.J. Harrison at sheffield City Polytechnic). The purity of the sample was checked by elemental micro analysis and was 99% assay (3). Phenyl stearic acid is liquid at room temperature, and so the sample was again sandwiched between two sodium chloride plates with a 50×10^{-6} m PTFE spacer.

Figure 6.4 shows part of the CH_2 defect wagging region for phenyl stearic acid, and as can be seen the 1369 cm^{-1} gtg/gtg' defect band is much broader than was observed for the n-carboxylic acids without a phenyl ring attached (see figure 6.1). There is also the additional band present that was observed in LiPS, at 1363 cm^{-1} . This seems to indicate that the nature of the phase does not affect the presence or absence of the additional band, as it is present in both liquid and reverse hexagonal phase. This is consistent with the cause being a distorted gtg/gtg' defect (see section 4.3.3) (4).

6.2 Rotational isomeric state model

By measuring the intensity of the 1369 cm^{-1} gtg/gtg' defect mode it should be possible to determine the validity of the rotational isomeric state model: in this case if the intensity varies linearly with increasing number of carbon

Figure 6.4 Infrared spectrum of phenyl stearic acid at room temperature, in the CH₂ defect wagging region of the spectrum.



atoms, and the number of defects estimated from the intensity is as predicted by the rotational isomeric state model, then we can assume the model to be valid.

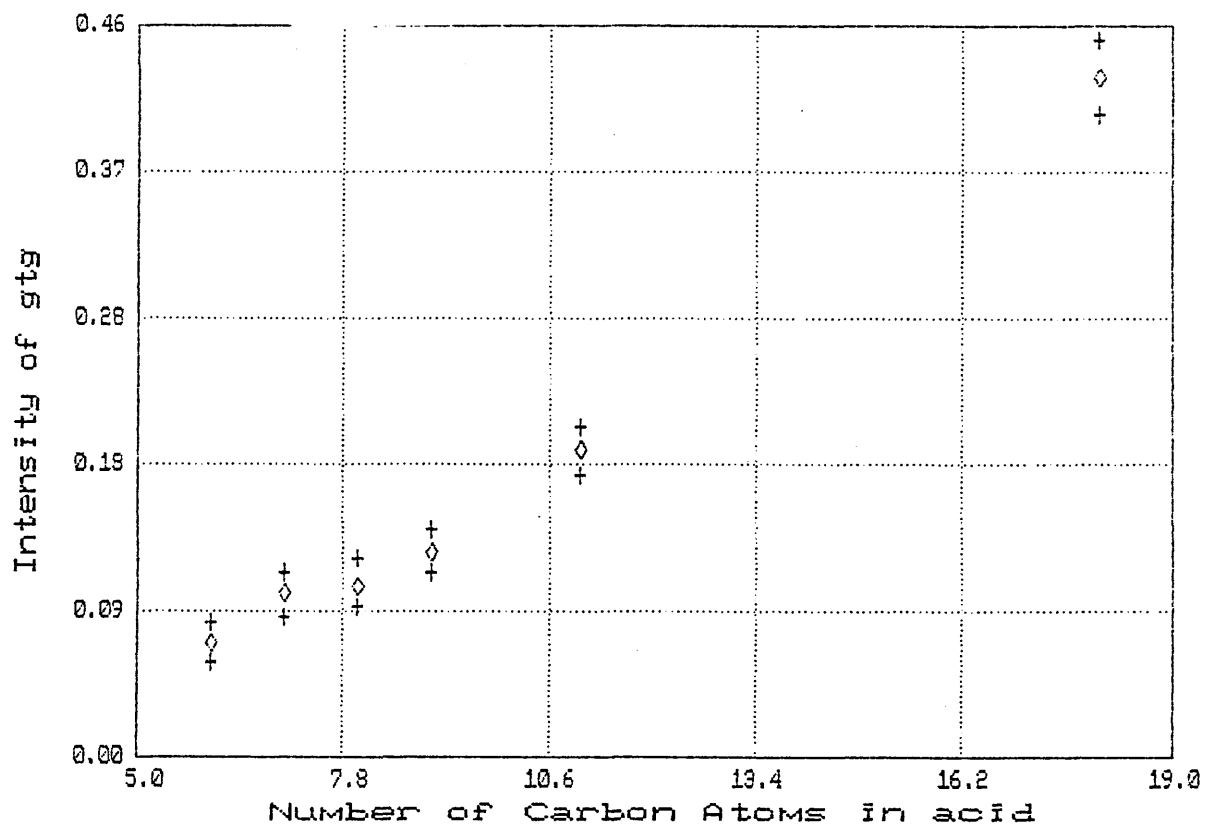
Figure 6.5 shows the variation in the intensity of the 1369 cm^{-1} defect band with number of carbon atoms N_c . The intensity of the methyl group was used to normalise the intensity of the gtg band. The figure shows that the intensity of the 1369 cm^{-1} gtg/gtg' defect band increases linearly with increasing number of carbon atoms N_c . The intercept on the N_c axis is at $N_c \approx 4.2$, while the rotational isomeric state model predicts an intercept of $N_c = 4.58$ (see section 4.1.2). The number of gtg/gtg' defects determined from figure 6.5 using a value for the constant, K_{gtg} , of 3.27 (see section 5.3.2) for $N_c = 18$, is $n_{gtg} = 1.44$ defect per molecule, while the rotational isomeric state model predicts a $n_{gtg} = 1.54$ defects per molecule.

Within the range of experimental error, these results show that the rotational isomeric state model is a good description for these molecules in liquid state.

6.3 Cadmium stearate

The additional band present in the defect region of lithium phenyl stearate at 1363 cm^{-1} , has previously been shown not to be as a result of a weak phenyl vibration (section 6.1.2), or of the phenyl group effectively decoupling the aliphatic backbone into two smaller chains (section 6.1.1). The presence of the additional band in phenyl stearic acid seems to indicate a strained gtg conformation, but to confirm that the band is not simply a result of the phase involved, a molecule that forms a reverse

Figure 6.5 Variation of the 1369 cm^{-1} gtg/gtg' defect band normalised with the 1377 cm^{-1} methyl band v the number of carbon atoms in the n-fatty acid chain.



hexagonal phase at a relatively low temperature is required.

Cadmium stearate was observed by Hattiangdi et al (5), using DTA, to begin changing phase from crystalline solid to a mesophase at about 85⁰C. The mesophase formed was shown by Spegt and Skoulios (6) to be a reverse hexagonal phase, having a lattice parameter, *a*, of 36.9Å.

6.3.1 Preparation

Cadmium stearate was prepared by titrating an ethanolic solution of stearic acid (BDH Chemical, specially pure with minimum assay of 99%) with a 50% aqueous/ethanol solution of sodium hydroxide to a phenolphthalein end point, at 60⁰C. The sodium stearate was reheated to 60⁰C (to keep the stearic acid and sodium stearate in solution) and cadmium chloride added (7). This precipitates cadmium stearate, which was filtered and washed with water, ethanol and acetone all at about 60⁰C. This helps to remove any excess sodium stearate, stearic acid and cadmium chloride. The sample was then dried under vacuum at 75⁰C over P₂O₅ for several hours to remove excess water.

The purity of the sample was checked using elemental micro analysis (MEDEC LTD. Brunel University, Uxbridge), which gives percentages of carbon and hydrogen of 62.60% and 10.31% respectively. The expected percentages of carbon and hydrogen are 63.35% and 10.39% respectively. If we assume that water is the only contamination, then the variation in the carbon concentration will give a measure of the purity, and this leads to a value of 98.3% cadmium stearate in the sample.

For an infrared sample a 0.5% w/w solution of cadmium

stearate with toluene was prepared. The mixture was heated up to about 85°C (beginning of the phase transition see section 7.1.2) to dissolve the cadmium stearate. On cooling, the solution becomes a gel, which was then cast onto a sodium chloride plate and dried to a constant weight.

6.3.2 Crystalline phase

Cadmium stearate in its crystalline phase (below 85°C) shows some interesting vibrational features. Figure 6.6 shows the CH₂ wagging region of the cadmium stearate spectrum at room temperature. Here can be seen a progression of bands, from 1187.2 to 1332.9 cm⁻¹, which are present only in the crystal form of n-carboxylic acids and their soaps (8). The number of peaks present in the progression is determined by the chain length (9): for n-fatty acids and n-fatty acid salts with even numbers of carbon atoms there are $\frac{N_c}{2}$ peaks and for odd numbers of carbon atoms there are $\frac{N_c+1}{2}$ peaks, where N_c is the number of carbon atoms.

Figure 6.7 shows the CH₂ wagging region of the cadmium stearate 120°C (above the phase transition to reverse hexagonal phase). As can be seen from figure 6.7, once the soap changes phase, the CH₂ wagging progression disappears. This makes these bands a useful tool in observing the phase transition. Figure 6.8 shows the change in intensity of the CH₂ wagging band at 1187 cm⁻¹ with change in temperature.

Figure 6.6 The CH_2 wagging region of the infrared spectrum of cadmium stearate at 25°C .

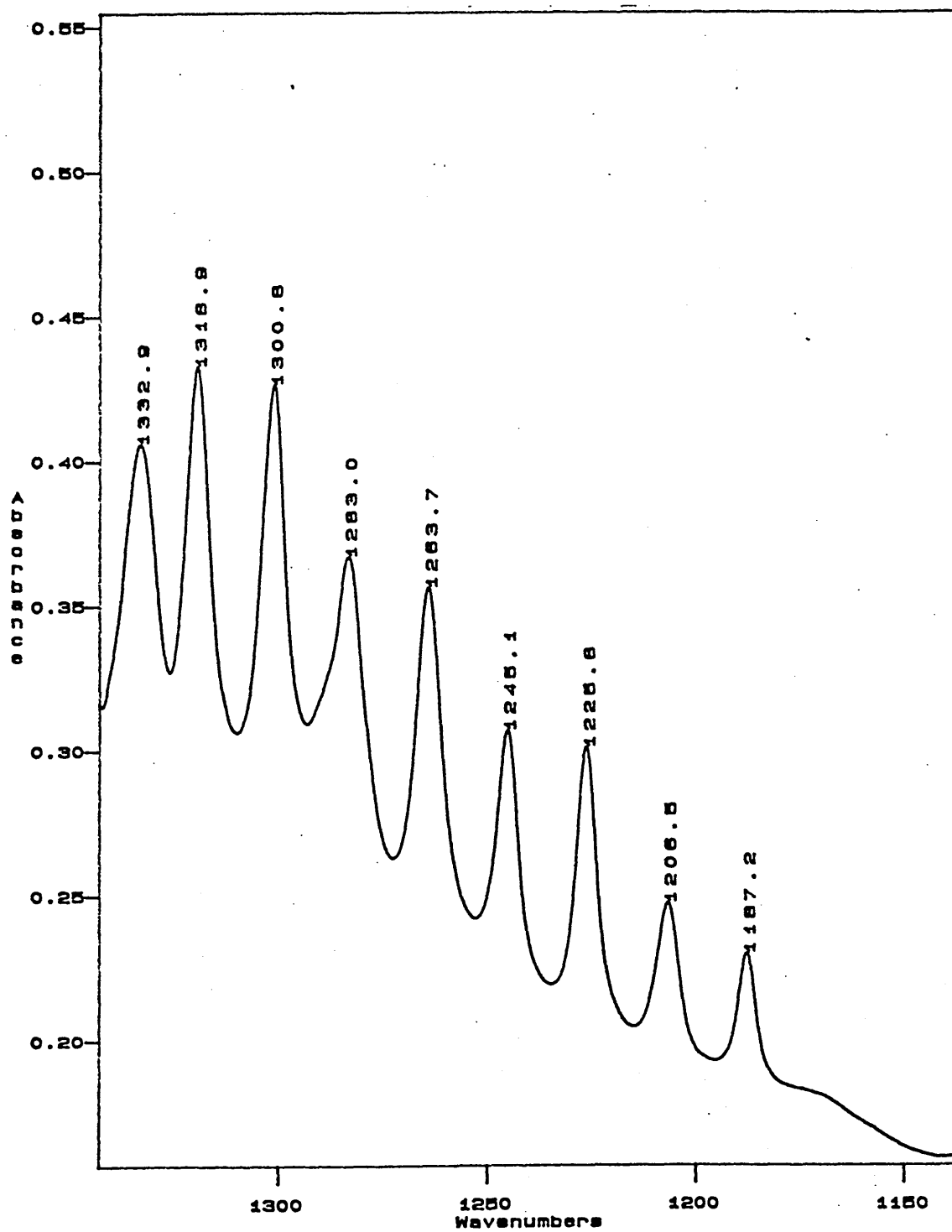


Figure 6.7 The CH_2 wagging region of the infrared spectrum of cadmium stearate at 120°C .

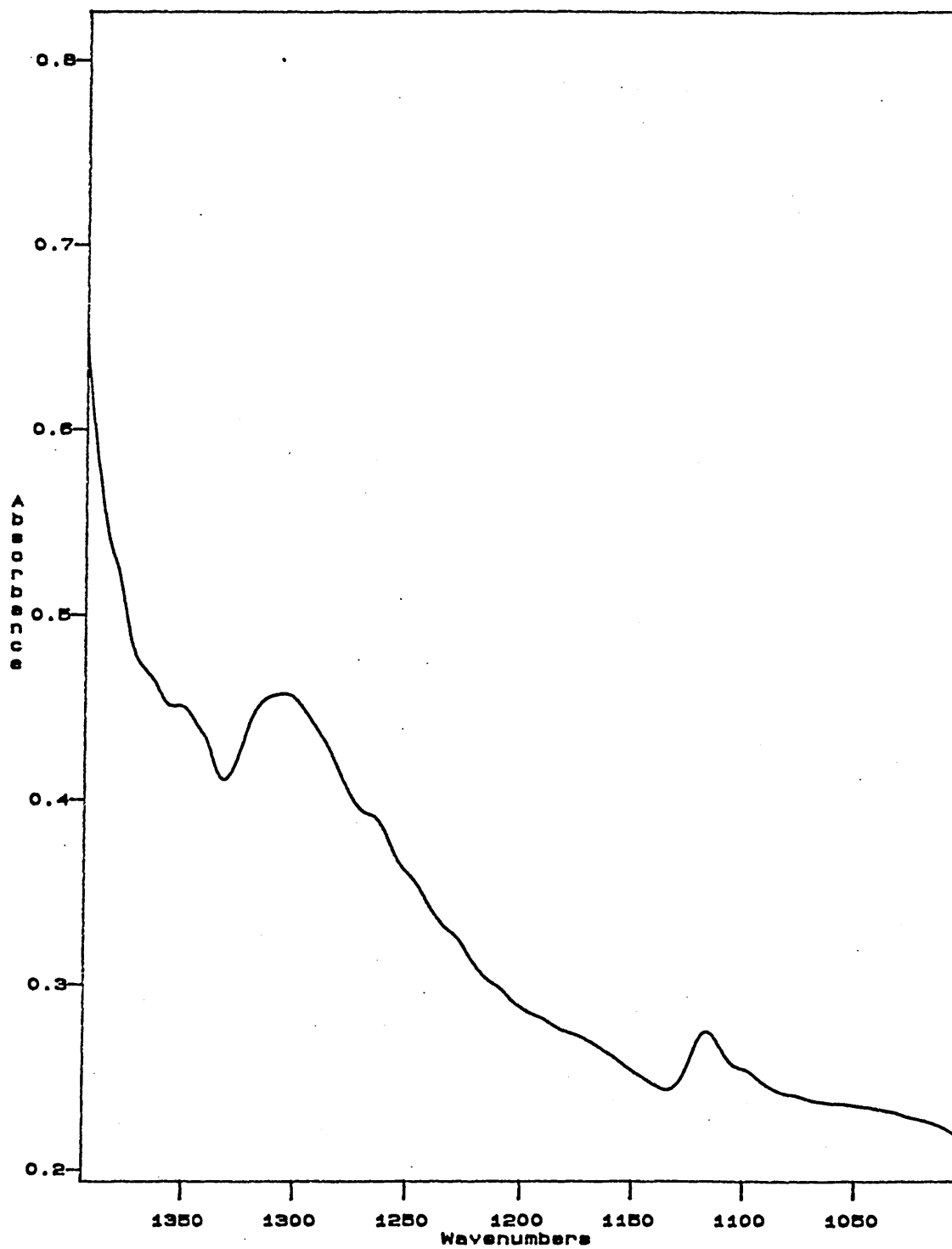
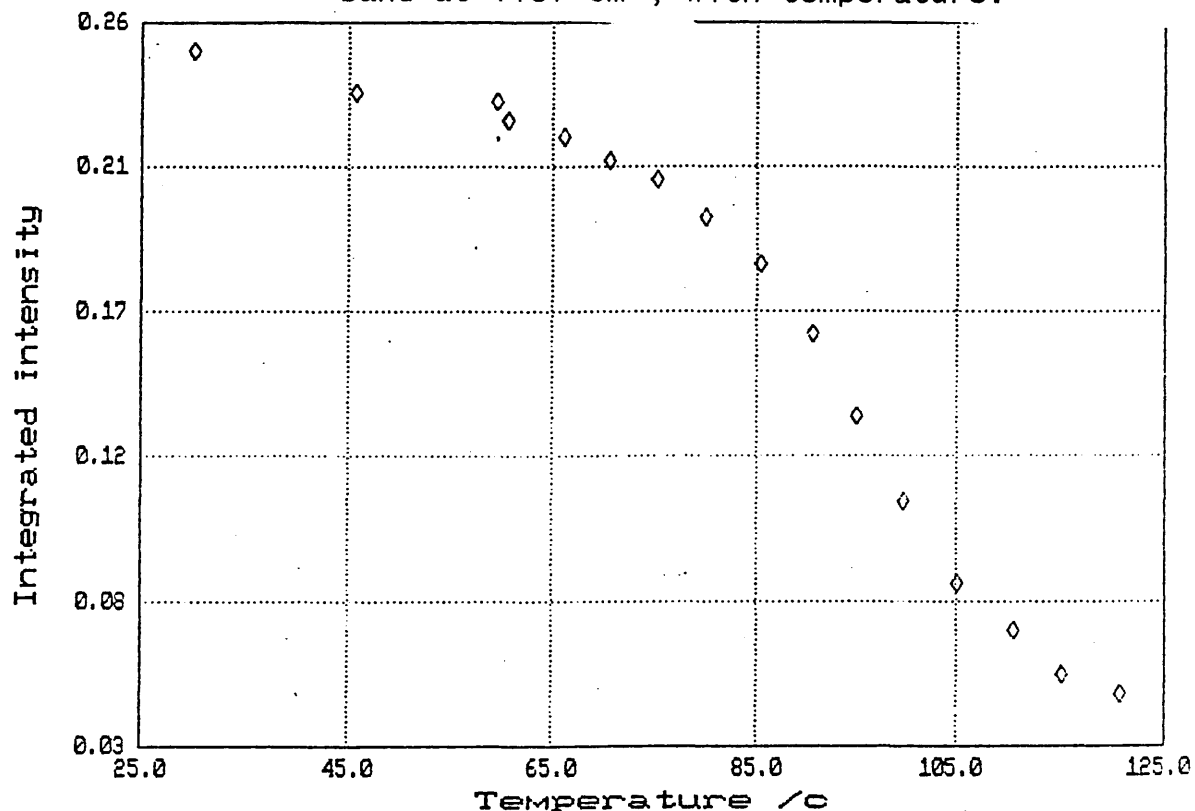


Figure 6.8 The variation of the CH₂ wagging progression band at 1187 cm⁻¹, with temperature.



The intensity decreases linearly from 25°C to 70°C, at which point the intensity begins to decrease more rapidly with a maximum rate of change occurring at about 90°C. The change in intensity then begins to slow down and the transition is completed by about 115°C.

The 720 cm⁻¹ CH₂ rocking vibration is another interesting band. Figure 6.9 shows that the band splits into several components as a result of crystalline interactions. The band at 730 cm⁻¹ is usually associated with an orthorhombic crystal lattice (10). The bands at 711 and 703 cm⁻¹ show that there could be additional crystal forms present (possibly monoclinic, see section 7.4). On going through the phase transition the bands of crystalline origin disappear leaving only the 720 cm⁻¹ CH₂ rocking vibration (see figure 6.10).

Figure 6.9 The CH_2 rocking region of the infrared spectrum of cadmium stearate at 25°C .

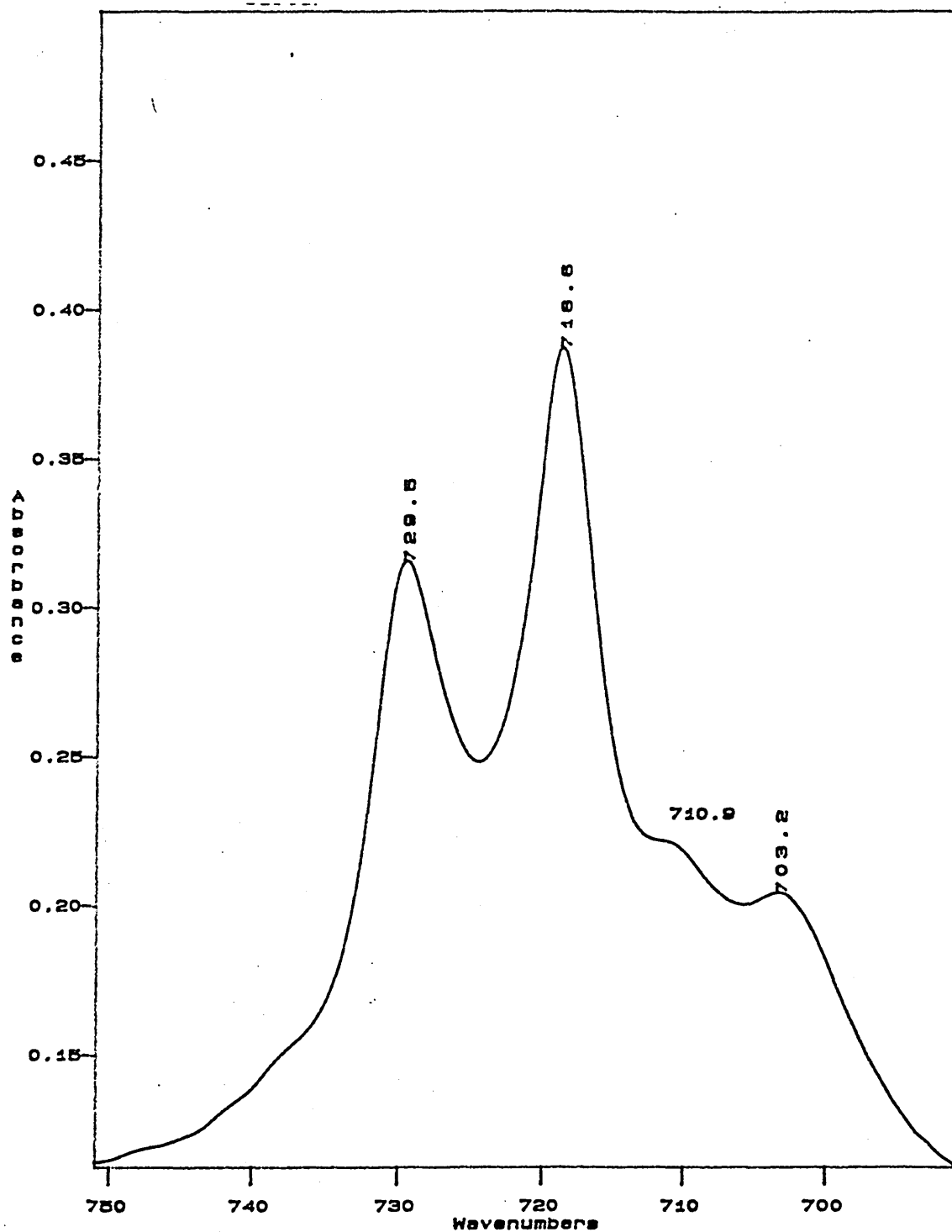
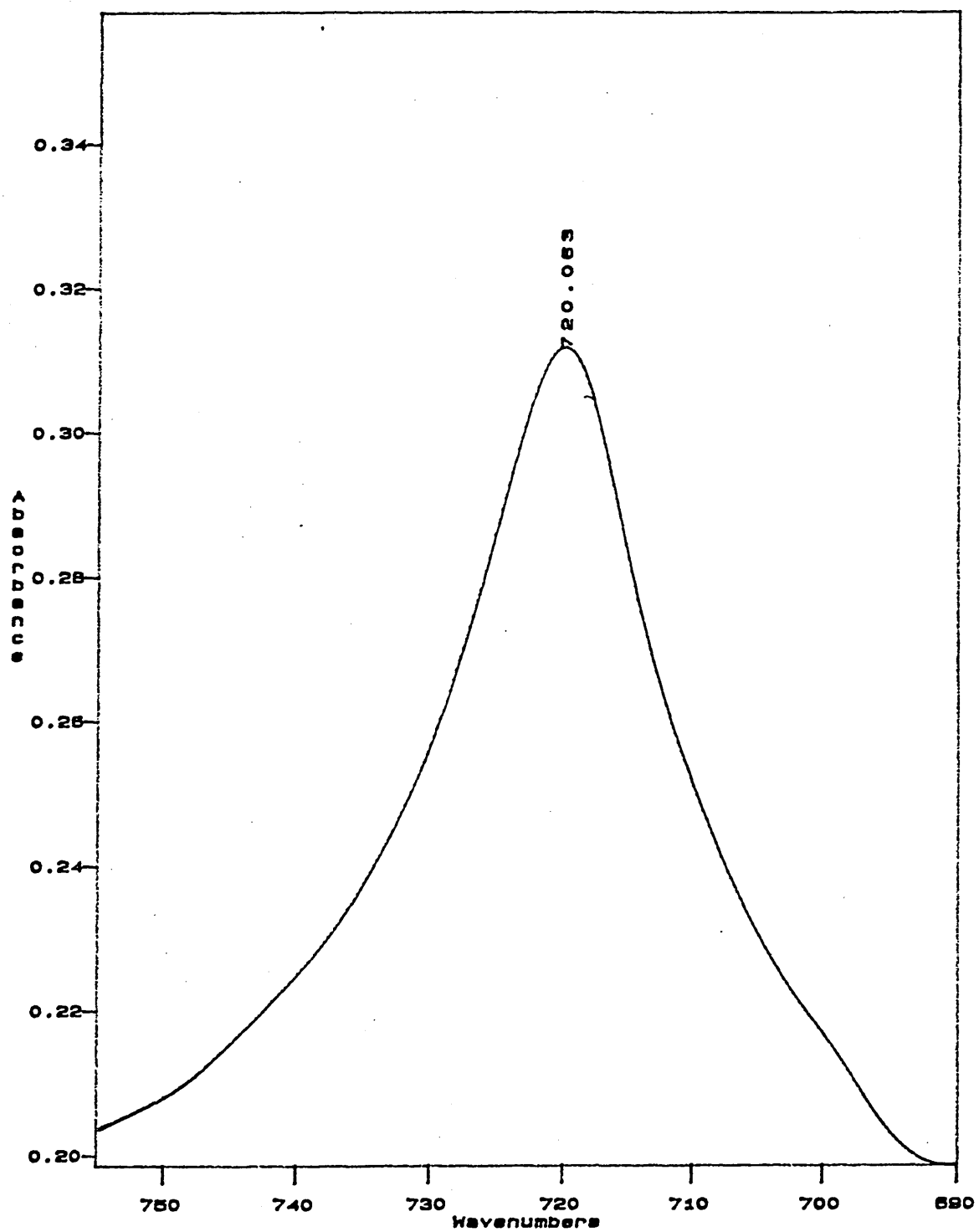


Figure 6.9 The CH_2 rocking region of the infrared spectrum of cadmium stearate at 120°C .



6.3.3 Reverse hexagonal phase

Figure 6.11 shows the CH₂ wagging region of the cadmium stearate infrared spectrum at 120°C. Both the gtg/gtg' and gg/g'g' modes at 1369 cm⁻¹ and 1352 cm⁻¹ respectively are present, indicating a certain amount of disorder. The 1369 cm⁻¹ gtg/gtg' defect does not have an additional shoulder at 1363 cm⁻¹ (as is the case with LiPS), so this additional band is not simply a consequence of the reverse hexagonal phase.

Figure 6.12 shows the defect region of cadmium stearate with the background subtracted. The background was approximated by a series of straight lines, leaving just the methyl, gtg and gg bands present. Again, as with LiPS, this shows up the required peak positions much better, and it also shows that there is no additional band present as a shoulder to the 1369 cm⁻¹ gtg/gtg' defect mode. The integrated intensity was determined the same way as LiPS (see section 5.3.1 and section 8.1) by fitting a background and several bands to the 1377 cm⁻¹ methyl vibration, and subtracting this from the original. The intensities of the 1369 cm⁻¹ and 1352 cm⁻¹ bands can be determined directly from the subtracted spectrum. The integrated intensities of these bands are:-

Vibration	Frequency /cm ⁻¹	Integrated Intensity	
Methyl CH ₃ U	1377	0.038	
CH ₂ wagging	gtg/gtg'	1368	0.019
	gg/g'g'	1351	0.012

Figure 6.11 The CH_2 wagging region of the infrared spectrum of cadmium stearate at 120°C .

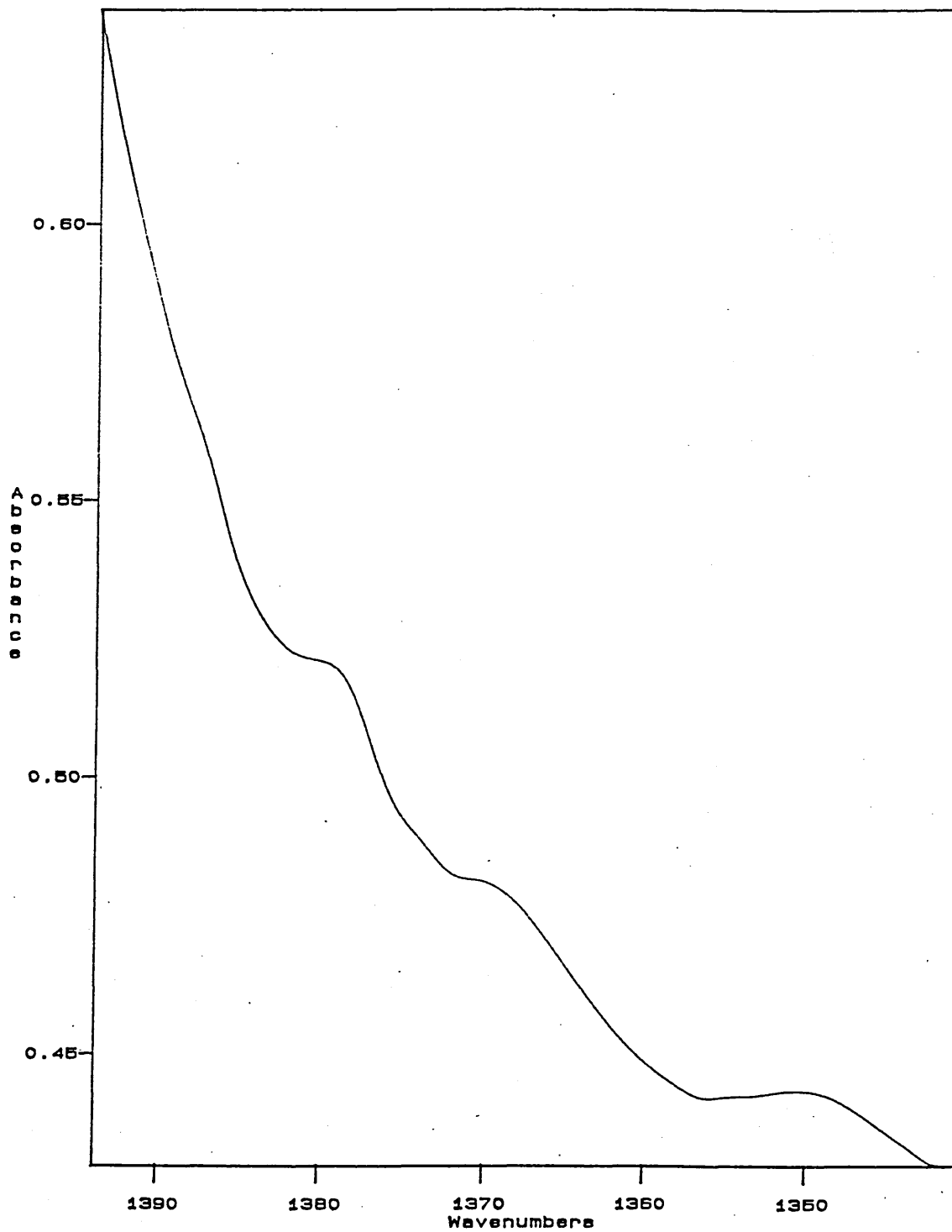
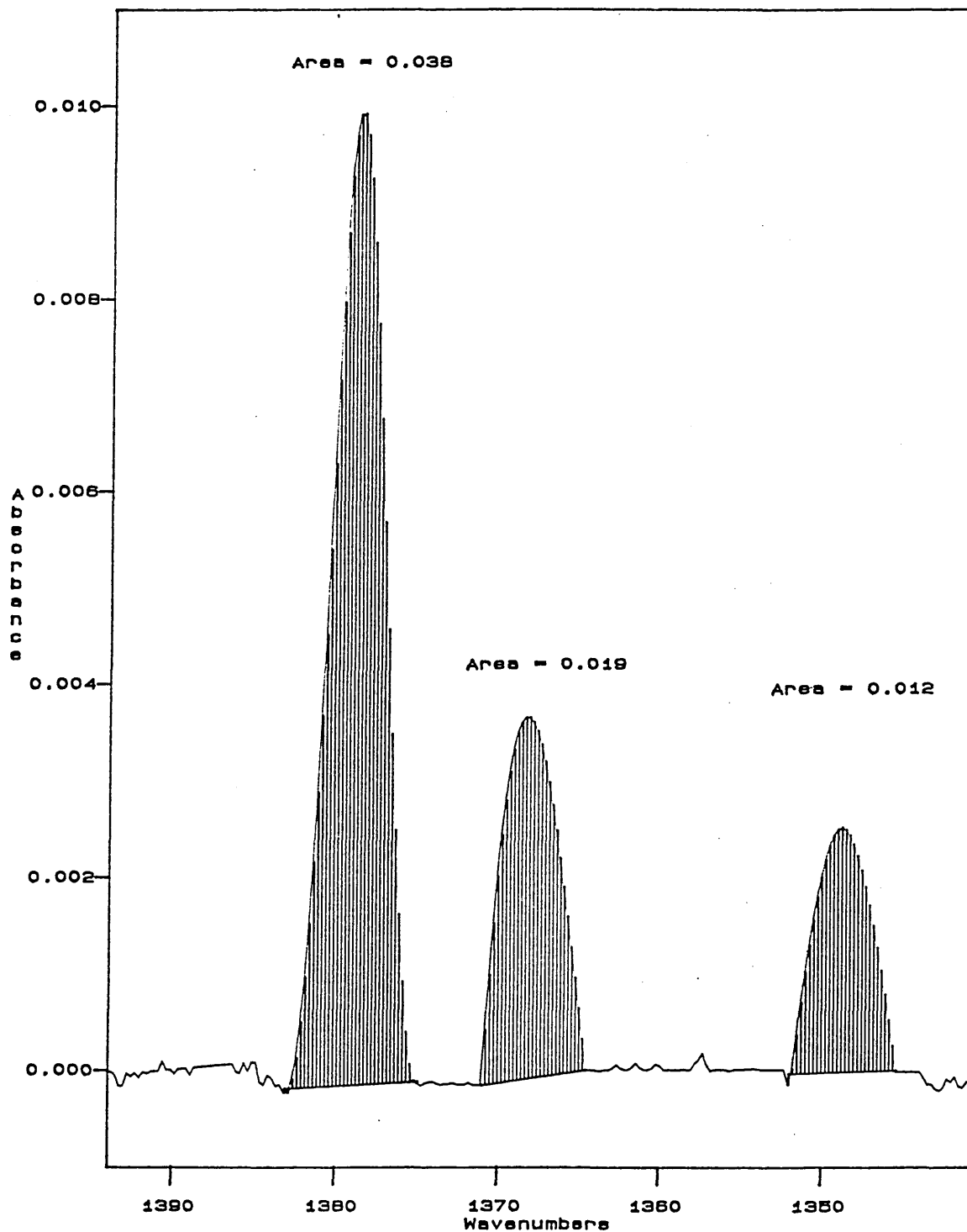


Figure 6.12 The CH_2 wagging region of the infrared spectrum of cadmium stearate at 120°C with the background subtracted, the background being approximated by a series of straight lines.



Using the value for K_{gtg} and K_{gg} determined in section 5.3.2, the numbers of defects present in cadmium stearate at 120°C are:-

$$n_{gtg} = 1.66 \pm 0.15$$

$$n_{gg} = 1.64 \pm 0.17$$

Values expected for n_{gtg} and n_{gg} from an isotropic chain at 120°C, calculated from the rotational isomeric state model, are:-

$$n_{gtg} = 1.79$$

$$n_{gg} = 1.74$$

Within experimental errors, these defect concentrations agree with those for an isotropic liquid. The number of defects present corresponds to an average chain extension of 9.5Å (see section 4.1.4). The core radius, as determined in section 4.2.1, is 4.9 to 6.32Å, giving cylinder dimensions between 28.8Å and 31.7Å. The hexagonal lattice parameter, a , determined by Spegt (6) for cadmium stearate is 36.9Å. This appears to leave a gap of about 5Å between adjacent cylinders.

From the calculation of R , the chain extension (see section 4.1.4), the probability of the chain extending beyond the average chain extension, R_{av} , of 9.5Å is 0.40. Also the probability of the chain extending out to come into contact with the neighbouring cylinder ($R=12.13Å$) is 0.22. This shows that although the average dimensions of the cylinders do not come into contact, a significant proportion of chains from neighbouring cylinders are in contact.

There is a possibility that either the model for calculating the core radius of the divalent metal soaps is in

error (see section 4.2.1) or that the value of n , the number of ions per unit length, estimated by Spegt (6) is incorrect. The value of R_c estimated by Small (11), for cadmium stearate from the data of Spegt (6) is $\approx 8.5\text{\AA}$. This would give a hexagonal cylinder diameter of 36\AA , using the value of $R_{av} = 9.5\text{\AA}$ calculated above. This is comparable with the value of a , the hexagonal lattice parameter ($a=36.9\text{\AA}$) by Spegt (6).

One problem with the model proposed in section 4.2.1 is that it assumes that the two stearate ions associated with each cadmium ion behave independently, i.e. one cadmium stearate soap molecule behaves like two independent monovalent soap molecules. This may not in fact be the case. The two stearate ions in each cadmium stearate molecule may pack closer than expected for monovalent soap, so additional assumptions would have to be made to correct the model for divalent soaps.

6.4 References

- 1) M. Maroncelli, S.P. Qi, H.L. Strauss and R.G. Snyder, J. Am. Chem. Soc. 104, 6237, 1982
- 2) P.J. Flory, "Statistical mechanics of chain molecules", Interscience, New York, 1969
- 3) W.J. Harrison, PhD. Thesis, Sheffield City Polytechnic, 1987
- 4) S.J. Spells, S.J. Organ, A. Keller and G. Zerbi, Polymer 28, 697, 1987
- 5) G.S. Hattiangdi, M.J. Vold and R.D. Vold, Ind. Eng. Chem. 41, 2320, 1949
- 6) P.A. Spegt and A.E. Skoulios, Acta Cryst. 16, 301, 1963
- 7) R.D. Vold, G.S. Hattiangdi and M.J. Vold, Ind. Eng. Chem. 41, 2311, 1949
- 8) G. Zerbi, G. Conti, G. Minoni, S. Pison and A. Bigotto, J. Phys. Chem. 91, 2386, 1987
- 9) R.A. Meiklejohn, R.J. Mayer and R.G. Sinclair, Anal. Chem. 29, 329, 1957
- 10) D. Chapman "The structure of lipids", Methuen, London, 1965
- 11) D.M. Small, "Handbook of lipid research 4, The physical chemistry of lipids", Plenum Press, New York, 1986

Chapter 7

7 Other techniques	171
7.1 D.S.C.	171
7.1.1 Lithium phenyl stearate	171
7.1.2 Cadmium Stearate	173
7.2 Low frequency Raman spectroscopy	173
7.2.1 Lithium phenyl stearate	173
7.2.2 Cadmium Stearate	176
7.3 Nuclear magnetic resonance	179
7.4 X-ray crystallography	184
7.5 References	187

7 Other techniques

As well as infrared spectroscopy, several other techniques have been used to investigate the structure and phase behaviour of lithium phenyl stearate and cadmium stearate.

7.1 D.S.C.

All D.S.C measurements were carried out on a Mettler DSC-30 unit under nitrogen atmosphere and the heating rate was $5^{\circ}\text{C min}^{-1}$.

7.1.1 Lithium phenyl stearate

Figure 7.1 shows the D.S.C. trace of lithium phenyl stearate from 0°C to 400°C . There are three phase transitions which were assigned by Harrison et al (1) to:-

	152.8 ⁰ C		226.8 ⁰ C		371.1 ⁰ C	
				Liquid		
Reverse (H ₁)	---->	Reverse (H ₂)	---->	Crystalline	---->	Isotropic
Hexagonal		Hexagonal		Hexagonal		melt
				focal conic		

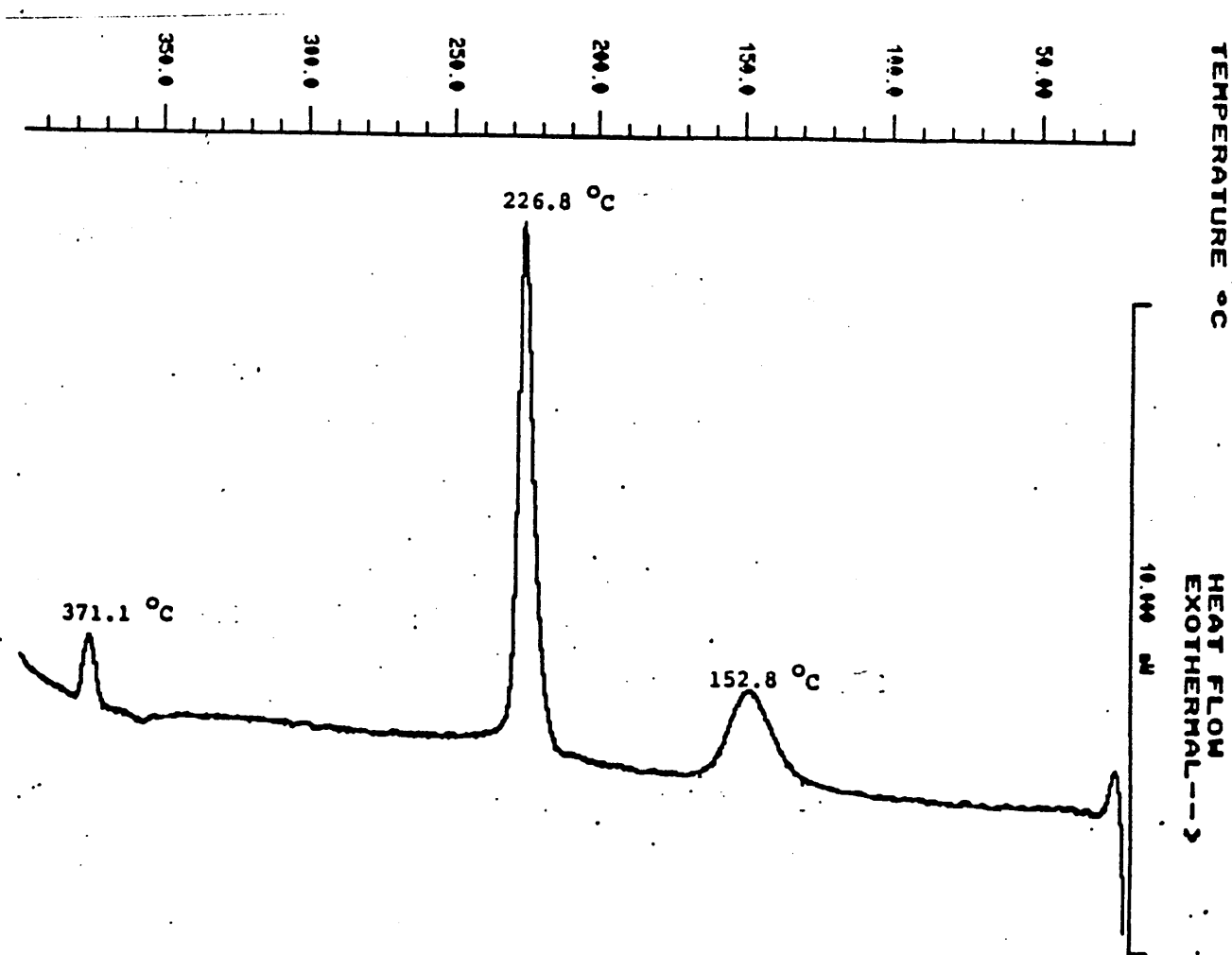
Temperatures shown are taken at the peak heat flow.

The transition being considered in the present study is from H₁ to H₂. In addition to the D.S.C. scan of the bulk sample as produced in section 5.2.1, another D.S.C. scan was taken of a sample of LiPS that had been dissolved in toluene and then solvent cast. A comparison was then made to find the effect, if any, of solvent casting on the phase transition enthalpy and temperature. Table 7.1 shows the transition temperature and enthalpy for both samples and as can be seen there is little or no change in the transition temperature and enthalpy, so we can conclude that the solvent casting has little or no effect the phase of LiPS.

Table 7.1 Transition temperatures and enthalpies of bulk LiPS and LiPS which has been solvent cast.

	LiPS /Standard	LiPS /Solvent cast
Temperature °C	152.0	150.5
Energy /kJ mol ⁻¹	5.9±0.5	5.7±0.5

Figure 7.1 D.S.C. trace of lithium phenyl stearate for 0 to 400°C.



7.1.2 Cadmium Stearate

Figure 7.2 shows the D.S.C trace of cadmium stearate. As can be seen there are two peaks, one at 105⁰C and the other at 112⁰C, which would probably indicate two crystal phases present. Spegt and Skoulios (2) only observed one phase transition when investigating the effect of temperature on the long spacing of cadmium stearate, but Hattiangdi et al (3) observed many peaks in the differential heating curve (not D.S.C.) of cadmium stearate, at 82, 107, 117, 128 and 150⁰C. The peak at 82⁰C is the start of the phase transition and is at a similar temperature to the start of the phase transition observed in figure 7.2, which is at 87⁰C. The differential heating peaks at 107 and 117⁰C are also at similar temperatures to those observed in figure 7.2. The peaks observed by Hattiangdi (3) at 128⁰C and 150⁰C have no corresponding peaks in figure 7.2: in fact in figure 7.2 the phase transition of cadmium stearate is complete by 120⁰C. The peaks observed by Hattiangdi may be due to impurities, but they could also be due to differences in the technique used to examine the samples.

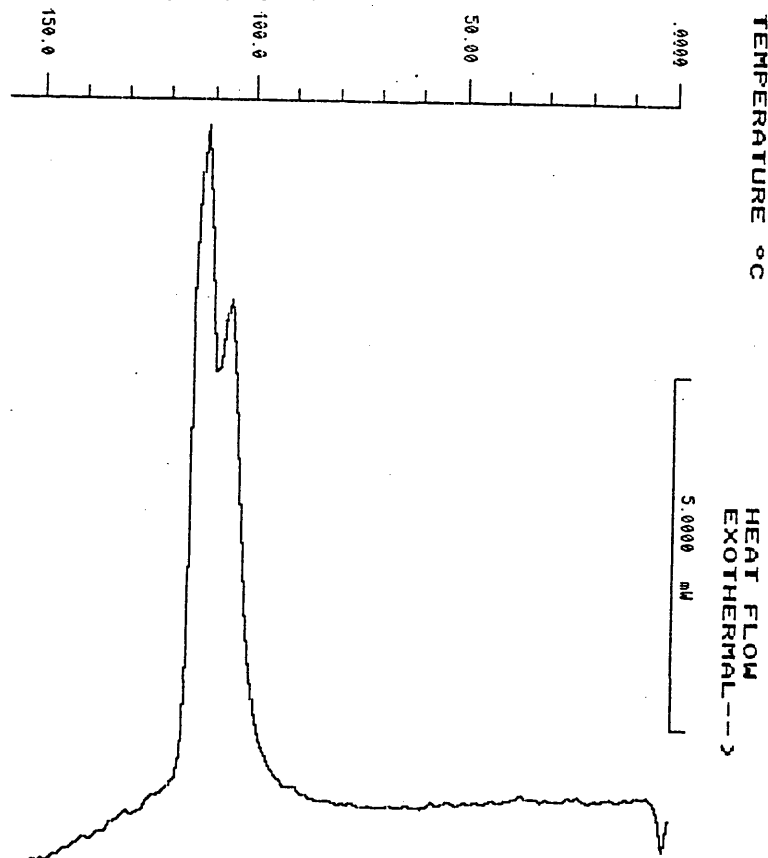
7.2 Low frequency Raman spectroscopy

All measurements were taken on a Spex laser Raman spectrometer with triple gratings. All the measurements were taken at 4 cm⁻¹ spectral bandwidth.

7.2.1 Lithium phenyl stearate

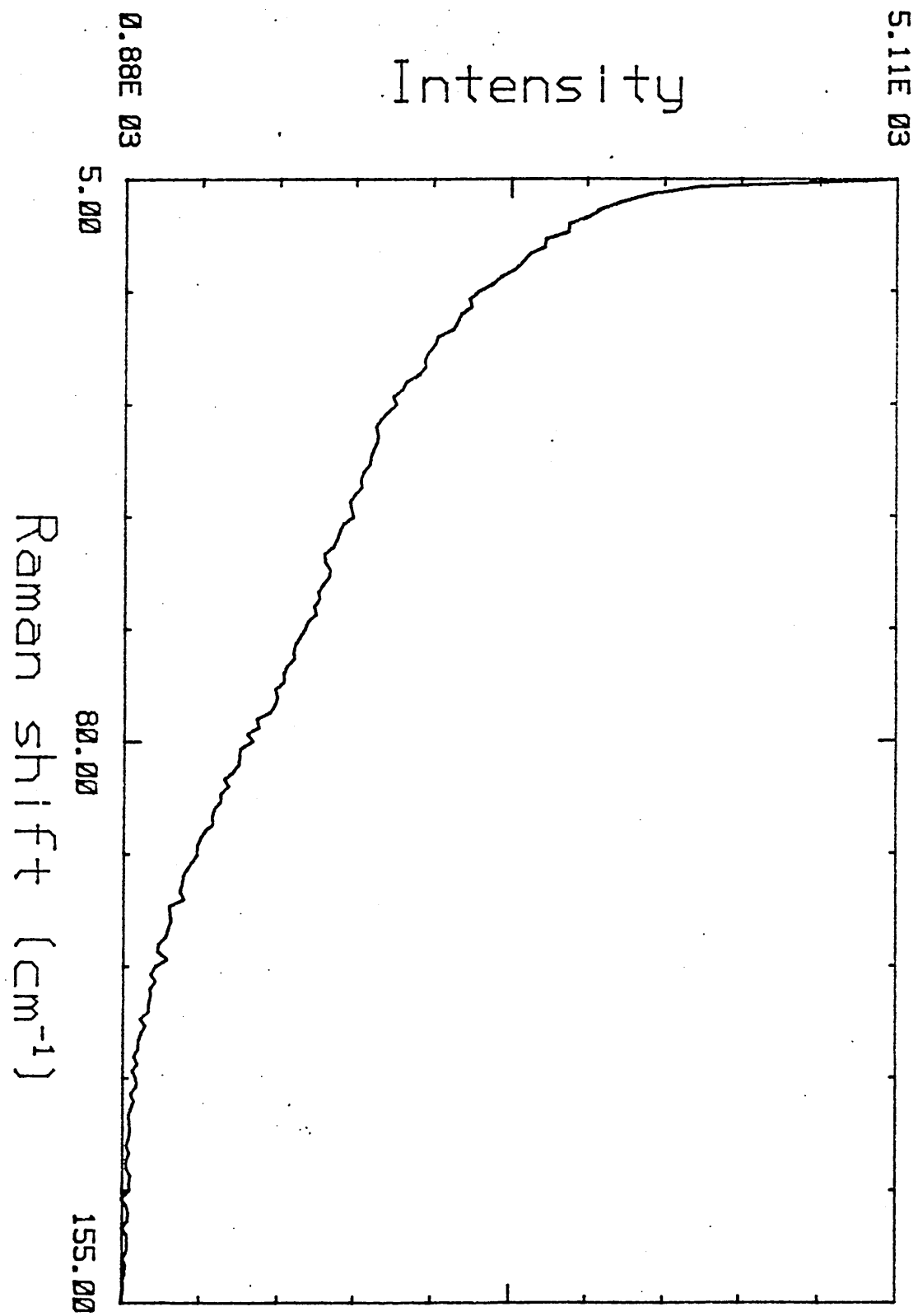
Figure 7.3 shows the low frequency Raman spectrum of lithium phenyl stearate, and present in this spectrum is a rather broad band at ≈ 65 cm⁻¹, having a bandwidth (full width at half height) of 47cm⁻¹. Spells and Shepherd (4,5) found a

Figure 7.2 D.S.C. trace of cadmium stearate taken from 0 to 150°C.



band of similar width at a similar position in the polystyrene Raman spectrum to be a phenyl torsional mode coupled to a CH₂ backbone mode. A comparison of the results obtained by Spells (4,5) for atactic and partially crystalline isotactic polystyrene with LiPS (see table 7.2) for the low frequency Raman phenyl torsional mode shows that the bandwidths for amorphous atactic polystyrene and for LiPS are of a similar magnitude. The phenyl groups in the atactic polystyrene are completely disordered in terms of translational or rotational register. The similarity between LiPS and atactic polystyrene shows that the phenyl ring in LiPS are very disordered, but the fact that the LiPS bandwidth is slightly smaller may be evidence of a slightly more regular phenyl group conformation in LiPS. The number of

Figure 7.3 The low frequency Raman spectrum of lithium phenyl stearate.



isomers present in LiPS may account for much of the disorder of the phenyl group. It is possible that this does not allow any translational ordering, but permits some rotational alignment, giving some regularity to the phenyl conformations.

Table 7.2 Bandwidths and frequencies of the low frequency Raman phenyl torsional mode of LiPS, atactic and isotactic polystyrene (4,5).

	Frequency /cm ⁻¹	Bandwidth /cm ⁻¹
LiPS	65	47
Atactic	63	63
Isotactic	56	15

7.2.2 Cadmium Stearate

The variation of n-paraffin LAM vibrational frequency with chain length has been well established (see section 3.3.1) (6). Figure 7.4 shows the LAM 1 mode of cadmium stearate but two peaks are present instead of the one expected. This splitting is also present in the LAM 3 mode (see figure 7.5). This would seem to indicate two structures with different chain lengths, densities or Young's moduli present in the sample. There are two possible reasons for the additional peaks:-

- i) Impurities in the sample giving rise to the two peaks.
- ii) Different crystal forms present in the sample.

The peaks are of similar intensity, which would indicate an approximate 50% proportion of impurity, if impurities were the cause of the additional LAM 1 and LAM 3 modes. As can be seen from section 6.3.1 the cadmium stearate sample is 98.35%

Figure 7.4 The low frequency Raman spectrum of cadmium stearate in the region of the LAM 1 mode.

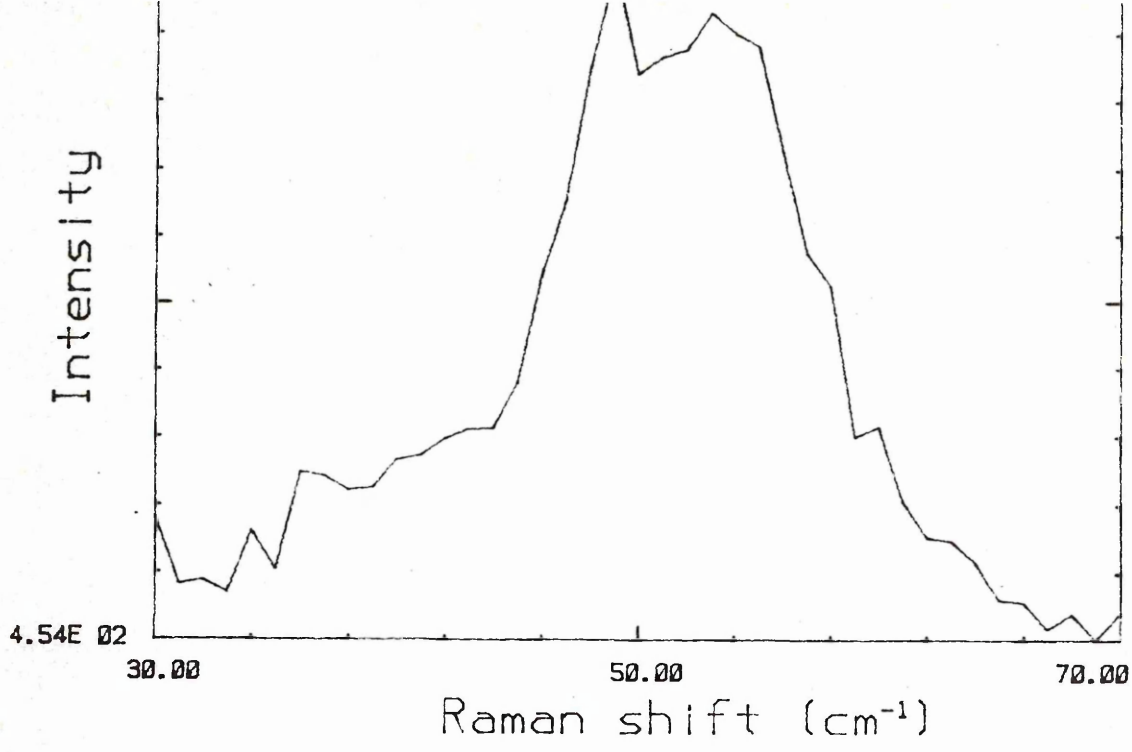
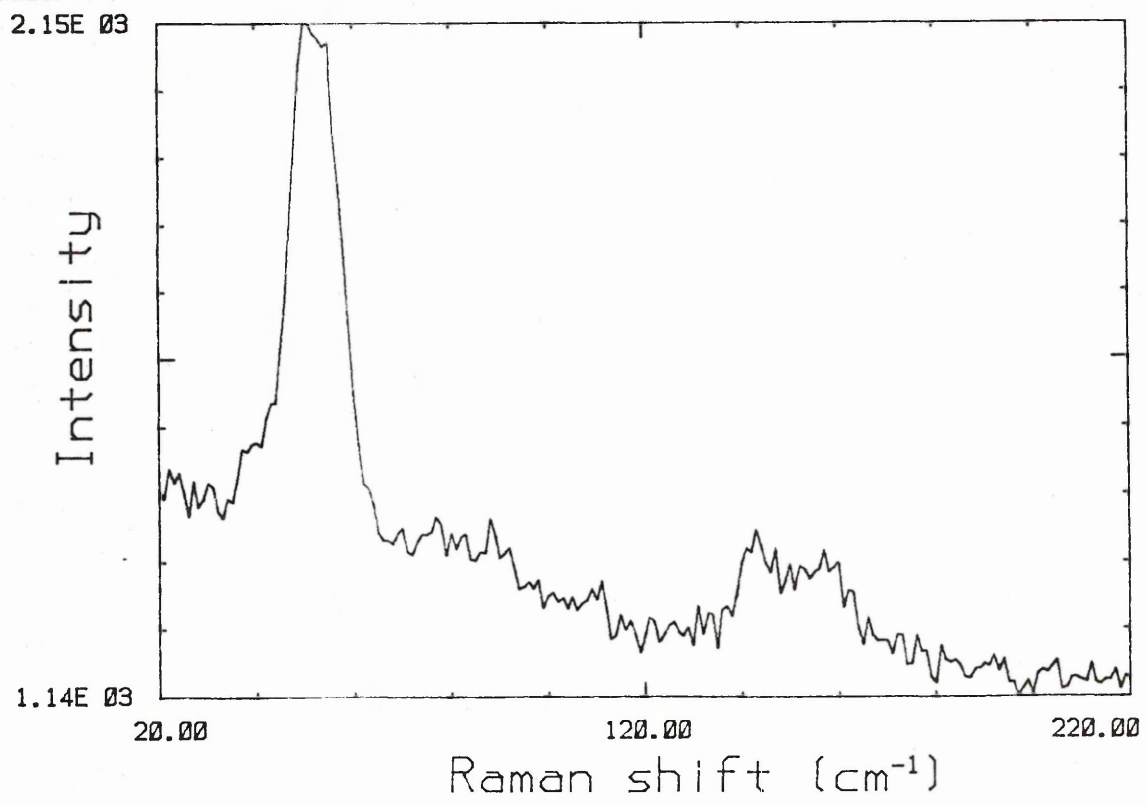


Figure 7.5 The low frequency Raman spectrum of cadmium stearate in the region of the LAM 1 and LAM 3 modes.



pure, so this hypothesis can be rejected. This leaves different crystal forms as the probable cause of the additional Raman LAM 1 and LAM 3 bands.

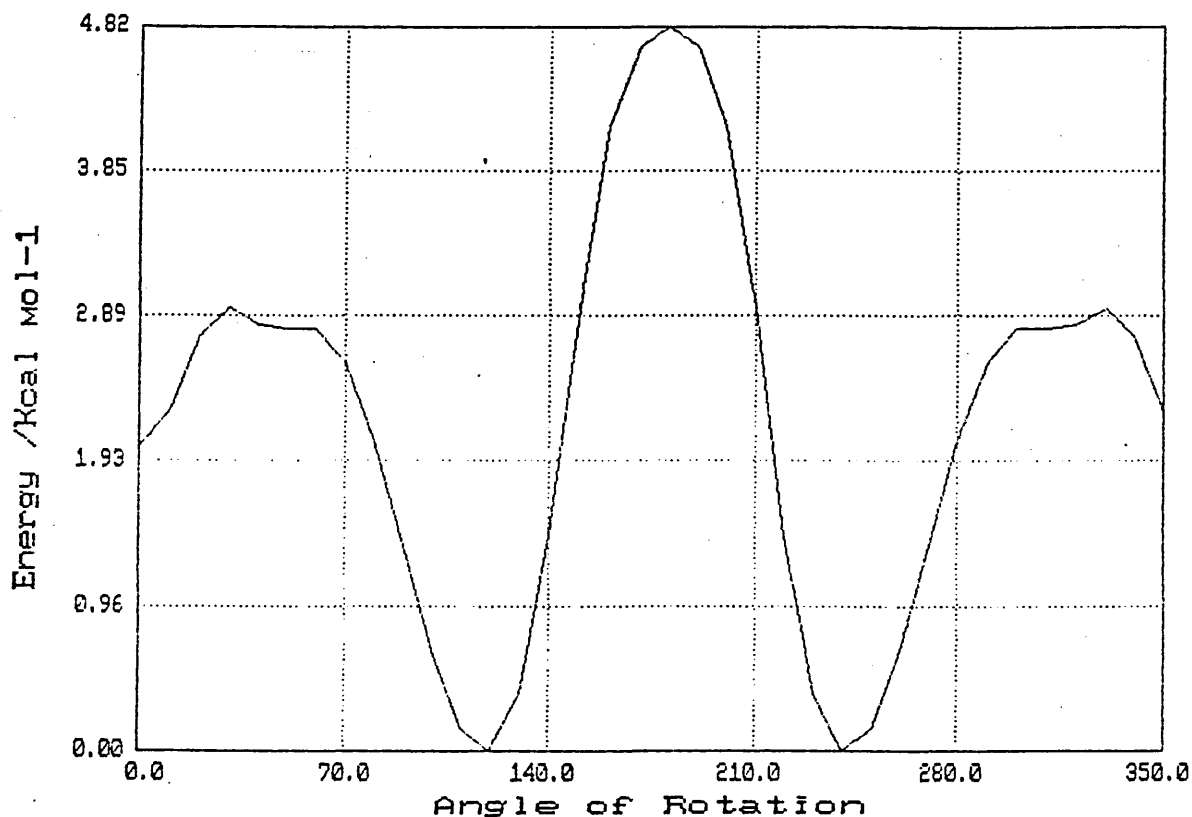
The frequency of the two LAM 1 modes are 49.2 and 54.0 cm^{-1} . The LAM 1 frequencies for the n-alkanes $n\text{-C}_{18}\text{H}_{38}$ and $n\text{-C}_{36}\text{H}_{74}$ are 132.2 and 66.1 cm^{-1} respectively (6). The fact that the frequency of the cadmium stearate LAM 1 mode is close to that for $n\text{-C}_{36}\text{H}_{74}$ indicates that the stearate ions extend almost fully from the cadmium ion in opposite directions. Khoury et al (6) also observed that the LAM 1 frequency observed for $n\text{-C}_{36}\text{H}_{74}$ is 66.1 cm^{-1} for the orthorhombic form, and 68.8 cm^{-1} in the monoclinic form, so that differences in LAM 1 modes of cadmium stearate are possibly due to different crystal forms.

7.3 Nuclear magnetic resonance

Modelling of phenyl stearic acid (see section 4.3.4) showed that the rotation of the phenyl group about the CH_2 backbone is restricted to an arc of maximum angular displacement of $\approx \pm 30^\circ$. If the phenyl group were attached on to the end carbon atom then this would be expected to give an unrestricted rotation. Figure 7.6 shows the variation in conformational energy with angle of rotation of the phenyl group for 1-phenyl heptane, modelled using Moly '86 (see section 4.3 for more details of the model) with the heptane chain fully extended. Using the same criterion as was applied to phenyl stearic acid in section 4.3.4, there is a 99% probability of finding the phenyl group at an angle ϕ (displaced from the 0° position) of $\pm 150^\circ$. This would indicate that 1-phenyl heptane has a less restricted rotation than

phenyl stearic acid. If this is the case it may be possible to observe the difference using proton nuclear magnetic resonance.

Figure 7.6 The variation in conformational energy with angle of rotation of the phenyl group for 1-phenyl heptane.



NMR spectra were taken on a Bruker instrument running at 250MHz. Figures 7.7 and 7.8 show the proton NMR spectra of 1-phenyl heptane and phenyl stearic acid respectively, in the region of the phenyl hydrogen interaction. Table 7.3 shows the total bandwidths of each wing of the phenyl hydrogen interaction (not individual peaks) centred at 7.15 and 7.27 ppm, and also the total bandwidth of the phenyl region. As can be seen from table 7.3 the total bandwidth is larger for phenyl stearic acid than for 1-phenyl heptane. The interaction centred on 7.27 ppm has approximately the same

bandwidth for both phenyl stearic acid and 1-phenyl heptane, but the band centred on 7.15 ppm is much broader for phenyl stearic acid than for 1-phenyl heptane, with individual components in the phenyl stearic acid spectrum broader as well. This could be evidence to show the more restricted phenyl rotation in phenyl stearic acid than in 1-phenyl heptane, but it could also be caused by the different number of isomers present in phenyl stearic acid.

Table 7.3 NMR bandwidths of the phenyl hydrogen interaction for phenyl stearic acid and 1-phenyl heptane.

	Total bandwidth /ppm	Bandwidth of the 7.15 ppm peak /ppm	Bandwidth of the 7.27 ppm peak /ppm
1-phenyl heptane	1.88	0.80	0.80
Phenyl stearic acid	2.28	0.84	1.12

Figure 7.7 NMR spectrum of 1-phenyl heptane in the region of the phenyl hydrogen interaction.

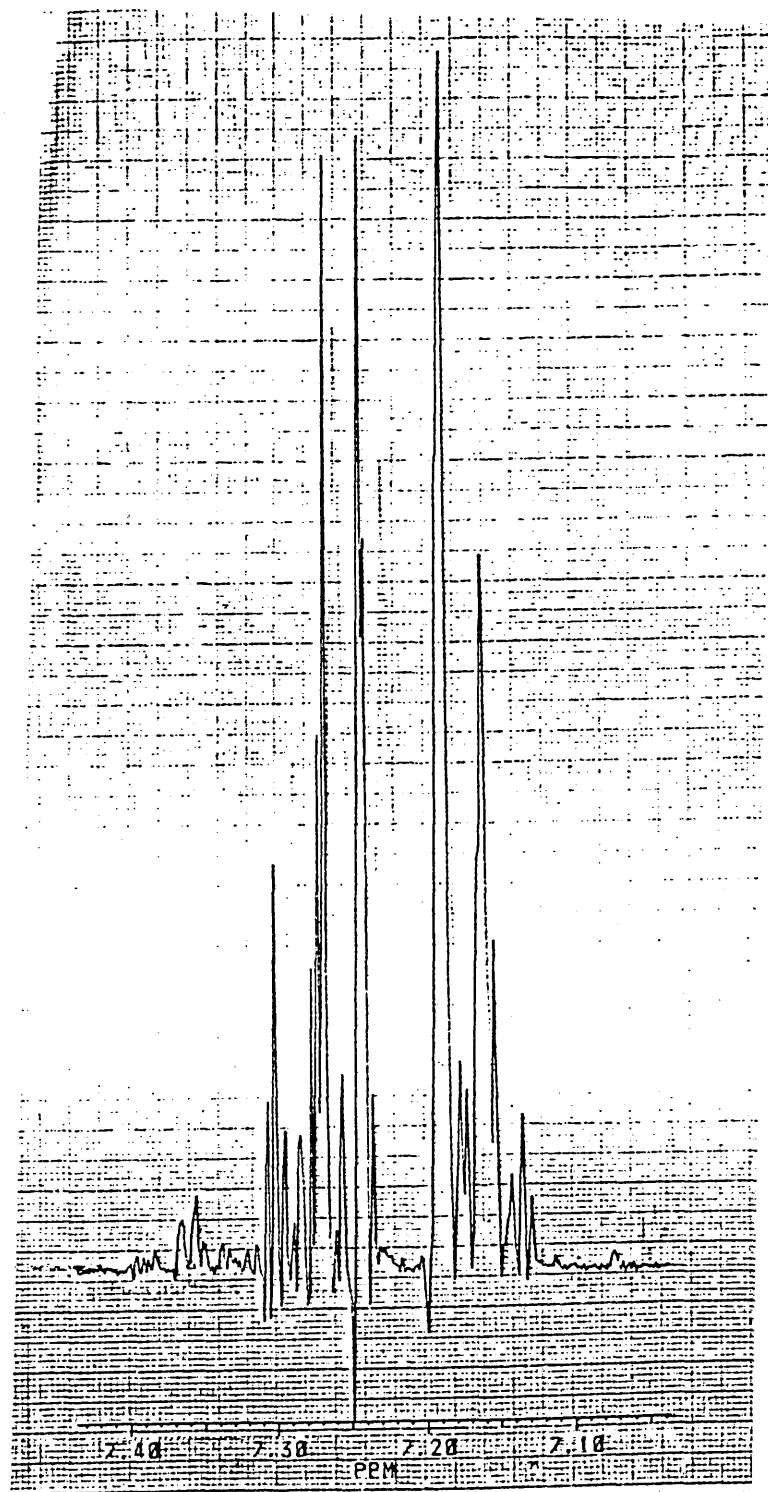
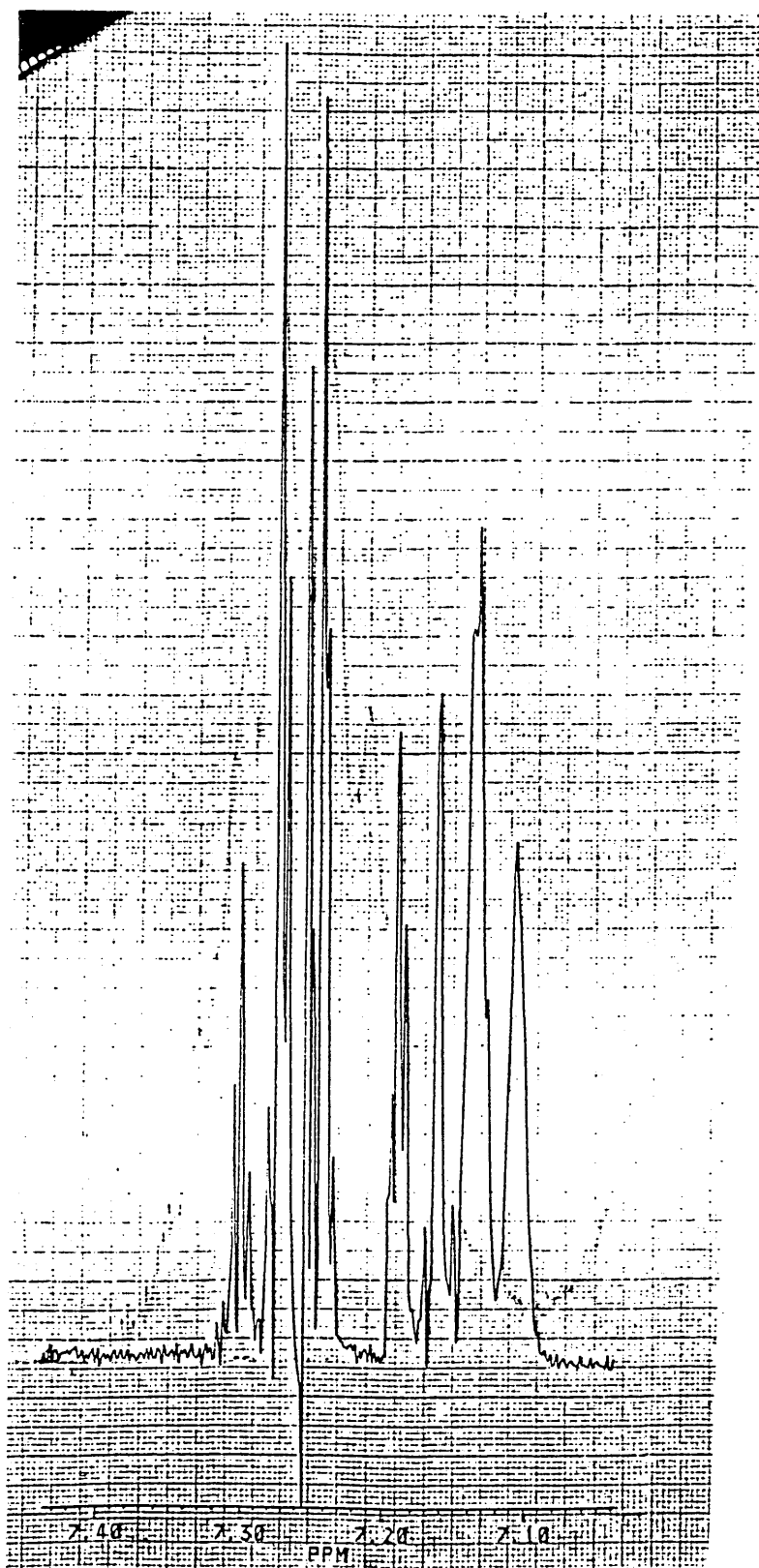


Figure 7.8 NMR spectrum of phenyl stearic acid in the region of the phenyl hydrogen interaction.



7.4 X-ray crystallography

The D.S.C., infrared and low frequency Raman data gathered for cadmium stearate point to the fact that there are two crystal forms present. The infrared results (see section 6.3.2) in the CH₂ rocking region of the spectrum of cadmium stearate show that there is an orthorhombic phase present along with another, possibly monoclinic, phase.

Table 7.4 shows the X-ray diffraction peaks present in cadmium stearate. The data was obtained using a Phillips generator with a Cu K_α fine focus tube and using a pinhole-collimated Worhus camera. The sample was a powder held in a 0.5mm Lindemann tube.

Table 7.4 X-ray diffraction pattern of cadmium stearate, with the assignments based on an orthorhombic structure.

Plane spacing /Å	Possible assignments	n
48.60	001	1
24.30	001	2
16.20	001	3
12.15	001	4
9.72	001	5
8.10	001	6
7.36	010	1
7.28	011	1
6.94	001	7
6.08	001	8
5.40	001	9
5.06	100	1
4.45	?	?
4.18	110	1
3.91	?	?
3.68	020	1
1.87	?	?

The pattern was assigned assuming an orthorhombic unit cell using an indexing program called INDEXING developed by

W. Paszkowicz (7). This gave orthorhombic unit cell dimensions of $a_0=5.05\text{\AA}$, $b_0=7.36\text{\AA}$ and $c_0=48.6\text{\AA}$. As can be seen from table 7.4, the higher orders of the 001 reflection extend into the wide angle region of the diffraction pattern, making interpretation very difficult. Table 7.4 also shows several diffraction lines in the region of $\approx 4\text{\AA}$. The two lines at 4.18 and 3.68 \AA are consistent with an orthorhombic crystal lattice (8) which gives strong reflections from the {110} and {020} planes. The additional lines at 4.45 and 3.91 \AA have two possible origins, triclinic or monoclinic crystal lattices. Turner-Jones (9) observed X-ray diffraction lines at 4.55 and 3.80 \AA in the triclinic crystalline forms of various n-paraffins and polyethylene. These lines were indexed to the {010} and {100} planes respectively. Seto et al (10) used X-ray diffraction to observe the phase transition and deformation process in oriented polyethylene. The phase transition was from orthorhombic to monoclinic and was achieved by straining the polyethylene sample. Without the sample being strained the {110} and {020} of the orthorhombic lattice can be clearly seen in the diffraction pattern. When the sample is strained two additional diffraction lines appear at 4.55 and 3.85 \AA , which have been assigned by Seto to monoclinic {001} and {200} planes respectively.

Von Sydow (11) investigated the X-ray diffraction patterns of various n-fatty acids. These showed 7 possible crystal structures depending on the chain length and odd/even carbon number effects. None gives a particularly close match to cadmium stearate, but the β -form of stearic acid, which has a monoclinic unit cell with orthorhombic sub cell has two

lines in the pattern at 4.2 and 3.8Å¹ which could be equivalent to the 4.45 and 3.91Å reflections in cadmium stearate.

Goto and Asada (12) found that the β-form of stearic acid does not adopt an all trans conformation. The bond between carbon atom 2 and carbon atom 3 is in the gauche conformation, which would account for the different LAM 1 modes in the low frequency Raman spectrum of cadmium stearate, if the additional crystalline phase was similar to the monoclinic β-form of stearic acid.

So the additional peaks in the diffraction pattern of cadmium stearate are probably due to a monoclinic crystalline phase, although the presence of a triclinic crystalline phase cannot be ruled out.

¹ The exact position of these lines is unknown, and had to be determined from a diffraction pattern in reference 10.

7.5 References

- 1) W.J. Harrison, M.P. McDonald and G.J.T. Tiddy, *Liquid Crystals* 7, 509, 1990
- 2) P.A. Spegt and A.E. Skoulios, *Acta Cryst.* 16, 301, 1963
- 3) G.S. Hattiangdi, M.J. Vold and R.D. Vold, *Ind. Eng. Chem.* 41, 2320, 1949
- 4) S.J. Spells, I.W. Shepherd and C.J. Wright, *Polymer* 18, 905, 1977
- 5) S.J. Spells and I.W. Shepherd, *J. Chem. Phys.* 66, 1427, 1977
- 6) F. Khoury, B. Fanconi, J.D. Barnes and L.H. Bolz, *J. Chem. Phys.* 59, 5849, 1973
- 7) W. Paszkowicz, *J. App. Cryst.* 20, 166, 1987
- 8) C.W. Bunn, *Trans. Faraday Soc.* 35, 482, 1939
- 9) A. Turner-Jones, *J. Poly. Sci.* 62, S53, 1962
- 10) T. Seto, T. Hara and K. Tanaka, *Jap. J. App. Phys.* 7, 31, 1968
- 11) E. Von Sydow, *Arkiv. for Kemi.* 9, 231, 1956
- 12) M. Goto and E. Asada, *Bull. Chem. Soc. Jap.* 51, 2456, 1978

Chapter 8

8 Discussions and Conclusions	189
8.1 Problems with interpretation	189
8.2 Lithium phenyl stearate	193
8.2.1 Cylinder dimensions	195
8.2.2 Phenyl rotation	196
8.3 Cadmium stearate	197
8.3.1 Crystal Structure	197
8.3.2 Hexagonal phase	199
8.4 Conclusions	201
8.5 References	204

8 Discussions and Conclusions

8.1 Problems with interpretation

One of the major problems with the technique of infrared spectroscopy when used to determine quantitative results, is that of determining the baseline and the number of bands in a multiplet. The interpretation of these factors can give rise to different results, depending on how the data is interpreted.

The method chosen here to analyse the spectrum of LiPS was to attempt to fit a background and methyl peak (the band at 1377 cm^{-1}) to the original spectrum using the Mattson peak generation program. Figure 8.1 shows the spectrum of LiPS at 25°C as well as the fitted spectrum. Two peaks were required for a reasonable fit in the region 1380 to 1370 cm^{-1} . The fitted spectrum was then subtracted from the original spectrum, and the resultant spectrum had its baseline corrected to give a zero intensity baseline. Figure 8.2 shows the subtracted spectrum of LiPS at 25°C with the baseline corrected and also a synthetically generated methyl band (at 1377 cm^{-1}), which was used as part of the subtraction procedure. The integrated intensities thus determined by this method were then used to determine numbers of defects.

The problems with this method are two fold: Has the correct baseline been applied, and were the numbers of peaks fitted into the experimental spectrum correct? The answer to the above questions is uncertain, as the baseline depends on the points in the experimental data used for its determination. As for the number of peaks used, this again is uncertain, as a good fit does not necessarily mean the

correct number of peaks have been used. So the results gathered from same spectrum could be interpreted differently by different methods, but as long as a consistent method is used in calculating integrated intensities then problems should be kept to a minimum.

Other methods of interpretation can be used: for example Senak et al (1) used a peak fitting algorithm to determine the peak intensity of bands in the CH_2 defect wagging of the spectrum, 1390 to 1330 cm^{-1} . By subtracting a straight line baseline from 1390 to 1330 cm^{-1} and then assuming only 4 peaks were present in this portion of the spectrum, the peak fitting algorithm produced a very good fit to the experimental data.

The resulting data, for liquid n-alkanes, showed the number of gg defects increased with temperature in line with the rotational isomeric state model, but the number of gtg defects decreased with increasing temperature, which is contrary to the rotational isomeric state model. The difference between the RISM and the experimental results of Senak could be explained by the baseline used, giving larger or smaller intensity for individual bands than is in fact the case. Also Senak assumes that there are only four peaks present in this portion of the spectrum and that these peaks are symmetrical. Maroncelli et al (2) showed that is not in fact the case, with the frequency of the gtg/gtg' defect mode having a small dependence on the position of the defect along the chain, giving rise to asymmetrical bands. So different methods chosen to interpret data can give different results, so care is needed when analysing infrared and Raman data.

Figure 8.1 The infrared spectrum of Lithium Phenyl Stearate at room temperature and the fitted spectrum containing the background and the methyl vibration.

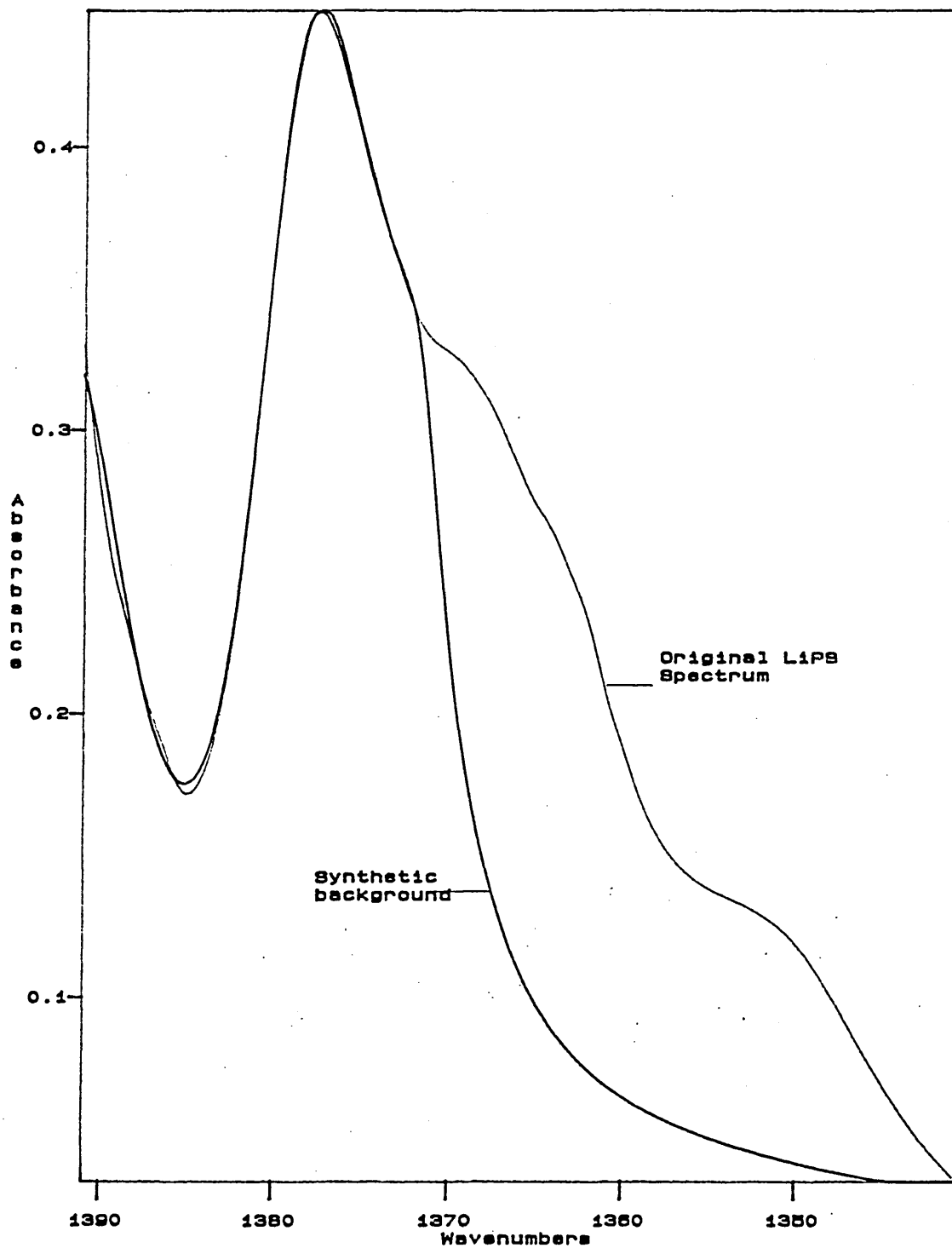
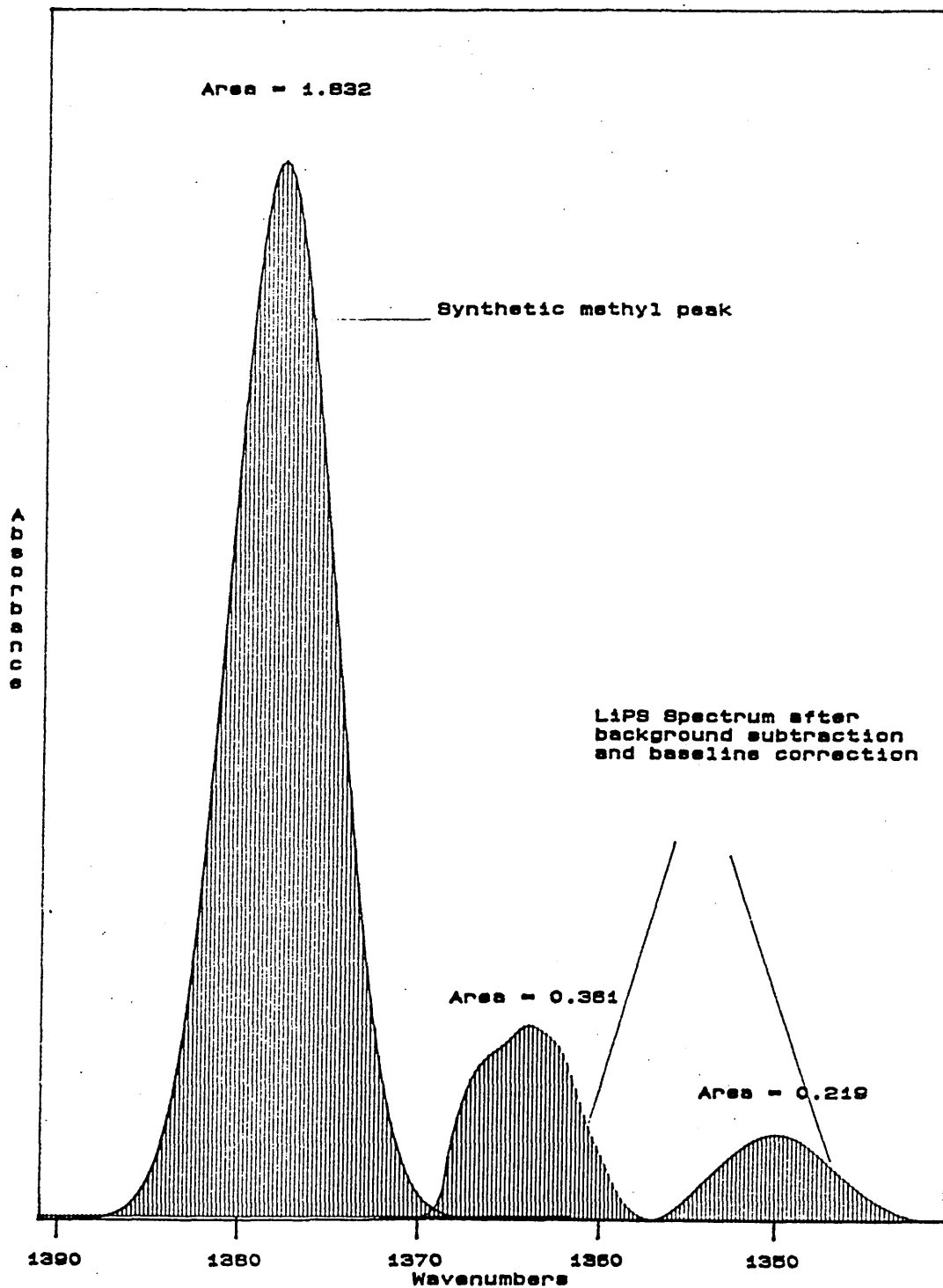


Figure 8.2 The subtracted spectrum of Lithium Phenyl Stearate, with the baseline corrected, and also the synthetic methyl band used in the subtraction.



8.2 Lithium phenyl stearate

The CH_2 wagging region of the infrared spectrum of lithium phenyl stearate shows some interesting variations on what would be expected for a straight chain hydrocarbon without the additional phenyl group. The additional band present at 1363 cm^{-1} (see section 5.3) is one such case. We assumed that the band could have one of four possible origins:-

- i) The band results from a chain conformation that is specifically found in the reverse hexagonal phase.
- ii) The band is due to a weak phenyl group vibration which had not been previously assigned.
- iii) The band is due to the phenyl group decoupling the carbon backbone into effectively two shorter chains which could give rise to different $\text{gtg/gtg}'$ wagging frequencies.
- iv) The phenyl groups prevents certain bonds adopting true rotational isomeric state conformations.

Having examined the infrared spectrum of cadmium stearate in the reverse hexagonal phase (section 6.3), no band at 1363 cm^{-1} was found, so option i) can be eliminated as the source of this additional band. Similarly the infrared spectrum of phenyl undecanoic acid (section 6.2) shows no sign of a band at 1363 cm^{-1} ruling out option ii).

The infrared spectrum of various n-fatty acids, n-pentanoic acid to n-nonanoic acid (see section 6.3) were investigated to determine the effect of chain length on frequency. The longer chain n-fatty acids were not

investigated, as these have been shown by Zerbi et al (3) to have gtg/gtg' defect frequencies of approximately 1369 cm^{-1} , while only n-fatty acids with six or more carbon atoms are expected to show any gtg/gtg' defects (see section 4.1.2). This reduced the possible range of chain lengths that can have an effect on the frequency of the gtg/gtg' defect. The results show that although the frequency of the gtg/gtg' CH_2 defect vibration at around 1369 cm^{-1} may vary slightly with chain length, it never becomes as low as 1363 cm^{-1} . So option iii) can be rejected as the possible source of the band at 1363 cm^{-1} .

The molecular modelling of an individual phenyl stearic acid molecule using Moly '86 (see section 4.3.3), showed that most of the carbon-carbon bonds in the aliphatic backbone are unaffected by the presence of the phenyl group. There are, however, two bonds on either side of the phenyl group which are prevented from adopting true rotational isomeric state conformations. From the model the probability of these bonds adopting a conformation containing gg or g'g' is much lower than that for an n-alkane, but the probability of a gtg or gtg' conformation is more or less unchanged.

If the results from the Moly '86 model are correct then it should be possible to see the difference in the experimentally determined number of defects for LiPS by comparison with rotational isomeric state model predictions (see section 5.3.2). On reaching the phase transition at $\approx 130^\circ\text{C}$, the number of gtg defects obtained experimentally for LiPS is the same ^{as} would be expected for an isotropic n-alkane of equivalent chain length. The number of gg defects,

however, is lower than expected for an isotropic n-alkane of equivalent length, and this tends to indicate that some of the bonds are prohibited from, or have a lower probability of adopting, a gg or g'g' defect.

The conclusion that can be drawn from this is that the additional band at 1363 cm^{-1} present in the infrared spectrum of LiPS is most likely caused by the inability of bonds near the phenyl group to adopt a true rotational isomeric state conformation. For crystalline polyethylene, there is evidence for similar behaviour. Spells et al (4) assigned a band at 1346 cm^{-1} to a tight fold and Ungar et al (5) showed this tight fold was a tight {110} fold. The defects in the fold can be approximated to a gtggg'g' defect. Distortion away from true gg and g'g' defects accounts for the shift from 1352 cm^{-1} to 1346 cm^{-1} (a similar amount to the shift observed in LiPS from 1369 cm^{-1} to 1363 cm^{-1}). Similarly, for LiPS, it appears from the discussion above that the bonds near the phenyl group are prevented from adopting gg or g'g' defects.

8.2.1 Cylinder dimensions

The double helix model proposed in section 4.2.1 gave the radius of the ionic core of LiPS as between 5.6 and 7.1Å. When the average chain length of the aliphatic portion of the LiPS molecule is calculated, this gives an overall cylinder diameter of 33.9 to 36.8Å at 25°C , 30.8 to 33.8Å at 123°C and 30.2 to 33.2Å at 135°C (see Table 5.2). The hexagonal lattice parameter, a , determined by Harrison et al (6), 35.9Å at 25°C , 36.1Å at 123°C and 31.4Å at 135°C .

The dimensions estimated from infrared spectroscopy and X-ray diffraction at room temperature give very good

agreement, giving confidence in the model used to calculate the ionic core radius R_c . As the temperature is increased to 123°C the cylinder diameter decreases to between 30.8 and 33.8Å, while the cylinder centre-to-centre distance, determined by X-ray diffraction, remains approximately constant at 36.1Å. As the phase transition begins, the hexagonal lattice parameter, a , changes to 31.4Å while the cylinder diameter lies in the range 30.2 to 33.2Å. Hence, at the phase transition a changes abruptly from the cylinder diameter at 25°C to the cylinder diameter at 135°C. i.e. the hexagonal lattice parameter characterises the phase, whereas the cylinder diameter determined by infrared spectroscopy changes continuously.

Another curious fact is that the aliphatic portion of LiPS becomes "isotropic" at the temperature where the phase transition begins. It seems unlikely that these two events are coincidental, but the mechanism linking the two is uncertain and is a field for further investigation. There is the possibility that the "melting" of the aliphatic chain allows the ionic core more rotational and translational freedom, thus allowing the core to rearrange. It is known that the aliphatic portion of LiPS, even after "melting" must still have an influence on the phase and phase transition temperatures, as lithium stearate becomes an isotropic liquid at 219°C (7), while LiPS does not become an isotropic liquid until 370°C (6).

8.2.2 Phenyl rotation

The molecular modelling results from section 4.3.4 show that the phenyl group is restricted to a maximum angle of

oscillation of 60° . A comparison of the NMR spectra of phenyl stearic acid and 1-phenyl heptane (see section 7.4), reveals a small increase in the overall bandwidth of the phenyl hydrogen rotations (the phenyl group of 1-phenyl heptane is expected to be able to go through a complete rotation), but individual bands do show an increase in the bandwidth from 1-phenyl heptane to phenyl stearic acid, but this could be due to the number of isomers present in phenyl stearic acid. So the evidence for restricted rotation comes only from modelling and the literature (8), although the infrared results for LiPS (see section 5.3.2) do seem to confirm the modelling data.

8.3 Cadmium stearate

8.3.1 Crystal Structure

The infrared, Raman, DSC and X-ray data all show that there are two crystal forms present in the cadmium stearate sample used. The 720 cm^{-1} CH_2 rocking vibration in the infrared spectrum of crystalline cadmium stearate shows that the band splits into several components as a result of crystalline interactions (see section 6.3.2). The band at 730 cm^{-1} is usually associated with an orthorhombic crystal lattice (9), while the bands at 711 and 703 cm^{-1} show that there could be additional crystal forms present (possibly monoclinic, see section 7.4).

The low frequency Raman spectrum of cadmium stearate (see section 7.2.2) shows there are two LAM 1 modes, which could be either due to impurities or two crystal forms. The purity of the sample used was found to be 98.3%, so the possibility of impurities can be ignored. The additional band

is consistent with the results of Khoury et al (10) who observed slightly different frequencies for the orthorhombic and the monoclinic forms of $n\text{-C}_{36}\text{H}_{74}$. For $n\text{-C}_{36}\text{H}_{74}$ the frequency of the LAM 1 band for the orthorhombic form is 66.1 cm^{-1} and for the monoclinic form is 68.8 cm^{-1} ; although this does not confirm conclusively the additional crystal structure in cadmium stearate is monoclinic. Also the frequency of the two LAM 1 modes are 49.2 and 54.0 cm^{-1} , and the LAM 1 frequency for the n-alkanes $n\text{-C}_{18}\text{H}_{38}$ and $n\text{-C}_{36}\text{H}_{74}$ are 132.2 and 66.1 cm^{-1} respectively (10). The fact that the frequency of the cadmium stearate LAM 1 mode is close to that for $n\text{-C}_{36}\text{H}_{74}$ indicates that the stearate ions extend almost fully from the cadmium ion in opposite directions.

The X-ray diffraction pattern of cadmium stearate showed a series of diffraction lines in the region of $\approx 4\text{\AA}$. The two lines at 4.18 and 3.68\AA are consistent with an orthorhombic crystal lattice (11). The additional lines at 4.45 and 3.91\AA have two possible origins, triclinic or monoclinic crystal lattices. Turner-Jones (12) observed X-ray diffraction lines at 4.55 and 3.80\AA in the triclinic crystalline forms of various n-paraffins and polyethylene. These lines were indexed to the $\{010\}$ and $\{100\}$ planes respectively. Seto et al (13) used X-ray diffraction to observe the orthorhombic and monoclinic phases in strained polyethylene. The 110 and 020 peaks of the orthorhombic lattice can be clearly seen in the diffraction pattern. There are also two additional diffraction lines at 4.55 and 3.85\AA , which have been assigned by Seto to monoclinic $\{001\}$ and $\{200\}$ planes respectively.

The fact that the monoclinic and triclinic polyethylene

samples have diffraction lines that are close to each other makes the prediction of crystal lattice very difficult. The long spacing of the orthorhombic and the other crystalline form present in cadmium stearate are so close that they are indistinguishable (ie. only one long spacing is observed in the X-ray pattern), which would tend to favour the assignment of a monoclinic lattice to the other phase present in the cadmium stearate sample.

Goto et al (14) found that the monoclinic β -form of stearic acid has a gauche conformation at the bond between carbon atom 2 and carbon atom 3. Khoury et al (10) found that the difference in frequency of the LAM 1 modes of $n\text{-C}_{36}\text{H}_{74}$ in the orthorhombic phase and in the monoclinic phase with 1 gauche conformation present is 2.7 cm^{-1} . The difference in the frequency of the LAM 1 modes present in the Raman spectrum of cadmium stearate is 4.8 cm^{-1} , so if the additional phase present in cadmium stearate is similar to the β -form of stearic acid, then there will be two gauche defects present in each molecule. So if one gauche shifts the frequency of an n -alkane by 2.7 cm^{-1} then it would be expected that two gauche would approximately double this value, which is consistent with what happens with cadmium stearate. With the X-ray data and the Raman data taken into account the most likely structure of the other crystalline phase present in cadmium stearate is monoclinic, but this is by no means certain.

8.3.2 Hexagonal phase

The number of gtg and gg defects present in the hexagonal phase of cadmium stearate at 120°C (within experimental error), was determined to be the same as values

determined from an isotropic chain of equivalent chain length at 120°C, calculated from the rotational isomeric state model. The number of defects present corresponds to an average chain extension of 9.5Å. With core radius, as determined in section 4.2.1, of 4.9 to 6.32Å, the total cylinder dimension of cadmium stearate is between 28.8Å and 31.7Å. Spegt (14) determined the hexagonal lattice parameter of cadmium stearate to be 36.9Å. This appears to leave a gap of about 5Å between adjacent cylinders.

The probability of the chain extending beyond the average chain extension of 9.5Å is 0.40 and the probability of the chain extending out to come into contact with the neighbouring cylinder (a distance of 12.13Å) is 0.22. This shows that a significant proportion of chains from neighbouring cylinders are in contact, but unlike LIPS the average dimensions of the cylinders are not in contact. This leads to the possibility that the model for calculating the core radius of the divalent metal soaps is wrong. The assumption that the stearate ions attached to the cadmium ion behave like two independent monovalent soap molecules is probably incorrect, but the work would have to be extended to other divalent metal soap systems which form reverse hexagonal phases, such as calcium stearate, to correct the model. This can be achieved by determining the maximum chain extension of the aliphatic portion of the molecule using infrared spectroscopy. The lattice parameter, a , and number of ions per unit length, n , for cadmium and calcium stearate have already been determined by Spegt and Skoulios (14,15). By subtracting the lattice parameter from the maximum chain

extension the ionic core radius can be found, thus allowing the correction of the model in section 4.2.1 for divalent metal soaps.

8.4 Conclusions

The infrared results for lithium phenyl stearate show that the aliphatic portion of the soap molecule is much more ordered at room temperature than had been thought (6), having only 0.62 and 0.60 gtg and gg defects per molecule respectively when an isotropic chain would have 1.35 and 1.21 gtg and gg defects per chain respectively. As the temperature is increased the number of conformational defects increases continuously, until at 123°C the chain reaches an isotropic disorder. At this point the phase transition begins, so the chain has to reach liquid like disorder before the phase transition begins^{and} whether these two events are just coincidental is not certain.

The modelling of the phenyl stearic acid showed both that the phenyl group was restricted to certain angles of rotation, and that bonds close to the phenyl group were prevented from attaining true rotational isomeric state conformations. This showed that the gtg defect was distorted slightly from its usual angular positions and the gg defect had a much reduced probability of occurring near the phenyl group. The infrared spectrum showed an additional band at 1363 cm⁻¹ which has been assigned to a distorted gtg/gtg' defect. The number of gg defects present at the phase transition was only 75% of those expected for an isotropic n-alkane of equivalent chain length and at the same temperature. This would tend to confirm the fact that the

four bonds nearest to the phenyl group have a reduced probability of forming a gg defect.

The modelling of the ionic core of LiPS appears to give a reasonable estimate of the core radius. When this is used to calculate the dimensions of the LiPS lattice, at room temperature, along with the average chain extension, it gives a value for the hexagonal cylinder diameter of between 33.9 to 36.8Å. When this is compared with the hexagonal lattice parameter determined by X-ray diffraction, which has a value 35.9Å, the results fall within the error range. Also after the LiPS sample has gone through the phase transition beginning at $\approx 130^{\circ}\text{C}$, the hexagonal lattice parameter is 31.4Å and the cylinder diameter determined from infrared data lies between 30.2 and 33.2Å.

Cadmium stearate in the crystalline state contains two crystal forms, orthorhombic which has lattice dimensions of $a_0=5.05\text{\AA}$, $b_0=7.35\text{\AA}$ and $c_0=48.6\text{\AA}$ and the other either monoclinic or triclinic, with monoclinic the most probable. However this has not been proved conclusively. In the reverse hexagonal phase, cadmium stearate behaves like an isotropic phase n-alkane of equivalent chain length and at the same temperature. The model used to predict the core radius of divalent metal soaps appears to be in error. The cylinder dimensions estimated from the average chain extension and the core radius gives a result between 28.8Å to 31.7Å, while the lattice parameter determined by X-ray diffraction gives a value of 36.9Å. This leads to the conclusion that the assumption that the n-carboxylate ions in a divalent metal soap behave like two independent monovalent metal ion soaps

8.5 References

- 1) L Senak, M. A. Davis and E. Mendelsohn, J. Phys. Chem. 95, 2565, 1991
- 2) M. Maroncelli, S.P. Qi, H.L. Strauss and R.G. Snyder, J. Am. Chem. Soc. 104, 6237, 1982
- 3) G. Zerbi, G. Conti and G. Minoni, J. Phys. Chem. 91, 2386, 1987
- 4) S.J. Spells, S.J. Organ, A Keller and G. Zerbi, Polymer 28, 679, 1987
- 5) G. Ungar and S.J. Organ, Polymer Com. 28, 232, 1987
- 6) W.J. Harrison, M.P. McDonald and G.J.T. Tiddy, Liquid Crystals 7, 509, 1990
- 7) B. Gallot and A. Skoulios, Kolloid Z. and Z. Polymere 209, 164, 1966
- 8) A.E. Tonelli, Macromolecules 5, 683, 1973
- 9) D. Chapman "The structure of lipids", Methuen, London, 1965
- 10) F. Khoury, B. Fanconi, J.D. Barnes and L.H. Bolz, J. Chem. Phys. 59, 5849, 1973
- 11) C.W. Bunn, Trans. Faraday Soc. 35, 482, 1939
- 12) A. Turner-Jones, J. Poly. Sci. 62, S53, 1962
- 13) T. Seto, T. Hara and K. Tanaka, Jap. J. App. Phys. 7, 31, 1968
- 14) P.A. Spegt and A.E. Skoulios, Acta Cryst. 16, 301, 1963
- 15) P.A. Spegt and A.E. Skoulios, Acta Cryst. 17, 198, 1964

Courses and conferences

Courses attended

- i) M.Sc. Chemistry, molecular spectroscopy.
- ii) B.Sc. Chemistry (Sheffield University), Symmetry and vibrational spectroscopy.
- iii) Liquid Crystal discussion group (Sheffield University).

Conferences attended

- i) Sira, Infrared technology and applications: Fourier transform infrared spectroscopy, London, June 1988
- ii) British Liquid Crystal Society annual conference, Sheffield, April 1989
- iii) Royal Society of Chemists annual conference, Hull, March 1990
- iv) British Liquid Crystal Society annual conference, Bristol, April 1990, Poster presentation given.